EXPLAINING EXTREME EVENTS OF 2018

From a Climate Perspective

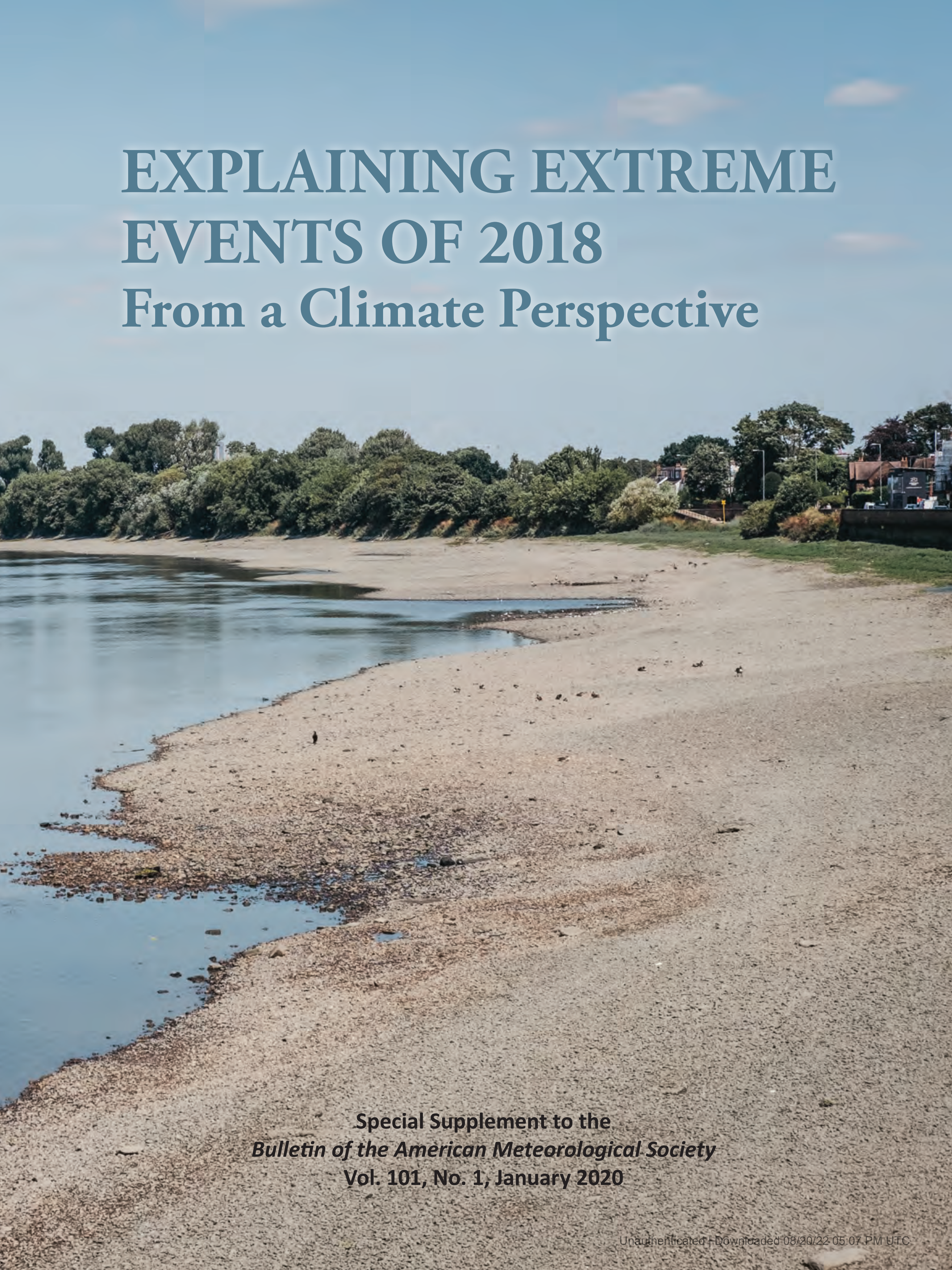

Special Supplement to the
Bulletin of the American Meteorological Society
Vol. 101, No. 1, January 2020

EXPLAINING EXTREME EVENTS OF 2018 FROM A CLIMATE PERSPECTIVE

Editors

Stephanie C. Herring, Nikolaos Christidis, Andrew Hoell,
Martin P. Hoerling, and Peter A. Stott

***BAMS* Special Editors for Climate**

Andrew King, Thomas Knutson,
John Nielsen-Gammon, and Friederike Otto

Special Supplement to the

Bulletin of the American Meteorological Society

Vol. 101, No. 1, January 2020

American Meteorological Society

Corresponding Editor:

Stephanie C. Herring, PhD
NOAA National Centers for Environmental Information
325 Broadway, E/CC23, Rm 1B-131
Boulder, CO, 80305-3328
E-mail: stephanie.herring@noaa.gov

Cover Credit: iStock.com/Alena Kravchenko—River Thames receded during a heatwave in summer 2018 in London, United Kingdom.

HOW TO CITE THIS DOCUMENT

Citing the complete report:

Herring, S. C., N. Christidis, A. Hoell, M. P. Hoerling, and P. A. Stott, Eds., 2020: Explaining Extreme Events of 2018 from a Climate Perspective. *Bull. Amer. Meteor. Soc.*, **101 (1)**, S1–S128, doi:10.1175/BAMS-ExplainingExtremeEvents2018.1.

Citing a section (example):

Mahoney, K., 2020: Extreme Hail Storms and Climate Change: Foretelling the Future in Tiny, Turbulent Crystal Balls? [in "Explaining Extremes of 2018 from a Climate Perspective"]. *Bull. Amer. Meteor. Soc.*, **101 (1)**, S17–S22, doi:10.1175/BAMS-D-19-0233.1.

TABLE OF CONTENTS

THE NORTHERN CALIFORNIA 2018 EXTREME FIRE SEASON

Timothy Brown, Steve Leach, Brent Wachter, and Billy Gardunio

The fire season of 2018 was the most extreme on record in Northern California in terms of the number of fatalities (95), over 22,000 structures destroyed, and over 600,000 ha burned (https://www.fire.ca.gov/media/5511/top20_destruction.pdf; accessed 24 November 2019). The most deadly and destructive fire in California history, the Camp Fire, occurred in Butte County in the Sierra Nevada foothills in early November, and caused 85 fatalities and destroyed nearly 19,000 structures. The largest fire complex in state history, the Mendocino Complex, which included the Ranch fire, the largest single fire in state history, burned nearly 186,000 ha. It occurred in July and August, killing one firefighter. In western Shasta County nearly 138,000 ha burned from July through September in the Carr, Hirz, and Delta Fires. These fires caused multiple closures of Interstate 5 and exhibited some of the most extreme fire behavior ever observed in California. The Carr Fire caused eight fatalities, including two firefighters and two workers supporting firefighting efforts, burned over 1,100 homes in west Redding, caused the evacuation of one-third of the city, and produced an extreme fire vortex with an Enhanced Fujita scale rating between 136 to 165 mph, making it arguably the strongest tornado type event in state history, and one of the strongest documented cases in the world (Lareau et al. 2018).

Actual weather during the onset of these large fires was not outside of what would normally be expected during periods of higher fire danger that occur during most fire seasons, as opposed to the extreme offshore wind event that led to the October 2017 wine country fires (Nauslar et al. 2018). The Tubbs fire during that period caused 22 fatalities and the loss of 5,636 structures, and at the time was California's most destructive fire on record dating back to the early 1900s. Instead, a series of climate and fuels conditions aligned to create an exceptional and explosive fire environment between June to November 2018 in naturally fire-prone areas with a substantial wildland–urban interface—a zone where human development meets and intermingles with wildland fuels.

AFFILIATIONS: Brown—Western Regional Climate Center, Desert Research Institute, Reno, Nevada; Leach—Bureau of Land Management, Redding, California; Wachter and Gardunio—USDA Forest Service, Redding, California
CORRESPONDING AUTHOR: Timothy Brown, tim.brown@dri.edu

DOI:10.1175/BAMS-D-19-0275.1

CLIMATE AND FUELS. Climate enables fire and weather drives fire. The 2018 Northern California fire season origins began during the winter of 2016/17. Precipitation, which was much above normal, exceeded the 90th percentile ranking across much of the state at low to middle elevations. Some of the higher elevations in the Sierra Nevada range were the wettest on record. November through April is climatologically the wet season in northern California. This particular wet winter ended the statewide hydrologic drought from 2011–17. The significance of this wet season was that it led to the second consecutive spring with above average fine fuel (grasses) crop across much of Northern California.

The 2017–18 Northern California wet season was drier than normal, and temperatures were generally above normal, with the warmest conditions from the Cascade–Sierra foothills through the Sacramento Valley and into the northern Coast Range. A lack of stormy weather during this period allowed above normal standing carry-over fine fuels from the previous wet year. April 2018 was warmer and wetter than normal. This was perfectly timed to produce above normal spring brush growth and grow a record fine fuel crop at elevations below 1,200 m, despite the overall wet season rainfall deficit (Fig. 1). This was the third straight spring with an above average fine fuel crop based on data taken at the University of California Sierra Foothill Research and Extension Center. The Brown's Valley, California, research station forage production data have been reported continuously since the 1979/80 growing season. Three straight above normal growing seasons had not occurred in the dataset prior to the 2017/18 growing season. Peak forage production toward the end of spring was 150% of normal (https://ucanr

Fig. 1. Photo of fine fuel grass loading taken on 12 Sep 2018 about 60 miles northwest of the Camp Fire location. Left of the fence line shows a continuous bed of fine fuel. The paddock to the right of the fence line has less fuel due to grazing. Photo: Brent Wachter, Predictive Services.

.shinyapps.io/SFREC_Web_Application/; accessed 24 November 2019) and the maximum value during the 40-yr history. As a testament to the abundant and continuous fine fuel growth, firefighters during 2018 often described arriving to a larger fire compared to what was normally observed during initial attack situations, thus making the fires harder to contain (Northern California Predictive Services, personal communication, 24 July 2019).

The summer of 2018 in Northern California had two notable climate anomalies—lack of rain and warmer than average temperatures. This led to a rapid curing of the annual fine fuels and drying of live fuels. For the most part, rain shut off in late April and did not return until late November. In the Sacramento Valley and foothills only two light rain events produced approximately 15 mm each, one in late May and the other in late September to early October. The lack of precipitation from late spring through the middle of November caused fuels to dry out to record levels.

The summer of 2018 was warmer than average in Northern California. Afternoon maximum temperatures were not extraordinarily high compared to 2017. Rather, it was the warm morning minimum temperatures that pushed the overall average temperature in July 2018 to record high levels. Record high lows for California were observed in July, continuing a positive trend of nighttime warming since 1895, (https://www.climate.gov/news-features/event-tracker/extreme-overnight-heat-california-and-great-basin-july-2018; accessed 24 November 2019). These warm temperatures led to more nights of poor overnight humidity recovery, which has direct implications on the flammability of fuel. The poor recoveries led to unusually long active burn periods during the overnights and set the stage for earlier active burning during the daytime hours. This created more hours of active to extreme fire behavior and provided less opportunity for direct attack by firefighters (Northern California Predictive Services, personal communication, 24 July 2019).

WEATHER. Long periods dominated by strong high pressure occurred in July, which hastened the summer drying of fuels. The hottest day of the year in the Sacramento Valley was 26 July, setting all-time records for the date, and was a key element in the conditions that rapidly brought the Carr Fire into Redding, California. Other large-scale fires started that week as well, including the Mendocino Complex. Interestingly, temperatures were slightly cooler than normal during August and September in areas where thick smoke from nearby wildfires persisted for unusually long periods. Northern California had a very low occurrence of lightning during the 2018 fire season. Roughly 12,000 lightning strikes were recorded during the fire season, compared to the long-term average of more than 30,000 strikes (in Northern California lightning accounts for the majority of fire ignitions, while in Southern California human causes dominate ignitions; Balch et al. 2017). Dry offshore wind events, which typically increase in occurrence after the middle of September, occurred with fuels at extreme and record dry levels. The Camp Fire on 8 November was the result of an ignition occurring in extremely dry fuels during an enhanced strong and dry downslope wind pattern.

FIRE ENVIRONMENT. The precipitation deficit at the close of the 2017/18 rainy season combined with drier and warmer than normal summer conditions caused an expansion and intensification of short-term drought across northern California. The Evaporative Demand Drought Index (EDDI; Hobbins et al. 2016; McEvoy et al. 2016) clearly illustrates the intensity of short-term drought conditions during late July when significant fires started (Fig. 2a), and even more so in November as dry northeast/offshore wind patterns became more frequent and the Camp Fire broke out (Fig. 2b). Evaporative demand relates to the thirst of the atmosphere which directly corresponds to fuel stress (higher values equate to more stress). There is a close correlation between EDDI values and fire danger (McEvoy et al. 2019) including extreme fire behavior and spread rates. EDDI comprises inputs of temperature, humidity, wind speed, and solar radiation. These are also key factors in determining dead fuel moisture calculated in the newly updated National Fire Danger Rating System (https://gacc.nifc.gov/eacc/predictive_services/fuels_fire-danger/documents/Overview%20of%20NFDRS2016%20and%20Implementation%20and%20Evaluation.pdf; accessed 24 November 2019). Starting in late July, fire danger indicators in northern California such as the energy release component (the amount of energy at the head of fire's flaming front) approached all-time record high values accentuating the impact of the anomalously warm and dry summer on fuels. In effect, fuel regimes found at all elevations (sea level to over 3,000 m) had a large fire potential by July.

SUMMARY. Both 2017 and 2018 were extreme fire years in California. While this paper has focused on Northern California in 2018, Southern California that year also saw its share of extreme fire including the Ferguson (two firefighter fatalities, 19 structures destroyed, and approximately 39,000 ha burned), Cranston, and Holy Fires. On the same day as the Camp Fire, 8 November, two large fires developed in Ventura and Los Angeles County, including the Woolsey Fire (approximately 39,000 ha burned and over 1,600 structures destroyed). Following the unusually late season December 2017 Thomas Fire in

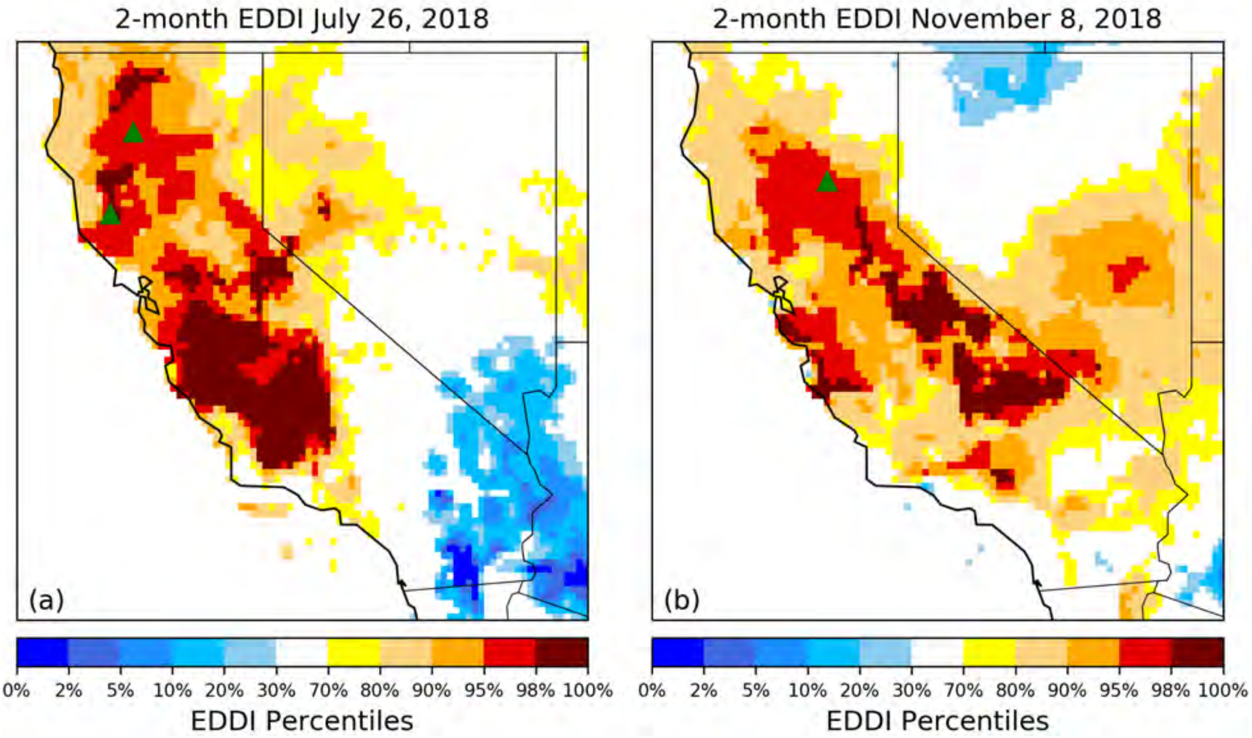

Fig. 2. Evaporative Demand Drought Index 2-month categories for (a) 26 Jul 2018, and (b) 8 Nov 2018. Triangles represent the Mendocino (lower),Carr (upper), and Camp fire locations, respectively.

the Ventura and Santa Barbara county area, a postfire debris flow event occurred over the burn area on 9 January resulting in 23 fatalities and 246 structures destroyed (Oakley et al. 2018).

Climate, fuels, and people are the three confluent factors for California's recent destructive wildfires. The wildland–urban interface has been growing extensively within the state during the past few decades (e.g., Radeloff et al. 2018), placing people in fire-prone areas. Climate is an enabler of wildfire by providing seasonal moisture to grow fuels, and seasonal warming and drying that increases fuel flammability. Increasing temperature trends enable longer and more extreme fire seasons. California's annual temperatures have been increasing substantially during the past four decades and are expected to continue warming this century (California's Fourth Climate Assessment; Bedsworth et al. 2018). Abatzoglou and Williams (2016) have shown that California (as well as all of the West) has had significantly enhanced fuel aridity due to anthropogenic increases in temperature and vapor pressure deficit over the past several decades. This can also be seen in the increasing number of days of fire weather season length based on fire danger indicators (e.g., Jolly et al. 2015). Nighttime temperature trends especially may be playing an important role in more extreme fire behavior. Research is currently underway to examine the specific relationship of this warming to nighttime fuel drying and subsequent extreme fire behavior that was observed during the California 2018 fire season.

An estimated 54% of California ecosystems are fire dependent and most of the rest are fire adaptive (Pyne 2016). California has always had fire given its climate, topography, and distinctive varieties of combustible vegetation. Today it is a state of nearly 40 million people, and one in four Californians live in a "high risk" wildfire area (https://www.latimes.com/local/lanow/la-me-california-braces-for-new-wildfires-20190614-story.html; accessed 24 November 2019). California insured losses in 2018 from wildfire topped \$13 billion (https://www.insurancejournal.com/news/west/2019/05/08/525930.htm; accessed 24 November 2019). The year 2018 now holds the record for the most destructive wildfire, the largest wildfire, and the costliest wildfire season in California state history.

REFERENCES

Abatzoglou, J. T., and A. P. Williams, 2016: Impact of anthropogenic climate change on wildfire across western US forests. *Proc. Natl. Acad. Sci. USA*, **113**, 11 770–11 775, https://doi.org/10.1073/pnas.1607171113.

Balch, J. K., B. A. Bradley, J. T. Abatzoglou, R. C. Nagya, E. J. Fuscod, and A. L. Mahood, 2017: Human-started wildfires expand the fire niche across the United States. *Proc. Natl. Acad. Sci. USA*, **114**, 2946–2951, https://doi.org/10.1073/pnas.1617394114.

Bedsworth, L., D. Cayan, G. Franco, L. Fisher, and S. Ziaja, 2018: Statewide Summary Report. California's Fourth Climate Change Assessment, California Public Utilities Commission Publication SUM- CCCA4-2018-013, 133 pp.

Hobbins, M., A. Wood, D. McEvoy, J. Huntington, C. Morton, M. Anderson, and C. Hain, 2016: The evaporative demand drought index. Part I: Linking drought evolution to variations in evaporative demand. *J. Hydrometeor.*, **17**, 1745–1761, https://doi.org/10.1175/JHM-D-15-0121.1.

Jolly, W. M., M. A. Cochrane, P. H. Freeborn, Z. A. Holden, T. J. Brown, G. J. Williamson, and D. M. J. S. Bowman, 2015: Climate-induced variations in global wildfire danger from 1979 to 2013. *Nat. Commun.*, **6**, 7537, https://doi.org/10.1038/ncomms8537.

Lareau, N. P., N. J. Nauslar, and J. T. Abatzoglou, 2018: The Carr fire vortex: A case of pyrotornadogenesis? *Geophys. Res. Lett.*, **45**, 13 107–13 115, https://doi.org/10.1029/2018GL080667.

McEvoy, D. J., J. L. Huntington, M. T. Hobbins, A. Wood, C. Morton, M. Anderson, and C. Hain, 2016: The evaporative demand drought index. Part II: CONUS-wide assessment against common drought indicators. *J. Hydrometeor.*, **17**, 1763–1779, https://doi.org/10.1175/JHM-D-15-0122.1.

—, M. Hobbins, T. J. Brown, K. VanderMolen, T. Wall, J. L. Huntington, and M. Svoboda, 2019: Establishing relationships between drought indices and wildfire danger outputs: A test case for the California–Nevada drought early warning system. *Climate*, **7**, 52, https://doi.org/10.3390/cli7040052.

Nauslar, N. J., J. T. Abatzoglou, and P. T. Marsh, 2018: The 2017 North Bay and Southern California fires: A case study. *Fire*, **1** (1), 18, https://doi.org/10.3390/fire1010018.

Oakley, N. S., F. Cannon, R. Munroe, J. T. Lancaster, D. Gomberg, and F. M. Ralph, 2018: Brief communication: Meteorological and climatological conditions associated with the 9 January 2018 post-fire debris flows in Montecito and Carpinteria, California, USA. *Nat. Hazards Earth Syst. Sci.*, **18**, 3037–3043, https://doi.org/10.5194/nhess-18-3037-2018.

Pyne, S. J., 2016: *California: A Fire Survey*. The University of Arizona Press, 203 pp.

Radeloff, V. C., and Coauthors, 2018: Rapid growth of the US wildland–urban interface raises wildfire risk. *Proc. Natl. Acad. Sci. USA*, **115**, 3314–3319, https://doi.org/10.1073/pnas.1718850115.

chapter 2

ANTHROPOGENIC IMPACTS ON THE EXCEPTIONAL PRECIPITATION OF 2018 IN THE MID-ATLANTIC UNITED STATES

JONATHAN M. WINTER, HUANPING HUANG, ERICH C. OSTERBERG, AND JUSTIN S. MANKIN

Exceptional January–September total precipitation contributed to flooding across the mid-Atlantic United States from May to September 2018, and was made 1.1 to 2.3 times more likely by anthropogenic climate change.

Flash flooding surged through the old district of Ellicott City, Maryland, on 27 May 2018, turning Main Street into whitewater rapids, upending cars, destroying businesses, and leading to one death (Campbell and Rentz 2018). As of May 2019, damage from the Ellicott City flood had cost $12 million, and the city was considering flood mitigation plans that ranged from $63 to $175 million (Logan 2019). Ellicott City was just one of 12 significant heavy precipitation and flooding events that occurred between May and September of 2018, shattering precipitation records across the region (National Weather Service 2019). Other notable events included 3 June, when eight West Virginia counties declared states of emergency after intense precipitation flooded bridges and washed out roads (Maher 2018), and 21–24 July, when historic rainfall across the Washington, D.C., Metropolitan Area and northern Baltimore County in Maryland resulted in more than a dozen high-water rescues of motorists stranded by flash flooding (Halverson and Samenow 2018). These exceptional heavy rainfall events are consistent with expectations from global warming (Pendergrass 2018) and observed increases in extreme precipitation across the broader northeastern United States (Huang et al. 2017; Hoerling et al. 2016; Frei et al. 2015).

We examine the mid-Atlantic states of Pennsylvania, New Jersey, Maryland, Washington, D.C., Delaware, and West Virginia, which all experienced remarkable total and extreme (99th percentile wet days) precipitation in 2018 that contributed to flooding. For the years 1920–2018, 2018 has the highest or one of the three highest January–September total precipitation amounts at 33% and 62% of stations (Fig. 1a), respectively, and the highest or one of the three highest May–September extreme precipitation amounts at 6% and 13%, respectively (Fig. 1b). Spatially averaged, 2018 has the highest total precipitation on record (1-in-99 year event), while extreme precipitation is the fourth highest (4-in-99 year event), shown in Figs. 1c and 1d. Here, we assess the fraction of 2018 total and extreme precipitation risk attributable to anthropogenic forcing using station observations and a large ensemble of climate simulations.

DATA AND METHODS. Station observations are from the Global Historical Climatology Network-Daily (GHCN-D) dataset (Menne et al. 2012a,b). Our analysis is conducted using the 63 stations in our domain with daily observations that are at least 80% complete for 1920–2018 and 2018 (Fig. 1a). We treat any years less than 80% complete as missing. We choose 1920 as the start date of our analysis to balance spatial and temporal coverage of station data as well as to maximize overlap with climate simulations. We use gridded area averaging following Huang et al. (2017).

To assess the contribution of anthropogenic climate change to the exceptional precipitation of 2018, we use the historical climate simulations from version 1 of the Community Earth System Model (CESM1) under the Large Ensemble Project (LENS) from the

AFFILIATIONS: WINTER AND MANKIN—Department of Geography, and Department of Earth Sciences, Dartmouth College, Hanover, New Hampshire; and HUANG AND OSTERBERG—Department of Earth Sciences, Dartmouth College, Hanover, New Hampshire
CORRESPONDING AUTHOR: Jonathan M. Winter, jonathan.m.winter@dartmouth.edu

DOI:10.1175/BAMS-D-19-0172.1

A supplement to this article is available online (10.1175/BAMS-D-19-0172.2)

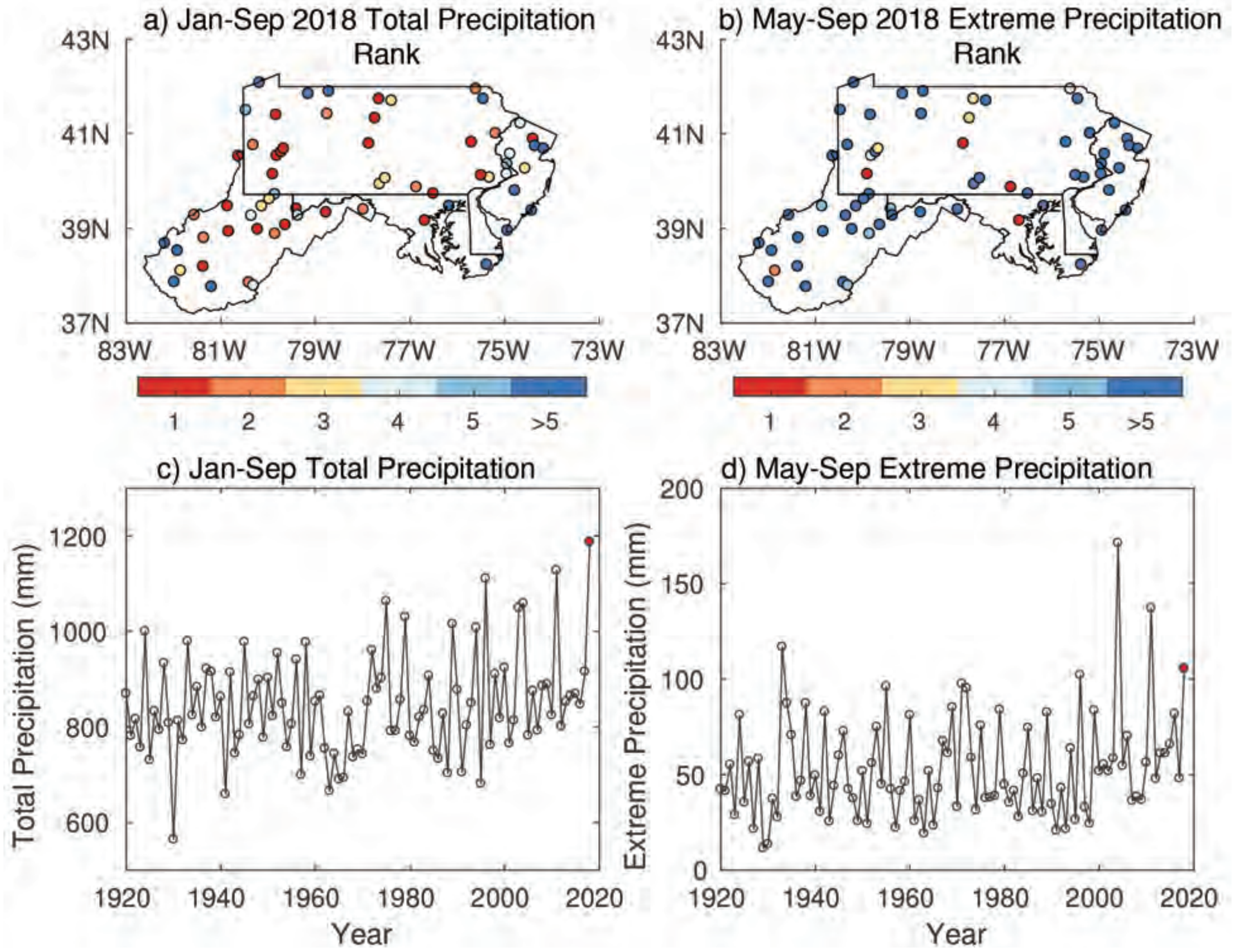

Fig. 1. GHCN-D (a) January to September 2018 total precipitation rank and (b) May to September 2018 extreme precipitation rank by station for 1920–2018. Regionally averaged time series of GHCN-D (c) January to September total precipitation and (d) May through September extreme precipitation. Red dots highlight 2018 precipitation.

National Center of Atmospheric Research (Kay et al. 2015). LENS uses CESM1 at ~1° × 1° spatial resolution to create a single model large ensemble where each run is initialized with a small roundoff error (10^{-14}K) in the atmospheric temperature fields (Kay et al. 2015). As such, each ensemble member is a plausible trajectory of historical climate due to the model's representation of forced and unforced variability, and together the 40 ensemble members provide a much larger range of outcomes from internal variability than either observations or any one model run can provide. We combine historical (1920–2005) and future climate simulations (2006–18) forced with RCP 8.5 to create forty 99-yr transient simulations from 1920 to 2018.

We consider two precipitation metrics that contributed to the extensive mid-Atlantic flooding of 2018. The first is May through September extreme precipitation (hereafter extreme precipitation). We define extreme precipitation as the sum of precipitation falling on the top 1% of wet days (99th percentile wet days) from 1 May to 30 September, because the flooding of interest occurred during those months. The second metric is January through September precipitation (hereafter total precipitation). We define total precipitation as the sum of precipitation 1 January to 30 September, and use it as a proxy for antecedent soil moisture because flooding can be exacerbated by high antecedent soil moisture (Collins 2019; Lapenta et al. 1995). To determine the 99th percentile wet day threshold, we use all wet days (defined as days with precipitation ≥ 1 mm in all 12 months) ranked from highest to lowest. GHCN-D thresholds are calculated by station from 1920–2018, and LENS thresholds are calculated by grid cell from 1920 to 2018. We determine the rank of 2018 for regionally averaged total and extreme precipitation from GHCN-D over the 99-yr record (Fig. 1). From each LENS historical ensemble member time series of total precipitation, we first remove the time-evolving ensemble mean, which represents the externally forced response common to all simulations (Maher et al. 2019), creating anomalies. Then, we add the climatological ensemble mean magnitude of total precipitation from the early part of the record (1920–50) to the anomalies. We repeat the process for extreme precipitation. This creates a 40-member ensemble of regional total and extreme precipitation for 1920–2018 in a counterfactual world without late twentieth century (1951–2018) forcing (hereafter historical reduced forcing). Results are insensitive to the time period used to calculate climatological ensemble mean magnitudes (not shown). We choose to modify LENS historical data as our counterfactual because while CESM1 reasonably captures mid-Atlantic precipitation (Fig. S1), the LENS preindustrial data are substantially wetter than the LENS historical data (not shown), which is inconsistent with paleoclimate data (Ljungqvist et al. 2016).

Using elements of Diffenbaugh et al. (2017), we assess the fraction attributable risk (FAR; Allen 2003; Stott et al. 2016) to anthropogenic climate change by 1) finding the magnitude of total precipitation with the same rank as 2018 in the GHCN-D observations (hereafter similar to 2018) in each of the 40 LENS historical reduced forcing 99-yr time series; 2) averaging those 40 magnitudes to calculate a threshold defining LENS historical reduced forcing total precipitation similar to 2018; 3) using that mean to calculate the probability of total precipitation similar to 2018 in the 40 LENS historical and historical reduced forcing 99-yr time series; and 4) calculating FAR as

$$\mathrm{FAR} = 1 - \frac{P_0}{P_1},$$

where P_0 is the probability of exceeding the threshold of precipitation similar to 2018 in the LENS historical time series conditional on the presence of natural and early twentieth-century anthropogenic forcings (historical reduced forcing), and P_1 is the probability of exceeding the threshold of precipitation similar to 2018 in the LENS historical time series conditional on the presence of natural and full twentieth-century anthropogenic forcings (historical), and P_1/P_0 is the risk ratio (RR). We then calculate FAR for extreme precipitation similar to 2018, and the combined occurrence of total precipitation and extreme precipitation similar to 2018, using the same methodology. We calculate uncertainty around FAR and RR by bootstrapping (Efron and Tibshirani 1986) the 40 ensemble members from the LENS historical data 1,000 times, repeating the analysis above, and determining 95% confidence intervals (CI) using the bootstrap standard error estimate of Paciorek et al. (2018).

RESULTS. LENS reasonably simulates regionally averaged GHCN-D total precipitation [see Fig. S1a in the online supplemental material; $p = 0.29$, Kolmogorov-Smirnov (K-S) test], but not extreme precipitation (Fig. S1b; $p < 0.001$, K-S test). Figure 2 shows the probability and cumulative probability of total precipitation and extreme precipitation similar to 2018 from the LENS historical and historical reduced forcing simulations. These figures indicate that the historical simulations have larger total and extreme precipitation than the historical reduced forcing simulations.

Table 1 shows the fraction of risk attributable to anthropogenic climate change for total and extreme precipitation similar to 2018. The 1-in-99 year total precipitation and 4-in-99 year extreme precipitation mean magnitudes from the historical reduced forcing data are 1070.1 mm and 52.7 mm, respectively. In LENS, the late-twentieth-century anthropogenic forcing is responsible for 35% of 1-in-99 year January to September total precipitation occurrences, and a 1.5 times increase in the likelihood of total precipita-

Table 1. LENS historical reduced forcing (HIST-RF) and historical (HIST) probability of mid-Atlantic total and extreme precipitation similar to 2018, and the resulting risk ratio (RR) and fraction attributable risk (FAR).

Precipitation condition	HIST-RF (P_0)	HIST (P_1)	RR (95% CI)	FAR (95% CI)
Total Jan–Sep	0.68%	1.04%	1.53 (1.09, 2.25)	0.35 (0.17, 0.59)
Extreme May–Sep	3.69%	4.14%	1.12 (1.05, 1.21)	0.11 (0.05, 0.18)
Total Jan–Sep and extreme May–Sep	0.15%	0.23%	1.53 (0.85, 4.65)	0.35 (−0.15, 0.82)

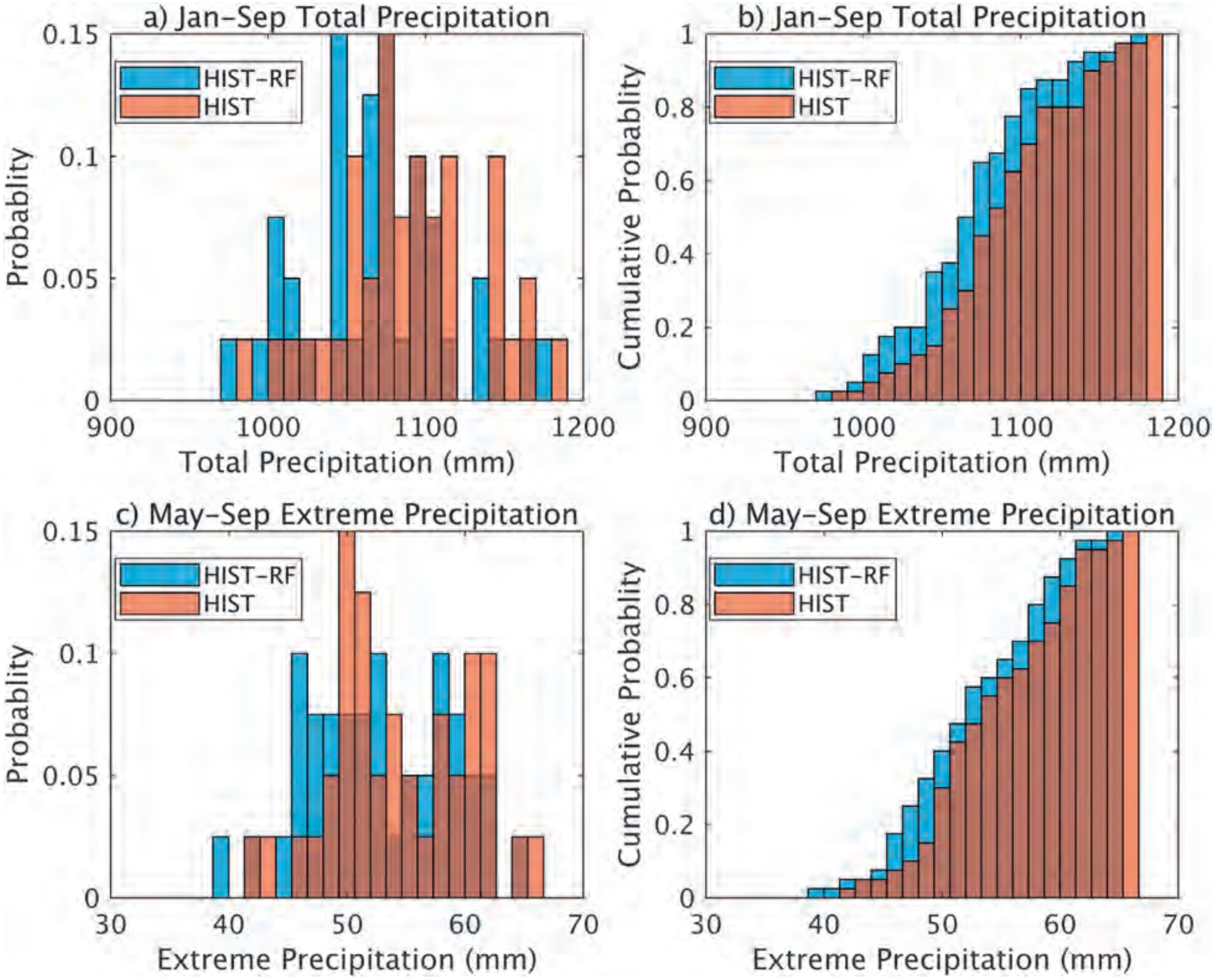

Fig. 2. LENS historical (HIST) and historical reduced forcing (HIST-RF) (a) 1-in-99 year January to September total precipitation probability, (b) 1-in-99 year January to September total precipitation cumulative probability, (c) 4-in-99 year May to September extreme precipitation probability, and (d) 4-in-99 year May to September extreme precipitation cumulative probability.

tion similar to 2018. In addition, 11% of 4-in-99 year May to September extreme precipitation occurrences are attributable to the LENS late-twentieth-century anthropogenic forcing. We find no statistically significant influence of late-twentieth-century anthropogenic forcing on combined 1-in-99 year January to September total precipitation and 4-in-99 year May to September extreme precipitation occurrences. Extreme precipitation FAR should be interpreted with caution given the limitations of LENS historical simulations in accurately representing extreme precipitation when compared to GHCN-D observations (Fig. S1b). We evaluated the sensitivity of our findings to methodology, and find qualitatively similar, but larger, responses to anthropogenic forcing (see the online supplemental material).

CONCLUSIONS. The mid-Atlantic region was impacted by damaging floods throughout the warm season of 2018 (National Weather Service 2019). These floods were associated with the highest total precipitation from January to September and the fourth highest extreme precipitation from May to September for 1920–2018. Contrasting LENS historical and LENS historical reduced forcing, we find that anthropogenic climate change increased the probability of total precipitation associated with the exceptional flooding of 2018 by 1.1 to 2.3 times. Incorporating additional large ensembles, especially from models that better reproduce observed extreme precipitation in the mid-Atlantic, as well as partitioning greenhouse gas and aerosol anthropogenic forcings, would strengthen this attribution.

ACKNOWLEDGMENTS. This work was supported by the Vermont Established Program for Stimulating Competitive Research (NSF Award OIA 1556770). GHCN-D data were provided by NOAA NCEI. LENS data were provided by the National Center for Atmospheric Research CESM Large Ensemble Community Project, with supercomputing resources provided by NSF/CISL/Yellowstone and the University of Toronto, and archiving provided by the Earth System Grid (www.earthsystemgrid.org). We thank Dartmouth Research Computing for their help and administration of the Discovery Cluster.

REFERENCES

Allen, M., 2003: Liability for climate change. *Nature*, **421**, 891–892, https://doi.org/10.1038/421891a.

Campbell, C., and C. Rentz, 2018: How Ellicott City flooded: A timeline. *Baltimore Sun*, 1 June, https://www.baltimoresun.com/weather/bs-md-ellicott-city-flooding-timeline-20180530-story.html.

Collins, M. J., 2019: River flood seasonality in the Northeast United States: Characterization and trends. *Hydrol. Processes*, **33**, 687–698, https://doi.org/10.1002/hyp.13355.

Diffenbaugh, N. S., and Coauthors, 2017: Quantifying the influence of global warming on unprecedented extreme climate events. *Proc. Natl. Acad. Sci. USA*, **114**, 4881–4886, https://doi.org/10.1073/pnas.1618082114.

Efron, B., and R. Tibshirani, 1986: Bootstrap methods for standard errors, confidence intervals, and other measures of statistical accuracy. *Stat. Sci.*, **1**, 54–75, https://doi.org/10.1214/ss/1177013815.

Frei, A., K. E. Kunkel, and A. Matonse, 2015: The seasonal nature of extreme hydrological events in the northeastern United States. *J. Hydrometeor.*, **16**, 2065–2085, https://doi.org/10.1175/JHM-D-14-0237.1.

Halverson, J., and J. Samenow, 2018: Here's how Saturday's storm unleashed a historic July deluge in Washington. Washington Post, 22 July, https://www.washingtonpost.com/news/capital-weather-gang/wp/2018/07/22/heres-how-saturdays-storm-unleashed-a-historic-july-deluge-in-washington/.

Hoerling, M., J. Eischeid, J. Perlwitz, X.-W. Quan, K. Wolter, and L. Cheng, 2016: Characterizing recent trends in U.S. heavy precipitation. *J. Climate*, **29**, 2313–2332, https://doi.org/10.1175/JCLI-D-15-0441.1.

Huang, H., J. M. Winter, E. C. Osterberg, R. M. Horton, and B. Beckage, 2017: Total and extreme precipitation changes over the northeastern United States. *J. Hydrometeor.*, **18**, 1783–1798, https://doi.org/10.1175/JHM-D-16-0195.1.

Kay, J. E., and Coauthors, 2015: The Community Earth System Model (CESM) Large Ensemble Project: A community resource for studying climate change in the presence of internal climate variability. *Bull. Amer. Meteor. Soc.*, **96**, 1333–1349, https://doi.org/10.1175/BAMS-D-13-00255.1.

Lapenta, K. D., and Coauthors, 1995: The challenge of forecasting heavy rain and flooding throughout the eastern region of the National Weather Service. Part I: Characteristics and events. *Wea. Forecasting*, **10**, 78–90, https://doi.org/10.1175/1520-0434(1995)010<0078:TCOFHR>2.0.CO;2.

Ljungqvist, F. C., P. J. Krusic, H. S. Sundqvist, E. Zorita, G. Brattström, and D. Frank, 2016: Northern Hemisphere hydroclimate variability over the past twelve centuries. *Nature*, **532**, 94–98, https://doi.org/10.1038/nature17418.

Logan, E., 2019: Howard to bore a tunnel and raze four buildings to ease Ellicott City flooding, could cost $140 million. *Baltimore Sun*, 13 May, https://www.baltimoresun.com/maryland/howard/ph-ho-cf-flood-plan-20190513-story.html.

Maher, K., 2018: Flood warnings in effect in parts of West Virginia, Maryland and Virginia. Wall Street Journal, 4 June, https://www.wsj.com/articles/flood-warnings-in-effect-in-parts-of-west-virginia-maryland-and-virginia-1528135632.

Maher, N., and Coauthors, 2019: The Max Planck Institute Grand Ensemble: Enabling the exploration of climate system variability. *J. Adv. Model. Earth Syst.*, 11, 2050–2069, https://doi.org/10.1029/2019MS001639.

Menne, M. J., and Coauthors, 2012a: Global historical climatology network-daily (GHCN-daily), version 3.22. NOAA National Climatic Data Center, accessed 1 May 2019, https://doi.org/10.7289/V5D21VHZ.

Menne, M. J., I. Durre, R. S. Vose, B. E. Gleason, and T. G. Houston, 2012b: An overview of the Global Historical Climatology Network–Daily Database. *J. Atmos. Oceanic Technol.*, **29**, 897–910, https://doi.org/10.1175/JTECH-D-11-00103.1.

National Weather Service, 2019: Record rain and flooding of 2018. NWS, accessed 1 May 2019, https://www.weather.gov/lwx/2018floods.

Paciorek, C. J., D. A. Stone, and M. F. Wehner, 2018: Quantifying statistical uncertainty in the attribution of human influence on severe weather. *Wea. Climate Extremes*, **20**, 69–80, https://doi.org/10.1016/j.wace.2018.01.002.

Pendergrass, A. G., 2018: What precipitation is extreme? Science, 360, 1072–1073, https://doi.org/10.1126/science.aat1871.

Stott, P. A., and Coauthors, 2016: Attribution of extreme weather and climate-related events. *Wiley Interdiscip. Rev.: Climate Change*, **7**, 23–41, https://doi.org/10.1002/wcc.380.

QUANTIFYING HUMAN-INDUCED TEMPERATURE IMPACTS ON THE 2018 UNITED STATES FOUR CORNERS HYDROLOGIC AND AGRO-PASTORAL DROUGHT

Emily Williams, Chris Funk, Shraddhanand Shukla, and Daniel McEvoy

Human-induced (HI) warming increased Four Corners' vapor pressure deficits and reduced the Normalized Difference Vegetation Index by ~18%–30%. Without HI warming, March snow water equivalent would have been ~20% higher.

In water year (WY) 2018 (October 2017 to September 2018), temperatures in the Four Corners region of the western United States (Fig. 1a) were the warmest on record. These high temperatures occurred during a severe meteorological drought (West Wide Drought Tracker; Abatzoglou et al. 2017). According to the U.S. Drought Monitor (USDM), nearly 95% of the region was in severe drought in February 2018, and 56% of the region was in exceptional drought in September 2018. The Navajo Nation issued a drought declaration, finding that "drought conditions…created a critical shortage of water and range feed for livestock" (Navajo Nation 2018). Widespread agricultural and ranching losses contributed to an estimated three billion U.S. dollars in losses (NOAA NCEI 2019). The drought was characterized by significant hydrologic (limited surface water) and agropastoral (poor soil and vegetation conditions) impacts; thus, this study examines the influence of elevated temperature on hydrologic and agropastoral drought.

AFFILIATIONS: Williams and Shukla—University of California, Santa Barbara, Santa Barbara, California; Funk—U.S. Geological Survey Earth Resources Observation and Science Center and University of California, Santa Barbara, Santa Barbara, California; McEvoy—Western Regional Climate Center, Desert Research Institute, Reno, Nevada

CORRESPONDING AUTHOR: Emily Williams, ewilliams@ucsb.edu

DOI:10.1175/BAMS-D-19-0187.1

A supplement to this article is available online (10.1175/BAMS-D-19-0187.2)

Past studies indicate that above-normal temperatures have exacerbated droughts in the Southwest (McCabe et al. 2017; Weiss et al. 2009; Udall and Overpeck 2017; Woodhouse et al. 2016) by reducing snowpack and driving earlier snowmelt (Shukla et al. 2015; AghaKouchak et al. 2014; Cook et al. 2015) and increasing saturation vapor pressure (SVP), thereby increasing the vapor pressure deficit (VPD) (Seager et al. 2015). Increased VPD can lead to drying of the land surface, potentially stressing rangelands in late spring and summer months. Thus, above-normal temperatures co-occurring with meteorological drought may increase the risk of severe hydrologic and agropastoral drought (National Academies of Sciences, Engineering, and Medicine 2016, p. 98; Diffenbaugh et al. 2015; Williams et al. 2015; Shukla et al. 2015; Trenberth et al. 2014).

Given high probabilities that the twenty-first century will bring continued warming and the relatively uncertain influence of human-induced (HI) warming on precipitation in the Four Corners (Garfin et al. 2013), it is important to explore how temperature alone may contribute to enhancing hydrologic and agropastoral droughts. In this study, we estimate the potential temperature increase due to HI warming and subsequently examine the impacts of elevated temperature (i) on VPD using a statistical model, (ii) on agropastoral drought using a statistical model relating VPD and the Normalized Difference Vegetation Index (NDVI), and (iii) on hydrologic drought using a hydrologic model.

DATA AND METHODS. The study region (34°–39°N, 112°–105°W) encompasses the spatial extent of exceptional drought in WY2018 as defined by the USDM (Fig. 1a). Observationally based gridded monthly means of daily minimum and maximum

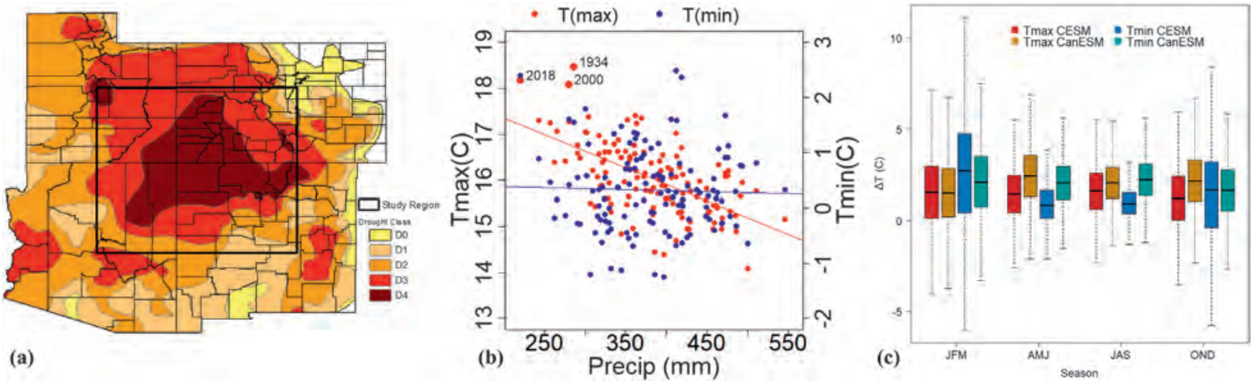

Fig. 1. Context for the WY2018 drought. (a) Study region bounding box, encompassing large portions of New Mexico, Arizona, Utah, and Colorado, overlaid on USDM 9 Oct 2018 drought extent. (b) Scatterplot demonstrating observed annual precipitation and mean T_{min} and T_{max} for each water year. Blue and red lines show T_{min} and T_{max} regression lines, respectively. (c) Human-induced temperature increases for WY2018 spatially averaged over the study region. Each boxplot displays the distribution of spatially averaged differences between the seasonal RCP8.5 and PI simulations over the 2013–23 time period. The lower and upper extent of the boxes depict the 25th and 75th percentiles of the distribution of differences. The center bar represents the median and the whiskers represent the less extreme of the maximum/minimum value or the 3rd/1st quartile + 1.5 * (interquartile range).

temperature (T_{min}, T_{max}), minimum and maximum vapor pressure deficit (VPD_{min}, VPD_{max}), and precipitation data from 1895 to 2018 for the region were obtained from the PRISM Climate Group (www.prism.oregonstate.edu/; 4 km × 4 km resolution) and, alongside snow water equivalent (SWE) measurements from SNOTEL (Fig. ES2), were examined to place the WY2018 drought in historical context.

To attribute the role of HI forcing on the temperature anomaly, factual and counterfactual estimates of T_{min} and T_{max} were derived. To derive factual $T_{min/max}$ estimates, representative concentration pathway 8.5 (RCP8.5) simulations from two large ensembles (LENS) were chosen: the Canadian Earth System Model version 2 (CanESM2) (Kirchmeier-Young et al. 2017) (50-member ensemble, 1950–2100) and the Community Earth System Model version 1 (CESM1) (Kay et al. 2015) (40-member large ensemble; 1920–2100). We selected the two models with the largest ensembles to account for the internal variability in the climate system. Counterfactual estimates were based on pre-industrial (PI) CMIP5 simulations for the same models, obtained from the Climate Explorer (https://climexp.knmi.nl/). A bias correction (described in online supplemental material) was used to align the CESM1 PI (CMIP5) simulations (Taylor et al. 2012) with the 40 CESM1 LENS simulations (Kay et al. 2015). As WY2018 experienced a weak La Niña, only model simulations with similar Niño-3.4 SST anomalies (with ±0.4°C buffer) were used. HI influence on temperature was determined by comparing monthly T_{min} and T_{max} averages from RCP8.5 simulations for 2013–23 (sample sizes: $N_{CESM1} = 1439$; $N_{CanESM2} = 2012$) with those from the PI simulations ($N_{CESM1} = 760$; $N_{CanESM2} = 1103$).

To estimate counterfactual VPD (minimum and maximum), we calculated counterfactual SVP (SVP_{cf}) and combined these values with actual vapor pressure (AVP) to calculate VPDcf. Since we focus on temperature dependencies in this set of experiments, and since 1895–2018 AVP shows no significant linear trend, we assume that human-induced warming did not change AVP. Actual SVP was first calculated using PRISM temperatures, then AVP was calculated using actual SVP and VPD. Then, the warming anomaly (from the counterfactual temperature experiment) was subtracted from PRISM temperature and used to calculate SVP_{cf}, based on the equation for VPD from Daly et al. (2015). Finally, SVP_{cf} and actual AVP were used to derive VPD_{cf}.

To estimate the effects of VPD on the NDVI (Normalized Difference Vegetation Index; a measure of greenness and vegetative stress), counterfactual NDVI was derived using counterfactual SVP and observed precipitation. NDVI observations were obtained from MODIS *Terra* 16-day (Spruce et al. 2016). Seasonal 2000–18 June–August mean SVP and precipitation were regressed onto the spatially aggregated magnitude of change from April to August NDVI (ΔNDVI). Various SVP, AVP, and precipitation lags and combinations were tested to find the optimal regression (i.e., the best predicting months and variables). June–August SVP and precipitation proved to be the best for April–August ΔNDVI (the "greenup" phase) (DNDVI = 0.17 + −0.00558 × SVP + 0.00073 × precip; R2 = 0.766). These regression coefficients were then used with SVP_{cf} and actual precipitation means to calculate ΔNDVIcf.

Finally, the effect of elevated temperature on hydrologic drought (specifically SWE and runoff) was estimated by using the variable infiltration capacity (VIC) hydrologic model (Liang et al. 1994) which has been used in similar attribution studies (such as Shukla et al. 2015; Xiao et al. 2018). The VIC is a physically based hydrologic model that uses atmospheric forcings including precipitation, temperature, and wind speed to compute SWE, soil moisture (SM), evapotranspiration (ET), and runoff. The VIC was run using PRISM precipitation, T_{min} and T_{max} data, and climatological wind speed [as in Livneh et al. (2013)] (upscaled from 4 km × 4 km to 6 km × 6 km). After a long-term spinup period, the VIC was run first to simulate the water budget given the observed WY2018 conditions, and then twice using counterfactual WY2018 temperatures obtained by adjusting the observed WY2018 temperatures using the difference between factual and counterfactual temperatures derived from CESM and CanESM while keeping precipitation the same.

RESULTS. WY2018 precipitation was the lowest on record (~220 mm) averaged over the study area. There is no significant correlation between precipitation and annual T_{min} (cor = −0.03; *p* value = 0.73); however, a significant negative correlation exists between precipitation and annual T_{max} (cor = −0.60; *p* value = 0.16e-12) (Fig. 1b). WY2018 T_{max} and T_{min} values were both among the warmest on record (Fig. 1b). Estimates of the human-induced temperature increases from the counterfactual experiment indicate substantial warming (Fig. 1c). The mean annual difference in temperature between RCP8.5 and PI ensemble runs is ~ +2°C for CanESM2 (+2.0°C T_{max}, +2.0°C T_{min}) and ~1.3°C for CESM1 (+1.3°C T_{max}, +1.4°C T_{min}) for the 2013–23 decade. PRISM suggests a temperature increase of ~1.9°C (T_{max}) and ~0.9°C (T_{min}) from 1895–1929 to 2013–18.

Figure 2a shows the climatological (1895–1980) VPD (black line), actual WY2018 VPD (red line), and "alternative" WY2018 VPD (blue line, CESM1-adjusted; green line, CanESM2-adjusted) estimated using the counterfactual T_{min} and T_{max}. In June–August, actual VPD_{max} (VPD_{min}) was on average 6.6 hPa (3.1 hPa) greater than the climatology. Counterfactual estimates (blue and green lines in Fig. 2a) suggest that the HI-induced temperature anomalies could account for 3.7–4.9 hPa (VPD_{max}) and 0.7–2.2 hPa (VPD_{min}), or 59%–80% (VPD_{max}) and 26%–74% (VPD_{min}), of the difference between the climatological VPD and 2018 actual June–August VPD. Average 2000–18 ΔNDVI (greenup) was 0.088—the region experienced severe drought during the first decade. April–August modeled 2018 ΔNDVI (representing greenup) was 0.067; under counterfactual temperature conditions, ΔNDVI was estimated to have been 0.080–0.088 based on CESM1- and CanESM2-estimated VPD_{cf}, respectively (Fig. 2b).

VIC estimates of SWE (for elevations > 2,000 m) and runoff are summarized in Figs. 2c and 2d. Evapotranspiration results are shown in the supplemental material. Climatologically, peak SWE months are February–April, whereas peak runoff months are May–June. The simulated 2018 March SWE peak (annual WY runoff) was ~71% (~57%) less than the climatological average. Comparing VIC simulations—those driven with adjusted temperature forcings versus those driven with WY 2018 actual temperature—reveals that March SWE would have been ~24% (CanESM) or ~19% (CESM) higher than WY 2018 observation-based SWE. Likewise, annual WY runoff would have been ~1.3% (CanESM) or ~1.43% (CESM) higher than WY 2018 observed temperature-based simulated annual runoff. These results indicate that human-induced temperature increases had a measurable impact on SWE, but little discernable impacts on runoff; the SWE effects, however, were secondary to the influence of record-low precipitation during WY 2018 (Fig. 1b).

DISCUSSION AND CONCLUSIONS. WY2018 was exceptionally warm and dry (Figs. 1a,b), and an assessment of the CESM1 and CanESM2 simulations suggested that HI warming increased air temperatures by ~1.3° to ~2°C, respectively (Fig. 1c). Relatively small changes in temperature can result in large changes in VPD; thus, if AVP remains constant, human-induced warming, alone, could explain ~60%–80% of the observed WY2018 VPD_{max} anomalies (Fig. 2a). WY2018 experienced low NDVI values as reflected in the poor rangeland conditions reported by the USDM for much of New Mexico, Utah, and Arizona during the same period. HI increases in SVP values likely contributed to reduced August NDVI; the magnitude of greenup was smaller in actual 2018 NDVI compared to the counterfactuals (Fig. 2b). VIC simulations suggest that without the HI warming March SWE would have been ~24% (CanESM) or ~19% (CESM) higher and annual WY runoff would have been ~1.3% (CanESM) or ~1.43% (CESM) higher (Figs. 2c,d).

This study did not assess the potential effect of positive land–atmosphere feedbacks under drought conditions, in which HI temperature anomalies can

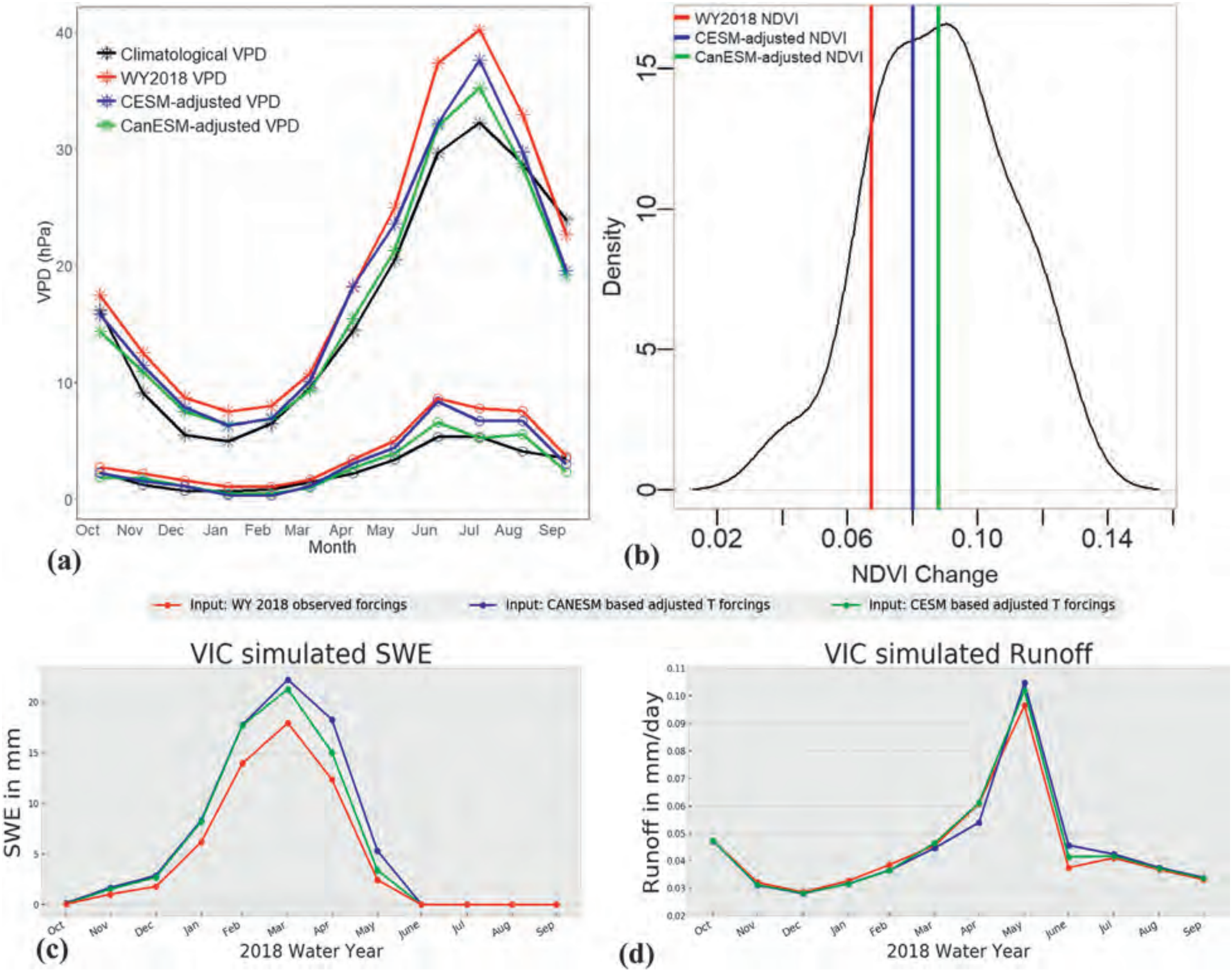

Fig. 2. Hydrologic and agropastoral effects of HI-forced temperature anomalies. Climatology of each variable is shown in black [in (a) and (b) only], WY2018 actual ("observed"/factual) conditions in red, and counterfactual estimates in blue (CESM1-adjusted) and green (CanESM2-adjusted). (a) Comparison between climatological VPD, WY2018 VPD, and estimated counterfactual WY2018 VPD, estimated using the difference between counterfactual and factual temperatures as shown in Fig. 1c. VPD$_{max}$ is shown using an asterisk (*) and VPD$_{min}$ using an open circle (o). (b) PDF of spatially aggregated actual NDVI greenup (or magnitude of change in NDVI from April to August) in black for 2000–18, modeled 2018 NDVI greenup (red), and counterfactual estimates of greenup without HI temperature increases (blue and green). Also shown are VIC model-based estimates of (c) SWE and (d) runoff derived from CanESM2- and CESM1-adjusted (counterfactual) temperatures, and actual ("observed"/ factual) temperatures for WY2018. SWE is aggregated over only those grid cells at >2,000-m mean elevation.

yield even greater observed anomalies as energy is released as sensible heat instead of latent heat (as suggested by the negative correlation between precipitation and annual average T_{max}). Therefore, our estimates of climate change–induced temperature increase on hydrology (particularly SWE) and VPD (and its influence on NDVI) may be conservative estimates. Future research will expand this analysis to cover the full time series (1900–present), allowing us to assess potential temperature impacts under less extreme precipitation deficits.

REFERENCES

Abatzoglou, J. T., D. J. McEvoy, and K. T. Redmond, 2017: The West Wide Drought Tracker: Drought monitoring at fine spatial scales. *Bull. Amer. Meteor. Soc.*, **98**, 1815–1820, https://doi.org/10.1175/BAMS-D-16-0193.1.

AghaKouchak, A., L. Cheng, O. Mazdiyasni, and A. Farahmand, 2014: Global warming and changes in risk of concurrent climate extremes: Insights from the 2014 California drought. *Geophys. Res. Lett.*, **41**, 8847–8852, https://doi.org/10.1002/2014GL062308.

Cook, B. I., T. R. Ault, and J. E. Smerdon, 2015: Unprecedented 21st century drought risk in the American Southwest and Central Plains. *Sci. Adv.*, **1**, e1400082, https://doi.org/10.1126/sciadv.1400082.

Daly, C., J. J. Smith, and K. V. Olson, 2015: Mapping atmospheric moisture climatologies across the conterminous United States. PLOS ONE, 10, e0141140, https://doi.org/10.1371/JOURNAL.PONE.0141140.

Diffenbaugh, N. S., D. L. Swain, and D. Touma, 2015: Anthropogenic warming has increased drought risk in California. *Proc. Natl. Acad. Sci. USA*, **112**, 3931–3936, https://doi.org/10.1073/pnas.1422385112.

Garfin, G., and Coauthors, Eds., 2013: Assessment of Climate Change in the Southwest United States: A Report Prepared for the National Climate Assessment. Island Press, 506 pp., https://doi.org/10.5822/978-1-61091-484-0.

Kay, J., and Coauthors, 2015: The Community Earth System Model (CESM) large ensemble project: A community resource for studying climate change in the presence of internal climate variability. *Bull. Amer. Meteor. Soc.*, **96**, 1333–1349, https://doi.org/10.1175/BAMS-D-13-00255.1.

Kirchmeier-Young, M. C., F. W. Zwiers, and N. P. Gillett, 2017: Attribution of extreme events in Arctic sea ice extent. *J. Climate*, **30**, 553–571, https://doi.org/10.1175/JCLI-D-16-0412.1.

Liang, X., D. P. Lettenmaier, E. F. Wood, and S. J. Burges, 1994: A simple hydrologically based model of land surface water and energy fluxes for general circulation models. *J. Geophys. Res.*, **99**, 14 415–14 428, https://doi.org/10.1029/94JD00483.

Livneh, B., E. A. Rosenberg, C. Lin, B. Nijssen, V. Mishra, K. M. Andreadis, E. P. Maurer, and D. P. Lettenmaier, 2013: A long-term hydrologically based dataset of land surface fluxes and states for the conterminous United States: Update and extensions. *J. Climate*, **26**, 9384–9392, https://doi.org/10.1175/JCLI-D-12-00508.1.

McCabe, G. J., D. M. Wolock, G. T. Pederson, C. A. Woodhouse, and S. McAfee, 2017: Evidence that recent warming is reducing upper Colorado River flows. *Earth Interact.*, **21**, https://doi.org/10.1175/EI-D-17-0007.1.

National Academies of Sciences, Engineering, and Medicine, 2016: Attribution of Extreme Weather Events in the Context of Climate Change. The National Academies Press, 186 pp., https://doi.org/10.17226/21852.

Navajo Nation, 2018: State of Emergency Declaration. http://frontiernet.net/~nndwr_wmb/PDF/CurrentPosts/CEM%2018-02-26%20StateOfEmergency-DroughtDeclaration.pdf.

NOAA NCEI, 2019: Billion-dollar weather and climate disasters: Overview. NOAA National Centers for Environmental Information, accessed 29 May 2019, https://www.ncdc.noaa.gov/billions/.

Seager, R., A. Hooks, A. P. Williams, B. Cook, J. Nakamura, and N. Henderson, 2015: Climatology, variability, and trends in the U.S. vapor pressure deficit, an important fire-related meteorological quantity. *J. Appl. Meteor. Climatol.*, **54**, 1121–1141, https://doi.org/10.1175/JAMC-D-14-0321.1.

Shukla, S., M. Safeeq, A. Aghakouchak, K. Guan, and C. Funk, 2015: Temperature impacts on the water year 2014 drought in California. *Geophys. Res. Lett.*, **42**, 4384–4393, https://doi.org/10.1002/2015GL063666

Spruce, J. P., G. E. Gasser, and W. W. Hargrove, 2016: MODIS NDVI Data, Smoothed and Gap-filled, for the conterminous US: 2000–2015. ORNL DAAC, Oak Ridge National Laboratory, accessed 3 Sept 2019, http://dx.doi.org/10.3334/ORNLDAAC/1299.

Taylor, K. E., R. J. Stouffer, and G. A. Meehl, 2012: An overview of CMIP5 and the experiment design. *Bull. Amer. Meteor. Soc.*, **93**, 485–498, https://doi.org/10.1175/BAMS-D-11-00094.1.

Trenberth, K. E., A. Dai, G. van der Schrier, P. D. Jones, J. Barichivich, K. R. Briffa, and J. Sheffield, 2014: Global warming and changes in drought. *Nat. Climate Change*, **4**, 17–22, https://doi.org/10.1038/nclimate2067.

Udall, B., and J. Overpeck, 2017: The twenty-first century Colorado River hot drought and implications for the future. *Water Resour. Res.*, **53**, 2404–2418, https://doi.org/10.1002/2016WR019638.

Weiss, J. L., C. L. Castro, and J. T. Overpeck, 2009: Distinguishing pronounced droughts in the southwestern United States: Seasonality and effects of warmer temperatures. *J. Climate*, **22**, 5918–5932, https://doi.org/10.1175/2009JCLI2905.1.

Williams, P., R. Seager, J. Abatzoglou, B. Cook, J. Smerdon, and E. Cook, 2015: Contribution to California drought during 2012–2014. *Geophys. Res. Lett.*, 42, 6819–6828, https://doi.org/10.1002/2015GL064924.

Woodhouse, C. A., G. T. Pederson, K. Morino, S. A. McAfee, and G. J. McCabe, 2016: Increasing influence of air temperature on upper Colorado River streamflow. *Geophys. Res. Lett.*, **43**, 2174–2181, https://doi.org/10.1002/2015GL067613.

Xiao, M., B. Udall, and D. P. Lettenmaier, 2018: On the causes of declining Colorado River streamflows. *Water Resour. Res.*, **54**, 6739–6756, https://doi.org/10.1029/2018WR023153.

chapter 4

EXTREME HAIL STORMS AND CLIMATE CHANGE: FORETELLING THE FUTURE IN TINY, TURBULENT CRYSTAL BALLS?

Kelly Mahoney

In 2018, hailstorms accounted for three of the fourteen 2018 U.S. billion dollar disasters: a 6 June 2018 storm in Texas, and two Colorado hailstorms (18–19 June and 6–7 August). What is the role of climate change in changing hail risk? Can current research methods address the space and time scales required to adequately assess hail risk? Can the available data distinguish between changes in storm frequency, changes in storm reporting practices, and changes in economic risk and our built environment? The billion dollar hailstorms of 2018 have highlighted the limited capabilities of the scientific community to predict how climate change will impact hail storm risks, while raising concern about the vulnerability of society to these storms. Like any weather disaster, 2018's hailstorms provide an opportunity to re-evaluate methods for anticipating similar future weather extremes.

HAILSTORMS: WHAT WE DO(N'T) KNOW. Hail forms in thunderstorms when strong vertical air motions allow frozen particles to grow by the accretion of supercooled liquid water. When hailstones grow large enough such that they are no longer supported by surrounding rising air motions, they begin to fall. Smaller ice particles melt more quickly and at levels nearer to the melting level than larger ones; warmer and moister sub-cloud air accelerates the melting process. Anticipating the potential for hail on any given day—much less anticipating possible changes to the frequency and intensity of hail in the more distant future—thus requires understanding the interplay between the environmental support for hail-generating convective storms, key microphysical and dynamical characteristics of the storm updraft region over which hail growth occurs, and the depth and temperature of the lower atmosphere where melting occurs. In short, this is a tall order!

Severe convective storms (SCSs) are the parent weather phenomenon responsible for producing most damaging hail. SCSs are relatively small and short-lived, and as a result, their impacts (e.g., strong winds, large hail, tornadoes) are very localized and not comprehensively captured by conventional meteorological observations. While research and available model data continue to actively expand in this area [e.g., see recent workshop summaries by Martius et al. (2018) and NCAR (2018)], these challenges of scale and limited observations render the consensus state of knowledge regarding future projected changes in hail largely unchanged from the IPCC Special Report on Extremes (Seneviratne et al. 2012): "confidence is still low for hail projections particularly due to a lack of hail-specific modelling studies, and a lack of agreement among the few available studies" (p. 148). Yet for stakeholders affected by potential changes in hail risk, what can be done given this apparent lack of actionable scientific guidance? Here we briefly examine the state of the science, areas of emergent scientific consensus, and how—even in the face of significant uncertainty—research can best serve end-user needs.

AFFILIATIONS: Mahoney—National Oceanic and Atmospheric Administration, Earth System Research Laboratory, Physical Sciences Division, Boulder, Colorado.
CORRESPONDING AUTHOR: Kelly Mahoney, kelly.mahoney@noaa.gov

DOI:10.1175/BAMS-D-19-0233.1

STATE OF THE RESEARCH: HOW DO WE CURRENTLY CONSIDER HAIL AND CLIMATE CHANGE?

Historical hail trends and observing challenges. Vast data heterogeneities of observed hail means that detection of past hail trends is also exceedingly difficult. For example, observations of U.S. hail do indicate significant increases over the latter half of the twentieth century, but these are widely understood to be artifacts of increased reporting frequency rather than actual meteorological trends (e.g., National Academies of Sciences, Engineering, and Medicine 2016; Allen and Tippett 2015; Fig. 1). Studies considering the effects of observed warming on hail have largely relied upon the linkage of proxy atmospheric indicators and (usually sparse) hail observations, and are thus fundamentally inhibited by 1) the inadequate historical record of past hailstorms, 2) the coarseness of the datasets employed (usually global data and climate model simulations), and 3) the questionable connection between large-scale environmental parameters and small-scale weather extremes. Thus, despite a small sample of specific regions demonstrating robust observed changes [e.g., downward trends in both hail days and hailstorm frequency in China (e.g., Xie et al. 2008; Li et al. 2016) and increasing hail intensity (with decreasing hail frequency) in SW France (Dessens et al. 2015)], the conclusions that can be drawn from these types of studies are limited (e.g., Allen 2018).

Climate model projections: Assessing hailstorm ingredients. Global and regional climate models (GCMs and RCMs) are generally run at resolutions far too coarse to realistically simulate SCSs, much less SCS impacts. While climate model projections generally indicate increasing SCS likelihood as a result of increasing thermodynamic instability (e.g., Diffenbaugh et al. 2013; Hoogewind et al. 2017), details pertaining to changes in seasonality, regionality, and SCS impacts are less certain.

A common approach to understanding how SCSs may change in the future is to use GCM and RCM projections to evaluate how SCS-favorable environmental parameters change in future climate projections, thereby focusing on SCS "ingredients" as proxies for SCS impacts such as hail (e.g., Brooks et al. 2003; Trapp et al. 2007; Diffenbaugh et al. 2013; Tippett et al. 2015; Allen 2018). As noted above, studies of this nature are also inherently inhibited by both the coarseness of the datasets employed and the often tenuous connection between environmental proxies and weather impacts. These studies are also incapable of describing storm-scale criticalities including possible changes in convective mode (i.e., a shift away from severe-hail-generating rotating supercells), the relationship between in-cloud hail generation versus surface-impacting hail, and the fundamental reality that specific SCS hazards (large hail, damaging winds, and tornadoes) do not favor the same environmental conditions (Brooks 2013).

Some climate model signal consistency has emerged, however: for example, European Coordinated Regional Climate Downscaling Experiment (EURO-CORDEX) models find an expected future increase in hail frequency for parts of Europe (e.g., Martius et al. 2018; Rädler et al. 2019). Similarly, Brimelow et al. (2017) used an offline single-column hail growth model to ingest environmental profiles from 50-km RCM output, also finding fewer days with smaller hail over the some regions of the United States, with increases in spring and summer large hail over the northern plains. While using GCM/RCM output as proxies or as input into offline models reduces computational limitations, the general approach does not actually simulate storms; this, and other limitations of the environmental approach, have thus pushed the research community to seek additional approaches to refine and complement the guidance that can be gleaned from larger-scale data.

High-resolution, convection-permitting simulations. Leveraging computing power increases, high-resolution convection-permitting (CP) model simulations allow a more direct representation of SCSs likely to produce hail. Some CP simulations have adapted the pseudo–global warming approach, where present-day hail events are simulated in high resolution in both current and future atmospheric environments (e.g., Mahoney et al. 2012). Such studies generally support the notion of increased likelihood of large hail and decreased likelihood of small hail and, at such high resolution, also offer insight into a physical process-based rationale to explain aggregate hail changes. Another recent CP modeling approach applied to hail specifically uses a "continual restart approach" to downscale GCM projections over the continental United States (CONUS) in 30-yr historical and future time slices, and finds broad increases in the frequency of large hail during all four seasons and mixed signals in small–medium hail (Trapp et al. 2019). These results and others (e.g., NCAR 2018)—while computationally limited in the number of climate projections or events that can be evaluated—also share some consensus that the seasonality of hail risk is likely subject to change, with several studies indicating a lengthening at both the beginning and end of the convective season, and also possibly exhibiting more interannual variability in the future.

Fig. 1. Despite a number of recent hail records and high-impact hail events, such as (a) 2019 Colorado new record hailstone size and (b) multiple high-impact 2018 and 2019 hail storms, detecting past hail trends is challenged by inconsistent observations. (c) The 1998–2017 time series of the fraction of hail reports ≥0.75 in (1.9 cm). Adapted from Allen and Tippett (2015, their Fig. 3a).

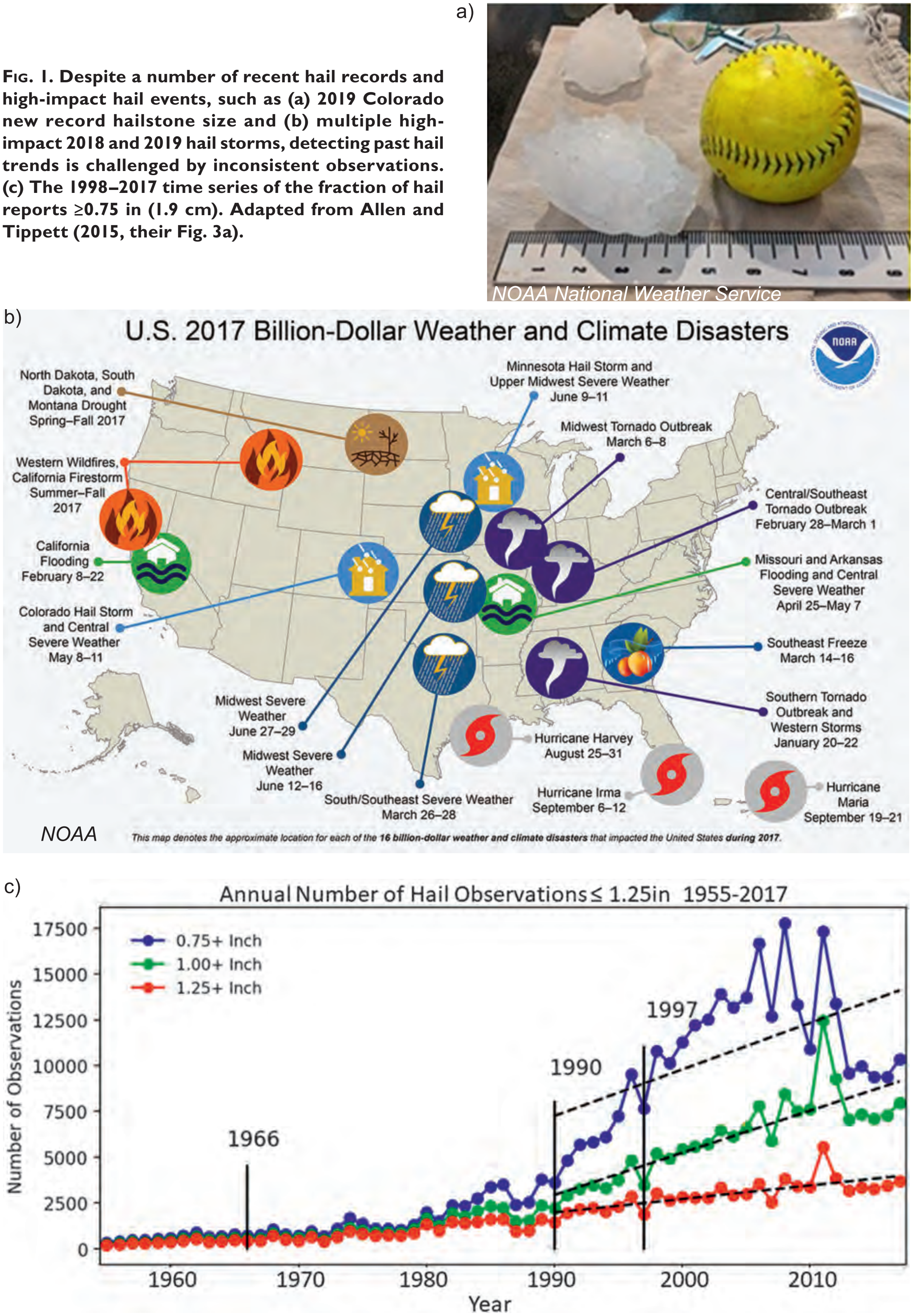

NOAA National Weather Service

NOAA

*This map denotes the approximate location for each of the **16 billion-dollar weather and climate disasters** that impacted the United States **during 2017**.*

Near-term opportunities and challenges. Although high-resolution simulations offer increasing insight by explicitly simulating hail-producing storms in future climate states, it is important to underscore that even at these relatively high resolutions, these studies still only resolve the parent SCS and not the details of hail production or hail size spectra. Additional caveats exist: for example, even very recent, state-of-the-art high-resolution CP studies such as that of Trapp et al. (2019) often rely on a hail diagnostic to connect model-produced hydrometeor concentration output with heuristically generated hail diameter assignments. The enduring requirement for microphysical parameterization to approximate hail formation and maintenance processes further clouds the connection between model-approximated hail and surface damage potential. Furthermore, effects including the role of atmospheric aerosols, the storm-scale interplay between theoretically increasing updraft strength and potentially decreased buoyancy due to additional hydrometeor weight, and hydrologic sensitivities as previously frozen precipitation instead melts and falls as rain all point to a daunting chain of uncertain—yet critical—small-scale physical system dependencies and interactions.

It is impossible to choose a single "best" method given the basic computational trade-offs in 1) *many* coarse-scale GCM projections (which cannot simulate physically realistic SCSs) and 2) *singular*, or limited-member, high-resolution downscaled projections (which lack fundamental uncertainty and robustness indicators). But perhaps recognizing outright the impracticality of a perfect blend can ultimately yield greater insight into the future of hail via a holistic, thoughtful curation of complementary research approaches including observational, theoretical, and model-based study methods (e.g., Shepherd 2016).

ACTIONABLE ATTRIBUTION SCIENCE.

Despite the considerable uncertainties surrounding the future of hail risk, key industries and stakeholders must still act—ideally on the best information that our collective weather and climate research communities can provide. Decision-making under the conditions of deep uncertainty ("DMDU"; e.g., Marchau et al. 2019) is a concept well-known in certain stakeholder communities (e.g., water supply planning) and accepts that traditional, deterministic science approaches are unlikely to provide usable stakeholder answers in isolation. "Storytelling" frameworks (e.g., Hazeleger et al. 2015; Shepherd 2016) in particular focus on "multiple futures" or "scenarios" (e.g., Star et al. 2016) and thus complement and add physical insight to traditional climate projections.

Considering approaches beyond those rooted purely in the physical sciences, Owen (2019) details the actuarial industry's extensive experience in managing uncertainty. Insured events are evaluated in risk models according to 1) the probability the event will occur, 2) the timing of the event, and 3) the distribution of the severity of the expense of the event. Of course, the addition of economic or other supporting data does not reduce the original uncertainties in the physical system; Owen (2019) further highlights the large cost sensitivity in these models: even "small deviations from estimations of future costs have considerable financial consequences" (p. S6).

Just as a priori economic valuation data may usefully bound potential economic losses from hail, it is key to recognize also that hail disaster planning also requires assessment of vulnerability (i.e., exposure). Figure 2 borrows an "expanding target" schematic from Ashley et al.'s (2014) study on tornado risk, illustrating the concept that as populations grow and spread, hazards to lives and property increase.

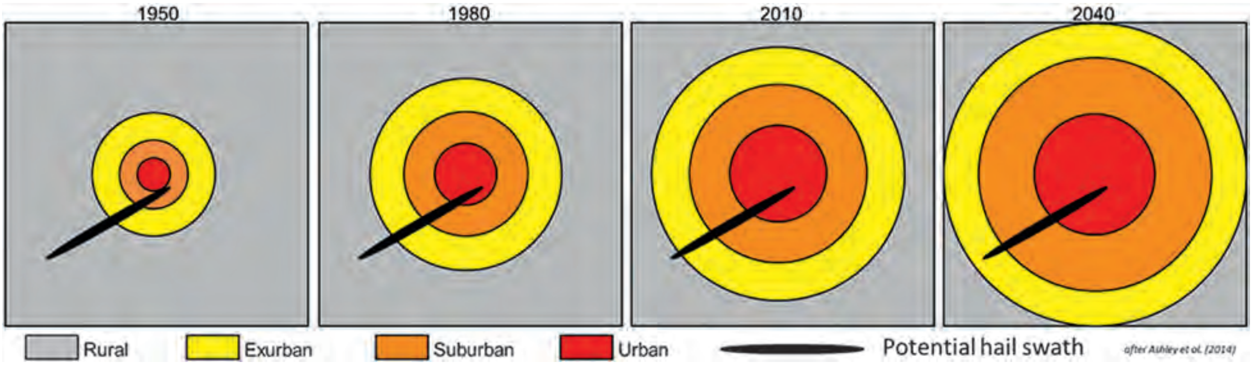

Fig. 2. Adapted from Ashley et al. (2014), a conceptual model of the "expanding bull's-eye effect" for a hypothetical metropolitan region characterized by increasing development spreading from an urban core over time. A sample hail swath is overlaid to show how expanding development creates larger areas of potential impacts from hazards.

Combining physical science methods with vulnerability and economic assessment may enable scientists and risk experts to provide a more informed menu of future hail risk scenarios.

SUMMARY. Assessing potential changes in hail frequency, intensity, and hailstone size distribution in a warmer climate is complex. While research to date provides some indication of more intense hailstorms in a warming climate alongside enhanced melting of small hailstones, considerable uncertainty and variability qualifies these findings. As computing power increases, attribution studies of SCSs may become increasingly feasible, but for hail itself, explicit simulation in global or regional model attribution studies is unlikely to be practicable in the near future. Integrated, curated, complementary research approaches suited to specific decision-making applications are likely required to optimally address this challenging question.

REFERENCES

Allen, J. T., 2018: Climate change and severe thunderstorms. Oxford Research Encyclopedias: Climate Science, https://doi.org/10.1093/acrefore/9780190228620.013.62.

——, and M. K. Tippett, 2015: Characteristics of the United States Hail Observations Dataset 1955–2014. *Electron. J. Severe Storms Meteor.*, **10**, 1–31, .

Ashley, W. S., S. Strader, T. Rosencrants, and A. J. Krmenec, 2014: Spatiotemporal changes in tornado hazard exposure: The case of the expanding bull's eye effect in Chicago, IL. *Wea. Climate Soc.*, **6**, 175–193, https://doi.org/10.1175/WCAS-D-13-00047.1.

Brimelow, J. C., W. R. Burrows, and J. M. Hanesiak, 2017: The changing hail threat over North America in response to anthropogenic climate change. *Nat. Climate Change*, **7**, 516–522, https://doi.org/10.1038/nclimate3321.

Brooks, H. E., 2013: Severe thunderstorms and climate change. *Atmos. Res.*, **123**, 129–138, https://doi.org/10.1016/j.atmosres.2012.04.002.

——, J. W. Lee, and J. P. Craven, 2003: The spatial distribution of severe thunderstorm and tornado environments from global reanalysis data. *Atmos. Res.*, **67–68**, 73–94, https://doi.org/10.1016/s0169-8095(03)00045-0.

Dessens, J., C. Berthet, and J. L. Sanchez, 2015: Change in hailstone size distributions with an increase in the melting level height. *Atmos. Res.*, **158–159**, 245–253, https://doi.org/10.1016/j.atmosres.2014.07.004.

Diffenbaugh, N. S., M. Scherer, and R. J. Trapp, 2013: Robust increases in severe thunderstorm environments in response to greenhouse forcing. *Proc. Natl. Acad. Sci. USA*, **110**, 16 361–16 366, https://doi.org/10.1073/pnas.1307758110.

Hazeleger, W., B. J. J. M. van den Hurk, E. Min, G. J. van Oldenborgh, A. C. Petersen, D. A. Stainforth, E. Vasileiadou, and L. A. Smith, 2015: Tales of future weather. *Nat. Climate Change*, **5**, 107–113, https://doi.org/10.1038/nclimate2450.

Hoogewind, K. A., M. E. Baldwin, and R. J. Trapp, 2017: The impact of climate change on hazardous convective weather in the United States: Insight from high-resolution dynamical downscaling. *J. Climate*, **30**, 102081–102100, https://doi.org/10.1175/JCLI-D-16-0885.1.

Li, M., Q. Zhang, and F. Zhang, 2016: Hail day frequency trends and associated atmospheric circulation patterns over China during 1960–2012. *J. Climate*, **29**, 7027–7044, https://doi.org/10.1175/JCLI-D-15-0500.1.

Mahoney, K., M. A. Alexander, G. Thompson, J. J. Barsugli, and J. D. Scott, 2012: Changes in hail and flood risk in high-resolution simulations over Colorado's mountains. *Nat. Climate Change*, **2**, 125–131, https://doi.org/10.1038/nclimate1344.

Marchau, V. A. W. J., W. E. Walker, P. J. T. M. Bloemen, and S. W. Popper, Eds., 2019: *Decision Making under Deep Uncertainty: From Theory to Practice*. Springer, 405 pp., https://doi.org/10.1007/978-3-030-05252-2.

Martius, O., A. Hering, M. Kunz, A. Manzato, S. Mohr, L. D. Nisi, and S. E. Trefalt, 2018: Challenges and recent advances in hail research. *Bull. Amer. Meteor. Soc.*, **99**, ES51–ES54, https://doi.org/10.1175/BAMS-D-17-0207.1.

National Academies of Sciences, Engineering, and Medicine, 2016: *Attribution of Extreme Weather Events in the Context of Climate Change*. The National Academies Press, 186 pp., https://doi.org/10.17226/21852.

NCAR, 2018: *Proc. 2018 North American Workshop on Hail & Hailstorms*. Boulder, CO, NCAR, https://www.mmm.ucar.edu/north-american-hail-workshop.

Owen, R., 2019: Actuaries are paying attention to climate data [in "Explaining Extremes of 2017 from a Climate Perspective"]. *Bull. Amer. Meteor. Soc.*, **100** (1), S5–S8, https://doi.org/10.1175/BAMS-D-18-0293.1.

Rädler, A. T., P. H. Groenemeijer, E. Faust, E., R. Sausen, and T. Púčik, 2019: Frequency of severe thunderstorms across Europe expected to increase in the 21st century due to rising instability. *npj Climate Atmos Sci.* **2,** 30, https://doi.org/10.1038/s41612-019-0083-7.

Seneviratne, S. I., and Coauthors, 2012: Changes in climate extremes and their impacts on the natural physical environment. *Managing the Risks of Extreme*

Events and Disasters to Advance Climate Change Adaptation, C. B. Field et al., Eds., Cambridge University Press, 109–230.

Shepherd, T. G., 2016: A common framework for approaches to extreme event attribution. *Curr. Climate Change Rep.*, **2**, 28–38, https://doi.org/10.1007/s40641-016-0033-y.

Star, J., and Coauthors, 2016: Supporting adaptation decisions through scenario planning: enabling the effective use of multiple methods. *Climate Risk Manage.*, **13**, 88–94, https://doi.org/10.1016/j.crm.2016.08.001.

Tippett, M. K., J. T. Allen, V. A. Gensini, and H. E. Brooks, 2015: Climate and hazardous convective weather. *Curr. Climate Change Rep.*, **1**, 60–73, https://doi.org/10.1007/s40641-015-0006-6.

Trapp, R. J., N. S. Diffenbaugh, H. E. Brooks, M. E., Baldwin, E. D., Robinson, and J. S. Pal, 2007: Changes in severe thunderstorm frequency during the 21st century due to anthropogenically enhanced global radiative forcing. *Proc. Natl. Acad. Sci. USA*, **104,** 19 719–19 723, https://doi.org/10.1073/pnas.0705494104.

——, K. A. Hoogewind, and S. Lasher-Trapp, 2019: Future changes in hail occurrence in the United States determined through convection-permitting dynamical downscaling. *J. Climate*, **32**, 5493–5509, https://doi.org/10.1175/JCLI-D-18-0740.1.

Xie, B., Q. Zhang, and Y. Wang, 2008: Trends in hail in China during 1960–2005. *Geophys. Res. Lett.*, **35**, L13801, https://doi.org/10.1029/2008GL034067.

chapter 5

THE EXTREMELY COLD START OF THE SPRING OF 2018 IN THE UNITED KINGDOM

Nikolaos Christidis and Peter A. Stott

Observational and model analyses suggest a 6- and 12-fold increase in the likelihood of extremely cold days in March in central England, as in year 2018, without anthropogenic climate change.

Red warnings, the U.K. Met Office's most severe and rare alerts, signaled the arrival of an anticipated deadly cold spell in the country in early March 2018.[1] Extremely cold conditions developed as a persistent easterly circulation, associated with a sudden stratospheric warming (Karpechko et al. 2018), steered a massive Arctic airmass toward the British Isles at the end of February 2018, where it collided with winter storm Emma in the first days of March. The combination of the storm with the frigid Siberian weather system, dubbed "the Beast from the East," led to freezing temperatures, blizzards, and heavy snow in excess of 50 cm on high ground. U.K. media widely reported on the substantial impacts of the extreme weather, including loss of life, business and travel disruptions, cancellation of hospital operations, food shortages, and several thousand car accidents with insurance costs of over £10 million.[2] Daily mean temperature time series from the Central England Temperature (CET) instrumental record (Parker et al. 1992) show a prominent dip at the start of spring (Fig. 1a), making the first day of March markedly colder than all days in the preceding winter season. Sub-zero temperatures (in °C) were also observed later in the month during a less intense cold snap nicknamed the "Mini Beast from the East." Despite these extremely cold days, the month of March as a whole was not extreme, but had a mean temperature within the middle tercile of the post-1659 distribution based on the CET data. On the other hand, observational time series of the coldest day in March since 1772 have their fourth coldest value in 2018 (Fig. 1b). This study concentrates mainly on such low daily temperatures and defines extremely cold events as instances when the coldest day in March has a temperature lower than the one observed in 2018. Although heavy snowfall was another interesting aspect of the 2018 cold wave, the lack of long and reliable observations hinders a snowfall analysis, although this aspect will also be briefly considered using modeled data only. It should be noted that the time series shown in Fig. 1b have a positive long-term trend of 0.07°C decade^{-1}, suggesting that cold events are becoming rarer. Synoptic conditions over Europe in March 2018 are illustrated in Fig. 1c. The 500-hPa geopotential height (Z500) field from the NCEP–NCAR reanalysis (Kalnay et al. 1996) displays a large-scale cyclonic circulation southwest of the United Kingdom, transporting cold air from eastern Europe across the northern parts of the continent. Moreover, CRUTEM4 observations (Jones et al. 2012) reveal large cold anomalies over Russia where the cold air originated. This state of the atmosphere combined with the development of storm Emma and the influence of anthropogenic climate change are factors that made the event unique. Here, while the focus remains on the role of climate change, the contribution of the easterly circulation to cold events will also be assessed with modeled data, to help establish a link between circulation and extremes and compare it with the

---

[1] See https://www.metoffice.gov.uk/climate/uk/interesting/february2018-snow.

[2] See https://www.theguardian.com/uk-news/2018/mar/01/beast-from-east-storm-emma-uk-worst-weather-years.

AFFILIATIONS: Christidis and Stott—Met Office Hadley Centre, Exeter, United Kingdom
CORRESPONDING AUTHOR: Nikolaos Christidis, nikos.christidis@metoffice.gov.uk

DOI:10.1175/BAMS-D-19-0084.1

A supplement to this article is available online (10.1175/BAMS-D-19-0084.2)

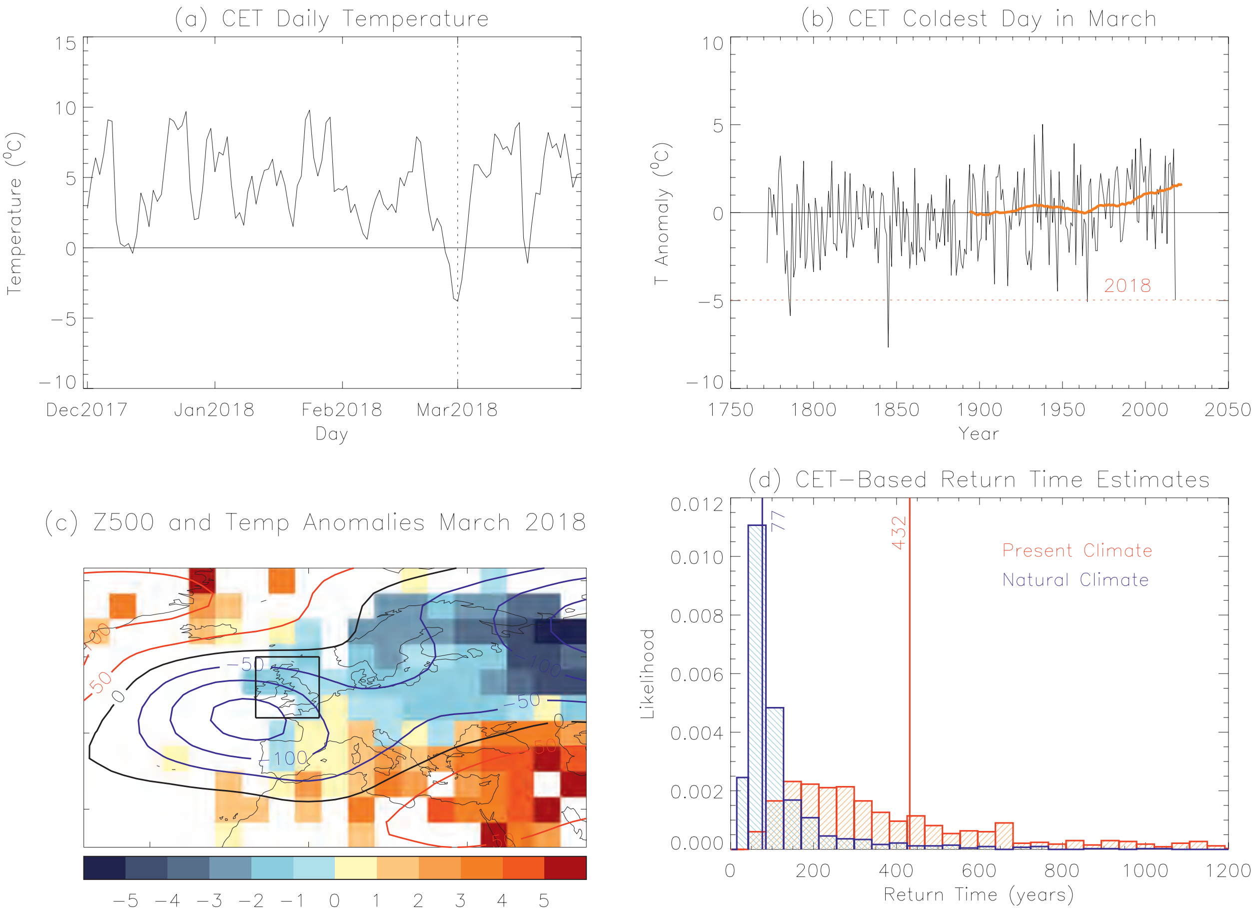

Fig. 1. (a) Time series of the observed daily mean temperature in central England. (b) Time series of the coldest day in March in central England from observations. Temperatures are expressed as anomalies relative to the 1901–30 mean. The 2018 anomaly is marked by the red dotted line. The orange line represents the forced response derived from CMIP5 simulations. (c) NCEP–NCAR Z500 anomalies (contours) and CRUTEM4 monthly mean temperature anomalies (colored grid boxes) in March 2018. Anomalies are relative to the period 1961–90. (d) Normalized distributions of the return time of extremely cold events estimated from CET observations for the present-day (red histogram) and natural (blue histogram) climate. The best estimate (50th percentile) is marked by the vertical lines.

anthropogenic impact. The attribution study follows the popular risk-based approach (Stott et al. 2016), whereby the likelihood of extreme events is estimated in the present-day climate and in a hypothetical "natural" world without any human influence on the climate. The risk ratio measuring the anthropogenic effect is subsequently computed as the ratio of the two likelihood estimates. Two analyses are carried out, one with the CET observational data and one using simulations with 18 models that contributed data to the phase 5 of the Coupled Model Intercomparison Project (CMIP5; see the supplemental material).

OBSERVATIONAL ANALYSIS. Empirical event attribution assessments can be derived from observational data (van Oldenborgh 2007). The main assumption of this methodology is that the non-stationarity in long records is primarily driven by anthropogenic influence and needs to be accounted for, such as by allowing the position parameter of an extreme distribution to vary with the global mean temperature (Kew et al. 2019). CET temperature anomalies of the coldest day in March since 1900 are used here. The anthropogenic component is represented independently by the mean of 39 CMIP5 simulations of the historical climate extended to future years with the RCP4.5 scenario (orange line in Fig. 1b). The anthropogenic component is then removed from the observations and the remaining time series represent the natural climate. The accuracy of this approximation depends on how well the CMIP5 models simulate the forced response. A Kolmogorov–Smirnov test indicates that the distribution of the coldest day in March in our representation of the natural climate is not significantly different (*p* value: 0.3) from the one based on a multimodel ensemble of CMIP5 simulations without anthropogenic forcings (see Table ES1 in the supplemental material).

To get a representation of the present-day climate, the natural time series are adjusted to the mean anthropogenic response in period 2008–28. The GEV distribution is then applied to the two time series data and the likelihoods of cold events with anomalies below the one in 2018 (–5°C) are estimated for the present day and the natural world, while a Monte Carlo bootstrap procedure (Christidis et al. 2013) is employed to estimate the uncertainties. Distributions of the return time (inverse probability) of cold events are illustrated in Fig. 1d. Human influence is estimated to increase the return time from 77 (37–478)[3] years to 432 (109 to >103) years. The probability of cold events without the effect of human influence increases by 5.84 (best estimate). However, as the observational sample is relatively small to provide the estimate the low present-day probability of cold extremes, the associated uncertainty in the risk ratio is large (Fig. 2a).

CMIP5 ANALYSIS. Ensembles of 39 and 49 simulations with and without the effect of human influence generated by the 18 CMIP5 models (see the supplemental material) are used next to estimate the change in the risk of cold events. Temperature anomalies of the coldest day in March in central England (0°–3°E, 51°–54°N) are computed for each simulated year. Common model evaluation assessments against the observations (Christidis

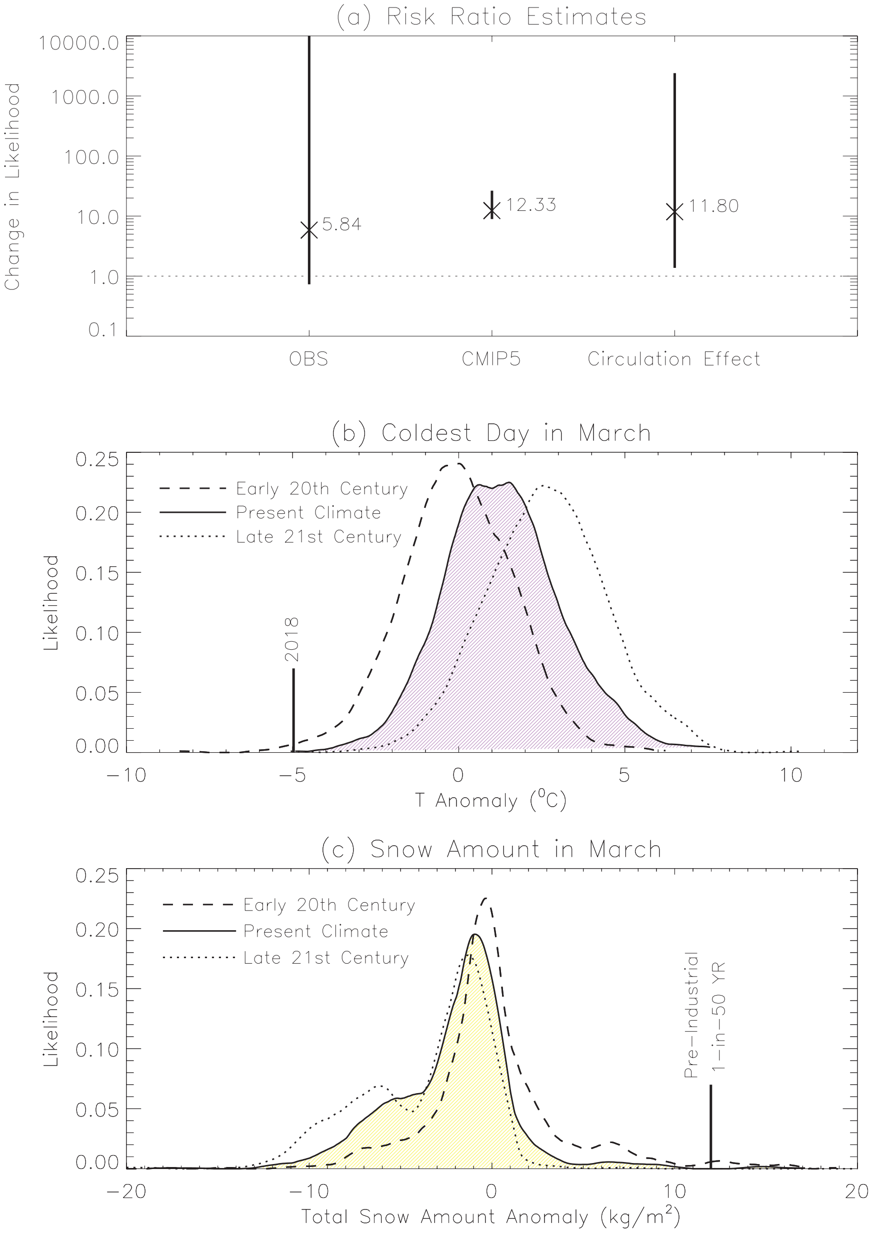

Fig. 2. (a) Risk ratio estimates measuring the change in the likelihood of cold extremes without anthropogenic forcings estimated with observations (left) and CMIP5 models (middle). The change in the likelihood under easterly circulation is shown on the right. The best estimates are represented by crosses and the 5%–95% range by whiskers. Also shown are normalized distributions of (b) the coldest day in March and (c) the total snow amount in central England constructed with CMIP5 data for the present climate (solid line; colored distribution), the early twentieth century (dashed line), and the end of the twenty-first century (dotted line). The 2018 event is marked in (b) and a 1-in-50-yr event in the natural climate is marked in (c). Anomalies are relative to 1901–30.

---

[3] The 5%–95% uncertainty range in return time estimates is reported in parentheses.

et al. 2013; Vautard et al. 2019) show that the models represent well the observed variability and long-term trend in the coldest day in March. More specifically a trend analysis, power spectra, and a quantile–quantile (Q-Q) plot are employed and provide strong evidence that the simulated trends, variability, and distribution of the coldest day in March are consistent with the CET observations (supplemental material). The likelihood of cold extremes in the natural world is estimated from all the simulated years provided by the ensemble without the effect of anthropogenic forcings. The present-day likelihood is estimated from simulations with all forcings, which are processed the same way as the CET data in the observational analysis. In this approach, the estimate of the forced response is removed from each simulation and the remaining time series are adjusted to the 2008–28 mean response. As before, probability estimates are calculated with the generalized extreme value (GEV) distribution and uncertainties with the Monte Carlo bootstrapping procedure (resampling with replacement 1000 times). Cold extremes are found to be 12.33 times more likely without human influence (Fig. 2a) and human influence is estimated to increase the return time from 108 (92–133) years to 1307 (1039–2815) years. Compared to the observational analysis, the CMIP5 methodology yields smaller uncertainties in the estimated probabilities and risk ratio, as it relies on larger samples. Temporal changes in the distribution of the coldest day in March are illustrated in Fig. 2b. Using data from simulations with all forcings, the distributions are constructed for three different periods: the early twentieth century (1900–20), the present climate (2008–28), and the end of the twenty-first century (2080–2100). As the climate warms, the 2018 anomaly moves farther into the cold tail and becomes extremely unlikely by the end of the century. To test the effect of the persistent easterly circulation on cold extremes, simulated data of the present-day climate were sub-sampled (Christidis et al. 2018) to represent years when the circulation in March matches the one in 2018 (Fig. 1c) and years when it does not. Correlations with the Z500 pattern in March 2018 above 0.6 indicate a similar easterly circulation. In total, there are 289 events with high-correlation patterns and 2363 events with low-correlation patterns. The persistence of the circulation pattern following a sudden stratospheric warming justifies the use of the monthly mean Z500 pattern, instead of the circulation pattern during the actual coldest days, as in the work by Cattiaux et al. (2010). Therefore, the attribution question asked here is what is the change in the likelihood of cold events in months with persistent flow from the European continent over the United Kingdom. By computing the likelihood of cold events in months with high and low correlation patterns, it is estimated that the presence of this circulation pattern increases the chance of cold extremes by a factor of 11.80 (Fig. 2a), although the uncertainty range is larger than the one estimated for the anthropogenic effect, because the sample size is reduced by sub-sampling. Finally, modeled distributions of the total snow (Fig. 2c) are found to shift to smaller amounts as the climate warms and tend to form a second peak at lower values, as snow-free years increase. The models suggest that snow events that occurred once every 50 years in the natural climate have almost zero probability by the end of the century. An accelerated decrease in snow over Europe in recent decades has been seen in observations (Fontrodona Bach et al. 2018), while differences between changes in mean and extreme snowfall have also been suggested (O'Gorman 2014).

CONCLUSIONS. Extremely cold daily temperatures in England, as in March 2018, are found to have become less frequent. The observational analysis gives a smaller present-day probability of cold extremes than the CMIP5 models, but as it relies on a smaller data sample, the probability estimate is more uncertain. Although changes in the circulation are expected to be less influenced by anthropogenic forcings than changes in the thermodynamic state (Trenberth et al. 2015), stratospheric warming events, like the one that triggered the 2018 cold wave, have been suggested to become more common in a warmer world (Kang and Tziperman 2017). However, U.K. seasons are still projected to become warmer during the course of the century (Murphy et al. 2018).

ACKNOWLEDGMENTS. This work was supported by the Met Office Hadley Centre Climate Programme funded by BEIS and Defra and the EUPHEME project, which is part of ERA4CS, an ERA-NET initiated by JPI Climate and co-funded by the European Union (Grant 690462).

REFERENCES

Cattiaux, J., R. Vautard, C. Cassou, P. Yiou, V. Masson-Delmotte, and F. Codron, 2010: Winter 2010 in Europe: A cold extreme in a warming climate. *Geophys. Res. Lett.*, **37**, L20704, https://doi.org/10.1029/2010GL044613.

Christidis, N., P. A. Stott, A. Scaife, A. Arribas, G. S. Jones, D. Copsey, J. R. Knight, and W. J. Tennant, 2013: A new HadGEM3-A based system for attribution of weather and climate-related extreme events.

J. Climate, **26**, 2756–2783, https://doi.org/10.1175/JCLI-D-12-00169.1.

——, A. Ciavarella, and P. A. Stott, 2018: Different ways of framing event attribution questions: The example of warm and wet winters in the UK similar to 2015/16. *J. Climate*, 31, 4827–4845, https://doi.org/10.1175/JCLI-D-17-0464.1.

Fontrodona Bach, A., G. van der Schrier, L. A. Melsen, A. M. G. Klein Tank, and A. J. Teuling, 2018: Widespread and accelerated decrease of observed mean and extreme snow depth over Europe. *Geophys. Res. Lett.*, **45**, 122 312–122 319, https://doi.org/10.1029/2018GL079799.

Jones, P. D., D. H. Lister, T. J. Osborn, C. Harpham, M. Salmon, and C. P. Morice, 2012: Hemispheric and large-scale land surface air temperature variations: An extensive revision and an update to 2010. *J. Geophys. Res.*, **117**, D05127, https://doi.org/10.1029/2011JD017139.

Kalnay, E., and Coauthors, 1996: The NCEP/NCAR 40-Year Reanalysis Project. *Bull. Amer. Meteor. Soc.*, **77**, 437–471, https://doi.org/10.1175/1520-0477(1996)077<0437:TNYRP>2.0.CO;2.

Kang, W., and E. Tziperman, 2017: More frequent sudden stratospheric warming events due to enhanced MJO forcing expected in a warmer climate. *J. Climate*, **30**, 8727–8743, https://doi.org/10.1175/JCLI-D-17-0044.1.

Karpechko, A. Y., A. Charlton-Perez, M. Balmaseda, N. Tyrell, and F. Vitart, 2018: Predicting sudden stratospheric warming 2018 and its climate impacts with a multimodel ensemble. *Geophys. Res. Lett.*, **45**, 13 538–13 546, https://doi.org/10.1029/2018GL081091.

Kew, S. F., S. Y. Philip, G. J. van Oldenborgh, G. van der Schrier, F. E. L. Otto, and R. Vautard, 2019: The exceptional summer heat wave in southern Europe [in "Explaining Extremes of 2017 from a Climate Perspective"]. *Bull. Amer. Meteor. Soc.*, **100** (1), S49–S53, https://doi.org/10.1175/BAMS-D-18-0109.1.

Murphy, J. M., and Coauthors, 2018: UKCP18 Land Projections: Science Report. Met Office, 191 pp., https://www.metoffice.gov.uk/research/collaboration/ukcp/guidance-science-reports.

O'Gorman, P., 2014: Contrasting responses of mean and extreme snowfall to climate change. *Nature*, **512**, 416–418, https://doi.org/10.1038/nature13625.

Parker, D. E., T. P. Legg, and C. K. Folland, 1992: A new daily Central England Temperature Series, 1772–1991. *Int. J. Climatol.*, **12**, 317–342, https://doi.org/10.1002/joc.3370120402.

Stott, P. A., and Coauthors, 2016: Attribution of extreme weather and climate-related events. *Wiley Interdiscip. Rev.: Climate Change*, **7**, 23–41, https://doi.org/10.1002/wcc.380.

Trenberth, K. E., J. T. Fasullo, and T. G. Shepherd, 2015: Attribution of climate extreme events. *Nat. Climate Change*, **5**, 725–730, https://doi.org/10.1038/nclimate2657.

van Oldenborgh, G. J., 2007: How unusual was autumn 2006 in Europe? *Climate Past*, **3**, 659–668, https://doi.org/10.5194/cp-3-659-2007.

Vautard, R., and Coauthors, 2019: Evaluation of the HadGEM3-A simulations in view of detection and attribution of human influence on extreme events in Europe. *Climate Dyn.*, **52**, 1187–1210, https://doi.org/10.1007/s00382-018-4183-6.

chapter 6

THE EXCEPTIONAL IBERIAN HEATWAVE OF SUMMER 2018

D. Barriopedro, P. M. Sousa, R. M. Trigo, R. García-Herrera, and A. M. Ramos

August 2018 saw the warmest Iberian heatwave since that of 2003. Recent climate change has exacerbated this event making it at least »1°C warmer than similar events since 1950–83.

The summer of 2018 was exceptionally warm in Europe, with outstanding temperatures over widespread non-contiguous areas, including Scandinavia, central Europe, Iberia, and the British Isles (e.g., WMO 2019). Different from other extraordinary summers, extreme temperatures did not occur during the same weeks everywhere, hitting the British Isles in June, Scandinavia and central Europe in July, and southwestern Europe in August. Together, they yielded the warmest European summer of the last 519 years, above the record-breaking summers of 2003 and 2010, albeit by a small margin, as inferred from instrumental and proxy data (Fig. 1a). Although northern and central Europe captured the attention of the media, Spain and Portugal experienced the warmest August after that of 2003 (AEMET 2019; IPMA 2019). Temperature anomalies were more pronounced during daytime over southwestern Iberia, and Portugal saw its warmest month in maximum temperature (TX) since 1931. Heat peaked during 1–7 August 2018, when an exceptional heatwave caused four (two) out of the five warmest days of the twenty-first century in Portugal (Spain), with country-mean daily TX reaching 41.6°C (36.4°C). We use observational and reanalysis data for 1950–2018 to quantify recent changes in the intensity of this kind of events.

METHODS. We describe the exceptionality (Fig. 1) and changing risk (Fig. 2) of the 2018 Iberian heatwave by using daily TX from E-OBS at 0.25° × 0.25° for 1950–2018 (Cornes et al. 2018) and historical series from the European Climate Assessment and Dataset (ECA&D) (Klein Tank et al. 2002) and the Instituto Português do Mar e da Atmosfera (IPMA). The atmospheric circulation is described with daily geopotential height at 500 hPa (Z500) and 2.5° × 2.5° from the NCEP–NCAR reanalysis (Kalnay et al. 1996). We use the analog method, which infers the probability distribution of a target field from the atmospheric circulation during the event (Stott et al. 2016, and references therein). Flow analog days are defined from their root-mean-square differences (RMSD) with the actual Z500 anomaly field over 20°W–10°E, 32.5°–50°N. We reconstructed the Iberian (10°W–3.5°E, 36°–43.5°N) mean TX by randomly picking one of the 20 best analogs for each heatwave day (1–7 August). This process was repeated 5,000 times with circulation analogs of the present (1984–2017) and past (1950–83) subperiods separately, building flow-conditioned distributions of Iberian TX for two different "worlds." Their comparison provides the overall changes in heatwave intensity, including those due to non-anthropogenic factors [see Sánchez-Benítez et al. (2018) for details].

AFFILIATIONS: Barriopedro—Instituto de Geociencias, Consejo Superior de Investigaciones Científicas–Universidad Complutense de Madrid, Madrid, Spain; Sousa and Ramos—Instituto Dom Luiz, Faculdade de Ciências, Universidade de Lisboa, Lisbon, Portugal; Trigo—Instituto Dom Luiz, Faculdade de Ciências, Universidade de Lisboa, Lisbon, Portugal, and Departamento de Meteorologia, Instituto de Geociências, Universidade Federal do Rio de Janeiro, Rio de Janeiro, Brazil; García-Herrera—Departamento de Física de la Tierra y Astrofísica, Facultad de Ciencias Físicas, Universidad Complutense de Madrid, Madrid, Spain, and Instituto de Geociencias, Consejo Superior de Investigaciones Científicas-Universidad Complutense de Madrid, Madrid, Spain
CORRESPONDING AUTHOR: David Barriopedro, david.barriopedro@csic.es

DOI:10.1175/BAMS-D-19-0159.1

A supplement to this article is available online (10.1175/BAMS-D-19-0159.2)

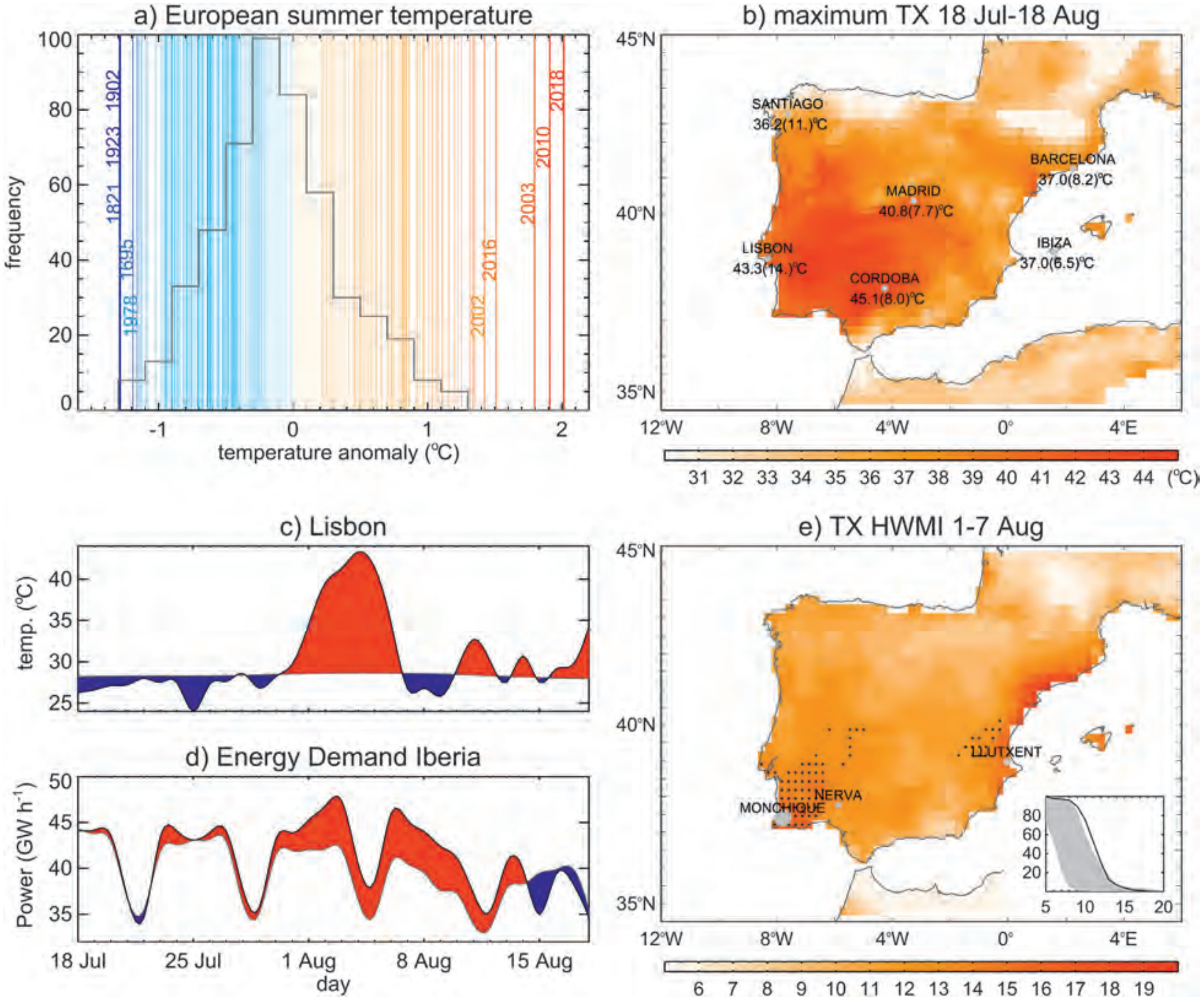

Fig. 1. (a) European summer land temperature anomaly (°C; wrt 1981–2010) over 25°W–40°E, 35°–70°N for 1500–2018 (lines) and its 1500–2000 frequency distribution (bars) using GISS (Hansen et al. 2010) for 1901–2018 and a multi-proxy reconstruction (Luterbacher et al. 2004). (b) Warmest daily TX for 18 Jul–18 Aug 2018 (shading) and selected stations (dots), with anomalies in parentheses (°C; wrt 1981–2010). Daily series of (c) Lisbon TX (°C) and (d) maximum electricity demand for Iberia (GW h^{-1}), with red (blue) denoting periods above (below) average (1981–2010 and week-equivalent days of 2013–17, respectively). (e) HWMI (dimensionless) for 1–7 Aug 2018 and percentage of Iberia exceeding a given value (inset plot, with the 1981–2000 5th–95th percentile range in shading). Black dots indicate record-breaking values (wrt all 7-day intervals of 18 Jul–18 Aug) and gray dots indicate major fires.

RESULTS. Figure 1b shows the highest TX of the 18 July–18 August 2018 period, which is close to the warmest 31-day interval of the year over Iberia. TX climbed to 46.8° and 46.6°C in weather stations of Portugal and Spain (both on 4 August), close to their national records. Although the highest TX occurred in southern and western Iberia (≫40% of the Portuguese stations broke their all-time records), unprecedented temperatures were also reported in central Iberia (e.g., 40.8°C, Madrid), the Mediterranean coast (e.g., 39.8°C, near Barcelona), and the Balearic Islands (e.g., 37.0°C, Ibiza). Likewise, minimum temperatures were exceptionally high, with more than 25% of the Portuguese stations setting absolute records and some Spanish locations reporting the warmest nights of the last century (e.g., 25.9°C, Madrid). Tropical nights affected 50% of Portugal and extended to the Mediterranean coast (e.g., >25°C, Barcelona) during seven consecutive days.

The first week of August saw the warmest anomalies (Fig. 2a, shading), as illustrated by the time series of Lisbon (Fig. 1c), where TX surpassed 40°C for three days, breaking its previous record twice by a large margin (≫2°C of exceedance). The atmospheric

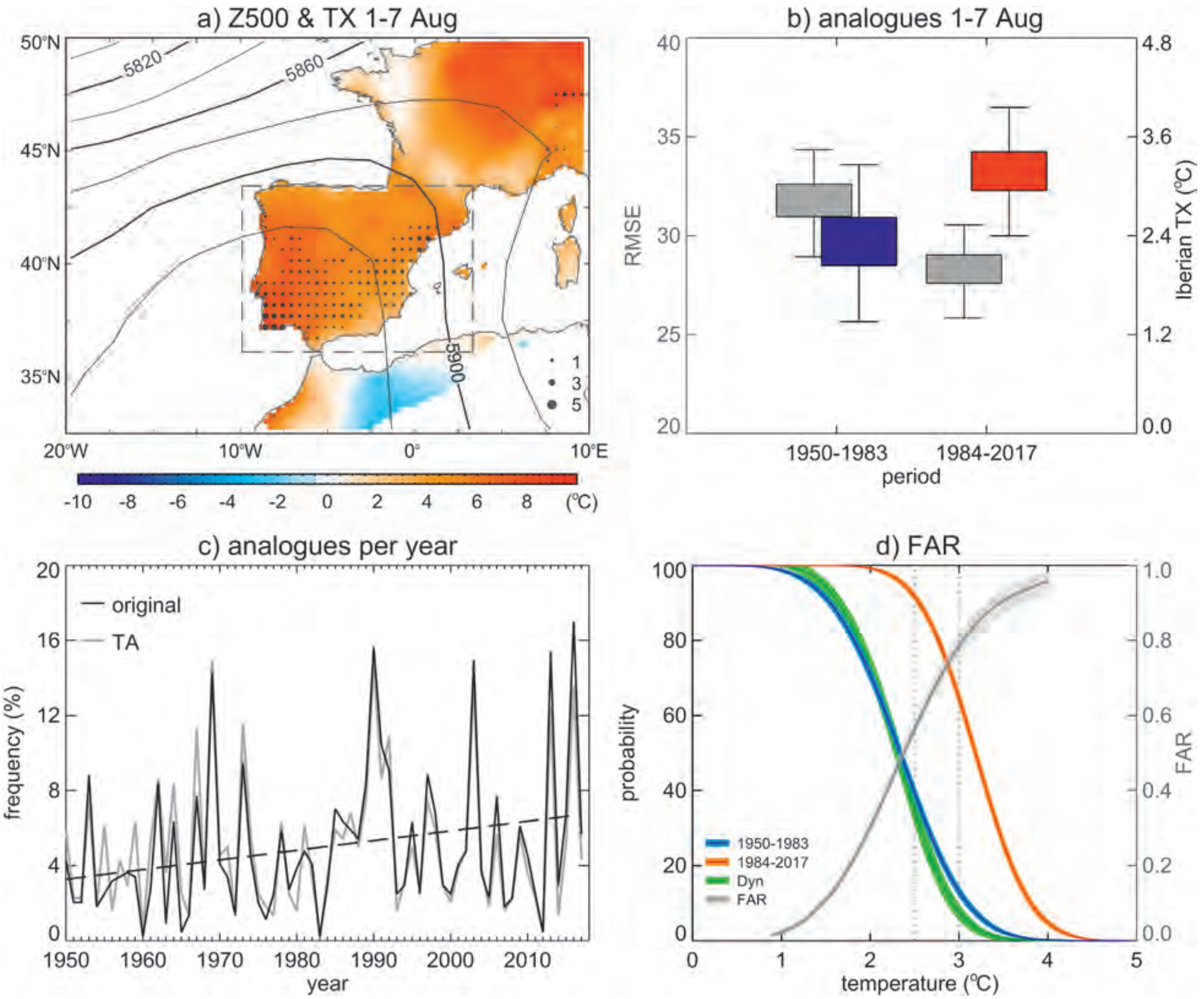

Fig. 2. (a) Z500 (m; contours) and TX anomaly (°C; shading) for 1–7 Aug 2018. Dots denote TX exceedance over previous records for that calendar period; (b) Flow-conditioned distributions of Iberian TX anomaly (°C; wrt 1981–2010; right *y* axis) for 1–7 Aug 2018 in past (1950–83; blue) and present (1984–2017; red) climates. Gray boxplots show their RMSD (left *y* axis); (c) Frequency series of good flow analogs (percentage of days) from raw (black) and detrended (gray) Z500 data. Dashed line indicates statistically significant trend ($p < 0.05$); (d) Past (blue) and present (red) flow-conditioned probabilities (%; left *y* axis) of Iberian TX anomaly above given thresholds (°C; *x* axis). The gray line represents the estimated FAR (dimensionless; right *y* axis) and the green line indicates the contribution of dynamical changes. Shading shows the 5th–95th percentile range from 1,000 random subsamples.

circulation displayed an outstanding subtropical ridge, with above-normal pressures extending to central Europe (Fig. 2a, contours). Enhanced stability and stagnant conditions worsened air quality, being aggravated by a Saharan dust episode (Sousa et al. 2019). Despite the wet and mild spring, two out of the three major Spanish fires of 2018 deflagrated during the heatwave, causing ≫4.500 ha of burned area and thousands of evacuated people. During 15 days (3–17 August), the largest European fire of 2018 devastated 27,000 ha in southern Portugal, surpassing the already unusual total area burned in Sweden (21,000 ha) or the United Kingdom (18,000 ha) all year round (San-Miguel-Ayanz et al. 2019). According to the media, daily mortality nearly doubled in Portugal (≫500 fatalities above the seasonal mean for 2–7 August) and some Spanish regions registered the highest number of deaths by heatstroke since official records started in 2004. Health-related impacts were partially minimized by an outsized use of air conditioning, which caused a 10% rise in Iberian energy consumption (Fig. 1d) and blackouts in Lisbon suburbs. Above-normal energy consumption extended beyond the heatwave, likely due to the concentration of population in major touristic destinations, where the heat persisted the most. According to the Heatwave Magnitude Intensity (HWMI) index [Russo et al. 2015; also see the online supplemental material (SM)], more than half of Iberia experienced extreme HWMI values (unprecedented in the southern half of Portugal and some Mediterranean areas; Fig. 1e), resulting in the most intense Iberian heatwave on 7-day time scales since 1950 after the 2003 episode (Table ES1).

Figure 2b shows the distribution of Iberian TX averaged for the heatwave period, as inferred from flow analogs of the past (blue boxplot) and present (red) climate. Present-day analogs explain almost 60% of the observed Iberian TX, the remaining being attributed to non-dynamical processes (e.g., feedbacks) and limited sampling. The comparison reveals that similar atmospheric conditions trigger warmer Iberian TX (≫1°C) now than in the recent past (i.e., the observed circulation would have caused a less severe heatwave in the past). This agrees with a warming and poleward trend of 2018-like Saharan intrusions, as reconstructed from flow analogs (see Fig. ES1 in the SM). Figure 2d quantifies how recent trends have changed the intensity of these Iberian heatwaves, by counting the fraction of replicated analogs with 7-day mean Iberian TX above a certain threshold in each subperiod. The flow-conditioned probability of experiencing Iberian heatwaves with TX anomalies above ≫2.5°C has doubled in just 35 years, equivalent to a fraction of attributable risk (FAR) of ≫0.5 (see the SM). Under the atmospheric circulation conditions of the 2018 heatwave, the chances of exceeding 3°C have risen by more than five times (FAR of 0.8).

CONCLUSIONS AND DISCUSSION. As the atmospheric circulation is constrained, the reported FAR should be attributed to thermodynamical changes (warming trend). However, flow analogs of the 2018 event show significant differences between the two subperiods, displaying smaller RMSD in the present than in the past (gray boxplots, Fig. 2b). Figure 2c (black line) confirms a significant ($p < 0.05$) upward trend in the 1950–2018 frequency series of "good" flow analogs, defined as those days with RMSD below the 5th percentile of the event distribution. This trend may reflect dynamical (e.g., Z500 gradients) changes or thermodynamical effects (e.g., thermal Z500 rise). To address this, we repeated the analysis by removing the regional monthly mean trends of Z500 and TX. The resulting thermodynamically adjusted (TA) distributions for the two subperiods become much closer and the trend in the number of good flow analogs is no longer significant at $p < 0.05$ (gray line, Fig. 2c). Their difference has been added to the past distribution to estimate the contribution of dynamical changes (green line, Fig. 2d). Dynamical changes cannot explain the changing risk of Iberian TX anomalies. Therefore, regional warming is largely responsible for the FAR, particularly in the higher TX thresholds. Further studies are encouraged to pin down the key drivers and their contributing roles to the reported changes (e.g., land–atmosphere feedbacks).

ACKNOWLEDGMENTS. We acknowledge the E-OBS dataset from http://www.uerra.eu (EU-FP6), the Copernicus Climate Change Service, the data providers in ECA&D (https://www.ecad.eu), IPMA, the GISTEMP Team 2019 dataset (data.giss.nasa.gov/gistemp/) and J. Luterbacher for providing the proxy-based reconstruction. Energy data were retrieved from https://demanda.ree.es/ and http://www.centrodeinformacao.ren.pt. AMR, PMS, and RMT were supported by project IMDROFLOOD (Improving Drought and Flood Early Warning, Forecasting and Mitigation using real-time hydroclimatic indicators; WaterJPI/0004/2014) through Fundação para a Ciência e a Tecnologia (FCT), Portugal. AMR was also supported by the Scientific Employment Stimulus 2017 from FCT (CEECIND/00027/2017). We thank three reviewers for their comments.

REFERENCES

AEMET, 2019: Resúmenes Climatológicos: Agosto de 2018. Agencia Estatal de Meteorología, accessed 5 January 2019, 11 pp., http://www.aemet.es/documentos/es/serviciosclimaticos/vigilancia_clima/resumenes_climat/mensuales/2018/res_mens_clim_2018_08.pdf.

Cornes, R., G. van der Schrier, E. J. M. van den Besselaar, and P. D. Jones, 2018: An ensemble version of the E-OBS temperature and precipitation datasets. *J. Geophys. Res. Atmos.*, **123**, 9391–9409, https://doi.org/10.1029/2017JD028200.

Hansen, J., R. Ruedy, M. Sato, and K. Lo, 2010: Global surface temperature change. *Rev. Geophys.*, **48**, RG4004, https://doi.org/10.1029/2010RG000345.

IPMA, 2019: Boletim Climatológico: Agosto 2018, Portugal continental. Instituto Português do Mar e da Atmosfera, accessed 5 January 2019, 16 pp., http://www.ipma.pt/resources.www/docs/im.publicacoes/edicoes.online/20180924/QyzZvZwgxxBnLFiHkSkX/cli_20180801_20180831_pcl_mm_co_pt.pdf.

Kalnay, E., and Coauthors, 1996: The NCEP/NCAR 40-Year Reanalysis Project. *Bull. Amer. Meteor.*

Soc., **77**, 437–471, https://doi.org/10.1175/1520-0477(1996)077<0437:TNYRP>2.0.CO;2.

Klein Tank, A. M. G., and Coauthors, 2002: Daily dataset of 20th-century surface air temperature and precipitation series for the European Climate Assessment. *Int. J. Climatol.*, **22**, 1441–1453, https://doi.org/10.1002/joc.773.

Luterbacher, J., D. Dietrich, E. Xoplaki, M. Grosjean, and H. Wanner, 2004: European seasonal and annual temperature variability, trends, and extremes since 1500. *Science*, **303**, 1499–1503, https://doi.org/10.1126/science.1093877.

Russo, S., J. Sillmann, and E. Fischer, 2015: Top ten European heatwaves since 1950 and their occurrence in the coming decades. *Environ. Res. Lett.*, **10**, 124003, https://doi.org/10.1088/1748-9326/10/12/124003.

Sánchez-Benítez, A., R. García-Herrera, D. Barriopedro, P. M. Sousa, and R. M. Trigo, 2018: June 2017: The earliest mega-heatwave of reanalysis period. *Geophys. Res. Lett.*, **45**, 1955–1962, https://doi.org/10.1002/2018GL077253.

San-Miguel-Ayanz, J., and Coauthors, 2019: Advance EFFIS Report on Forest Fires in Europe, Middle East and North Africa 2018. EUR 29722 EN, Joint Research Centre, 36 pp., https://doi.org/10.2760/262459.

Sousa, P. M., D. Barriopedro, A. M. Ramos, R. García-Herrera, F. Espírito-Santo, and R. M. Trigo, 2019: Saharan air intrusions as a relevant mechanism for Iberian heatwaves: The record breaking events of August 2018 and June 2019. *Wea. Climate Extremes*, **26**, 100224, https://doi.org/10.1016/j.wace.2019.100224.

Stott, P. A., and Coauthors, 2016: Attribution of extreme weather and climate-related events. *Wiley Interdiscip. Rev.: Climate Change*, **7**, 23–41, https://doi.org/10.1002/wcc.380.

WMO, 2019: WMO Statement on the State of the Global Climate in 2018. WMO-No. 1233, World Meteorological Organization, 39 pp., https://library.wmo.int/doc_num.php?explnum_id=5789.

chapter 7

ANALYSES OF THE NORTHERN EUROPEAN SUMMER HEATWAVE OF 2018

P. Yiou, J. Cattiaux, D. Faranda, N. Kadygrov, A. Jézéquel, P. Naveau, A. Ribes,
Y. Robin, S. Thao, G. J. van Oldenborgh, and M. Vrac

A heatwave struck Northern Europe in summer 2018. The probability of this event increased with human-induced climate change primarily due to thermodynamic changes.

A heatwave struck northern Europe in the summer of 2018. Daily temperature anomalies reached +14 K in Scandinavia, the Netherlands, and Belgium, which are record-breaking temperatures. This heatwave was exacerbated by a drought caused by a persisting circulation anomaly (Kornhuber et al. 2019; Toreti et al. 2019; World Weather Attribution 2018). The heatwave and drought favored unprecedented forest fires in Scandinavia (NASA Earth Observatory 2018).

This paper aims at characterizing this heatwave event and determining its probability in present and future climate conditions. This paper presents how the 2018 heatwave can be analyzed in terms of temperature and atmospheric circulation patterns, and highlights the robustness of the signal to statistical hypotheses.

DEFINING THE EVENT. Defining the spatiotemporal scale of the event is inspired by the procedure of Cattiaux and Ribes (2018), which consists in selecting the space–time window for which the temperature has been the most extreme (i.e., its probability p is the smallest in present-day conditions). We use E-OBS (Haylock et al. 2008) daily mean temperatures over 1950–2018 and consider each N-day time window between 1 May and 31 October, and each n-country connected spatial domain. Overall, we find that the probability p is minimum for the 19-day window between 15 July and 2 August and the two-country domain covering Finland and Sweden. However, this minimum is not sharp and adding the Baltic countries, Denmark, and Norway to the spatial domain does not significantly change p. Since a larger domain is more robust for the latter analyses, we define the spatial scale as the 5°–30°E, 55°–70°N area (Fig. 1a). This corresponds to the "Scandinavian cluster" type of heatwave identified by Stefanon et al. (2012). Over this space–time window, the average temperature anomaly relative to the 1981–2010 climatology is +5.4 K (Fig. 1b), and each single day during this time period in 2018 is more than +3 K above the climatological mean seasonal cycle (see Fig. ES1a in the online supplemental material). The atmospheric circulation is characterized by prolonged high pressure conditions (Fig. 1c) over Scandinavia. This motivates the conditional attribution analysis with respect to the atmospheric circulation, because such circulation patterns generally enhance major heatwaves in the midlatitudes (Quesada et al. 2012; Mueller and Seneviratne 2012), as was observed in summers 2003 (Schär et al. 2004) or 2010 (Barriopedro et al. 2011).

AFFILIATIONS: Yiou, Kadygrov, Naveau, Thao, and Vrac—Laboratoire des Sciences du Climat et de l'Environnement, UMR8212 CEA-CNRS-UVSQ, IPSL and U Paris Saclay, Gif-sur-Yvette, France;Cattiaux, Ribes, and Robin—Centre National de Recherches Météorologiques, Université de Toulouse, Météo-France, CNRS, Toulouse, France; Faranda—London Mathematical Laboratory, London, United Kingdom, and Laboratoire des Sciences du Climat et de l'Environnement, UMR8212 CEA-CNRS-UVSQ, IPSL and U Paris Saclay, Gif-sur-Yvette, France; Jézéquel—Laboratoire de Météorologie Dynamique, UMR CNRS-ENS-UPMC-X, Paris, and Ecole Nationale des Ponts et Chaussées, Champs-sur-Marne, France; van Oldenborgh—KNMI, De Bilt, Netherlands

CORRESPONDING AUTHOR: Pascal You, pascal.yiou@lsce.ipsl.fr

DOI:10.1175/BAMS-D-19-0170.1

A supplement to this article is available online (10.1175/BAMS-D-19-0170.2)

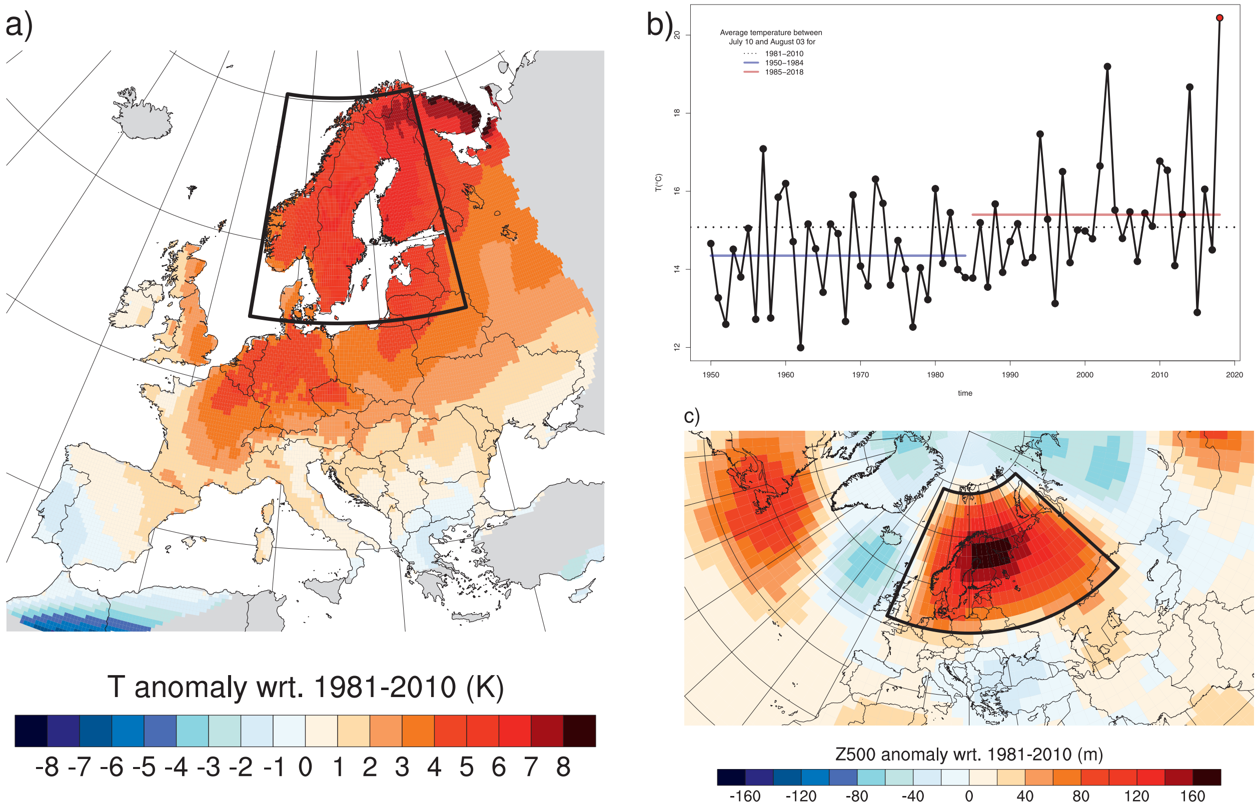

Fig. 1. Geographical and temporal features of the event from reanalyses and observations. (a) Map of temperature anomalies in E-OBS between 15 Jul 2018 and 2 Aug 2018, with respect to a 1981–2010 climatology. The rectangle indicates the zone to be analyzed (e.g., Scandinavia). (b) Time series of spatial [rectangle in (a)] and temporal (15 Jul to 2 Aug) average temperature (E-OBS) from 1950 to 2018, with reference 1981–2010 climatology. (c) Anomalies of Z500 in NCEP over the North Atlantic between 15 Jul 2018 and 2 Aug 2018, with respect to the 1981–2010 climatology. The rectangle indicates the zone for the computation of analogs.

UNCONDITIONAL ATTRIBUTION. The unconditional attribution compares the probability $p1$ of observing the event (exceeding a temperature threshold) in the present day or in a climate influenced by human activities (a factual world), and the probability $p0$ of the event in past conditions or in a climate without human influence (a counterfactual world). We focus on the probability ratio (PR) $p1/p0$. The results from two different statistical approaches are presented here.

First, we determined $p1$ and $p0$ from annual maximum 19-day averaged temperature over the region in E-OBS data by fitting the period 1950–2017 to a generalized extreme value (GEV) distribution. The location parameter μ is a linear function of a proxy for global warming, for which we take the 4-yr smoothed global mean surface temperature [as in (Kew et al. 2019)]. This procedure excludes the observed extreme in 2018, as GEV parameter estimates are sensitive to the last value of a time series. The fit was extrapolated to the global temperature of 1900 as a proxy of the preindustrial climate. The procedure was applied to a few ensembles of transient climate model experiments (EC-Earth2.3 T159 coupled 1860–2018; RACMO 2.2 11-km downscaling this EC-Earth ensemble 1950–2018; HadGEM3-A N219 prescribed SST 1960–2015; calibrated Euro-CORDEX ensemble 11-km 1971–2018; see Fig. 2a). These have realistic variability of 19-day heat extremes: the fitted scale and shape parameters are compatible with the fit to observations. Uncertainty ranges for each dataset were obtained from bootstrapping. Model spread was also added to the model estimates to obtain $\chi^2/\text{dof} = 1$. We plot the probability ratios and associated uncertainties in Fig. 2a. This diagnostic shows that PR values are significantly larger than 1, with a large range of variations (PR synthesis between models and observations between 5 and 2,000), indicating that such a heatwave is between 5 and 2,000 times more likely in the factual simulations.

A second unconditional attribution was performed on the E-OBS dataset and a CMIP5 (Taylor et al. 2012)

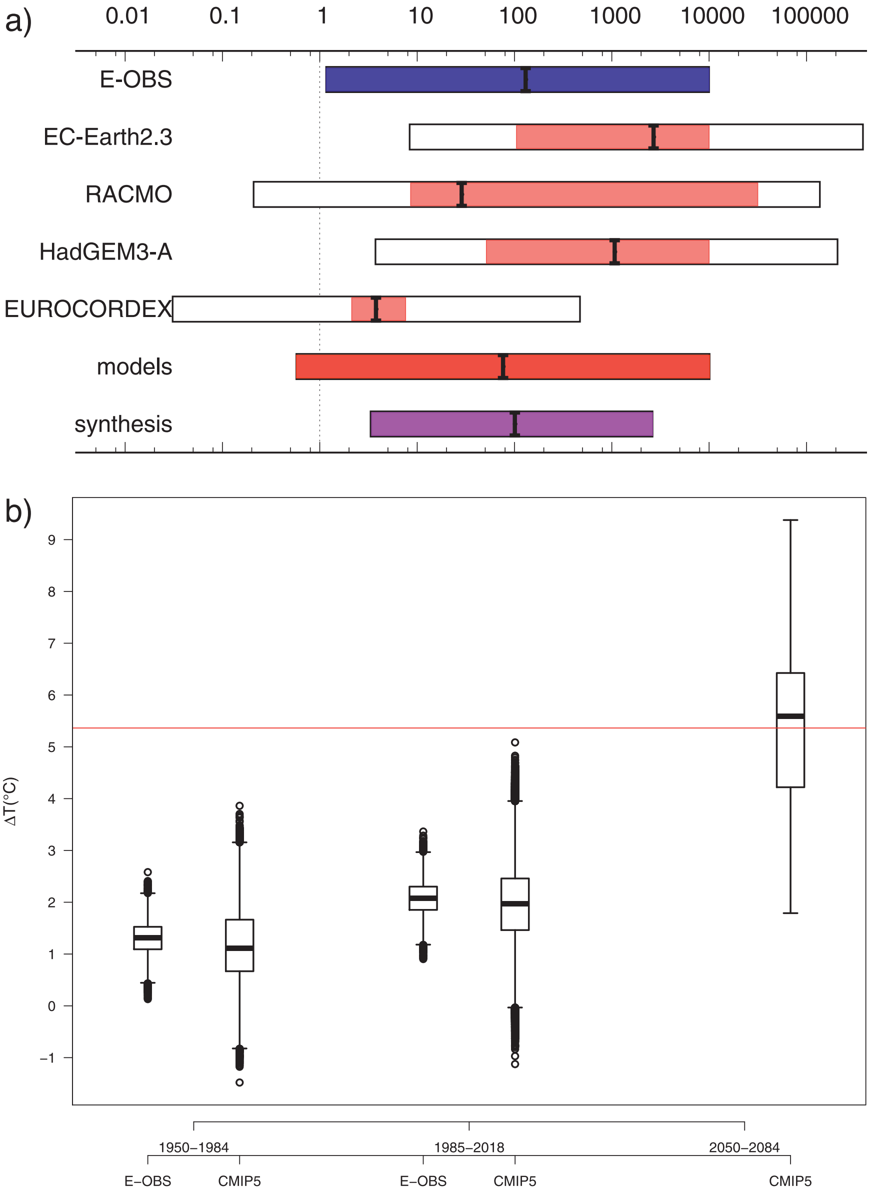

FIG. 2. (a) Probability ratios (PR) from observations (E-OBS) in blue, and climate model simulations (EC-EARTH, RACMO, HadGEM3, Euro-CORDEX ensemble) in pink, all models in red, and observation–model synthesis in purple. The black vertical lines indicate the value of the best fit. The white boxes represent the model spread that is added to the pink boxes, representing a conservative uncertainty due to natural variability to obtain χ^2/dof = 1. (b) Conditional temperature simulations in CMIP5 and in E-OBS for different periods. The boxplots represent the temperature distributions, conditioned to the atmospheric circulation observed during event that are simulated through the analog procedure for different periods. For the CMIP5 models, the temperatures are simulated independently for each model and the boxplots represent the distribution of all the temperatures simulated for the CMIP5 models altogether. The circle points on the boxplots represent the simulated temperatures that are 1.5 times the interquartile range above the upper quartile and bellow the lower quartile. The red line denotes the value of the observed mean temperature between 15 Jul and 2 Aug 2018.

simulation ensemble using the method of (Ribes et al. 2019). The distribution of mean temperature over the considered space–time domain is assumed to follow a Gaussian distribution, and to covary with a variable representing climate change. This covariate is the summer mean continental temperature over the box –10° to 30°E, 35° to 70°N. The probability of the event can be estimated continuously in time. This calculation is made for each CMIP5 model and summarized into a multimodel synthesis. Then, changes in the covariate and the temperature distribution are constrained by E-OBS observations [see Ribes et al. (2019) for details]. Figure ES2a shows the probability ratio from 1850 to 2100, under the high-emission RCP8.5 scenario (van Vuuren et al. 2011), according to the multimodel synthesis constrained by observations. The effect of human activities on the probability of such event cannot be detected before the end of twentieth century as the probability ratio is not significantly different from 1. After the year 2000, the probability ratio is significantly higher than 1 and suggests that human activities have increased the probability ratio of such events. In 2018, the probability of such events has increased by a factor of 39 (95% confidence interval: 3 to 3,400; see Fig. ES2a) due to human activities.

CONDITIONAL ATTRIBUTION. We determine the temperature distribution *conditional* to atmospheric patterns that are similar to 2018 changes with time. Following the procedure of Jézéquel et al. (2018b), we computed analogs of geopotential height at 500 mb (Z500) over a zone covering Scandinavia (rectangle in Fig. 1c), which optimizes the temperature/circulation correspondence. The analogs are computed from Z500 in two subperiods (1950–84 and 1985–2018) of the NCEP reanalysis (Kistler et al. 2001). The Z500 data are detrended with a smoothing spline before computing analogs, in order to avoid a bias due to the temperature increase. Ten days (out of 19) yield good analogs (distance < 30th quantile and spatial correlation > 70th quantile). Mean analog temperatures are simulated by random selections of analog days from each subperiod, following the procedure of Jézéquel et al. (2018b). The change of temperature probability distributions describes the thermodynamic changes on a summer that is similar to 2018. A total of 10,000 stochastic samples are generated, with analogs selected in the two subperiods. The changes are significant according to a two-sided Kolmogorov–Smirnov test (p value < 10^{-15}).

Although the simulated values do not reach the 2018 record, we find a significant increase of the temperature distribution between the two subperiods (Fig. 2b). This ?1-K increase is comparable to the average increase of temperature between the two subperiods. When analogs are selected in RCP8.5 CMIP5 simulations, we find that similar atmospheric patterns lead to summer temperatures that are consistent with the 2018 record values. This means that temperature anomalies of a similar heatwave (same domain, duration, and atmospheric circulation) would reach or exceed 5 K by the end of the twenty-first century (Fig. 2b).

CHANGES IN ATMOSPHERIC CIRCULATION. We diagnosed atmospheric circulation trends by analyzing the distance values of the best analogs (Jézéquel et al. 2018a), the local dimension, and persistence (Faranda et al. 2017). This was done by comparing the observed Z500 anomaly sequence (in NCEP), and other observed sequences in NCEP or simulated in the RCP4.5 and RCP8.5 scenarios.

First, we computed the distribution of Z500 distances to the hottest day of the heatwave (17 July 2018) in NCEP and the RCP4.5 and RCP8.5 scenario simulations. We then counted the number of analogs whose distance is below the 5th quantile of all distances, for each summer. The distance distribution informs on the likelihood to have a similar atmospheric pattern as the observed one (Jézéquel et al. 2018a). We find no significant trend in the number of good analogs in NCEP reanalysis or scenario simulations (Fig. ES2c): some CMIP5 simulations do identify marginally significant trends, but there is no consensus among models, as was found for the 2003 heatwave (Jézéquel et al. 2018a).

Second, we computed the *local dimension* of the observed Z500 sequence in CMIP5 RCP4.5 and RCP8.5 simulations. This assumes that the observed state belongs to the climate variability described by climate models, which is validated by the fact that the distribution of analog distances for each model is similar to the NCEP reanalysis distances (Rodrigues et al. 2018). The local dimension informs on the number of degrees of freedom of trajectories around a given state and hence on its predictability (Faranda et al. 2017). We find no significant trend in the local dimension of summer 2018 Z500 in CMIP5 RCP4.5 and RCP8.5 simulations.

Third, the *extremal index* informs on the persistence of a given state (i.e., the time it takes to leave its neighborhood in phase space) (Faranda et al. 2017). As for the local dimension, the local persistence of summer 2018 Z500 was evaluated on CMIP5 RCP simulations. We find a small but significant decrease of the persistence of these weather patterns (Fig. ES2d).

CONCLUSIONS. This paper refines the preliminary analyses of the World Weather Attribution for that event (World Weather Attribution 2018). Our analyses demonstrate the thermodynamic contribution of human-induced climate change to describe the probability and intensity of the summer 2018 event in Scandinavia. The bulk values and uncertainties of the probability ratios are significantly larger than 1 in two statistical approaches with different underlying technical assumptions. Hence we find a strong and robust contribution of human activities to 2018 heatwave in northern Europe from the unconditional attribution analysis. This is further supported by an analysis of record probabilities (see our online supplemental material S2b; Naveau et al. 2018). The wide range of probability ratios from the model ensemble calls for a calibration of the model outputs (Bellprat et al. 2019), which is outside the scope of this short paper. Therefore those probability ratios should be used in a qualitative manner, rather than quantitative.

The atmospheric conditions enhance the temperature signal (∼+2 K; Fig. 2b), but the conditional attribution simulations cannot reach the observed record values, possibly because some physical processes are not taken into account (soil moisture feedbacks and ocean variability).

Those results emphasize the necessity of systematic analyses of European heatwaves (Stefanon et al. 2012), for which the properties of the atmospheric circulation do not change uniformly in scenario simulations (Jézéquel et al. 2018a). This also highlights uncertainties in the changes of atmospheric circulation.

ACKNOWLEDGMENTS. This paper was supported by the EUPHEME project, which is part of ERA4CS, an ERA-NET initiated by JPI Climate and co-funded by the European Union (Grant 690462), ERC Grant 338965-A2C2, and French "Convention de Service Climatique". The analyses of this paper were obtained with the Climate Explorer (https://climexp.knmi.nl/start.cgi) and the "blackswan" Web Processing Service (https://github.com/bird-house/blackswan).

REFERENCES

Barriopedro, D., E. M. Fischer, J. Luterbacher, R. M. Trigo, and R. García-Herrera, 2011: The hot summer of 2010: Redrawing the temperature record map of Europe. *Science*, **332**, 220–224, https://doi.org/10.1126/science.1201224.

Bellprat, O., V. Guemas, F. Doblas-Reyes, and M. G. Donat, 2019: Towards reliable extreme weather and climate event attribution. *Nat. Commun.*, **10**, 1732, https://doi.org/10.1038/s41467-019-09729-2.

Cattiaux, J., and A. Ribes, 2018: Defining single extreme weather events in a climate perspective. *Bull. Amer. Meteor. Soc.*, **99**, 1557–1568, https://doi.org/10.1175/BAMS-D-17-0281.1.

Faranda, D., G. Messori, and P. Yiou, 2017: Dynamical proxies of North Atlantic predictability and extremes. *Sci. Rep.*, **7**, 41278, https://doi.org/10.1038/srep41278.

Haylock, M. R., N. Hofstra, A. M. G. Klein Tank, E. J. Klok, P. D. Jones, and M. New, 2008: A European daily high-resolution gridded data set of surface temperature and precipitation for 1950–2006. *J. Geophys. Res.*, **113**, D20119, https://doi.org/10.1029/2008JD010201.

Jézéquel, A., J. Cattiaux, P. Naveau, S. Radanovics, A. Ribes, R. Vautard, M. Vrac, and P. Yiou, 2018a: Trends of atmospheric circulation during singular hot days in Europe. *Environ. Res. Lett.*, **13**, 054007, https://doi.org/10.1088/1748-9326/aab5da.

—, P. Yiou, and S. Radanovics, 2018b: Role of circulation in European heatwaves using flow analogues. *Climate Dyn.*, **50**, 1145–1159, https://doi.org/10.1007/s00382-017-3667-0.

Kew, S., S. Y. Philip, G. J. van Oldenborgh, G. van der Schrier, F. E. Otto, and R. Vautard, 2019: The exceptional summer heat wave in southern Europe 2017. *Bull. Amer. Meteor. Soc.*, **100** (1), S49–S53, https://doi.org/10.1175/BAMS-D-18-0109.1.

Kistler, R., and Coauthors, 2001: The NCEP–NCAR 50-Year Reanalysis: Monthly means CD-ROM and documentation. *Bull. Amer. Meteor. Soc.*, **82**, 247–267, https://doi.org/10.1175/1520-0477(2001)082<0247:TNNYRM>2.3.CO;2.

Kornhuber, K., S. Osprey, D. Coumou, S. Petri, V. Petoukhov, S. Rahmstorf, and L. Gray, 2019: Extreme weather events in early summer 2018 connected by a recurrent hemispheric wave-7 pattern. *Environ. Res. Lett.*, **14**, 054002, https://doi.org/10.1088/1748-9326/ab13bf.

Mueller, B., and S. I. Seneviratne, 2012: Hot days induced by precipitation deficits at the global scale. *Proc. Natl. Acad. Sci. USA*, **109**, 12 398–12 403, https://doi.org/10.1073/pnas.1204330109.

NASA Earth Observatory, 2018: Scarcely seen Scandinavian fires. Accessed 6 September 2019, https://earthobservatory.nasa.gov/images/92454/scarcely-seen-scandinavian-fires.

Naveau, P., A. Ribes, F. Zwiers, A. Hannart, A. Tuel, and P. Yiou, 2018: Revising return periods for record events in a climate event attribution context. *J. Climate*, **31**, 3411–3422, https://doi.org/10.1175/JCLI-D-16-0752.1.

Quesada, B., R. Vautard, P. Yiou, M. Hirschi, and S. I. Seneviratne, 2012: Asymmetric European summer heat predictability from wet and dry southern winters and springs. *Nat. Climate Change*, **2**, 736–741, https://doi.org/10.1038/nclimate1536.

Ribes, A., S. Thao, and J. Cattiaux, 2019: Describing the relationship between a weather event and climate change: A new statistical approach. *J. Climate*, submitted (available online at https://hal.archives-ouvertes.fr/hal-02122780/document).

Rodrigues, D., M. C. Alvarez-Castro, G. Messori, P. Yiou, Y. Robin, and D. Faranda, 2018: Dynamical properties of the North Atlantic atmospheric circulation in the past 150 years in CMIP5 models and the 20CRv2c Reanalysis. *J. Climate*, **31**, 6097–6111, https://doi.org/10.1175/JCLI-D-17-0176.1.

Schär, C., P. Vidale, D. Lüthi, C. Frei, C. Häberli, M. Liniger, and C. Appenzeller, 2004: The role of increasing temperature variability in European summer heatwaves. *Nature*, **427**, 332–336, https://doi.org/10.1038/nature02300.

Stefanon, M., F. D'Andrea, and P. Drobinski, 2012: Heatwave classification over Europe and the Mediterranean region. *Environ. Res. Lett.*, **7**, 014023, https://doi.org/10.1088/1748-9326/7/1/014023.

Taylor, K. E., R. J. Stouffer, and G. A. Meehl, 2012: An overview of CMIP5 and the experiment design.

Bull. Amer. Meteor. Soc., **93**, 485–498, https://doi.org/10.1175/BAMS-D-11-00094.1.

Toreti, A., and Coauthors, 2019: The exceptional 2018 European water seesaw calls for action on adaptation. *Earth's Future*, **7**, 652–663, https://doi.org/10.1029/2019EF001170.

van Vuuren, D. P., and Coauthors, 2011: The representative concentration pathways: An overview. *Climatic Change*, **109**, 5–31, https://doi.org/10.1007/s10584-011-0148-z.

World Weather Attribution, 2018: Heatwave in northern Europe, summer 2018. WWA, Accessed 6 September 2019, https://www.worldweatherattribution.org/attribution-of-the-2018-heat-in-northern-europe/.

chapter 8

ANTHROPOGENIC INFLUENCE ON THE 2018 SUMMER WARM SPELL IN EUROPE: THE IMPACT OF DIFFERENT SPATIO-TEMPORAL SCALES

Nicholas J. Leach, Sihan Li, Sarah Sparrow, Geert Jan van Oldenborgh,
Fraser C. Lott, Antje Weisheimer, and Myles R. Allen

We demonstrate that, in attribution studies, events defined over longer time scales generally produce higher probability ratios due to lower interannual variability, reconciling seemingly inconsistent attribution results of Europe's 2018 summer heatwaves in reported studies.

The summer of 2018 was extremely warm in parts of Europe, particularly Scandinavia, the Iberian Peninsula, and central Europe, with a range of all-time temperature records set across the continent (Johnston 2018; NESDIS 2018). Impacts were felt across Europe, with wildfires burning in Sweden (Krikken et al. 2019; Watts 2018), heatstroke deaths in Spain (Publico 2018), and widespread drought (Harris 2018). During the summer, the World Weather Attribution (WWA) initiative released an analysis of the heat spell (World Weather Attribution 2018) based on observations/forecasts and models in specific locations (Dublin, Ireland; De Bilt, Netherlands; Copenhagen, Denmark; Oslo, Norway; Linkoping, Sweden; Sodankyla, Finland; Jokionen, Finland), which concluded that the increase in likelihood due to human-induced climate change was at least 2 to 5 times. In December, the U.K. Met Office (UKMO) stated that they found the 2018 U.K. summer temperatures were made 30 times more likely (Press Office 2018; McCarthy et al. 2019). These two estimates appear to quantitatively disagree; however, we show they can be reconciled by investigating the effects of using different spatial domains and temporal scales in the event definition. We also demonstrate that prescribed SST model simulations can underrepresent the variability of temperature extremes, especially near the coast, with implications for any derived attribution results.

EVENT DEFINITION. We consider various temperature-based event definitions to demonstrate the impact of this choice in attribution assessments, and assess to what extent human influence affected the seasonal and peak magnitudes of the 2018 summer heat event on a range of spatial scales. The statistic we use is the annual maximum of the 1-, 10-, and 90-day running mean of daily mean 2-m temperature (hereafter TM1x, TM10x, and TM90x respectively). We analyze three spatial scales: model grid box, regional, and European. For regional and European event definitions, the spatial mean is calculated before the running mean. Regional extents are taken from Christensen and Christensen (2007), and European extent is the E-OBS (Cornes et al. 2018) domain (land points within 25°–71.5°N, 25°W–45°E). The WWA

AFFILIATIONS: Leach—Department of Physics, Atmospheric Oceanic and Planetary Physics, University of Oxford, United Kingdom; Li—Oxford e-Research Centre, Department of Engineering Science, and Environmental Change Institute, School of Geography and the Environment, University of Oxford, United Kingdom; Sparrow—Oxford e-Research Centre, Department of Engineering Science, University of Oxford, United Kingdom; van Oldenborgh—Koninklijk Nederlands Meteorologisch Instituut, De Bilt, The Netherlands; Lott—Met Office Hadley Centre, Exeter, United Kingdom; Weisheimer—Department of Physics, Atmospheric Oceanic and Planetary Physics, and Department of Physics, National Centre for Atmospheric Science (NCAS), University of Oxford, Oxford, and European Centre for Medium-Range Weather Forecasts (ECMWF), Reading, United Kingdom; Allen—Department of Physics, Atmospheric Oceanic and Planetary Physics, and Environmental Change Institute, School of Geography and the Environment, University of Oxford, United Kingdom.

CORRESPONDING AUTHOR: Nicholas J. Leach, Nicholas.leach@stx.ox.ac.uk

DOI:10.1175/BAMS-D-19-0201.1

A supplement to this article is available online (10.1175/BAMS-D-19-0201.2)

used the annual maxima of 3-day mean daily maximum temperatures at specific grid points for its connection to local health effects (D'Ippoliti et al. 2010), whereas the UKMO used the JJA mean temperature over the entire United Kingdom in order to answer the question of how anthropogenic forcings have affected the likelihood of U.K. summer seasons as warm as 2018. The same justifications can be used here, although we add that different heat event time scales are important to different groups of people, and as such using several temporal definitions may increase interest in heat event attribution studies. However, we recognize that other definitions than those used here may be more relevant to some impacts observed (such as defining the event in the context of the atmospheric flow pattern and drought that accompanied the heat), and other lines of reasoning for selecting one particular event definition exist (Cattiaux and Ribes 2018).

MODEL SIMULATIONS AND VALIDATION. Three sets of simulations from the UKMO Hadley Centre HadGEM3-A global atmospheric model (Christidis et al. 2013; Ciavarella et al. 2018) are used. These are a historical ensemble (1960–2013; Historical) and factual (ACT) and counterfactual (a "natural" world without anthropogenic forcings; NAT) ensembles of 2018. We compare results from this factual-counterfactual analysis with those from a trend-based analysis of Historical, ensembles from EURO-CORDEX (Vautard et al. 2013; Jacob et al. 2014; Vrac and Vaittinada Ayar) (1971–2018) and RACMO (Aalbers et al. 2018; Lenderink et al. 2014) (1950–2018), and observations from E-OBS (1950–2018). A full model description is provided in the online supplemental information. Initially, we performed our analysis with the weather@home HadRM3P European-25 km setup (Massey et al. 2015) but found that this model overestimates the variability over all Europe for daily through seasonal-scale event statistics, and so it was omitted.

METHODOLOGY. We calculate the return period (RP) for the 2018 event in a distribution fit to E-OBS using the generalized extreme value (GEV) distribution to model TM1x and TM10x, and the generalized logistic distribution to empirically model TM90x throughout. Since the distribution of temperature extremes changes as the climate does, to account for the non-stationarity of the time series we first remove the trend attributable to low-pass-filtered globally-averaged mean surface temperature (GMST, from Berkeley Earth; Rohde et al. 2013) in an ordinary-least squares regression (the regression coefficient or trend is shown in the supplemental material in Fig. ES1; Diffenbaugh et al. 2017). We then find the temperature threshold corresponding to the RP in a distribution fit to the model's climatology. In the factual/counterfactual analysis, we do this by fitting parameters to a detrended (against GMST; trends shown in Figs. ES2c7–9) climatological ensemble of Historical plus 15 randomly sampled members of ACT. We finally calculate the probability (*P*) of exceeding this climatological temperature threshold in distributions fit to the ACT and NAT ensembles and calculate the probability ratio, $\mathrm{PR} = P_{\mathrm{ACT}}/P_{\mathrm{NAT}}$, representing the increased likelihood of the 2018 event in the factual compared to the counterfactual world. Using estimated event probabilities rather than observed magnitudes constitutes a quantile bias correction (Jeon et al. 2016), minimizing model biases in the mean and variability of the temperatures analyzed. A description of uncertainty calculation and the trend-based analysis discussed below is included in the supplemental material.

RESULTS. Extreme daily heat events, measured by TM1x, are distributed heterogeneously throughout Europe (Fig. ES1i). This is paralleled in the factual/counterfactual PRs seen in Fig. 1a, with large proportions of the Iberian Peninsula, the Netherlands, and Scandinavia experiencing events that were highly unlikely in a climate without anthropogenic influence. A similar result is found on the regional scale (Fig. 1d) with Scandinavia and the Iberian Peninsula respectively experiencing 1-in-150 [26–26,000][1] and 1-in-30 [9–550] year events in the current climate that were highly unlikely in the natural climate simulated in NAT. The remaining regions record maximum daily temperatures likely to be repeated within 4 years. Considering the whole of Europe, the likelihood of the 2018 maximum of daily European mean temperature occurring without climate change is zero. This result is consistent with Uhe et al. (2016) and Angélil et al. (2018), who showed that increasing spatial scale tends to increase the probability ratio.

Extreme 10-day heat events, TM10x, were also widespread in Europe, with the most extreme occurring in Scandinavia (Fig. ES1j). Regionally, the PRs become more uniform (Fig. 1d), although Scandinavia and the Iberian Peninsula still have very high best-estimate PRs of 185 [17–infinite] and 110 [18–56,000] respectively. The best-estimate PR for the average of Europe is still formally infinite.

---

[1] Numbers in brackets [ ] represent a 90% confidence interval.

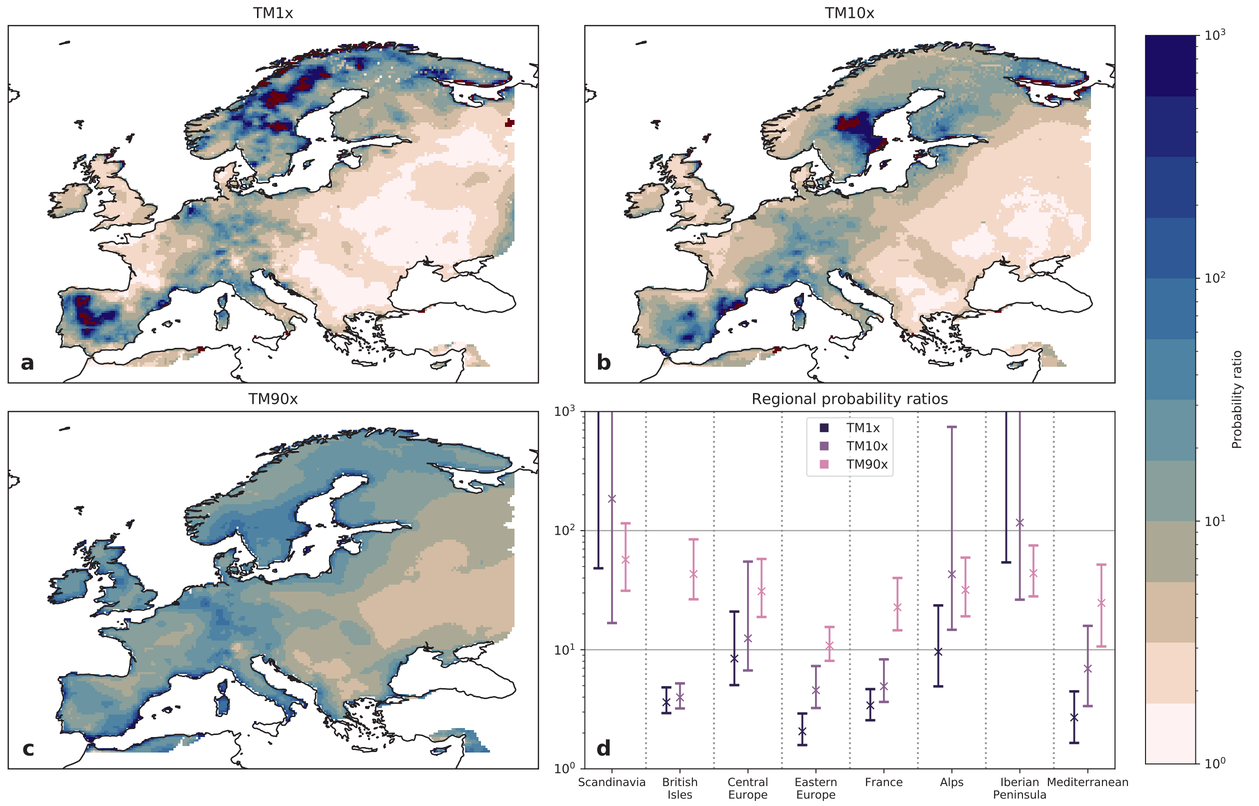

Fig. 1. Probability ratios for the 2018 summer heat-event derived from HadGEM3-A factual/counterfactual simulations. (a)–(c) Maps of increased likelihood in the real world at gridbox scale for the three event time scales analyzed respectively. Note that the upper limit on the color scale is 1,000 and grid boxes with an infinite probability ratio are shown in dark red. (d) The regional probability ratios for the three time scales; the crosses denote the best estimate, and the bars denote the 5th–95th percentiles. Note that the best-estimate probability ratios for TM1x in Scandinavia and the Iberian Peninsula were infinite and 2,000 respectively.

The PR map for season-long heat events measured by TM90x is more uniform throughout Europe (Fig. 1c). Scandinavia, the British Isles, France, and central and eastern Europe, all of which experienced on the order of 1-in-10 year events (Fig. ES1l), and the corresponding best-estimate PRs are between 10 and 100 for all regions (Fig. 1d), including those with lower return periods. The PR for the European average is 1,000 [500–2,000].

Trend-based analysis [Figs. ES1m–p (observations) and Fig. ES2b (models)] yields similar results, although we note that for HadGEM-3A this results in generally higher PRs, due to the linear trend with GMST in the climatology being greater than the difference between the two ensembles used in the factual/counterfactual analysis. Observational and model analysis contradict in some grid boxes in northern Scandinavia for TM1x and TM10x, since the observed best-estimate trend against GMST is negative, reducing the event probability for the present-day compared to the preindustrial climate, therefore yielding PRs of less than 1. Comparing the regional factual/counterfactual model with observational analysis (Fig. 1d vs Fig. ES1p) shows that the large observational uncertainties overlap with the model results: the difference could be due to natural variability affecting the small observational sample size. However, we are cautious of drawing any conclusions regarding the change in likelihood of extreme heat events as defined here for these locations.

The PR increases with the event statistic time scale for the majority of grid points and regions (shown in Fig. 1). Figure 2 illustrates the cause using the British Isles region: as the time scale increases, the event statistic distribution variance decreases, while the mean shift between the factual and counterfactual distributions remains constant. Figure ES1t shows that the similarity in trends with GMST between the three time scales is also true for the observations. The decrease in variance usually results in higher PRs, given a particular event return time, for the longer time scales. There are exceptions due to the bounded

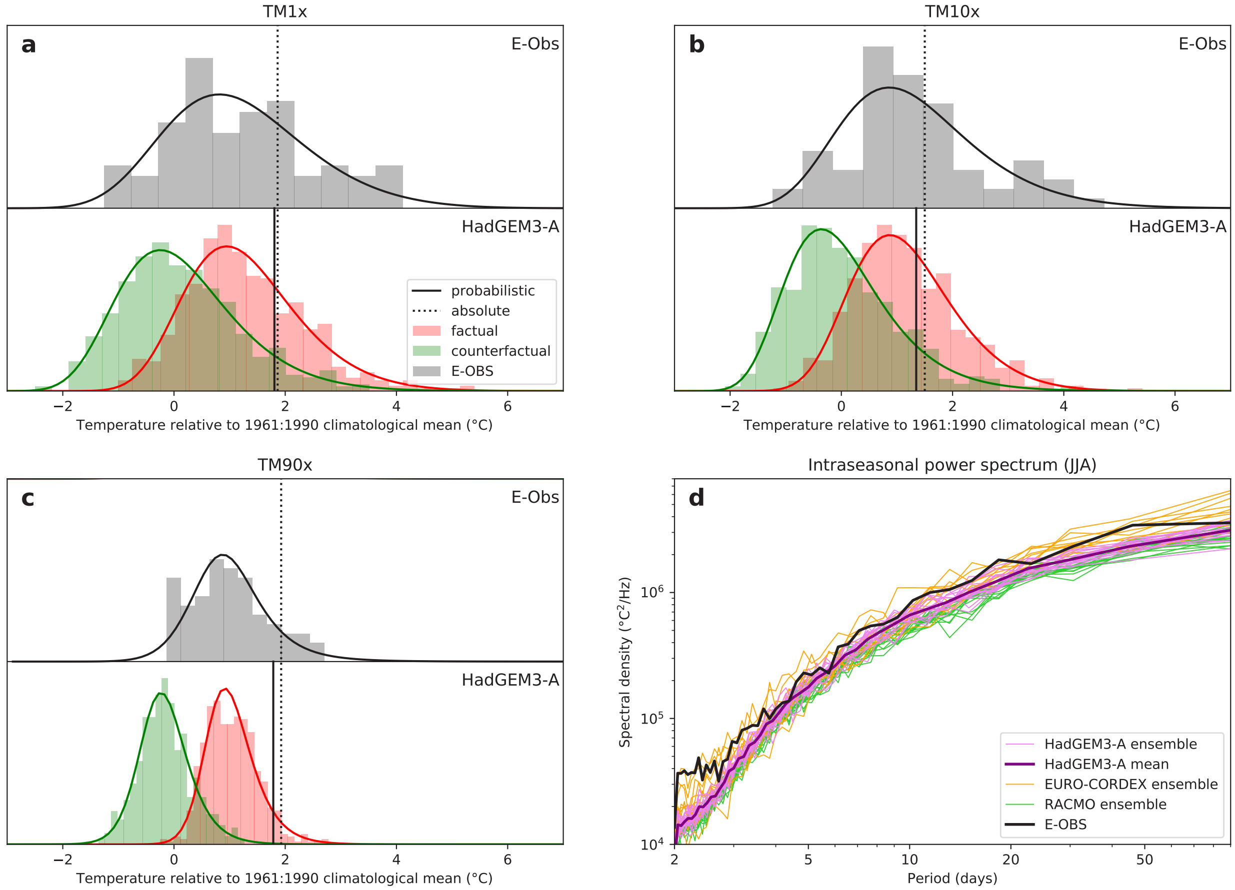

Fig. 2. (a)–(c) Probability density functions of the three temporal scales of event statistic for the British Isles, showing HadGEM3-A ACT (factual) and NAT (counterfactual) simulations, and observations from E-OBS; all as anomalies above the model or observed 1961:1990 mean climatology. Thick black lines show the 2018 event defined probabilistically as the HadGEM3-A Historical temperature threshold corresponding to the E-OBS return period; dotted black lines show the event defined in terms of the magnitude observed directly from E-OBS. (d) Periodograms of JJA daily mean temperature in the British Isles (seasonality and mean removed) calculated as the mean of intraseasonal periodograms for all available years. The HadGEM3-A power spectrum is calculated from the Historical ensemble.

upper tail of a GEV distribution with a negative shape parameter, resulting in the very high PRs for TM1x in Scandinavia, the Iberian Peninsula, and the Netherlands. The solid and dotted black lines compare the temperature thresholds when using event return periods to anomaly magnitudes in E-OBS. This explains why the TM90x PR is much higher than the other time scales for the British Isles: in addition to the decreased variance, the seasonal-scale heat event was more unusual than the other time scales, with a longer return period (10.6 [5.7–21] years) than TM10x (2.6 [1.8–3.9] years) and TM1x (3.6 [2.5–6.2] years). These factors together result in PRs of 3.6 [2.9–4.8] for TM1x and 43 [27–84] for TM90x. We suggest that the change in variance between the time scales used largely reconciles the differences between the "2 to 5" and "30" times increases in likelihood found by the WWA and UKMO reports, with other methodological factors playing a minor role as we have demonstrated for the British Isles.Although higher return periods for TM90x do impact the PRs found, this effect is generally less significant than changes in variability between the time scales.

Figure 2 also demonstrates a relevant deficiency in the model: the model distributions are narrower than the observed distributions, meaning the model has lower variability than the real world. This reduced variance has a significant impact on attribution results (Bellprat et al. 2019) and means that the PRs for the British Isles presented here, especially for TM90x, are likely to be overestimated. Underrepresented variability often occurs in prescribed SST models

(Fischer et al. 2018) and is visible in HadGEM-3A for many coastal locations over Europe (Figs. ES2a7–9). Figure 2d shows the power spectrum of JJA summer temperatures over the British Isles, indicating that HadGEM3-A has similar spectral characteristics to E-OBS, but underrepresents the intraseasonal 2-m temperature variability at almost all frequencies, which will likely result in overestimated PRs. Power spectra for other model ensembles are shown for comparison, demonstrating that the fully bias-corrected EURO-CORDEX ensemble has the same variability characteristics and magnitude as the observations.

DISCUSSION. Our analysis highlights a key property of extreme weather attribution: the variance of the event definition used, both in terms of the statistic itself and its representation within any models used. The use of longer temporal event scales in general increases both the spatial uniformity and magnitude of the probability ratios found, consistent with Kirchmeier-Young et al. (2019), due to a decrease in variance compared to shorter scales. The difference in temporal scale between two reports concerning the 2018 summer heat is sufficient to explain the large discrepancy in attribution result between them. We find that several European regions experienced season-long heat events with a present-day return period greater than 10 years. The present-day likelihood of such events occurring is approximately 10 to 100 times greater than a "natural" climate. The attribution results also show that the extreme daily temperatures experienced in parts of Scandinavia, the Netherlands, and the Iberian Peninsula would have been highly unlikely without anthropogenic warming. The prescribed SST model experiments used here tend to underestimate the variability of temperature extremes near the coast, which may lead to the attribution results overstating the increase in likelihood of such extremes due to anthropogenic climate change (Bellprat et al. 2019). We aim to properly quantify the impact of the underrepresented variability in further work. Although here we have used an unconditional temperature definition for consistency with the studies we try to reconcile, we plan to further investigate the effect of including both the atmospheric flow context and other impact-related variables such as precipitation in the event definition, and address issues models might have with realistically simulating the physical drivers of heatwaves.

ACKNOWLEDGMENTS. We acknowledge the E-OBS dataset from the EU-FP6 project UERRA (http://www.uerra.eu) and the Copernicus Climate Change Service, and the data providers in the ECA\&D project (https://www.ecad.eu). We thank all of the volunteers who have donated their computing time to Climateprediction.net and weather@home.

REFERENCES

Aalbers, E. E., G. Lenderink, E. van Meijgaard, and B. J. van den Hurk, 2018: Local-scale changes in mean and heavy precipitation in western Europe, climate change or internal variability? *Climate Dyn.*, **50**, 4745–4766, https://doi.org/10.1007/s00382-017-3901-9.

Angélil, O., and Coauthors, 2018: On the nonlinearity of spatial scales in extreme weather attribution statements. *Climate Dyn.*, **50**, 2739–2752, https://doi.org/10.1007/s00382-017-3768-9.

Bellprat, O., V. Guemas, F. Doblas-Reyes, and M. G. Donat, 2019: Towards reliable extreme weather and climate event attribution. *Nat. Commun.*, **10**, 1732, https://doi.org/10.1038/s41467-019-09729-2.

Cattiaux, J., and A. Ribes, 2018: Defining single extreme weather events in a climate perspective. *Bull. Amer. Meteor. Soc.*, **99**, 1557–1568, https://doi.org/10.1175/BAMS-D-17-0281.1.

Christensen, J. H., and O. B. Christensen, 2007: A summary of the PRUDENCE model projections of changes in European climate by the end of this century. *Climatic Change*, **81** (S1), 7–30, https://doi.org/10.1007/s10584-006-9210-7.

Christidis, N., P. A. Stott, A. A. Scaife, A. Arribas, G. S. Jones, D. Copsey, J. R. Knight, and W. J. Tennant, 2013: A new HadGEM3-A-based system for attribution of weather- and climate-related extreme events. *J. Climate*, **26**, 2756–2783, https://doi.org/10.1175/JCLI-D-12-00169.1.

Ciavarella, A., and Coauthors, 2018: Upgrade of the HadGEM3-A based attribution system to high resolution and a new validation framework for probabilistic event attribution. *Wea. Climate Extremes*, **20**, 9–32, https://doi.org/10.1016/j.wace.2018.03.003.

Cornes, R. C., G. van der Schrier, E. J. van den Besselaar, and P. D. Jones, 2018: An ensemble version of the E-OBS temperature and precipitation data sets. *J. Geophys. Res.*, **123**, 9391–9409, https://doi.org/10.1029/2017JD028200.

Diffenbaugh, N. S., and Coauthors, 2017: Quantifying the influence of global warming on unprecedented extreme climate events. *Proc. Natl. Acad. Sci. USA*, **114**, 4881–4886, https://doi.org/10.1073/pnas.1618082114.

D'Ippoliti, D., and Coauthors, 2010: The impact of heat waves on mortality in 9 European cities: Results from the EuroHEAT project. *Environ. Health*, **9**, 37, https://doi.org/10.1186/1476-069x-9-37.

Fischer, E. M., U. Beyerle, C. F. Schleussner, A. D. King, and R. Knutti, 2018: Biased estimates of changes in climate extremes from prescribed SST simulations. *Geophys. Res. Lett.*, **45**, 8500–8509, https://doi.org/10.1029/2018GL079176.

Harris, C., 2018: Heat, hardship and horrible harvests: Europe's drought explained. *Euronews*, 8 December 2018, https://www.euronews.com/2018/08/10/explained-europe-s-devastating-drought-and-the-countries-worst-hit.

Jacob, D., and Coauthors, 2014: EURO-CORDEX: New high-resolution climate change projections for European impact research. *Reg. Environ. Change*, **14**, 563–578, https://doi.org/10.1007/s10113-013-0499-2.

Jeon, S., C. J. Paciorek, and M. F. Wehner, 2016: Quantile-based bias correction and uncertainty quantification of extreme event attribution statements. *Wea. Climate Extremes*, **12**, 24–32, https://doi.org/10.1016/j.wace.2016.02.001.

Johnston, C., 2018: Heatwave temperatures may top 45C in southern Europe. *The Guardian*, 4 August 2018, https://www.theguardian.com/world/2018/aug/04/temperatures-in-southern-europe-top-45-heatwave-spain-portugal.

Kirchmeier-Young, M. C., H. Wan, X. Zhang, and S. I. Seneviratne, 2019: Importance of framing for extreme event attribution: The role of spatial and temporal scales. *Earth's Future*, **7**, 1192–1204, https://doi.org/10.1029/2019EF001253.

Krikken, F., F. Lehner, K. Haustein, I. Drobyshev, and G. J. van Oldenborgh, 2019: Attribution of the role of climate change in the forest fires in Sweden 2018. *Nat. Hazards Earth Syst. Sci. Discuss.*, https://doi.org/10.5194/nhess-2019-206.

Lenderink, G., B. J. van den Hurk, A. M. Klein Tank, G. J. van Oldenborgh, E. van Meijgaard, H. de Vries, and J. J. Beersma, 2014: Preparing local climate change scenarios for the Netherlands using resampling of climate model output. *Environ. Res. Lett.*, **9**, 115008, https://doi.org/10.1088/1748-9326/9/11/115008.

Massey, N., and Coauthors, 2015: weather@home—Development and validation of a very large ensemble modelling system for probabilistic event attribution. *Quart. J. Roy. Meteor. Soc.*, **141**, 1528–1545, https://doi.org/10.1002/qj.2455.

McCarthy, M., and Coauthors, 2019: Drivers of the UK summer heatwave of 2018. *Weather*, **74**, 390–396, https://doi.org/10.1002/wea.3628.

NESDIS, 2018: Record summer heat bakes Europe. NOAA/NESDIS, 10 August 2018, https://www.nesdis.noaa.gov/content/record-summer-heat-bakes-europe.

Press Office, 2018: Chance of summer heatwaves now thirty times more likely. *Met Office News*, 6 December 2018, https://www.metoffice.gov.uk/about-us/press-office/news/weather-and-climate/2018/2018-uk-summer-heatwave.

Publico, 2018: Neuve fallecidos por la ola de calor en Espana. *Publico*, accessed 17 August 2019, https://www.publico.es/sociedad/nueve-fallecidos-ola-calor-espana.html.

Rohde, R., and Coauthors, 2013: A new estimate of the average Earth surface land temperature spanning 1753 to 2011. *Geoinf. Geostat. Overview*, **1**, 1, https://doi.org/10.4172/2327-4581.1000101.

Uhe, P., F. E. L. Otto, K. Haustein, G. J. van Oldenborgh, A. D. King, D. C. H. Wallom, M. R. Allen, and H. Cullen, 2016: Comparison of methods: Attributing the 2014 record European temperatures to human influences. *Geophys. Res. Lett.*, **43**, 8685–8693, https://doi.org/10.1002/2016GL069568.

Vautard, R., and Coauthors, 2013: The simulation of European heat waves from an ensemble of regional climate models within the EURO-CORDEX project. *Climate Dyn.*, **41**, 2555–2575, https://doi.org/10.1007/s00382-013-1714-z.

Vrac, M., and P. Vaittinada Ayar, 2017: Influence of bias correcting predictors on statistical downscaling models. *J. Appl. Meteor. Climatol.*, **56**, 5–26, https://doi.org/10.1175/JAMC-D-16-0079.1.

Watts, J., 2018: Wildfires rage in Arctic Circle as Sweden calls for help. *The Guardian*. 18 July 2018, https://www.theguardian.com/world/2018/jul/18/sweden-calls-for-help-as-arctic-circle-hit-by-wildfires.

World Weather Attribution, 2018: Heatwave in northern Europe, summer 2018. 28 July 2018, https://www.worldweatherattribution.org/attribution-of-the-2018-heat-in-northern-europe/.

chapter 9

ON HIGH PRECIPITATION IN MOZAMBIQUE, ZIMBABWE, AND ZAMBIA IN FEBRUARY 2018

Neven S. Fučkar, Friederike E. L. Otto, Flavio Lehner, Izidine Pinto,
Emma Howard, Sarah Sparrow, Sihan Li, and David Wallom

This multi-method study of high precipitation over parts of Mozambique, Zimbabwe, and parts of Zambia in February 2018 indicates decreased likelihood of such events due to climate change, but with substantial uncertainty based on the used observations and models.

Precipitation in southern Africa displays a notable zonal gradient (south of about 15°S there is a dominant contrast between dry west and wet east) and is characterized by a pronounced annual cycle as well as high interannual variability (e.g., Lindesay 1988; Nicholson and Kim 1997; Nicholson et al. 2018). During austral summer the complex large-scale monthly precipitation pattern in southeast Africa is strongly guided by the Hadley circulation (Cook 2005) and movement of the associated main tropical cloud and rainband (Schneider et al. 2014; Nicholson 2018), also referred to as the south Indian Ocean convergence zone (Cook 2000; Hart et al. 2010; Barimalala et al. 2018). The main rainband of strongest tropical precipitation reaches the southernmost climatological position across parts of Madagascar, Mozambique, Malawi, Zimbabwe, and Zambia in February (see Figs. ES2 and ES3 in the online supplemental material; Tyson and Preston-Whyte 2002; Reason 2017).

In February 2018, the main tropical rainband moved much farther south and led to anomalous high rainfall over central and southern Mozambique, Zimbabwe, and southern Zambia (Figs. 1a–f and Figs. ES1a–c), which resulted in significant socioeconomic impacts in the region (e.g., flooding was reported in parts of Lusaka, Zambia, and floods in Manica province, Mozambique, triggered the country's emergency response). This study addresses whether and to what extent anthropogenic climate change has altered the likelihood of this large-scale high precipitation event in February 2018 to occur by applying a multi-method event attribution approach (National Academies of Sciences, Engineering, and Medicine 2016; Otto 2017).

AFFILIATIONS: Fučkar—Environmental Change Institute, University of Oxford, Oxford, United Kingdom, and Earth Sciences Department, Barcelona Supercomputing Center, Barcelona, Spain; Otto—Environmental Change Institute, University of Oxford, Oxford, United Kingdom; Lehner—Climate and Global Dynamics Laboratory, National Center for Atmospheric Research, Boulder, Colorado; Pinto—Climate System Analysis Group, University of Cape Town, Cape Town, South Africa; Howard—School of Geography and the Environment, University of Oxford, Oxford, United Kingdom; Sparrow and Wallom—Oxford e-Research Centre, Department of Engineering Science, University of Oxford, Oxford, United Kingdom; Li—Environmental Change Institute, and Oxford e-Research Centre, Department of Engineering Science, University of Oxford, Oxford, United Kingdom

CORRESPONDING AUTHOR: Neven Fučkar, neven.fuckar@ouce.ox.ac.uk

DOI:10.1175/BAMS-D-19-0162.1

A supplement to this article is available online (10.1175/BAMS-D-19-0162.2)

EVENT DEFINITION AND OBSERVATIONAL RESULTS.

First, to establish the spatial extent of the high precipitation event of interest, we use multiple high-resolution gridded satellite-era products. Figures 1a–c (and Figs. ES1a–c) show February 2018 total precipitation in such three analyses commonly used for monitoring of droughts and floods. Furthermore, Figs. 1d–f show the strong positive precipitation anomalies in February 2018, with variable spatial extents in different datasets in subtropical southern Africa (south of 15°S). To get a detailed spatial definition of this large-scale event to envelop the large anomalies in monthly precipitation (above 150 mm), we define the region "MZZ" as

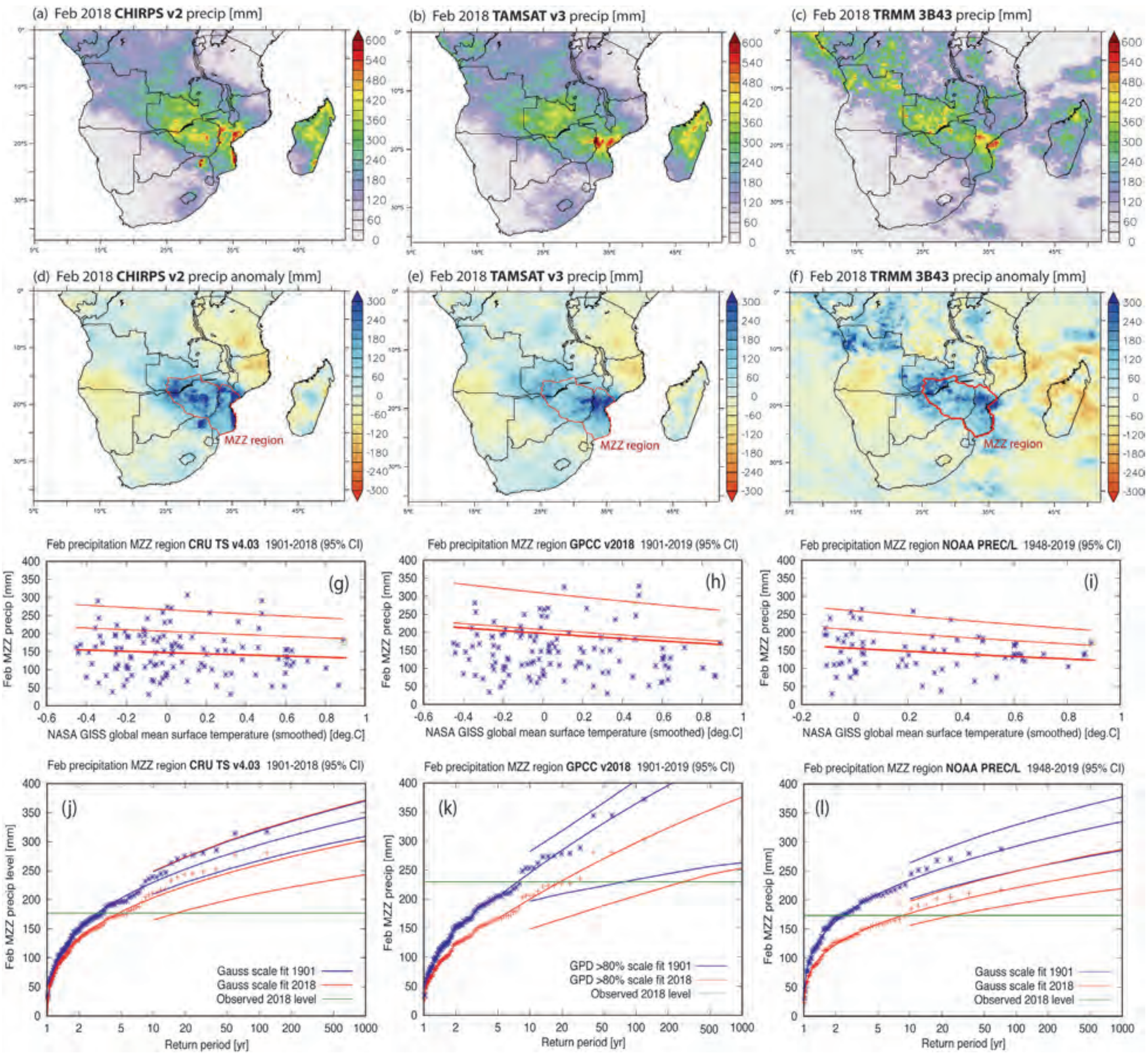

Fig. 1. The top panels show February 2018 total precipitation in the southern Africa from (a) UCSB CHIRPS v2.0 (0.05° resolution, available from 1981; Funk et al. 2015), (b) UR TAMSAT (4-km resolution, available from 1987; Maidment et al. 2014), and (c) NASA TRMM 3B43 (0.25° resolution, available from 1998; Huffman et al. 2010). The second-row panels show the associated February 2018 precipitation anomaly (with respect to the 1998–2018 climatology) from (d) CHIRPS v2, (e) TAMSAT v3, and (f) TRMM 3B43, and outline the MZZ region (red contours). (g)–(i) CRU TS v4.03 (0.5° resolution), GPCC v2018 (0.5°/1° resolution), and NOAA PREC/L (0.5°/1° resolution) February total precipitation averaged over the MZZ region as a function of NASA GISS global mean surface temperature (GMST: Hansen et al. 2010), respectively, and Gaussian or GPD (using the highest 20% values) scale fits. The red lines show fit mean μ, $\mu+\sigma$, and $\mu+2\sigma$ as function of GMST (4-yr running mean). (j)–(l) The return time plots of February MZZ precipitation with Gaussian, GPD (using the top 20%), and Gaussian scale fits (current/2018 climate in red vs 1901 climate in blue) in CRU TS v4.03 (Harris et al. 2014), GPCC v2018 (Schneider et al. 2018), and NOAA PREC/L (Chen et al. 2002), respectively (green lines show the 2018 event level in different long-term precipitation datasets). The red and blue lines show the mean and 95% confidence interval (CI; based on 1000-member bootstrap) for Gaussian or GPD scale fits.

encompassing provinces where significant positive anomalies are present in at least two of the satellite-era analyses shown in Figs. 1d–f: Gaza, Inhambane, Manica, and Sofala provinces in Mozambique; all of Zimbabwe; and Southern and Lusaka provinces in Zambia (red contour in Figs. 1d–f), covering about 0.78 M km^2.

We utilize three long-term gridded in situ datasets to determine the return time of the February 2018 total precipitation averaged over the MZZ region. February 2018 MZZ precipitation in the Climatic Research Unit (CRU) TS v4.03 (177 mm), the Global Precipitation Climatology Centre (GPCC) v2018 (230 mm), and NOAA's Precipitation Reconstruction over Land (PREC/L) (173 mm) appears to be less intense than in three used satellite-era datasets [Fig. ES1: 333 mm in the Climate Hazards Infrared Precipitation with Stations (CHIRPS2), 284 mm in Tropical Applications of Meteorology using Satellite and Ground-Based Observations (TAMSAT3), and 287 mm in the Tropical Rainfall Measuring Mission (TRMM) 3B43] since it has the 35th rank (out of 118 years), the 15th rank (out of 119 years), and the 21st rank (out of 72 years), respectively. The generalized Pareto distribution (GPD; Coles 2001) is a well-established choice for statistical modeling of extreme occurrences over high thresholds (Davison and Smith 1990). We utilize the GPD as a limiting high-tail distribution of precipitation and in the widest range it is commonly fit in the top 20% of distribution. However, February 2018 MZZ precipitation levels in CRU TS and NOAA PREC/L are just barely in the top 30%, and at these observed levels a more suitable fit is the Gaussian distribution. Hence, to get the return period of this event in CRU TS and NOAA PREC/L (GPCC) we fit a Gaussian distribution (a GPD to the top 20% values) whose parameters scale with a 4-yr smoothed NASA GISS global mean surface temperature (GMST) [for scale fit methodology see, e.g., Philip et al. (2018), Otto et al. (2018a), and the supplement]. Only NOAA PREC/L shows a statistically significant negative linear trend (95% confidence level) of –3.6 mm (0.1°C of GMST)$^{-1}$ with $p = 0.007$ (Figs. 1g–i), while it has a temporal trend of –5.2 mm decade^{-1} with $p = 0.012$. The mean return time of the event in CRU TS, GPCC, and NOAA PREC/L is 5, 20, and 9 years, respectively (Figs. 1j–l), so for the event definition we use a combined (and rounded) return time of 10 years (i.e., having 10% chance of occurring in a year). The 2018 versus 1901 probability (or risk) ratio in CRU TS and NOAA PREC/L based on a Gaussian scale fit with GMST is 0.63 [95% confidence interval (CI): 0.18, 1.45] and 0.27 (95% CI: 0.08, 0.71), respectively, while in GPCC based on a GPD scale fit with GMST is 0.40 (95% CI: 0.02, 48.68), where the 95% confidence interval is estimated from 1000-member nonparametric bootstrap. This probability ratio (PR) is the ratio between the occurrence probability (reciprocal return time) of the event under 2018 conditions (i.e., today's climate) divided by the occurrence probability under 1901 conditions (i.e., a historical climate approximately close to pre-industrial conditions).

MODELING RESULTS. We use large (≥10 members) and very large (>100 members) ensemble simulations with comprehensive (i.e., general circulation) climate models to assess whether and to what extent anthropogenic climate change modified the likelihood of this event following established methodology (e.g., Philip et al. 2018; van der Wiel et al. 2017; van Oldenborgh et al. 2017). To verify that we are using a suitable model for event attribution we assess whether it can reproduce key statistical aspects of the observed distribution; to that end we focus on the coefficient of variation σ/μ (the standard deviation over the mean) from long-term in situ observations. The value of σ/μ in CRU TS, GPCC, and NOAA PREC/L is 0.41 (95% CI: 0.34, 0.49), 0.44 (95% CI: 0.35, 0.53), and 0.35 (95% CI: 0.27, 0.45), respectively, so we require of models to have the mean coefficient of variation between 0.27 and 0.53 (Fig. ES4). We use as event definition the return period of 10 years in today's climate for a February total precipitation averaged over the MZZ region instead of a specific precipitation level to adjust for mean biases across climate models (e.g., Otto et al. 2018b). In other words, for each model the 10-yr return time corresponds to a slightly different total precipitation level.

First, we use weather@home2 (w@h2)—the regional atmosphere–land model HadRM3P with a southern African domain (50-km resolution) nested in the global atmosphere–land model HadAM3P (CMIP3 generation)—through the distributed computing system climateprediction.net (Guillod et al. 2017). In this study, we utilize 658 members of actual (factual/historic) February 2018 HadRM3P simulations (using observed SST, sea ice, greenhouse gases, and aerosol forcings), and 658 members of natural (counterfactual) February 2018 simulations that uses pre-industrial SSTs and sea ice (Schaller et al. 2016) as well as greenhouse gases and aerosols. The σ/μ value in both actual and natural HadRM3P ensemble simulations is 0.39. Direct comparison of these two ensembles, without using a scale fit with GMST, yields a PR of 1.21 (95% CI: 0.80, 1.83) for the event of interest with the return period of 10 years in 2018 actual climate (Fig. 2a, where the 95% CI is estimated by a 1000-member bootstrap).

Then we turn our attention to six fully coupled climate models (CMIP5 and CMIP6 generations), all with adequate σ/μ, and analyze their historical ensemble simulations (see the supplement for model details and Fig. ES4). We fit a GPD that scales with 4-yr smoothed GMST to the top 20% of February

MZZ precipitation to obtain the following 2018 versus 1901 probability ratios for the adjusted precipitation levels that match the return time of 10 years in 2018 (Figs. 2b–g):

1) 16 ensemble members of EC-Earth2.3 (σ/μ = 0.32): PR = 0.94 (95% CI: 0.27, 2.05).
2) 30 ensemble members of CSIRO-Mk3.6 (σ/μ = 0.50): PR = 0.78 (95% CI: 0.51, 1.27).
3) 10 ensemble members of MIROC6 (σ/μ = 0.38): PR = 0.74 (95% CI: 0.41, 4.58).
4) 40 ensemble members of CESM1-CAM5 (σ/μ = 0.41): PR = 0.68 (95% CI: 0.36, 1.01).
5) 20 ensemble members of GFDL-CM3 (σ/μ = 0.36): PR = 0.66 (95% CI: 0.21, 1.07).
6) 10 ensemble members of CNRM-CM6.1 (σ/μ = 0.48): PR = 0.51 (95% CI: 0.26, 1.48).

SYNTHESIS AND CONCLUSIONS. We performed a multi-method event attribution using three satellite-based and three long-term station-based monthly precipitation analyses along with seven

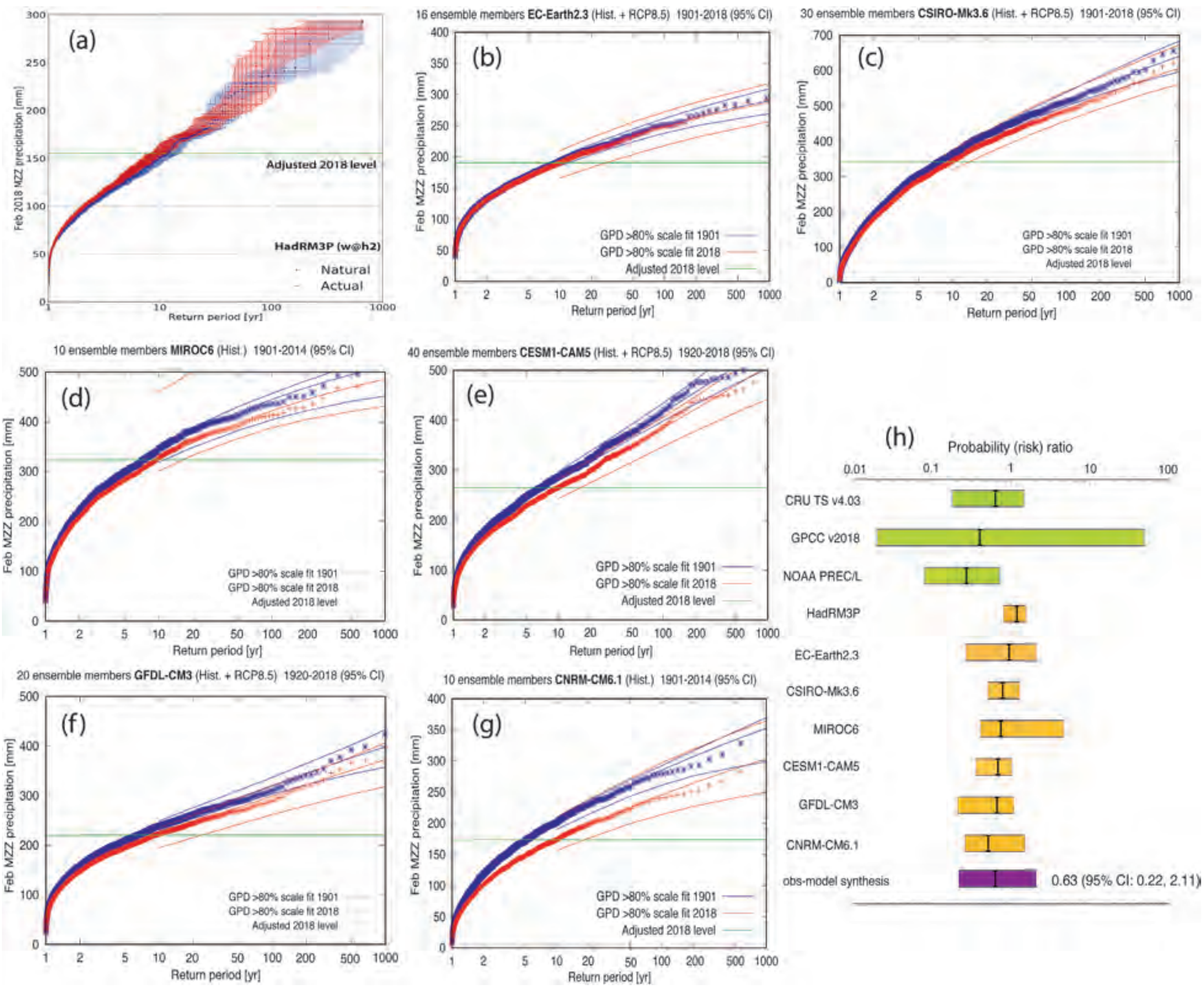

Fig. 2. (a) The return time plot of actual (658 runs) and natural (1749 runs) HadRM3P (weather@home2) simulations for this high total precipitation event in February 2018 averaged over the MZZ region (with 10-yr return time). The red and blue shadings show the 95% CI (based on 1000-member bootstrap). (b)–(g) The return time plots of 16-member EC-Earth2.3 1901–2018, 30-member CSIRO-Mk3.6 1901–2018, 10-member MIROC6 1901–2014, 40-member CESM1-CAM5 1920–2018, 20-member GFDL-CM3 1920–2018, and CNRM-CM6.1 1901–2014 simulations, respectively (a GPD scale fit used the highest 20% of February values to estimate the probability ratios). The red and blue lines show the mean and 95% CI (based on 1000-member bootstrap) for GPD scale fits. (h) Synthesis (purple bar) of the results of our multi-method approach as the probability ratio with 95% uncertainty interval based on the unweighted average (geometric means) of three used long-term observations (lime bars) and seven available climate models (orange bars).

climate models to examine the change in likelihood of the February 2018 high precipitation averaged over the MZZ region in southern Africa due to anthropogenic forcings. The overall PR result is illustrated by the purple "synthesis" bar in Fig. 2h, which shows the unweighted average (based on geometric means) of 0.63 (95% CI: 0.22, 2.11). The mean PR—indicating that such a high precipitation event has most likely become 37% less probable—is consistent with the expected poleward expansion of the Hadley cells and drying over southern Africa due to the global climate change (e.g., Ma et al. 2018; Munday and Washington 2019); however, the 95% CI of PR is substantial. More specifically, the PR could be ≥1 and thus encompasses the possibility of no significant change or even an increase in the probability of this event. In this attribution study, we do not aim to discriminate between the daily processes leading to such a large-scale monthly event. While extreme precipitation in the MMZ region is sometimes associated with intense tropical cyclones from the Indian Ocean, such as Idai in March 2019 and Eline in February 2000, this was not the case in February 2018, as no tropical cyclones made landfall that month [Météo France Regional Specialized Meteorological Center (MFR/RSMC) La Reunion]. Based on CHRIPS2 daily data February 2018 high total precipitation arose from 12 heavy large-scale daily rainfall events over the MZZ region. Furthermore, an analysis of tropical low tracks (Howard et al. 2019) in the ERA5 (Hersbach et al. 2018) and MERRA-2 (Gelaro et al. 2017) reanalyses shows that about 55% of this high daily precipitation occurred in association with an eastward migration of continental tropical lows into Mozambique during 8–13 February 2018 and 16–22 February 2018.

ACKNOWLEDGMENTS. The authors thank the editors, Dr. Karin van der Wiel, and two anonymous reviewers for their constructive inputs that substantially improved this manuscript. N.S.F. is supported by the HIASA project funded by the BNP Paribas. F.L. is supported by NSF Grant 2018-0281, by the Bureau of Reclamation under Cooperative Agreement R16AC00039, and the Regional and Global Model Analysis component of the Earth and Environmental System Modeling Program of the DOE (Cooperative Agreement DE-FC02-97ER62402). The authors thank Geert Jan van Oldenborgh for valuable discussions and the development of KNMI Climate Explorer (climexp.knmi.nl), which was extensively used in this study. We thank the Met Office Hadley Centre PRECIS team for their technical and scientific support for the development and application of weather@home2. Finally, we thank all of the volunteers around the globe who have donated their computing time to climateprediction.net and weather@home2.

REFERENCES

Barimalala, R., F. Desbiolles, R. C. Blamey, and C. Reason, 2018: Madagascar influence on the South Indian Ocean Convergence Zone, the Mozambique Channel Trough and southern African rainfall. *Geophys. Res. Lett.*, **45**, 11 380–11 389, https://doi.org/10.1029/2018GL079964.

Chen, M., P. Xie, J. E. Janowiak, and P. A. Arkin, 2002: Global land precipitation: A 50-yr monthly analysis based on gauge observations. *J. Hydrometeor.*, **3**, 249–266, https://doi.org/10.1175/1525-7541(2002)003<0249:GLPAYM>2.0.CO;2.

Coles, S., 2001: An Introduction to Statistical Modelling of Extreme Values. Springer, 209 pp.

Cook, K. H., 2000: The South Indian convergence zone and interannual rainfall variability over southern Africa. *J. Climate*, **13**, 3789–3804, https://doi.org/10.1175/1520-0442(2000)013<3789:TSICZA>2.0.CO;2.

Cook, K. H., 2005: Hadley circulation dynamics: Seasonality and the role of continents. The Hadley Circulation: Past, Present, and Future. H. F. Diaz and R. S. Bradley, Eds., Kluwer Academic, 61–83, https://link.springer.com/chapter/10.1007/978-1-4020-2944-8_3.

Davison, A. C., and R. L. Smith, 1990: Models for exceedances over high thresholds (with discussion). *J. Roy. Stat. Soc.*, **52B**, 393–442.

Funk, C., and Coauthors, 2015: The Climate Hazards Infrared Precipitation with Stations—A new environmental record for monitoring extremes. *Sci. Data*, **2**, 150066, https://doi.org/10.1038/sdata.2015.66.

Gelaro, R. W., and Coauthors, 2017: The Modern-Era Retrospective Analysis for Research and Applications, version 2 (MERRA-2). *J. Climate*, **30**, 5419–5454, https://doi.org/10.1175/JCLI-D-16-0758.1.

Guillod, B. P., and Coauthors, 2017: weather@home 2: Validation of an improved global–regional climate modelling system. *Geosci. Model Dev.*, **10**, 1849–1872, https://doi.org/10.5194/gmd-10-1849-2017.

Hansen, J., R. Ruedy, M. Sato, and K. Lo, 2010: Global surface temperature change. *Rev. Geophys.*, **48**, RG4004, https://doi.org/10.1029/2010RG000345.

Harris, I., P. D. Jones, T. J. Osborn, and D. H. Lister, 2014: Updated high-resolution grids of monthly climatic observations—The CRU TS3.10 dataset. *Int. J. Climatol.*, **34**, 623–642, https://doi.org/10.1002/joc.3711.

Hart, N. C. G., C. J. C. Reason, and N. Fauchereau, 2010: Tropical–extratropical interactions over southern Africa: Three cases of heavy summer season rainfall. *Mon. Wea. Rev.*, **138**, 2608–2623, https://doi.org/10.1175/2010MWR3070.1.

Hersbach, H., and Coauthors, 2018: Operational global reanalysis: Progress, future directions and synergies with NWP. ERA Report Series 27, ECMWF, 65 pp., https://doi.org/10.21957/tkic6g3wm.

Howard, E. R., R. Washington, and K. Hodges, 2019: Tropical lows in southern Africa: Tracks, rainfall contributions and the role of ENSO. *J. Geophys. Res. Atmos.*, https://doi.org/10.1029/2019JD030803, in press.

Huffman, G. J., R. F. Adler, D. T. Bolvin, and E. J. Nelkin, 2010: The TRMM Multi-satellite Precipitation Analysis (TMPA). Satellite Rainfall Applications for Surface Hydrology, F. Hossain and M. Gebremichael, Eds., Springer, 3–22.

Lindesay, J. A., 1988: South African rainfall, the Southern Oscillation and a Southern Hemisphere semi-annual cycle. *J. Climatol.*, **8**, 17–30, https://doi.org/10.1002/joc.3370080103.

Ma, J., and Coauthors, 2018: Responses of the tropical atmospheric circulation to climate change and connection to the hydrological cycle. *Annu. Rev. Earth Planet. Sci.*, **46**, 549–580, https://doi.org/10.1146/annurev-earth-082517-010102.

Maidment, R. I., D. Grimes, R. P. Allan, E. Tarnavsky, M. Stringer, T. Hewison, R. Roebeling, and E. Black, 2014: The 30 year TAMSAT African Rainfall Climatology and Time series (TARCAT) data set. *J. Geophys. Res.*, **119**, 10 619–10 644, https://doi.org/10.1002/2014JD021927.

Munday, C., and R. Washington, 2019: Controls on the diversity in climate model projections of early summer drying over southern Africa. *J. Climate*, **32**, 3707–3725, https://doi.org/10.1175/JCLI-D-18-0463.1.

National Academies of Sciences, Engineering, and Medicine, 2016: Attribution of Extreme Weather Events in the Context of Climate Change. The National Academies Press, 186 pp., https://doi.org/10.17226/21852.

Nicholson, S. E., 2018: The ITCZ and the seasonal cycle over equatorial Africa. *Bull. Amer. Meteor. Soc.*, **99**, 337–348, https://doi.org/10.1175/BAMS-D-16-0287.1.

——, and E. Kim, 1997: The relationship of the El Niño–Southern Oscillation to African rainfall. *Int. J. Climatol.*, **17**, 117–135, https://doi.org/10.1002/(SICI)1097-0088(199702)17:2<117::AID-JOC84>3.0.CO;2-O.

——, C. Funk, and A. Fink, 2018: Rainfall over the African continent from the 19th through 21st century. *Global Planet. Change*, **165**, 114–127, https://doi.org/10.1016/j.gloplacha.2017.12.014.

Otto, F. E. L., 2017: Attribution of weather and climate events. *Annu. Rev. Environ. Resour.*, **42**, 627–646, https://doi.org/10.1146/annurev-environ-102016-060847.

—, S. Philip, S. Kew, S. Li, A. King, and H. Cullen, 2018a: Attributing high-impact extreme events across timescales—A case study of four different types of events. *Climatic Change*, **149**, 399–412, https://doi.org/10.1007/s10584-018-2258-3.

—, and Coauthors, 2018b: Anthropogenic influence on the drivers of the Western Cape drought 2015–2017. *Environ. Res. Lett.*, **13**, 124010, https://doi.org/10.1088/1748-9326/aae9f9.

Philip, S., and Coauthors, 2018: Attribution analysis of the Ethiopian drought of 2015. *J. Climate*, **31**, 2465–2486, https://doi.org/10.1175/JCLI-D-17-0274.1.

Reason, C. J. C., 2017: Climate of Southern Africa. Oxford Research Encyclopaedias: Climate Science, https://doi.org/10.1093/acrefore/9780190228620.013.513.

Schaller, N., and Coauthors, 2016: Human influence on climate in the 2014 southern England winter floods and their impacts. *Nat. Climate Change*, **6**, 627–634, https://doi.org/10.1038/nclimate2927.

Schneider, T., T. Bischoff, and G. H. Haug, 2014: Migrations and dynamics of the Intertropical Convergence Zone. *Nature*, **513**, 45–53, https://doi.org/10.1038/nature13636.

Schneider, U., A. Becker, P. Finger, A. Meyer-Christoffer, and M. Ziese, 2018: GPCC Full Data Monthly Product Version 2018 at 0.5°: Monthly Land-Surface Precipitation from Rain-Gauges built on GTS-based and Historical Data. Xxxx, https://doi.org/10.5676/DWD_GPCC/FD_M_V2018_050.

Tyson, P. D., and R. A. Preston-Whyte, 2002: *The Weather and Climate of Southern Africa*. 2nd ed. Oxford University Press, 408 pp.

van der Wiel, K., and Coauthors, 2017: Rapid attribution of the August 2016 flood-inducing extreme precipitation in south Louisiana to climate change. *Hydrol. Earth Syst. Sci.*, **21**, 897–921, https://doi.org/10.5194/hess-21-897-2017.

van Oldenborgh, G. J., and Coauthors, 2017: Attribution of extreme rainfall from Hurricane Harvey. *Environ. Res. Lett.*, **12**, 124009, https://doi.org/10.1088/1748-9326/aa9ef2.

THE RECORD LOW BERING SEA ICE EXTENT IN 2018: CONTEXT, IMPACTS, AND AN ASSESSMENT OF THE ROLE OF ANTHROPOGENIC CLIMATE CHANGE

Richard L. Thoman Jr., Uma S. Bhatt, Peter A. Bieniek, Brian R. Brettschneider, Michael Brubaker, Seth L. Danielson, Zachary Labe, Rick Lader, Walter N. Meier, Gay Sheffield, and John E. Walsh

Record low Bering Sea sea ice in 2018 had profound regional impacts. According to climate models, human-caused warming was an overwhelmingly likely contributor, and such low levels will likely be typical by the 2040s.

During the 2017/18 Northern Hemisphere cold season, sea ice extent in the Bering Sea was less than any winter in the observed or reconstructed past. The eastern and northern Bering Sea covers a shallow and expansive continental shelf that has historically exhibited 40%–100% ice cover at its annual winter maximum. This sea ice provides many important ocean climate and ecosystem services. For example, winter ice insulates warmer ocean waters from extreme cold in the atmosphere. During spring, algae growth on the undersurface of sea ice initiates the annual onset of biological productivity (Szymanski and Gradinger 2016). The seasonal ice cover is critical to the regional climate, marine ecosystems, societal expectations, and economics through maintenance of a thermal barrier that separates two distinct temperature-adapted marine ecosystems in the northern and southern portions of the Bering Sea shelf (Schumacher et al. 1983; Mueter and Litzow 2008). We utilized remote sensing derived ice extent products for ice context; governmental and academic investigations, media, and public reports for impacts; and the Community Earth System Model's Large Ensemble Project (CESM-LENS) for assessment of the relative likelihoods of current low ice extent.

AFFILIATIONS: Thoman—Alaska Center for Climate Assessment and Policy, University of Alaska Fairbanks; Bhatt—Department of Atmospheric Sciences, Geophysical Institute, and International Arctic Research Center, University of Alaska Fairbanks; Bieniek, Brettschneider, Lader, and Walsh—International Arctic Research Center (IARC), University of Alaska Fairbanks; Brubaker—Alaska Native Tribal Health Consortium, Anchorage, Alaska; Danielson—College of Fisheries and Ocean Sciences, University of Alaska Fairbanks; Labe—Department of Earth System Science, University of California Irvine; Meier—National Snow and Ice Data Center (NSIDC), Cooperative Institute for Research in Environmental Sciences, University of Colorado, Boulder; Sheffield—Alaska Sea Grant, College of Fisheries and Ocean Sciences, University of Alaska Fairbanks, Nome, Alaska

CORRESPONDING AUTHOR: Richard L. Thoman Jr., rthoman@alaska.edu

DOI:10.1175/BAMS-D-19-0175.1

A supplement to this article is available online (10.1175/BAMS-D-19-0175.2)

OBSERVATIONS AND HISTORICAL CONTEXT.

Sea ice cover. Mean Bering Sea ice extent (SIE) for January through April for the 40-yr satellite-derived passive microwave record in the National Snow and Ice Data Center's Sea Ice Index version 3 (Fetterer et al. 2017) shows that 2018 was the lowest of record (Fig. 1a), with the greatest anomalies compared to a 1981–2010 baseline north and west of St. Matthew Island (Fig. 1b). Analysis of late winter Bering Sea ice extent 1956–80 (Pease et al. 1982) and reconstructed monthly Arctic-wide ice extent since 1850 (Walsh et al. 2017) also supports the unprecedented nature of the 2018 ice extent. The maximum daily Bering Sea SIE was reached in early February and was the lowest on record (~411,500 km^2), only 47% of the 1979–2016 mean seasonal maximum extent. The SIE then dropped ~215,000 km^2 (Perovich et al. 2018).

Ocean. Bering Sea sea surface temperatures (SSTs) and upper ocean heat content overall were both above the 1981–2010 mean during late summer and autumn 2017 (Timmermans et al. 2017) and this persisted

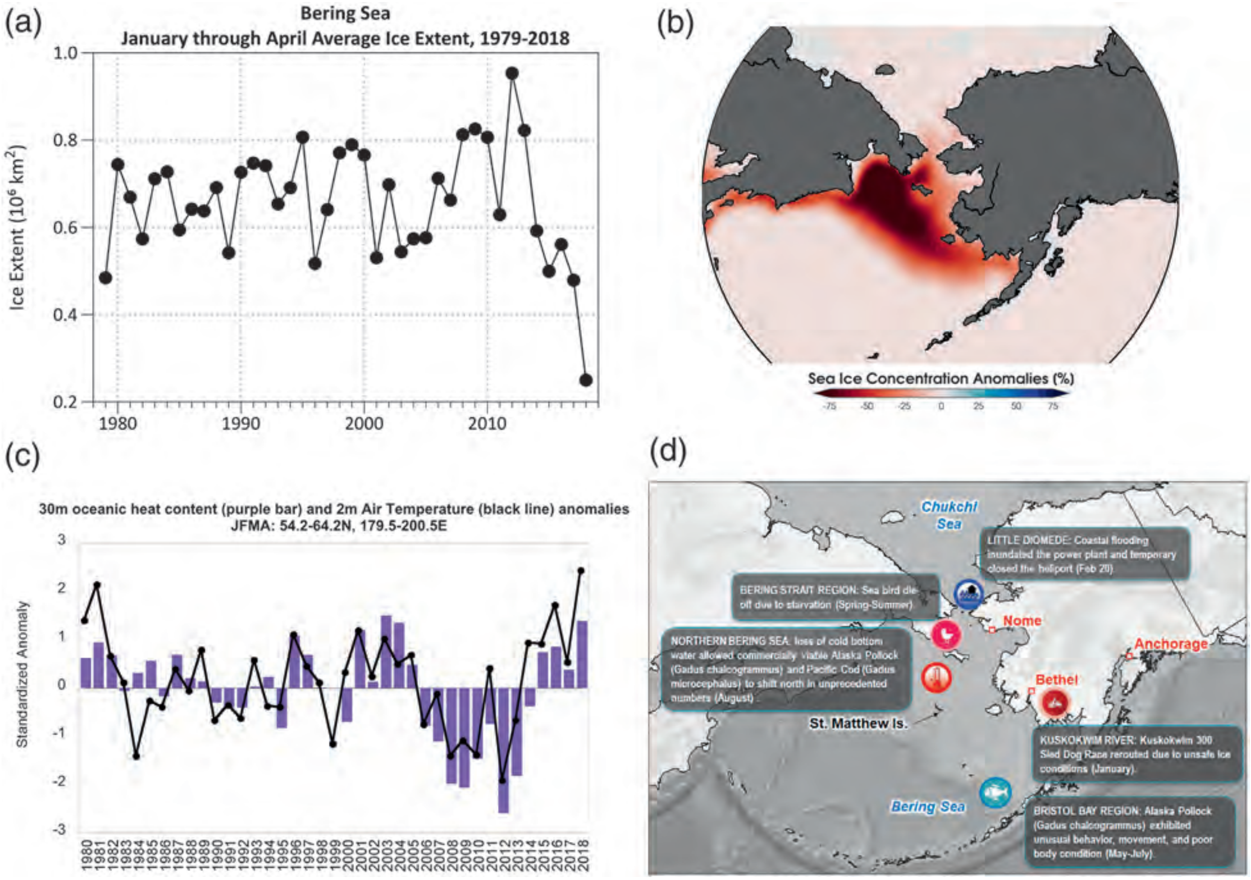

LITTLE DIOMEDE: Coastal flooding inundated the power plant and temporary closed the heliport (Feb 20).

BERING STRAIT REGION: Sea bird die-off due to starvation (Spring-Summer).

NORTHERN BERING SEA: loss of cold bottom water allowed commercially viable Alaska Pollock (Gadus chalcogrammus) and Pacific Cod (Gadus microcephalus) to shift north in unprecedented numbers (August).

KUSKOKWIM RIVER: Kuskokwim 300 Sled Dog Race rerouted due to unsafe ice conditions (January).

BRISTOL BAY REGION: Alaska Pollock (Gadus chalcogrammus) exhibited unusual behavior, movement, and poor body condition (May-July).

Fig. 1. (a) Annual time series of mean January–April Bering Sea ice extent since 1979 from the Sea Ice Index (Fetterer et al. 2017) (b) Mean January–April 2018 sea ice concentration anomalies calculated from a 1981–2010 climate baseline from NOAA/NSIDC climate data record of passive microwave sea ice concentration, version 3 (Meier et al. 2017). (c) Time series of normalized January–April upper 30-m Bering Sea heat content calculated from a 1981–2010 climate baseline from Global Ocean Data Assimilation System (Behringer 2007) and 2-m mean air temperature from ERA-Interim reanalysis. (d) Selected impacts of the low ice extent.

into early 2018 (Fig. 1c). Chukchi Sea SSTs were also above normal and delayed freeze-up north of Bering Strait, which possibly triggered atmosphere–ocean feedbacks that contributed to this winter's southerly airflow (Tachibana et al. 2019).

Atmosphere. The winter of 2017/18 was persistently stormy over the Bering Sea. The mean sea level pressure anomaly fields for both autumn (September–November) and winter (December–February) were characterized by negative anomalies over Chukotka and positive departures (>5 hPa) south of the Aleutians. The departures from normal air temperature (at 925 hPa) were positive throughout autumn and winter, with the largest positive anomalies in the January to March season, when the western Bering Sea was more than 5°C above normal (Overland et al. 2018a) and the eastern Bering Sea had the highest mean January–April 2-m air temperature of record (Fig. 1c). Stabeno and Bell (2019) highlight the particular importance of episodic but recurring southerly winds during this winter that advected relatively warm air over the Bering Sea and the relationship to the extremely low ice extent.

IMPACTS OF LOW ICE. Impacts of record low sea ice extent in the Bering Sea beyond the climate system were widespread and profound, and included unprecedented weather events, marine wildlife die-offs, and sightings of animals outside of their normal range, such as the ecosystem impacts discussed in Duffy-Anderson et al. (2019). The Local Environmental Observer (LEO) Network (https://www.leonetwork.org/bering-sea-ice-2018) received more than 50 reports of notable events in western Alaska through August 2018. Persistently warm weather contributed to poor ice conditions resulting in a fatal accident on the Kuskokwim River ice road (Alaska

Dispatch News 2018). In the Bering Strait, retreating and fractured sea ice during a late February storm allowed a coastal sea ice–laden flooding event that caused a power outage and infrastructure damage at Little Diomede, Alaska (Walsh 2018). Historically in February, stable landfast ice at Little Diomede Island provided an ice airstrip for primary transportation. In the Bering Strait region, the limited duration, poor quality, and unseasonable retreat of the sea ice was coincident with the loss or impairment of maritime subsistence activities for coastal communities. Ecologically, changes in the northern Bering Sea marine ecosystem included the first documented mass strandings of ice-associated seals in the Bering Strait region (Sheffield 2018), redistribution of thermally sensitive fish species, and a multi-species seabird die-off attributed to starvation (Siddon and Zador 2018).

ATTRIBUTION. To evaluate the role of anthropogenic climate change in the 2018 Bering Sea ice extreme anomaly, we employed monthly gridded sea ice concentration data from the CESM Large Ensemble (CESM-LENS). CESM-LENS features fully coupled simulations with 40 ensemble members reflecting historical (1850/1920–2005) and projected (2005–2100; RCP8.5) climate forcing and a pre-industrial control simulation (1,800 yr) reflecting climate forcing from 1850 (Kay et al. 2015). Arctic sea ice extent (Jahn et al. 2016) and sea ice thickness (Labe et al. 2018) in the CESM-LENS have been shown to be realistic when compared to satellite observations post-1978. The Bering Sea region grid points were masked and monthly SIE was derived by summing the area of the grid cells with concentrations greater than or equal to 15% annually for the January to April period. There is a weak (not statistically significant) negative trend in the observed January to April mean SEI (though a significant trend is found in other aspects of Bering Sea ice extent; see Fig. ES1 in the online supplemental material), although some sub-intervals (e.g., 1979–2012) show an increasing trend. This is expected since the subdecadal-scale variability of Bering SIE is known to be driven by internal atmospheric variability (e.g., Pease et al. 1982; Overland et al. 2018b). The CESM-LENS ensembles averages display declining trends over 1980–2018 that are mostly (35 of 40 members) greater in magnitude than the observed trend (and one member exceeds the 1979–2012 observed trend) while similar 39-yr subsets of the pre-industrial simulation have mixed increasing and decreasing trends (see Fig. ES2). The variances of the model ensembles are generally higher than the observations although the standard deviation decreases by about 50% between 2010 and 2080. The Bering SIE observations from 1980 to 2018 (Fetterer et al. 2017) were quantile-mapped to fit the CESM-LENS distribution (Fig. 2a). The SIE for each ensemble member during this period was sorted by increasing value and each quantile was then averaged over all ensemble members and matched to the corresponding quantile from the observations. The resulting distribution (see blue line in Fig. 2a) gives an model-adjusted observed 2018 SIE minimum of 406,332 km^2, which is used to assess the role of anthropogenic climate change. This is done by calculating the fraction of attributable risk (FAR; Stott et al. 2004; National Academies of Sciences, Engineering, and Medicine 2016) where FAR $= 1 - \text{Prob}_{\text{pre-Industrial}}/\text{Prob}_{\text{present}}$, and the probability is the likelihood of exceeding (i.e., being lower than) the 2018 SIE. Figure 2b shows the pre-industrial simulation of the January–April ice extent, together with the adjusted (blue) and unadjusted (red) values for 2018. There were two exceedances during the 1,800-yr pre-industrial simulation and a total of 117 from the 40 CESM-LENS ensemble members from the 2003–33 "present" climate, resulting in a FAR of 0.99. Individual LENS members ranged from 0 to 7 occurrences from 2003 to 2033. However, if the present climate were defined as the 1980–2018 historical period, there would have been only 29 exceedances of 2018 in the 40 ensemble members, making the FAR correspondingly smaller (0.94). Finally, Fig. 2c shows the probability, over all 40 CESM-LENS simulations, that the 2018 minimum will be exceeded in each decade. The probability is essentially zero through the 1990s, after which it increases to 0.06 in the 2010s, 0.14 in the 2020s, 0.29 in the 2030s, 0.52 in the 2040s, and 0.94 by the 2060s. Thus CESM-LENS indicates that 2018 extreme ice extent in the Bering Sea may become the mean extent by the 2040s and essentially an upper bound (with only a 6% probability of greater extent) by the 2060s.

CONCLUSIONS. The 2018 January through April sea ice extent in the Bering Sea was far lower than any previous winter in the reconstructed or observed past (since 1850). This had ramifications for the weather and climate system, economic impacts, and long-lasting ecosystem impacts. Ocean warmth, late ice development, and frequent atmospheric storminess were important factors. Using CESM-LENS, we find that the observed 2018 January through April mean sea ice extent to be extremely rare in the pre-industrial control simulation (2 out of 1,800) but becomes much more frequent in the current era. The FAR exceeds 0.9 using either the current era (2003–33) or recent

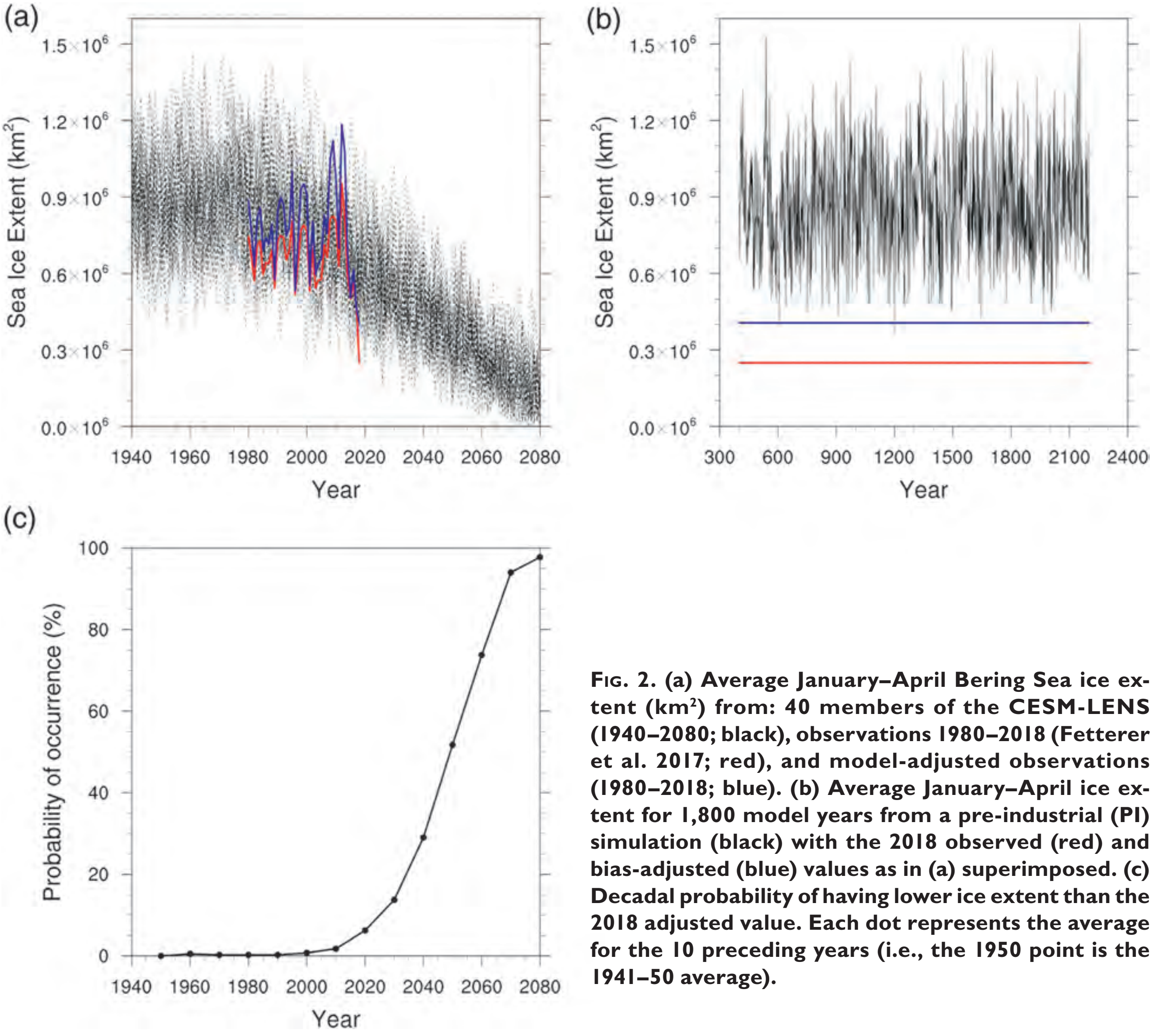

Fig. 2. (a) Average January–April Bering Sea ice extent (km²) from: 40 members of the CESM-LENS (1940–2080; black), observations 1980–2018 (Fetterer et al. 2017; red), and model-adjusted observations (1980–2018; blue). (b) Average January–April ice extent for 1,800 model years from a pre-industrial (PI) simulation (black) with the 2018 observed (red) and bias-adjusted (blue) values as in (a) superimposed. (c) Decadal probability of having lower ice extent than the 2018 adjusted value. Each dot represents the average for the 10 preceding years (i.e., the 1950 point is the 1941–50 average).

past (1980–2018) simulations and that with ongoing Earth system warming the 2018 extent and could potentially be typical by the 2040s and represent an upper bound within 50 years.

ACKNOWLEDGMENTS. This material is based upon work supported by the National Science Foundation under Award OPP-1749081 (USB, PAB, JEW) and by NOAA's Climate Program Office through Grant NA16OAR4310162 (RT, BRB, JEW). Computing resources (doi:10.5065/D6RX99HX) were provided by the Climate Simulation Laboratory at NCAR's Computational and Information Systems Laboratory, sponsored by the NSF and other agencies. Heather McFarland (UAF/IARC) provided graphics support. The authors thank the three anonymous reviewers for their thoughtful comments and suggestions.

REFERENCES

Alaska Dispatch News, 2018. Father dies, 5 people rescued after family falls through river ice near Bethel. 1 January 2018, *Alaska Dispatch News*, https://www.ktuu.com/content/news/Body-of-man-who-fell-through-ice-found-467631083.html.

Behringer, D. W., 2007: The Global Ocean Data Assimilation System (GODAS) at NCEP. *11th Symp. on Integrated Observing and Assimilation Systems for the Atmosphere, Oceans, and Land Surface.* San Antonio, TX, Amer. Meteor. Soc., 3.3, https://ams.confex.com/ams/87ANNUAL/webprogram/Paper119541.html.

Dee, D. P., and Coauthors, 2011: The ERA-Interim reanalysis: Configuration and performance of the data assimilation system. *Quart. J. Roy. Meteor. Soc.*, **137**, 553–597, https://doi.org/10.1002/qj.828.

Duffy-Anderson, J. T., and Coauthors, 2019: Responses of the northern Bering Sea and southeastern Bering Sea pelagic ecosystems following record-breaking low winter sea ice. *Geophys. Res. Lett.*, **46**, 9833–9842, https://doi.org/10.1029/2019GL083396.

Fetterer, F., K. Knowles, W. N. Meier, M. Savoie, and A. K. Windnagel, 2017 (updated daily): Sea Ice Index, Version 3. Regional Daily Data. National Snow and Ice Data Center, accessed April and August 2019, https://doi.org/10.7265/N5K072F8.

Jahn, A., J. E. Kay, M. M. Holland, and D. M. Hall, 2016: How predictable is the timing of a summer ice-free Arctic? *Geophys. Res. Lett.*, **43**, 9113–9120, https://doi.org/10.1002/2016GL070067.

Kay, J. E., and Coauthors, 2015: The Community Earth System Model (CESM) Large Ensemble Project: A community resource for studying climate change in the presence of internal climate variability. *Bull. Amer. Meteor. Soc.*, **96**, 1333–1349, https://doi.org/10.1175/BAMS-D-13-00255.1.

Labe, Z., G. Magnusdottir, and H. Stern, 2018: Variability of Arctic sea ice thickness using PIOMAS and the CESM Large Ensemble. *J. Climate*, **31**, 3233–3247, https://doi.org/10.1175/JCLI-D-17-0436.1.

Meier, W. N., F. Fetterer, M. Savoie, S. Mallory, R. Duerr, and J. Stroeve. 2017: NOAA/NSIDC Climate Data Record of Passive Microwave Sea Ice Concentration, Version 3. National Snow and Ice Data Center, accessed August 2019, https://doi.org/10.7265/N59P2ZTG.

Mueter, F. J., and M. A. Litzow, 2008: Sea ice retreat alters the biogeography of the Bering Sea continental shelf. *Ecol. Appl.*, **18**, 309–320, https://doi.org/10.1890/07-0564.1.

National Academies of Sciences, Engineering, and Medicine, 2016: *Attribution of Extreme Weather Events in the Context of Climate Change*. National Academies Press, 186 pp., https://doi.org/10.17226/21852.

National Ice Center and National Snow and Ice Data Center, 2010 (updated daily): Multisensor Analyzed Sea Ice Extent–Northern Hemisphere (MASIE-NH), version 1. NSIDC, accessed 6 August 2019, https://doi.org/10.7265/N5GT5K3K.

Overland, J. E., E. Hanna, I. Hanssen-Bauer, S. J. Kim, J. E. Walsh, M. Wang, U. S. Bhatt, and R. L. Thoman, 2018a: Surface air temperature [in "Arctic Report Card 2018"]. NOAA, https://arctic.noaa.gov/Report-Card/Report-Card-2018/ArtMID/7878/ArticleID/783/Surface-Air-Temperature.

Overland, J. E., M. Wang, and T. J. Ballinger, 2018b: Recent increased warming of the Alaskan marine Arctic due to midlatitude linkages. *Adv. Atmos. Sci.*, **35**, 75–84, https://doi.org/10.1007/s00376-017-7026-1.

Pease, C. H., S. A. Schoenberg, and J. E. Overland, 1982: A climatology of the Bering Sea and its relation to sea ice extent. NOAA Tech. Rep. ERL 419-PMEL 36, 29 pp.

Perovich, D., and Coauthors, 2018: Sea ice [in "Arctic Report Card 2018"]. NOAA, https://arctic.noaa.gov/Report-Card/Report-Card-2018/ArtMID/7878/ArticleID/780/SeanbspIce.

Schumacher, J. D., K. Aagaard, C. H. Pease, and R. B. Tripp, 1983: Effects of a shelf polynya on flow and water properties in the northern Bering Sea. *J. Geophys. Res.*, **88**, 2723–2732, https://doi.org/10.1029/JC088iC05p02723.

Sheffield, G., 2018: Response to reported mass seal stranding at Wales, Alaska–June 2018. Trip Report to Alaska Marine Mammal Stranding Network, Juneau, Alaska, 8 pp.

Siddon, E., and S. Zador, 2018: Ecosystem Status Report 2018: Eastern Bering Sea. NOAA Fisheries, accessed 9 May 2019, https://www.fisheries.noaa.gov/resource/data/2018-status-eastern-bering-sea-ecosystem.

Stabeno, P. J., and S. W. Bell, 2019: Extreme conditions in the Bering Sea (2017–2018): Record-breaking low sea-ice extent. *Geophys. Res. Lett.*, **46**, 8952–8959, https://doi.org/10.1029/2019GL083816.

Stott, P., D. Stone, and M. Allen, 2004: Human contribution to the European heatwave of 2003. *Nature*, **432**, 610–614, https://doi.org/10.1038/nature03089.

Szymanski, A., and R. Gradinger, 2016: The diversity, abundance and fate of ice algae and phytoplankton in the Bering Sea. *Polar Biol.*, **39**, 309–325, https://doi.org/10.1007/s00300-015-1783-z.

Tachibana, Y., K. K. Komatsu, V. A. Alexeev, L. Cai, and Y. Ando, 2019: Warm hole in Pacific Arctic sea ice cover forced mid-latitude Northern Hemisphere cooling during winter 2017–18. *Sci. Rep.*, **9**, 5567, https://doi.org/10.1038/s41598-019-41682-4.

Timmermans, M.-L., C. Ladd, and K. Wood, 2017: Sea surface temperature [in "Arctic Report Card 2017"]. NOAA, https://arctic.noaa.gov/Report-Card/Report-Card-2017/ArtMID/7798/ArticleID/698/Sea-Surface-Temperature.

Walsh, J., 2018: Sea ice in the Alaska region: The remarkable winter of 2017–18. Alaska Climate Dispatch—A state-wide seasonal summary and outlook, 1–3, https://uaf-accap.org/wp-content/uploads/2019/10/climate_dispatch_May_2018_FINAL.pdf.

——, F. Fetterer, J. S. Stewart, and W. L. Chapman, 2017: A database for depicting Arctic sea ice variations back to 1850. *Geogr. Rev.*, 107, 89–107, https://doi.org/10.1111/j.1931-0846.2016.12195.x.

THE LATE SPRING DROUGHT OF 2018 IN SOUTH CHINA

Lixia Zhang, Tianjun Zhou, Xiaolong Chen,
Peili Wu, Nikolaos Christidis, and Fraser C. Lott

HadGEM3-A indicates that anthropogenic forcing has increased the likelihood of the 2018 late spring drought in South China approximately 17 times, and such events do not occur in CAM5 without human influence.

Late spring (April–May) is normally the end of the dry season in South China, but 2018 was an exception. An extreme drought condition developed over South China (22°–29°N, 105°–120°E; box in Figs. 1a–c) during the late spring in 2018, affecting the provinces of Guangdong, Fujian, Jiangxi, Guizhou, and part of Hunan. South China received only about 40% of the 1951–2018 mean precipitation over Guangdong and Fujian provinces (Fig. 1a). The surface temperature reached 2.8°C above normal (1951–2018 mean) at a maximum (Fig. 1b), with record-breaking hot days in May reported in Guangdong, Jiangxi, and Fujian provinces. More than half stations over South China experienced a record-breaking drought seen from the anomalies in precipitation and the difference between precipitation and reference evapotranspiration (Pr-ET) (Figs. 1a,c). The 2018 late spring was ranked as the third year with extreme deficit rainfall (–2.6 mm day^{-1} less), the warmest year (2.0°C warmer) for 1951–2018 (Fig. 1d), and the second driest year on record (–2.8 mm day^{-1} less) measured by Pr-ET. It reported that this drought has resulted in shrinking reservoirs and water shortages (www.gdsw.gov.cn/zwgk_tjxx.html; http://slt.fujian.gov.cn/xxgk/tjxx/swxb/). The acreage and yield for early rice, which is mainly planted in South China, was reduced respectively by 350 thousand hectares and 1.28 million tons relative to 2017 (National Bureau of Statistics of China; www.stats.gov.cn/tjsj/zxfb/201808/t20180824_1618794.html).

Observations show that South China has experienced a drying trend in late spring since the 1950s (Xin et al. 2006; Qiu et al. 2009; Li et al. 2018). The internal variation, such as the interdecadal changes of North Atlantic Oscillation (Xin et al. 2006) and an increase in protracted El Niño events accompanied by a reduction in La Niña episodes (Qiu et al. 2009), and anthropogenic aerosol forcing (Kim et al. 2007) were documented to be contributing to this drying trend. So far it is still unclear whether the attribution of anthropogenic forcing is detectable in the extreme late spring drought events over South China. This study will investigate the cause of the 2018 late spring drought in South China, and will assess the contribution of anthropogenic climate change on the likelihood of the 2018 late spring drought over South China by both examining drought indices and associated circulation.

DATA AND METHODS. The observational and reanalysis datasets used in this study are 1) monthly surface air temperature and precipitation observations at 839 stations for 1951–2018 provided by the National Meteorological Information Center at the China Meteorological Administration (the station data are further area-weighted interpolated to a 0.5° grid cell) and 2) monthly circulation data from the Japanese 55-Year Reanalysis for 1959–2018 (JRA-55;

AFFILIATIONS: Zhang—LASG, Institute of Atmospheric Physics, Chinese Academy of Sciences (CAS), and CAS Center for Excellence in Tibetan Plateau Earth Sciences, Chinese Academy of Sciences, Beijing, China; Zhou and Chen—LASG, Institute of Atmospheric Physics, Chinese Academy of Sciences, Beijing, China; Wu, Christidis, and Lott—Met Office Hadley Centre, Exeter, United Kingdom

CORRESPONDING AUTHOR: Dr. Lixia Zhang, lixiazhang@mail.iap.ac.cn

DOI:10.1175/BAMS-D-19-0202.1

A supplement to this article is available online (10.1175/BAMS-D-19-0202.2)

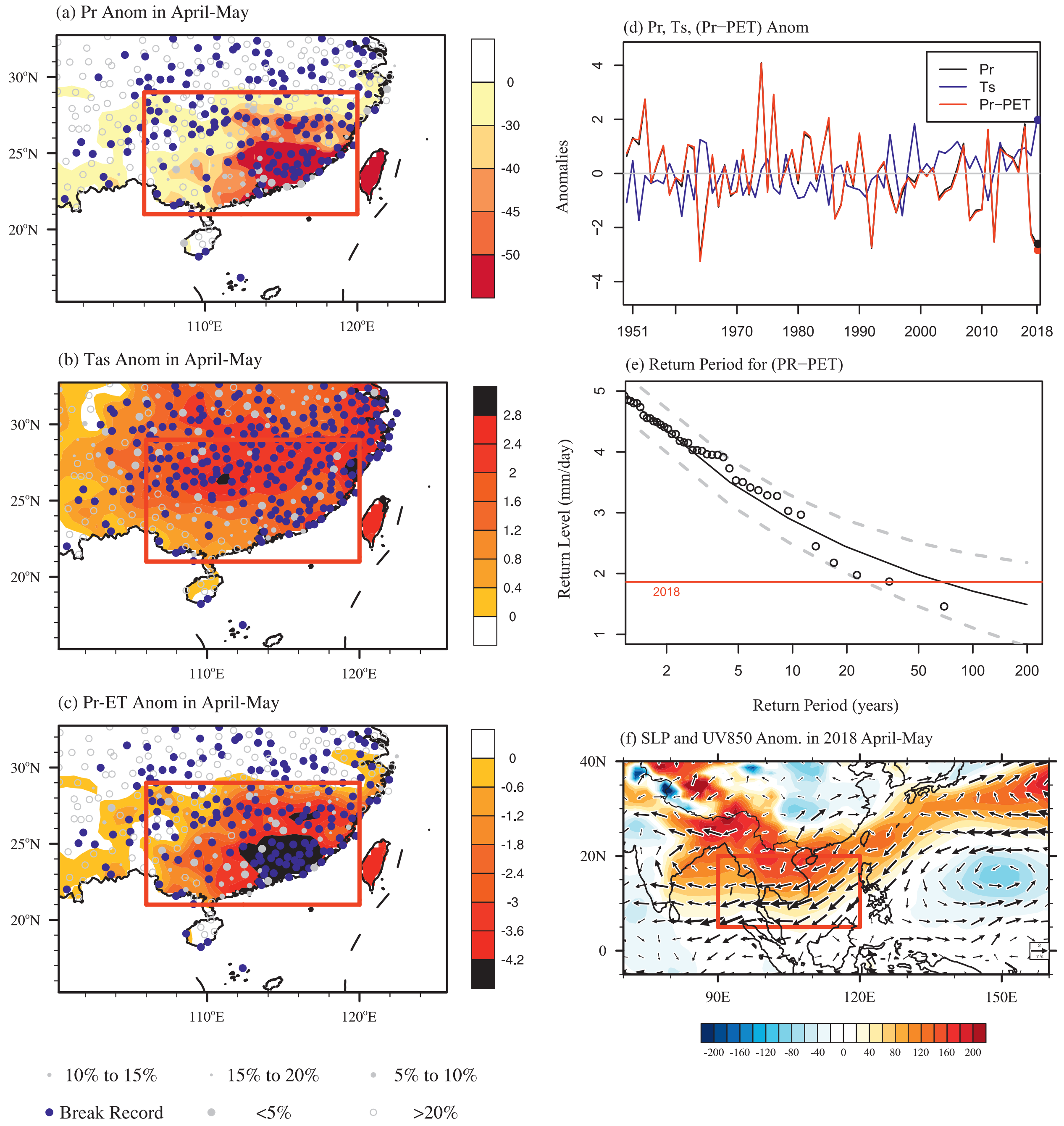

Fig. 1. The anomalies of (a) precipitation (%), (b) surface air temperature (°C), and (c) the difference between precipitation and reference evapotranspiration (Pr-ET; mm day^{-1}) in April–May 2018 relative to 1951–2018. The dots are the percentile ranks of April–May anomalies in 2018 at each station. Shadings are the anomalies based on the gridded data from the station observations. (d) Observed April–May mean surface air temperature (blue; °C), precipitation (black; mm day^{-1}), and Pr-ET (red; mm day^{-1}) anomalies regional averaged over South China [red box in (a)–(c)], where the dots denote the year 2018. (e) Return periods and 95% confidence intervals for April–May mean Pr-ET averaged over South China, where the red line denotes the year 2018. (f) April–May mean sea level pressure (shading; Pa) and 850-hPa winds (vector; m s^{-1}) anomalies in 2018 relative to 1959–2018.

Ebita et al. 2011). Reference evapotranspiration is calculated from surface temperature using the Hamon formulation (Haith and Shoemaker 1987).

We use outputs of two ensembles of simulations for the actual climate with all external forcing ("Factual") and for a hypotheticals natural climate without the effect of human influence ("Counterfactual") from two atmospheric general circulation models (Stone et al. 2019). One is HadGEM3-A-N216 from the Met Office HadGEM3-A-based operational event attribution system on a 0.83° × 0.56° grid (Christidis et al. 2013; Ciavarella et al. 2018). The other one is CAM5 from CLIVAR C20C+ Detection and Attribution project on a 1° × 1° grid (Angélil et al. 2017). 15 (50) members of historical simulations for 1960–2013 (1959–2017) and 525 (200) members for 2018 April–May were conducted for each experiment in HadGEM3-A (CAM5).

Two drought indices are used in this study, namely April–May mean Pr-ET and precipitation (Pr) averaged over the land grids in South China (22°–29°N, 105°–120°E), considering that precipitation deficit is the primary cause for agricultural failures and hydrological water shortages, and Pr-ET measures the balance between moisture supply and demand in the atmosphere. A circulation index is defined as the 850-hPa zonal winds (U850) averaged over 5°–20°N, 90°–120°E, a key region to define the South China Sea summer monsoon onset (Wang et al. 2004). Generalized extreme value (GEV) distribution is used to fit the April–May mean Pr, Pr-ET, and U850 distribution to estimate the return periods of drought events.

For the detection and attribution study, the following steps are carried out to make simulations and observations comparable. 1) We first extract the Pr, Pr-ET, and U850 indices in each experiment. This yields 525 (200) samples for year 2018 and 810 (2950) for the "historical" experiment from HadGEM3-A-N216 (CAM5). 2) Then we construct GEV distributions using all indices from the samples from this historical experiment, and derive the thresholds for the drought events in HadGEM3-A-N216 and CAM5, which have the same return periods as the year 2018 in observation. 3) Finally, the GEV probabilities of all simulated drought indices for year 2018 are derived from the Factual and Counterfactual experiments, and the risk ratio of such an event is calculated to see whether the anthropogenic forcing is detectable. The uncertainty of risk ratio is estimated via bootstrapping 1,000 times with showing the 5th–95th percentile ranges. We resample all model years with replacement and calculate the risk ratio for each bootstrap realization.

RESULTS. The return period of the 2018 late spring drought in observation is about once-in-66 years (Fig. 1e) and once-in-47 years based on Pr-ET and Pr, respectively. The dry condition in 2018 late spring was associated with an anomalous high sea level pressure (SLP) covering the Bay of Bengal and Southeast Asia, accompanied with easterly anomalies to its south flank (Fig. 1f). It prohibited the transition of low-level winds over the Bay of Bengal from easterlies to westerlies during April–May, thus delayed the onset of South China Sea summer monsoon (SCSSM) and the South China rainy season. Studies showed that the pre-rainy season onset began on 7 May 2018, 31 days later than the normal (www.cma.gov.cn/root7/auto13139/201903/t20190319_517664.html; Liu and Zhu 2019; Wang et al. 2016). A prominent feature of the low-level circulation anomalies is the anticyclonic circulation anomalies over the north Indian Ocean, demonstrating a weakened Walker circulation in late spring. At middle and high levels, the western North Pacific subtropical high was enhanced and westerly jet stream was weaker than the normal (Liu and Zhu 2019). These large-scale circulation anomalies are consistent with previous studies finding that a weakened Walker circulation is unfavorable for the airflow from the Indian Ocean into the SCS and easterly retreat of western North Pacific subtropical high, inducing a late SCSSM onset and South China late spring rainfall deficit (Feng and Hu 2014; Luo et al. 2016; Zhou and Chan 2007; Qiu et al. 2009). The U850 in 2018 April–May was only -1.7 m s^{-1}, which is about -1.8 m s^{-1} less than 1959–2017 mean, with a return period about 70 years.

ATTRIBUTION OF THE ANTHROPOGENIC FORCING ON 2018 LATE-SPRING DROUGHT.

Models reasonably represent the variation of South China drought for the period 1960–2013. It shows that the two models well simulate the ranges of observed anomalies both from yearly variation (see Figs. ES1a,b in the online supplemental material) and the dry tail as seen in the observation (Figs. ES1c,d), particularly for HadGEM3-A-N216. The correlation coefficient of Pr-ET between the ensemble mean for the Factual run of HadGEM3-A-N216 and observation is 0.29 for 1960–2013, statistically at 95% confidence level (Figs. ES1a,b). The climate mean distribution of 850-hPa winds in April–May can also be well simulated by models (Figs. ES3a,b). The thresholds at 2.4 (1.3) mm day^{-1} in Pr-ET and 4.7 (3.6) mm day^{-1} in Pr with the same return periods of observation are derived from HadGEM3-A-N216 (CAM5) for attribution, respectively. The difference between the two models indicates great uncertainty arising from model structure and the importance of multimodel comparison for attribution study.

An overall mean shift of Pr-ET toward a drier condition in Factual relative to Counterfactual is simulated both by HadGEM3-A-N216 and CAM5 for year 2018 (Figs. 2a,b), demonstrating increases in the probability of such drought events over South China with anthropogenic forcing. The likelihood of such drought events defined by Pr-ET is around 9.9% (P1) (8.2%–11.5%) from the 525 samples of 2018 in the Factual experiment but only 0.6% (P0) (0.05%–0.9%) in the Counterfactual experiment of HadGEM3-A-N216. The risk ratio (P1/P0) is approximately 17 (10–165), suggesting that human influences have increased the risk of such a drought event by 17 (10–165) times in year 2018 in HadGEM3-A-N216. The increase in the risk of such droughts event in 2018 is mainly caused by a higher probability of extreme precipitation deficit with human impact, which is 12.2% (5.3%–12.0%) in Factual but only 1.5% (0.6%–2.1%) in Counterfactual, with a risk ratio around 8.0 (5–19) (Fig. 2b). U850 also shows a shift toward an extreme weak tail (Fig. 2c). The events with U850 such as observed in 2018 never occur from the 525 members of HadGEM-N-216 either in the Factual or Counterfactual experiment. By lowering the threshold of U850 from one-in-70 years (–2.1 m s^{-1}) to one-in-20 years (–1.0 m s^{-1}), the likelihood of such events is about 0.1% in the 2018 Factual experiment, whereas it still never occurs in the 2018 Counterfactual experiment. CAM5 also supports the results from HadGEM3-A-N215, while the events similar to 2018 never occur in the Counterfactual world. Thus, risk ratio cannot be obtained from CAM5.

The width for GEV distributions of the three indices in Factual is comparable with that in Counterfactual, but with a shift in mean states toward a weaker magnitude. It demonstrates that the mean state of circulation in Factual is weaker than that in Counterfactual, which increases the likelihood of extreme weak U850 events and thus extreme drought in South China. Therefore, the 850-hPa wind difference between 2018 Factual and Counterfactual is examined (Figs. 2d,h). Their differences show the similar anomalies as observed in 2018, with anomalous lower-level divergence over the Maritime Continent, suggesting that anthropogenic forcing plays an importance role in the weakened Walker circulation in 2018 late spring. Thus, anomalous easterly winds are seen over (5°–20°N, 90°–120°E), increasing the likelihood of extreme weak U850 in the Factual experiment (Figs. 2c,g).

Under anthropogenic forcing, an El Niño–like SST warming pattern over the tropical Pacific Ocean under global warming and east–west SST gradients over the tropical Indo-Pacific Ocean are seen in 2018 late spring. Those SST anomaly patterns could both contribute to a weakened Walker circulation (Figs. 2d,h, Held and Soden 2006; Tokinaga et al. 2012). Consequently, the anomalous easterly winds are shown over the north Indian Ocean under anthropogenic forcing in the two models, increasing the likelihood of extreme late onset of the East Asian summer monsoon. In comparison, the circulation difference between Factual and Counterfactual is much stronger in HadGEM3-A-N216 relative to CAM5.

We further investigated the results from the full historical simulations to verify the robustness of the attributable results. The shifts toward the extreme weak tail of Pr-ET, Pr, and U850 under anthropogenic forcing can also be detected (Fig. ES2). In historical simulation, the risk ratio of the 2018 drought event estimated by Pr-ET is about 8 (2–42) and 75 (36–1389) in HadGEM3-A-N216 and CAM5, respectively, and 4 (2–14) and 58 (33–432) estimated by Pr. Similar to Fig. 2d, there is a weaker Walker circulation with easterly winds anomalies to the south of Bay of Bengal in the Factual experiment relative to the Counterfactual experiment associated with the same non-uniform distribution of SST warming under anthropogenic forcing (Figs. ES3c,d). A parallel analysis using the CAM5 simulations is similar to those based on the HadGEM3-A-N216, supporting that our findings have less model dependence.

CONCLUSIONS. An exceptional rainfall deficit combined with record-breaking warm temperatures ranked 2018 late spring as the second driest year since 1951. The extremely late onset of the SCSSM in 2018 played a major role, characterized by easterly anomalies to the south of the Bay of Bengal. We find that anthropogenic forcings have increased the likelihood of the observed 2018 late spring drought in South China by 17 times in HadGEM3-A-N216, and such events similar to 2018 would never occur in the CAM5 Counterfactual experiment. A weakening of the Walker circulation in late spring under anthropogenic forcing increases the likelihood of extreme weak westerly winds and then the occurrence of extremely late onset of SCSSM, and subsequently extreme drought over South China. The increase in drought risk of South China poses serious challenges for decision makers and the society as whole for water resource management and economic development.

ACKNOWLEDGMENTS. This work was jointly supported by the National Key R&D Program of China (2018YFE0196000) and the National Natural Science Foundation of China (41661144009 and 41675076). Peili Wu and Fraser C. Lott were supported by the U.K.–China Research

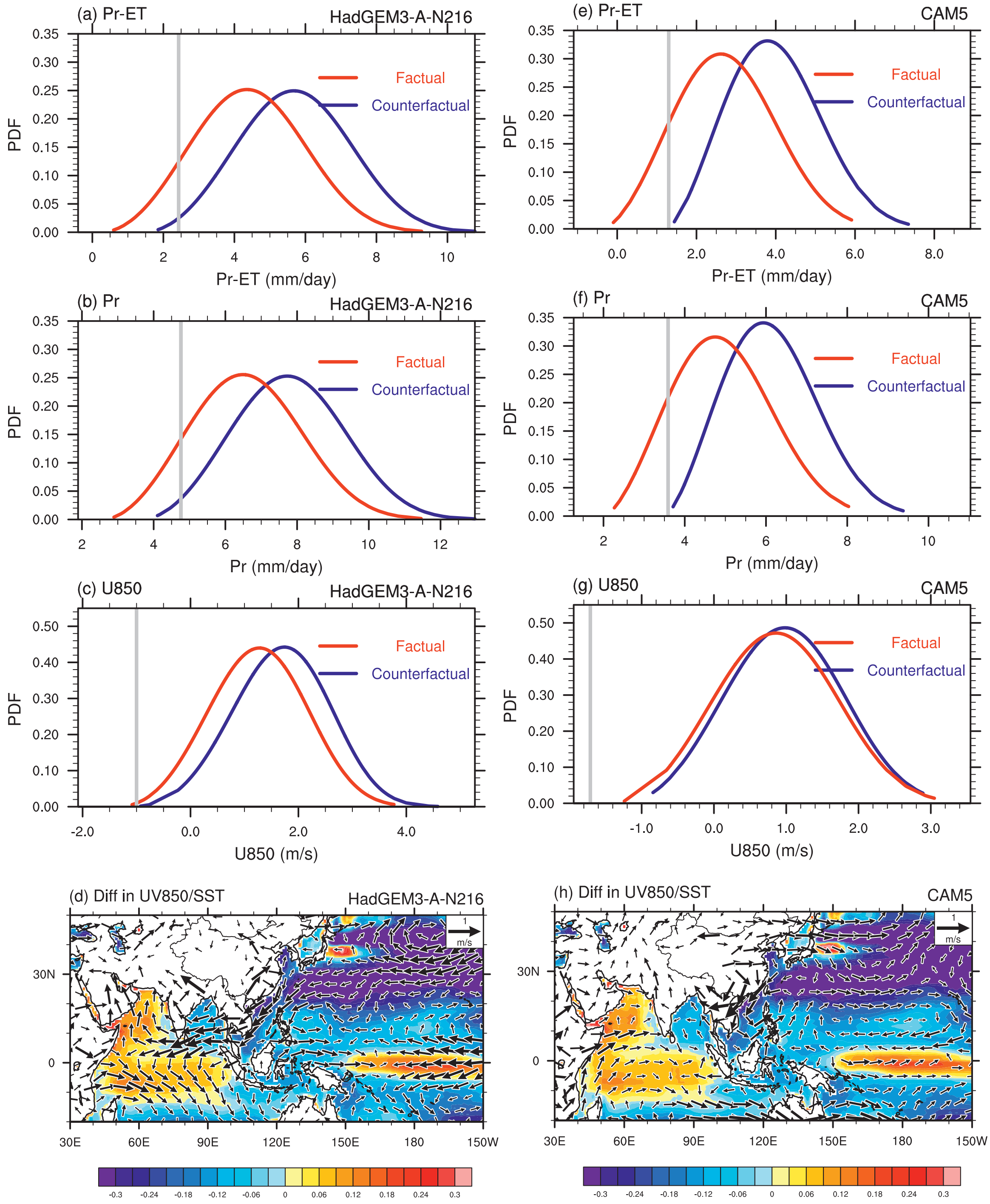

Fig. 2. GEV distributions of the April–May mean (a) Pr-ET and (b) precipitation (mm day^{-1}) averaged over South China with (Factual; red) and without (Counterfactual; blue) anthropogenic climate changes constructed for 2018 with HadGEM3-A. (c) As in (a) and (b), but for the 850-hPa zonal wind averaged over the red box in Fig. 1f. The gray lines denote the thresholds of drought events as observed in year 2018 except in (c), which shows the U850 with a 20-yr return period. (d) Difference in April–May mean 850-hPa winds and sea surface temperature (SST) between the 525 members mean of the Factual and Counterfactual experiments for the year 2018. To show the impact of non-uniform distribution in SST warming with anthropogenic forcing on circulation changes, we first get the SST difference between Factual and Counterfactual and then remove its area-average mean over 40°S–40°N. (e)–(h) As in (a)–(d), but for the results from CAM5.

and Innovation Partnership Fund through the Met Office Climate Science for Service Partnership (CSSP) China as part of the Newton Fund.

REFERENCES

Angélil, O., D. Stone, M. Wehner, C. J. Paciorek, H. Krishnan, and W. Collins, 2017: An independent assessment of anthropogenic attribution statements for recent extreme temperature and rainfall events. *J. Climate*, **30**, 5–16, https://doi.org/10.1175/JCLI-D-16-0077.1.

Christidis, N., P. A. Stott, A. A. Scaife, A. Arribas, G. S. Jones, D. Copsey, J. R. Knight, and W. J. Tennant, 2013: A new HadGEM3-A-based system for attribution of weather- and climate-related extreme events. *J. Climate*, **26**, 2756–2783, https://doi.org/10.1175/JCLI-D-12-00169.1.

Ciavarella, A., and Coauthors, 2018: Upgrade of the HadGEM3-A based attribution system to high resolution and a new validation framework for probabilistic event attribution. *Wea. Climate Extremes*, **20**, 9–32, https://doi.org/10.1016/J.WACE.2018.03.003.

Ebita, A., and Coauthors, 2011: The Japanese 55-year reanalysis "JRA-55": An interim report. *SOLA*, **7**, 149–152, https://doi.org/10.2151/SOLA.2011-038.

Feng, J., and D. Hu, 2014: How much does heat content of the western tropical Pacific Ocean modulate the South China Sea summer monsoon onset in the last four decades? *J. Geophys. Res. Oceans*, **119**, 4029–4044, https://doi.org/10.1002/2013JC009683.

Haith, D. A., and L. L. Shoemaker, 1987: Generalized watershed loading functions for stream flow nutrients. *Water Resour. Bull.*, **23**, 471–478, https://doi.org/10.1111/j.1752-1688.1987.tb00825.x.

Held, I. M., and B. J. Soden, 2006: Robust responses of the hydrological cycle to global warming. *J. Climate*, **19**, 5686–5699, https://doi.org/10.1175/JCLI3990.1.

Kim, M.-K., W. K. M. Lau, K.-M. Kim, and W.-S. Lee, 2007: AGCM study of effects of radiative forcing of sulfate aerosol on large scale circulation and rainfall in East Asia during boreal spring. *Geophys. Res. Lett.*, **34**, L24701, https://doi.org/10.1029/2007GL031683.

Li P., T. Zhou, and X. Chen, 2018: Water vapor transport for spring persistent rains over southeastern China based on five reanalysis datasets. *Climate Dyn.*, **51**, 4243–4257, https://doi.org/10.1007/s00382-017-3680-3.

Liu, B., and C. Zhu, 2019: Extremely late onset of the 2018 South China Sea summer monsoon following a La Niña event: Effects of triple SST anomaly mode in the North Atlantic and a weaker Mongolian cyclone. *Geophys. Res. Lett.*, **46**, 2956–2963, https://doi.org/10.1029/2018GL081718.

Luo, M., Y. Leung, H. Graf, and Coauthors, 2016: Interannual variability of the onset of the South China Sea summer monsoon. *Int. J. Climatol.*, **36**, 550–562, https://doi.org/10.1002/joc.4364.

Qiu, Y., W. Cai, X. Guo, and A. Pan, 2009: Dynamics of late spring rainfall reduction in recent decades over southeastern China. *J. Climate*, **22**, 2240–2247, https://doi.org/10.1175/2008JCLI2809.1.

Stone, D., and Coauthors, 2019: Experiment design of the International CLIVAR C20C+ detection and attribution project. *Wea. Climate Extremes*, **24**, 100206, https://doi.org/10.1016/j.wace.2019.100206.

Tokinaga, H., S.-P. Xie, C. Deser, Y. Kosaka, and Y. M. Okumura, 2012: Slowdown of the Walker circulation driven by tropical Indo-Pacific warming. *Nature*, **491**, 439–443, https://doi.org/10.1038/nature11576.

Wang, B., LinHo, Y. Zhang, and M. M. Lu, 2004: Definition of South China Sea monsoon onset and commencement of the East Asia summer monsoon. *J. Climate*, **17**, 699–710, https://doi.org/10.1175/2932.1.

Wang, S.-Y. S., Y. Lin, and C. Wu, 2016: Interdecadal change of the active-phase summer monsoon in East Asia (Meiyu) since 1979. *Atmos. Sci. Lett.*, **17**, 128–134, https://doi.org/10.1002/asl.603.

Xin X., R. Yu, T. Zhou, and B. Wang, 2006: Drought in late spring of South China in recent decades. *J. Climate*, **19**, 3197–3206, https://doi.org/10.1175/JCLI3794.1.

Zhou W., and J. C. L. Chan, 2007: ENSO and the South China Sea summer monsoon onset. *Int. J. Climatol.*, **27**, 157–167, https://doi.org/10.1002/joc.1380.

chapter 12

ANTHROPOGENIC INFLUENCE ON 2018 SUMMER PERSISTENT HEAVY RAINFALL IN CENTRAL WESTERN CHINA

Wenxia Zhang, Wei Li, Lianhua Zhu, Yuanyuan Ma, Linyun Yang, Fraser C. Lott,
Chunxiang Li, Siyan Dong, Simon F. B. Tett, Buwen Dong, and Ying Sun

Anthropogenic forcing has reduced the probability of summer persistent heavy rainfall in central western China similar to 2018 by ~47%, but increased that of daily extremes by ~1.5 times, based on HadGEM3-GA6 ensembles.

During mid-June to mid-July 2018, parts of Sichuan, Gansu, and Shaanxi provinces in China were affected by a persistent heavy rainfall event. Accumulated rainfall during the four-week period 18 June to 15 July was 38% above the 1961–2010 climatology. This was very close to the record (44% set in 2016) for maximum summertime four-week rainfall since 1961 (Figs. 1a,b). During this persistent rainfall event, the maximum 1-day rainfall was the fifth most extreme in the wet season on record. This persistent intense rainfall event caused floods, landslides, and house collapses, affecting 2.9 million people and resulting in a reported direct economic loss of over 8.9 billion Yuan (1.3 billion U.S. dollars; National Disaster Reduction Commission; https://reliefweb.int/disaster/tc-2018-000110-chn).

Central western China is located to the east of the Tibetan Plateau and in the marginal East Asian monsoon region. Summer heavy rainfall here is mainly caused by large-scale circulation anomalies involving the western North Pacific subtropical high (WNPSH) and southwest monsoon trough, as well as mesoscale and synoptic-scale weather systems such as Tibetan plateau vortices (Zhou and Yu 2005; Dong et al. 2007; Ueno et al. 2011; Xiang et al. 2013; Chen and Xu 2016). Anthropogenic influences have been found on extreme rainfall events in parts of China, particularly to increase the intensity of short-term

AFFILIATIONS: Zhang—State Key Laboratory of Numerical Modeling for Atmospheric Sciences and Geophysical Fluid Dynamics, Institute of Atmospheric Physics, Chinese Academy of Sciences, Beijing, China; Li—Key Laboratory of Meteorological Disaster, Ministry of Education (KLME)/Joint International Research Laboratory of Climate and Environment Change (ILCEC)/Collaborative Innovation Center on Forecast and Evaluation of Meteorological Disasters (CIC-FEMD), Nanjing University of Information Science and Technology, Nanjing, China; Zhu—Key Laboratory of Meteorological Disaster, Ministry of Education (KLME)/Joint International Research Laboratory of Climate and Environment Change (ILCEC)/Collaborative Innovation Center on Forecast and Evaluation of Meteorological Disasters (CIC-FEMD), and School of Mathematics and Statistics, Nanjing University of Information Science and Technology, Nanjing, China; Ma—Key Laboratory of Land-surface Process and Climate Change in Cold and Arid Regions, Northwest Institute of Eco-environment and Resources, Chinese Academy of Sciences, Lanzhou, China; Yang—CMA-NJU Joint Laboratory for Climate Prediction Studies, Institute for Climate and Global Change Research, School of Atmospheric Sciences, Nanjing University, Nanjing, China; Lott—Met Office Hadley Centre, Exeter, United Kingdom; Li—CAS Key Laboratory of Regional Climate–Environment for Temperate East Asia, Institute of Atmospheric Physics, Chinese Academy of Sciences, Beijing, China; S. Dong—National Climate Center, Laboratory for Climate Studies, China Meteorological Administration, Beijing, China; Tett—School of Geosciences, University of Edinburgh, Edinburgh, United Kingdom; B. Dong—National Centre for Atmospheric Science, Department of Meteorology, University of Reading, Reading, United Kingdom; Sun—National Climate Center, Laboratory for Climate Studies, China Meteorological Administration, Beijing, and China Collaborative Innovation Center on Forecast and Evaluation of Meteorological Disasters, Nanjing University of Information Science and Technology, Nanjing, China

CORRESPONDING AUTHOR: Wei Li, weili@nuist.edu.cn

DOI:10.1175/BAMS-D-19-0147.1

A supplement to this article is available online (10.1175/BAMS-D-19-0147.2)

storms (Burke et al. 2016). Furthermore, understanding how anthropogenic forcings affect the duration and intensity of heavy rainfall events is important (e.g., Burke and Stott 2017). This study examines how human activities have affected persistent heavy and daily extreme rainfalls in 2018 summer over central western China.

DATA AND METHODS. The 2018 rainfall event was largely confined to 30°–38°N, 100°–110°E (black

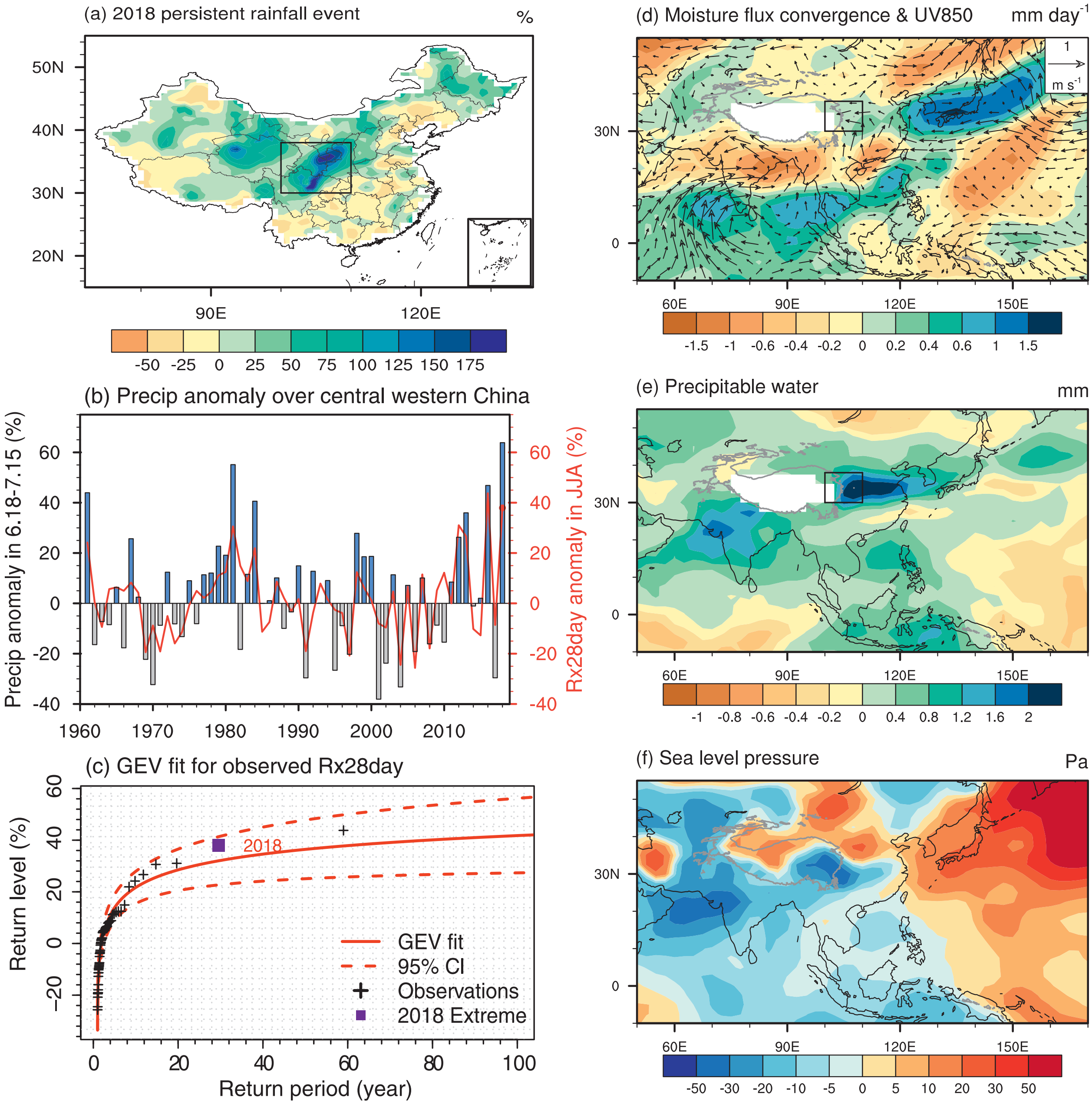
(a) 2018 persistent rainfall event

(b) Precip anomaly over central western China

(c) GEV fit for observed Rx28day

(d) Moisture flux convergence & UV850

(e) Precipitable water

(f) Sea level pressure

FIG. 1. (a) Observed rainfall anomalies accumulated during 18 Jun to 15 Jul 2018 relative to the 1961–2010 climatology over the same period (%). The black box denotes central western China (30°–38°N, 100°–110°E). (b) Time series of accumulated rainfall during 18 Jun to 15 Jul (bar) and Rx28day for June to August (red line) for the black box in (a), in percentage anomalies relative to 1961–2010. (c) GEV fit (red line) of observed Rx28day with 95% confidence intervals. The crosses are estimated from the empirical distributions of the observed Rx28day with the purple square denoting the 2018 event. Also shown are the regression of (d) column integrated moisture convergence (shading; mm day^{-1}) and 850-hPa horizontal winds (vector; m s-1), (e) total column water vapor (mm), and (f) sea level pressure (Pa) onto standardized rainfall anomalies over central western China during 18 Jun to 15 Jul for 1961–2018.

box in Fig. 1a). Gridded daily rainfall observations (0.5° × 0.5°) for 1961–2018 are from the China Meteorological Administration, using ~2400 stations over China with rigorous quality control (Shen et al. 2010). Daily circulation fields are from the NCEP–NCAR Reanalysis 1 (2.5° × 2.5°; Kalnay et al. 1996).

We use the latest Met Office HadGEM3-GA6-based attribution system at N216 resolution (hereafter simply HadGEM3-A; ~60 km at midlatitudes; Ciavarella et al. 2018). This attribution system comprises a pair of multidecadal ensembles, one with both natural and anthropogenic forcings (Historical) and the other with time-varying natural forcings and all anthropogenic forcings fixed at 1850 levels (HistoricalNat) and are described in the online supplemental material. The 2018 ensembles (termed HistoricalExt and HistoricalNatExt) are used in the attribution analysis.

We investigate the duration and intensity of heavy rainfall. The persistent heavy rainfall event is defined as the maximum accumulated rainfall over two to four weeks from June to August (hereafter Rx14day, Rx21day, and Rx28day), to avoid selection biases in the duration of events and test the robustness of the results. These three indices in 2018 summer were observed to be the second highest on record since 1961. The daily extremes are represented by the maximum 1-day and 3-day rainfalls (Rx1day, Rx3day), which, in summer 2018, were the fifth and third most extreme on record. Here Rx1day is defined as the summer maximum of regional average daily rainfall, considering that the occurrence of the Rx1day total in 2018 was associated with and occurred during the persistent rainfall. We mainly show results for Rx28day and Rx1day for conciseness.

As the model overestimates rainfall amount over this region compared to observations by 13% for the 1961–2010 climatology (see Figs. S1a,b in the online supplemental material), indices are normalized. We employ two methods of normalization. 1) RxNday (N = 1, 3, 14, 21, 28) is expressed as a percentage anomaly relative to the 1961–2010 climatology of RxNday. The Rx28day (Rx1day) in summer 2018 is 38% (27%) above the corresponding 1961–2010 climatology. 2) Daily rainfall is divided by the 1961–2010 June to August mean rainfall and then RxNday is computed (expressed in %). Thus, the intensity of Rx28day (Rx1day) in 2018 is 1.9 (5.5) times of the summer daily rainfall climatology. The two methods of normalization effectively correct the wet bias in the simulated rainfall indices (Figs. S2a–c). We show the results based on the first method of normalization in Figs. 2a–g. The two methods yield quantitatively consistent results (Figs. S2d–f), confirming the robustness of our results.

As the normalization only corrects the model climatologies of rainfall indices, we further evaluate the simulated heavy rainfall variability against observations using a Kolmogorov–Smirnoff (K-S) test. We fit the generalized extreme value (GEV) distribution to the rainfall indices and use it to estimate the occurrence probability and return periods for both observations and simulations. To estimate the changing likelihood due to anthropogenic forcing, the risk ratio (RR = P_{ALL}/P_{NAT}) is calculated using the GEV fit, which compares the occurrence probability between the HistoricalExt under all forcings (P_{ALL}) and HistoricalNatExt under natural forcings only (P_{NAT}). The risk ratio uncertainty is estimated via bootstrapping 1000 times, by resampling all ensemble members with replacement, and we show, as bracketed ranges after the value, the 5–95th percentiles of the empirical distribution throughout.

RESULTS.

The observed Rx28day in summer 2018 (38% above climatology) corresponds to a 1-in-60-yr event in the observed records, based on the GEV fits (Fig. 1c). This type of anomalous rainfall, associated with enhanced moisture convergence, is primarily driven by enhanced low-level southerly winds carrying warm moist air from the western Pacific. This in turn is associated with the intensification and westward extension of WNPSH, and anomalous atmospheric moisture availability (Figs. 1d,f).

It is crucial for the model to realistically reproduce the large-scale circulations responsible for rainfall events. Here we evaluate the simulated summer mean rainfall and circulation interannual variability, which gives a background relevant to persistent heavy rainfalls. For interannual variations, HadGEM3-A captures the large-scale circulation anomalies responsible for the anomalous rainfall in the target region well. In both model and observations, heavy rainfall is associated with low-level anticyclonic anomalies from eastern China to the western Pacific, favoring southwesterly moisture transport to this region (Figs. S1c,d). Burke and Stott (2017) report that HadGEM3-A can reproduce the main features of the East Asian summer monsoon (EASM), although the simulated mean WNPSH and EASM circulation is weaker and shifted east compared with observations (Figs. S1a,b; Rodríguez et al. 2017). Thus, the model generally reproduces the physical processes related to seasonal rainfall anomalies, which are relevant to persistent heavy rainfalls examined in this study.

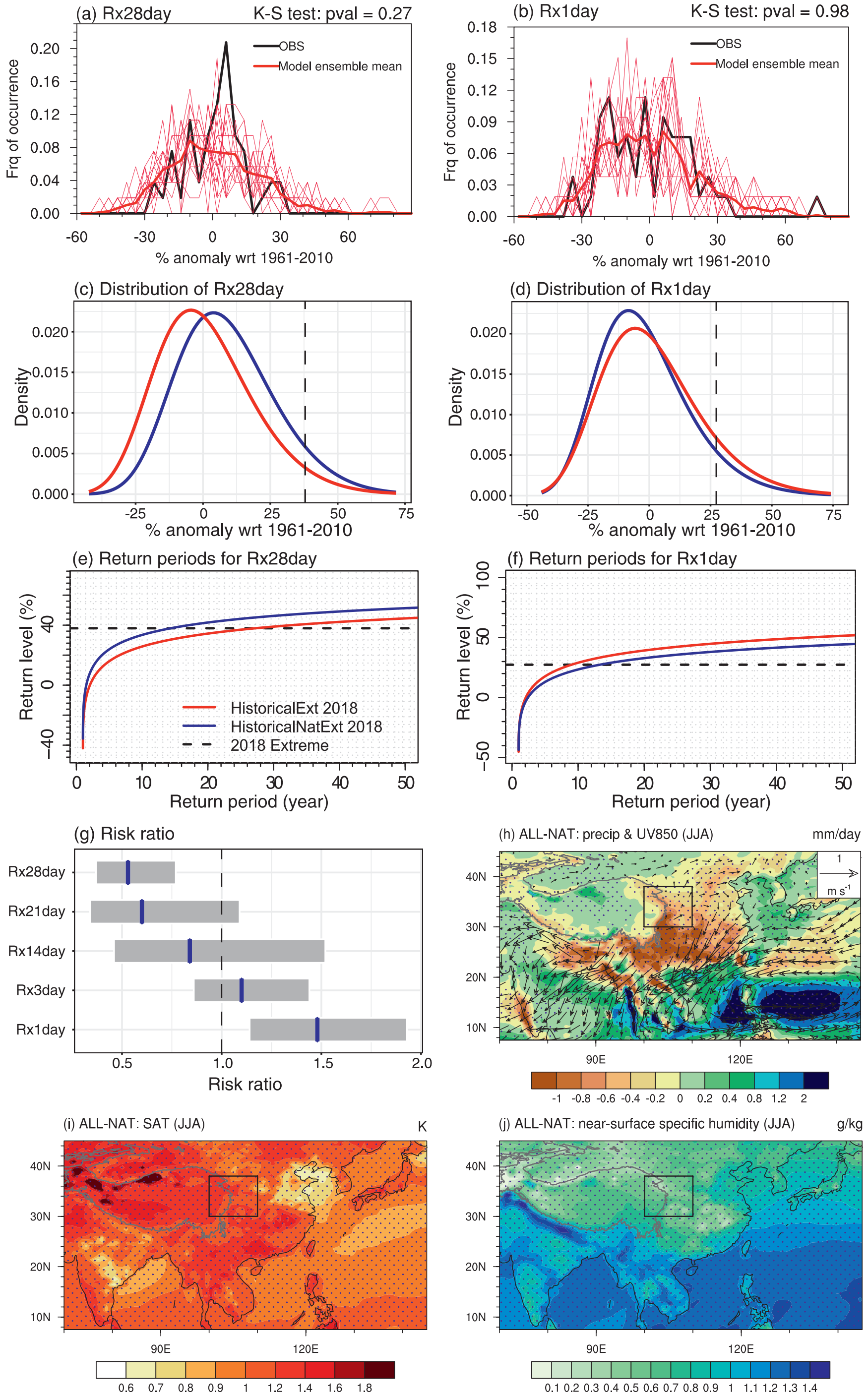

Fig. 2. (a),(b) Distributions of normalized Rx28day and Rx1day for observations (black) and Historical all-forcing simulations (red) for 1961–2013. The thin red lines denote individual members. The p values for the K-S test are shown at top right. (c),(d) GEV fits and (e),(f) return periods of normalized Rx28day and Rx1day for HistoricalExt (red) and HistoricalNatExt (blue) 2018 simulations. The dashed black lines denote the observed event in 2018. (g) The best estimates (blue lines) and 90% confidence intervals (gray shadings) of risk ratio for different rainfall indices. Also shown are multi-member mean differences of JJA mean rainfall and (h) 850-hPa winds, (i) near-surface air temperature, and (j) specific humidity between HistoricalExt and HistoricalNatExt ensembles. Dots indicate 10% significance level for the shaded fields.

The distributions of normalized heavy rainfall in the model and observations cannot be distinguished using the K-S test (p value > 0.05; Figs. 2a,b). We then compare the distributions of heavy rainfall in the HistoricalExt and HistoricalNatExt ensembles for 2018. For Rx28day, there is a shift toward weaker events if anthropogenic forcing is included, indicating a reduced probability of persistent heavy rainfalls (Figs. 2c,e). P_{NAT} for Rx28day > 38% above climatology is 0.070 (0.055–0.083), which reduces to 0.037 (0.028–0.046) for P_{ALL}. This gives a risk ratio of 0.53 (0.37–0.77; Fig. 2g), implying that the likelihood of the persistent heavy rainfall with a magnitude similar to 2018 summer in central western China is reduced by approximately 47% due to anthropogenic forcing by the best estimate.

For daily extremes, however, the distribution shifts toward intense events in HistoricalExt compared to HistoricalNatExt (Fig. 2d). Hence, anthropogenic forcing has increased the probability of Rx1day like that in summer 2018 from 0.075 (0.060–0.088) for P_{NAT} to 0.111 (0.091–0.128) for P_{ALL}, along with shortened return periods (Fig. 2f). This gives a risk ratio of 1.48 (1.14–1.93; Fig. 2g).

Thus, anthropogenic forcing has reduced the probability of persistent heavy rainfalls, but increased that of daily extremes. The risk ratio remains above one for Rx1day and decreases consistently as the duration of heavy rainfall increases (Fig. 2g).

Then why has anthropogenic forcing caused opposite changes in the probabilities of persistent heavy and daily extremes? Largely fueled by moisture convergence, the intensification of daily extreme rainfall is related to atmospheric moistening as temperature rises under anthropogenic forcing (Figs. 2i,j; Allen and Ingram 2002; Trenberth et al. 2003).

The weakened persistent heavy rainfalls under anthropogenic forcing are consistent with the significantly reduced EASM rainfall, due to the weakened EASM circulation (Fig. 2h). Thus, the weakened background mean circulations in response to anthropogenic forcing are unfavorable for summer persistent heavy rainfalls in central western China.

Further disentangling the contributions from greenhouse gases (GHG) and other anthropogenic forcings, specifically aerosols, would improve understanding of the attribution outcome (e.g., Rimi et al. 2019; Kumari et al. 2019). Despite the lack of separate forcing experiments from HadGEM3-A, we suspect that the weakening of the EASM and persistent heavy rainfalls due to anthropogenic forcings is largely induced by aerosols. These overwhelm the GHG-induced intensification of EASM and heavy rainfalls, based on physical understandings established in many previous studies using the CMIP5 ensemble (Song et al. 2014; Li et al. 2015; Zhang and Li 2016) and single models (Burke and Stott 2017; Tian et al. 2018).

However, with the future reductions in aerosols and continued increases in GHG, the probabilities of both daily and persistent heavy rainfalls in central western China would robustly increase, along with a wetter EASM, according to the CMIP5 ensemble (Table S1 and Figs. S2g–i; future projections directly comparable to the HadGEM3-A attribution runs are not available). This is consistent with previous studies indicating a general intensification in EASM circulation (Christensen et al. 2013; Wang et al. 2014) and persistent extreme rainfalls in East Asia (Chevuturi et al. 2018) under future warming. As such, the attribution outcome for the present day is not a simple analog for the future climate and the adverse impact of GHG-induced warming on flooding risks may exacerbate in the future.

We repeat our analysis with the northern boundary of the region modified from 38° to 40°N and find similar risk ratios. However, the model's ability to capture the persistent heavy rainfall variability decreases. This is possibly because the larger region additionally includes different climate regimes (cf. dashed and solid boxes in Fig. S1a), adding complexity to the rainfall variations. It implies the importance of selecting regions based on physical considerations (e.g., climate regimes) when testing the spatial scales.

CONCLUSIONS. We show that anthropogenic forcing has opposing contributions to the probabilities of persistent and daily heavy rainfalls in the current climate. Anthropogenic forcing has reduced the probability of 2018 summer persistent heavy rainfall in central western China by ~47%, but increased that of daily extremes by ~1.5 times. This result is robust against different choices of events and methods of normalization. While it is a caveat of the study that the attribution results are based on a single-model ensemble, the model's ability to generally reproduce the large-scale circulation anomalies related to seasonal rainfall anomalies enhances the confidence in the results.

However, the attribution result for the present day is not analogous to what may be experienced in future with reduced aerosols, making decision-making for floods in this region more challenging. The current state-of-the-art climate models actually project increasing probabilities of both daily and persistent heavy rainfalls in this region. Further disentangling the contributions of GHG and anthropogenic aerosols on the risks of heavy rainfall, as well as quantification of future risks, needs to be explored more.

ACKNOWLEDGMENTS. W. Z., W. L., and Y. S. were funded by the National Key R&D Program of China (2018YFC1507702, 2018YFC1507701), W. Z. was also funded by National Natural Science Foundation of China (41905064), W. L. was also funded by National Natural Science Foundation of China (41905078), L. Z. was funded by the National Key R&D Program of China (2017YFA0603804) and China Meteorological Administration Special Public Welfare Research Fund (GYHY201306024), Y. M. was funded by National Natural Science Foundation of China (41822501, 41805116), L. Y. was funded by National Key R&D Program of China (2018YFA0606003) and National Natural Science Foundation of China (41875124), C. L. was funded by National Natural Science Foundation of China (41790475). SFBT and BD funded by the RICHES project of the U.K.-China Research and Innovation Partnership Fund. This study was largely carried out during a workshop on Operational Attribution at the National Climate Centre sponsored by the U.K.-China Research and Innovation Partnership Fund through the Met Office Climate Science for Service Partnership (CSSP) China as part of the Newton Fund and the National Key R&D Program of China (2018YFC1507702). We thank Dr. Tianjun Zhou, Dr. Lixia Zhang, and Dr. Xiaolong Chen for their comments that helped improve this paper.

REFERENCES

Allen, M. R., and W. J. Ingram, 2002: Constraints on future changes in climate and the hydrologic cycle. *Nature*, **419**, 228–232, https://doi.org/10.1038/nature01092.

Burke, C., and P. Stott, 2017: Impact of anthropogenic climate change on the East Asian summer monsoon. *J. Climate*, **30**, 5205–5220, https://doi.org/10.1175/JCLI-D-16-0892.1.

——, ——, A. Ciavarella, and Y. Sun, 2016: Attribution of extreme rainfall in southeast China during May 2015 [in "Explaining Extreme Events of 2015 from a Climate Perspective"]. *Bull. Amer. Meteor. Soc.*, **97** (12), S92–S96, https://doi.org/10.1175/BAMS-D-16-0144.1.

Chen, B., and X. Xu, 2016: Spatiotemporal structure of the moisture sources feeding heavy precipitation events over the Sichuan Basin. *Int. J. Climatol.*, **36**, 3446–3457, https://doi.org/10.1002/joc.4567.

Chevuturi, A., N. P. Klingaman, A. G. Turner, and S. Hannah, 2018: Projected changes in the Asian-Australian monsoon region in 1.5°C and 2.0°C global-warming scenarios. *Earth's Future*, **6**, 339–358, https://doi.org/10.1002/2017EF000734.

Christensen, J. H., and Coauthors, 2013: Climate phenomena and their relevance for future regional climate change. Climate Change 2013: The Physical Science Basis. T. F. Stocker et al., Eds., Cambridge University Press, 1217–1308.

Ciavarella, A., and Coauthors, 2018: Upgrade of the HadGEM3-A based attribution system to high resolution and a new validation framework for probabilistic event attribution. *Wea. Climate Extremes*, **20**, 9–32, https://doi.org/10.1016/j.wace.2018.03.003.

Dong, H., S. Zhao, and Q. Zeng, 2007: A study of influencing systems and moisture budget in a heavy rainfall in low latitude plateau in China during early summer. *Adv. Atmos. Sci.*, **24**, 485–502, https://doi.org/10.1007/s00376-007-0485-z.

Kalnay, E., and Coauthors, 1996: The NCEP/NCAR 40-Year Reanalysis Project. *Bull. Amer. Meteor. Soc.*, **77**, 437–471, https://doi.org/10.1175/1520-0477(1996)077<0437:TNYRP>2.0.CO;2.

Kumari, S., K. Haustein, H. Javid, C. Burton, M. R. Allen, H. Paltan, S. Dadson, and F. E. L. Otto, 2019: Return period of extreme rainfall substantially decreases under 1.5°C and 2.0°C warming: A case study for Uttarakhand, India. *Environ. Res. Lett.*, **14**, 044033, https://doi.org/10.1088/1748-9326/ab0bce.

Li, X., M. Ting, C. Li, and N. Henderson, 2015: Mechanisms of Asian summer monsoon changes in response to anthropogenic forcing in CMIP5 models. *J. Climate*, **28**, 4107–4125, https://doi.org/10.1175/JCLI-D-14-00559.1.

Rimi, R. H., K. Haustein, M. R. Allen, and E. J. Barbour, 2019: Risks of pre-monsoon extreme rainfall events of Bangladesh: Is anthropogenic climate change playing a role? [in "Explaining Extreme Events of 2017 from a Climate Perspective"]. *Bull. Amer. Meteor. Soc.*, **100** (1), S61–S65, https://doi.org/10.1175/BAMS-D-18-0152.1.

Rodríguez, J. M., S. F. Milton, and C. Marzin, 2017: The East Asian atmospheric water cycle and monsoon circulation in the Met Office Unified Model. *J. Geophys. Res. Atmos.*, **122**, 102246–102265, https://doi.org/10.1002/2016JD025460.

Shen, Y., A. Xiong, Y. Wang, and P. Xie, 2010: Performance of high-resolution satellite precipitation products over China. *J. Geophys. Res.*, **115**, D02114, https://doi.org/10.1029/2009JD012097 .

Song, F., T. Zhou, and Y. Qian, 2014: Responses of East Asian summer monsoon to natural and anthropogenic forcings in the 17 latest CMIP5 models. *Geophys. Res. Lett.*, **41**, 596–603, https://doi.org/10.1002/2013GL058705.

Tian, F., B. Dong, J. Robson, and R. Sutton, 2018: Forced decadal changes in the East Asian summer monsoon: The roles of greenhouse gases and anthropogenic aerosols. *Climate Dyn.*, **51**, 3699–3715, https://doi.org/10.1007/s00382-018-4105-7.

Trenberth, K. E., A. Dai, R. M. Rasmussen, and D. B. Parsons, 2003: The changing character of precipitation. *Bull. Amer. Meteor. Soc.*, **84**, 1205–1217, https://doi.org/10.1175/BAMS-84-9-1205.Ueno, K., S. Sugimoto, T. Koike, H. Tsutsui, and X. Xu, 2011: Generation processes of mesoscale convective systems following midlatitude troughs around the Sichuan Basin. *J. Geophys. Res.*, **116**, D02104, https://doi.org/10.1029/2009JD013780.

Wang, B., S.-Y. Yim, J.-Y. Lee, J. Liu, and K.-J. Ha, 2014: Future change of Asian-Australian monsoon under RCP 4.5 anthropogenic warming scenario. *Climate Dyn.*, **42**, 83–100, https://doi.org/10.1007/s00382-013-1769-x.

Xiang, S., Y. Li, D. Li, and S. Yang, 2013: An analysis of heavy precipitation caused by a retracing plateau vortex based on TRMM data. *Meteor. Atmos. Phys.*, **122**, 33–45, https://doi.org/10.1007/s00703-013-0269-1.

Zhang, L., and T. Li, 2016: Relative roles of anthropogenic aerosols and greenhouse gases in land and oceanic monsoon changes during past 156 years in CMIP5 models. *Geophys. Res. Lett.*, **43**, 5295–5301, https://doi.org/10.1002/2016GL069282.

Zhou, T., and R. Yu, 2005: Atmospheric water vapor transport associated with typical anomalous summer rainfall patterns in China. *J. Geophys. Res.*, **110**, D08104, https://doi.org/10.1029/2004JD005413.

CONDITIONAL ATTRIBUTION OF THE 2018 SUMMER EXTREME HEAT OVER NORTHEAST CHINA: ROLES OF URBANIZATION, GLOBAL WARMING, AND WARMING-INDUCED CIRCULATION CHANGES

Chunlüe Zhou, Deliang Chen, Kaicun Wang, Aiguo Dai, and Dan Qi

The probability of the record-breaking summer heat of 2018 over Northeast China was increased by a combination of human-caused climate change influences on thermodynamics and circulation, and urbanization.

The averaged near-surface air temperature (T_a) of July–August 2018 over Northeast China is ~1.73°C above the 1971–2000 mean, the highest since 1961. One-third of the stations in the region broke the historical record (Figs. 1a,b), which posed a great threat to local ecosystems and human health because this region has seldom experienced such extreme heats in previous decades (Chen et al. 2019).

In addition to influences from global warming, summer hot days over Northeast China are typically accompanied by local anticyclonic anomalies (Chen et al. 2019; Wu et al. 2011), which provide favorable conditions for increased solar radiation-induced diabatic heating due to reduced cloud cover and subsidence-induced adiabatic heating (Chen and Lu 2015; He et al. 2018). Therefore, relative contributions from atmospheric circulation anomaly and global warming to the probability of such extreme summer heats are first investigated.

More importantly, we further quantify contributions of warming-induced circulation changes to such summer heats. Global warming may induce atmospheric circulation changes, which in turn can influence the intensity and frequency of heat waves (Horton et al. 2015; Zhou et al. 2019). However, few studies have quantified this effect, likely due to weak signal of climate change compared with large natural variability in atmospheric circulation. Thanks to the acceptable performance of CMIP5-simulated circulations at monthly time scales (see Figs. ES1 and ES2 in the online supplemental material), we make such an attempt to estimate the contribution from warming-induced circulation changes to the 2018 summer heat. Besides, the urban heat island effect makes T_a over urban areas higher than that of rural regions (Zhou et al. 2019), which could intensify summer heat. The contribution from urbanization to the 2018 summer heat is also examined in this study.

Therefore, this study tries to answer three questions: 1) What does the extreme summer heat of 2018 over Northeast China look like in a historical context? 2) How much does an anticyclone contribute to the 2018 summer heat? 3) What are relative roles of urbanization, global warming, and warming-induced circulation changes in forming the 2018 summer heat?

DATA AND METHODS. Daily T_a from 1961 to 2018 at ~690 meteorological stations over Northeast China (Fig. 1a) were collected (http://data.cma.cn/). The T_a dataset has undergone quality control tests including outlier and duplicates identification, and spatial and temporal consistency checks (Zhou et al. 2018).

AFFILIATIONS: Zhou and Dai—Department of Atmospheric and Environmental Sciences, University at Albany, State University of New York, Albany, New York;Chen—Regional Climate Group, Department of Earth Sciences, University of Gothenburg, Gothenburg, Sweden; Wang—College of Global Change and Earth System Science, Beijing Normal University, Beijing, China; Qi—National Meteorological Center, China Meteorological Administration, Beijing, China

CORRESPONDING AUTHOR: Dr. Chunlüe Zhou, chunluezhou@gmail.com

DOI:10.1175/BAMS-D-19-0197.1

A supplement to this article is available online (10.1175/BAMS-D-19-0197.2)

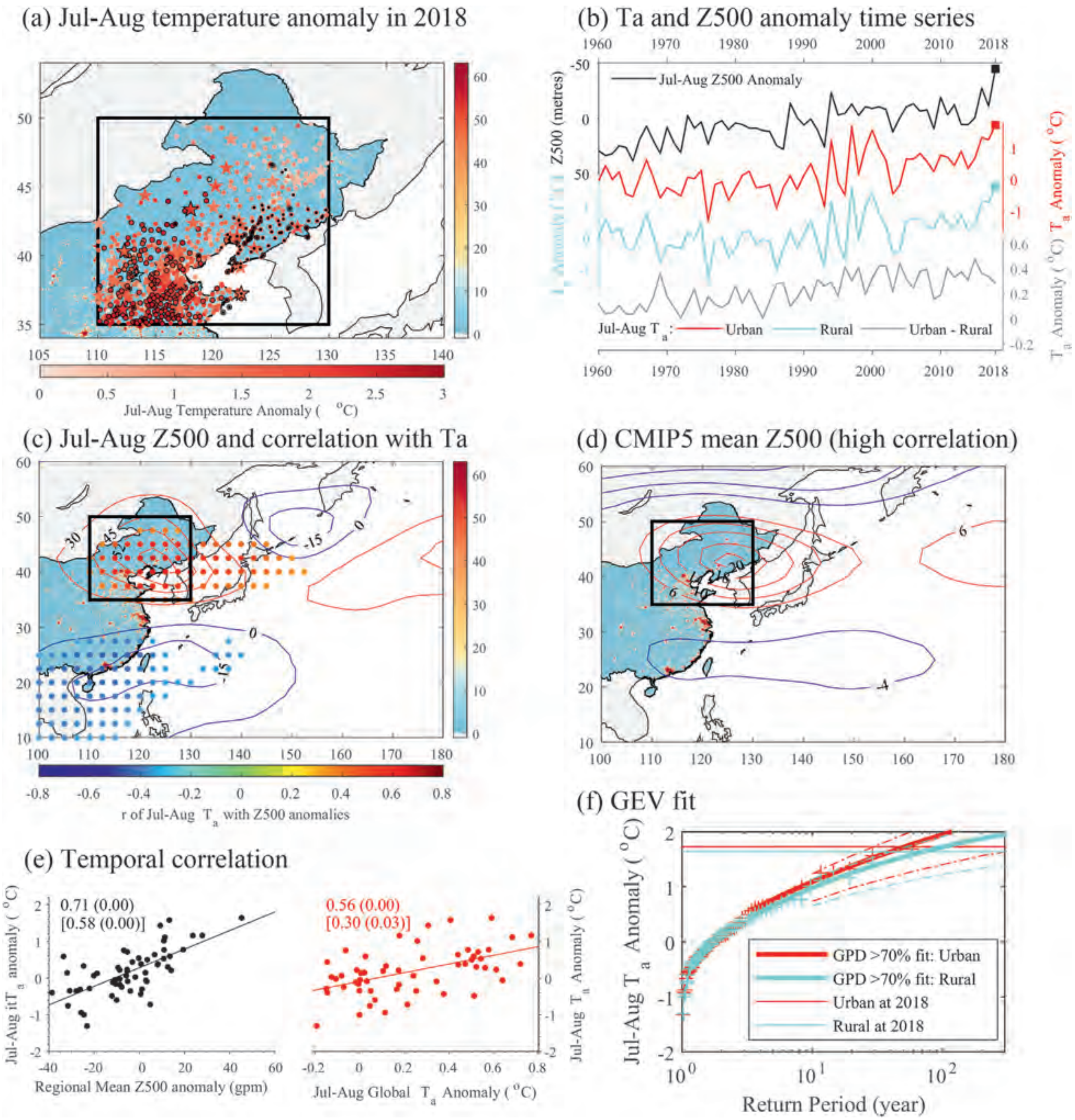

Fig. 1. (a) Spatial pattern of the observed July–August temperature (T_a) anomalies in 2018 over Northeast China. Stations having record-breaking July–August (daily) temperatures in 2018 summer since 1961 are marked with black edges (dots). Urban and rural stations are plotted as color-filled circles and pentagrams. (b) Time series of Z500 anomalies (in black) over the study region, and T_a over urban (in red), rural regions (in cyan) and their difference (in light black), relative to the period 1971–2000. Squares represents broken records in 2018. (c) Circulation regime in July–August 2018 (in red/blue contours). Correlations between the detrended region-averaged T_a and gridded Z500 are shown as color-filled circles ($p < 0.01$). (d) CMIP5-multi-ensemble-mean Z500 anomalies under high-correlation regimes from 40 ALL simulations. (e) Scatterplots of T_a with Z500 and global-mean T_a. Correlations were calculated before and after detrending (coefficients and significance levels in square brackets). (f) GDP fit (in solid) of T_a.

Based on Ren et al. (2015) and Zhou et al. (2019), 30 rural stations (stars in Fig. 1a) were identified in comparison with urban stations for quantifying the effect of urbanization (Sun et al. 2016). The latest stable night lights in 2013 from the Defense Meteorological Satellite Program (http://ngdc.noaa.gov/eog/

dmsp) were further used to show urban (light index >15) and rural regions (≤ 15). The July–August 2018 circulation anomaly regime (Fig. 1c) was depicted by the 2.5° × 2.5°500-hPa geopotential height ($Z500$) from NCEP-R1 (https://www.esrl.noaa.gov/) (Kalnay et al. 1996).

CMIP5 model outputs (http://cmip-pcmdi.llnl.gov/cmip5/) (Taylor et al. 2012) were used to quantify human influences on the probability of the 2018 summer heat. We first tested probability distributions of July–August T_a and $Z500$ anomalies from the CMIP5 historical all-forcings (ALL) simulations against observations via a Kolmogorov–Smirnov test ($p > 0.05$). Second, we assessed and selected the ALL simulations with a significant positive temporal correlation ($p < 0.05$) between the detrended July–August T_a and $Z500$ anomalies. As a result, 40 out of 54 simulations from 11 models were selected for this study, with the ALL runs extended through 2018 using the RCP4.5 runs (58 × 40 samples) and the corresponding natural-forcings-only runs (NAT) ending in 2012 (52 × 40 samples; Table ES1). Detailed time series can be seen in Fig. ES1.

To separate contributions from global warming and warming-induced circulation changes to the probability of the 2018 summer heat, following Christidis and Stott (2015), we defined years with CMIP5-based circulation regimes in individual model runs similar to the observed in July–August 2018 (i.e., a deep anticyclone within black rectangle in Fig. 1c) as high correlation years (pattern correlation ≥ 0.5; CMIP5 multimodel mean $Z500$ anomalies in Fig. 1d; more details in Fig. ES2), and defined neutral years with pattern correlations of -0.1 to 0.1. We realized that global warming in ALL runs will increase $Z500$ over most of globe including Northeast China, and such a background change in $Z500$ may not necessarily intensity the anomalous anticyclonic circulation over Northeast China, which requires further investigation. Therefore, the $Z500$ anomalies gradient was adopted to provide a better measure of the change in the circulation strength in this study.

To be consistent, observation and model data were converted into anomalies relative to the 1971–2000 mean; first regridded onto thirty 2.5° × 2.5° grids and then area-averaged over the study region (110°–130°E, 35°–50°N; Fig. 1a). Several statistical techniques were exploited:

1) Following Schaller et al. (2016), generalized Pareto distribution (GPD) with a properly selected threshold was used to fit the July–August T_a and $Z500$ anomalies.
2) The probability ratio [$\mathrm{PR1} = P_{(\text{Ta-urban}|\text{urban})}/P_{(\text{Ta-urban}|\text{rural})}$] was first calculated to quantify the urbanization effect on the likelihood of the 2018 summer heat (defined as ≥1.73°C averaged in urban regions over Northeast China). Here, $P_{(\text{Ta-urban}|\text{urban})}$ and $P_{(\text{Ta-urban}|\text{rural})}$ represent the probabilities of T_a anomalies exceeding 1.73°C in urban and rural scenarios.
3) After excluding the urban heat island effect, another $\mathrm{PR2} = P_{(\text{Ta-rural}|\text{ALL-high}Z500)}/P_{(\text{Ta-rural}|\text{ALL-neutral}Z500)}$ was calculated to estimate the role of an anticyclone existence in the probability of the 2018 summer heat. Here, $P_{(\text{Ta-rural}|\text{ALL-high}Z500)}$ and $P_{(\text{Ta-rural}|\text{ALL-neutral}Z500)}$ represent the probabilities of T_a anomalies to exceed 1.64°C (averaged in rural regions) under the high and neutral $Z500$ regimes in the ALL runs. $\mathrm{PR3} = P_{(\text{Ta-rural}|\text{ALL-high}Z500)}/P_{(\text{Ta-rural}|\text{NAT-high}Z500)}$] was used to quantify the influence of global warming (i.e., human-induced thermodynamical contribution). To further quantitively estimate the role of anthropogenic warming-induced circulation changes (i.e., human-induced dynamical contribution), we applied Bayesian statistics (Gelman et al. 2013; Yiou 2017) to modify PR as $\mathrm{PR4} = [P_{(\text{ALL-high}Z500)}/P_{(\text{NAT-high}Z500)}]\cdot[P_{(\text{high}Z500|\text{NAT-Ta-rural})}/P_{(\text{high}Z500|\text{ALL-Ta-rural})}]$. Here, $P_{(\text{Ta-rural}|\text{NAT-high}Z500)}$ represents the probability of T_a anomaly to exceed 1.64°C under the high $Z500$ regime in NAT runs; and $P_{(\text{high}Z500|\text{ALL-Ta-rural})}$ and $P_{(\text{high}Z500|\text{NAT-Ta-rural})}$ represent the probabilities of circulation anomaly regimes similar to the 2018 observed regime when such extreme summer heats (≥1.64°C) occur in ALL and NAT runs. 95% confidence intervals (CI) were estimated with a 1000-member bootstrap (with replacement) .

RESULTS. *Role of the anticyclone.* In 2018 summer, the 5,880-m contour of the western Pacific subtropical high moved northwestward and brought the record-breaking anticyclone anomaly over Northeast China (black square in Fig. 1b) , leading to the record-breaking summer heat of 2018 over both urban and rural areas (Figs. 1a,b). New daily T_a records were registered at stations near the center of the anomalous anticyclone (black dots in Fig. 1a). Figure 1c shows strong correlations between the detrended July–August T_a and $Z500$ anomalies (associated with local anticyclones) with correlation coefficient (r) of 0.71 ($p = 0.00$) in the study region (Fig. 1e).

The likelihoods of the 2018 summer heat in high-correlation years (with the pattern shown in Fig. 1d) and neutral years in ALL runs are 11% (20 out of 224 samples) and 2% (8 out of 437 samples), respectively

(Fig. 2a). In other words, an anomalous anticyclone could increase the PR to 6 (95% CI: 4–9; Fig. 2d).

Influence of urbanization. The record-breaking July–August T_a anomalies of 2018 occurred not only in the urban areas (averaged 1.73°C; black-edged circles in Fig. 1a), but also at rural stations (averaged 1.64°C; black-edged pentagrams in Fig. 1a). A Student's *t* test of temperature differences in 2018 between the 2.5° × 2.5° urban and rural grids shows a significance level of 0.07. The metropolitan area has vast built-up surfaces and frequent human activities, leading to higher temperatures than at rural stations (Fig. 1b). A GPD fit of the observed July–August T_a anomalies suggests that the 2018 extreme summer heat is a 1-in-60-year event (95% CI: 30–500) for the urban regions and a 1-in-80-year event (95% CI: 40–10^5) for the rural regions (Fig. 1f).

Compared with the probabilities of T_a anomaly exceeding 1.73°C in urban and rural scenarios (based on PR1; Fig. 1f), urbanization increases the PR to 1.17 (95% CI: 1–10^2) (Fig. 2e); that is, ~17% increase in the likelihood.

Influences of global warming and warming-induced circulation changes. July–August T_a anomalies over Northeast China significantly correlate with July–August global-mean temperature ($r = 0.56$, $p = 0.00$) (Fig. 1e), implying a strong footprint of global warming on the 2018 summer heat over Northeast China.

Compared with the probabilities of T_a anomaly exceeding 1.64°C under similar circulation regimes in ALL and NAT runs (based on PR3; Fig. 2a), we found that global warming has increases the probability by ~78% (95% CI: 53%–128%; Fig. 2f).

Global warming has been argued to have caused atmospheric circulation changes that have altered regional extreme events in different ways (Horton et al. 2015; Schär et al. 2004; Zhou and Wang 2016), increasing attribution challenge of human-induced dynamical and thermodynamical contributions to odds of the event.

The probabilities of CMIP5-simulated circulation regimes similar to the 2018 observed regime over Northeast China (i.e., with pattern correlations being 0.5 or more) are almost equivalent in ALL and NAT runs (Fig. 2b), but the intensity of the circula-

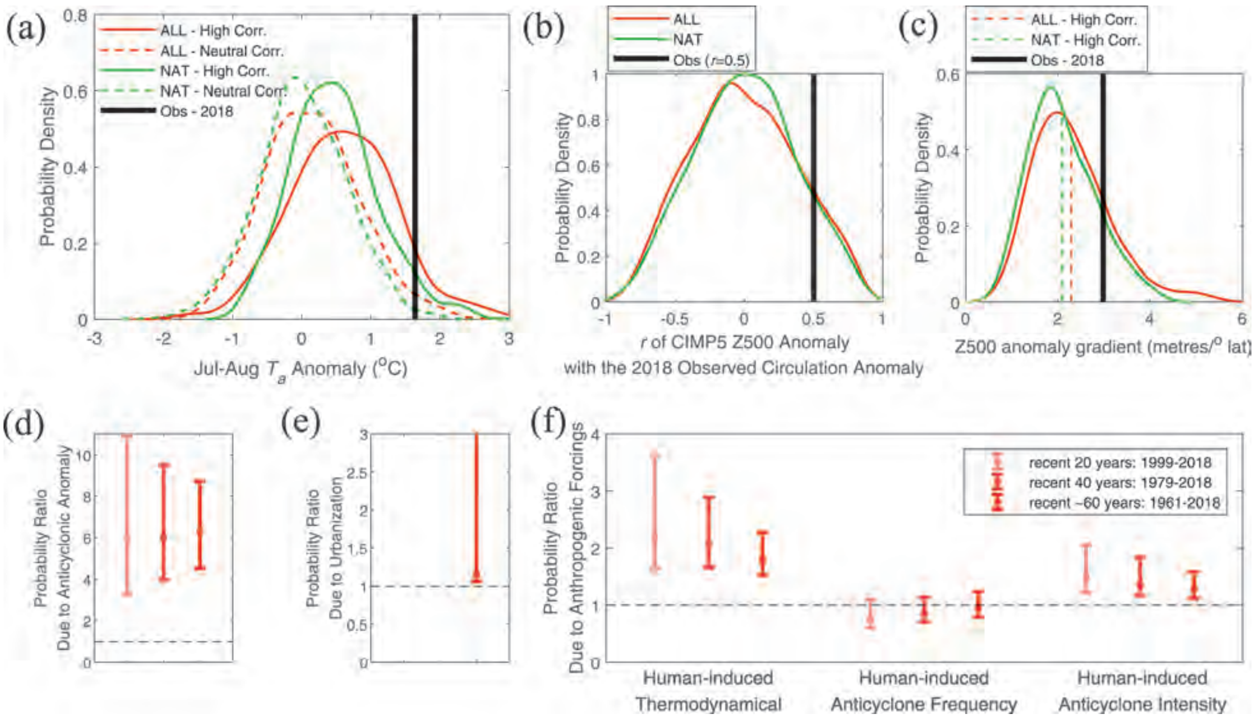

Fig. 2. (a) Probability density of July–August temperature anomalies (T_a) under high (in solid) and neutral (in dash) regimes in 40 all-forcings (ALL; in red) and natural-forcing-only (NAT; in green) simulations. The thick black line is the observed T_a of July–August 2018 over rural regions. (b) Probability density of pattern correlation coefficients (*r*) between CMIP5-based *Z*500 regimes and the 2018 observed regime in ALL/NAT runs. (c) Probability density of *Z*500 anomaly gradients with $r > 0.5$. Dashed lines are their mean. (d) Probability ratio (PR) of the 2018 summer heat due to the occurrence of anticyclone. (e) PR due to urbanization. (f) PR due to human influences from human-induced dynamical (frequency and intensity) and thermodynamical changes.

tion anomalies in high-correlation years increases by ~11% in ALL runs relative to NAT runs (mean of 2.29 vs 2.07 m per degree of latitude described by the *Z*500 anomaly gradient in Fig. 2c). These results imply that global warming has altered the *Z*500 field by strengthening the anomalous anticyclone over Northeast China, which in turn may have enhanced the severity of the 2018 summer heat.

Compared with the probabilities of T_a anomaly exceeding 1.64°C and circulation regimes similar to the 2018 observed regime in ALL and NAT runs (based on PR4), we found that an increased likelihood by ~27% (95% CI: 12%–59%) is attributable to the warming-induced circulation intensity change over Northeast China, while the warming-induced circulation frequency change has no significant impact on the likelihood (Fig. 2f).

CONCLUSIONS AND DISCUSSION. Our analyses based on surface observations and reanalysis fields indicate the record-breaking temperature and circulation anomalies in 2018 summer over Northeast China. Return period of the 2018 summer heat is 1-in-60 years for the urban areas and 1-in-80 years for the rural areas. CMIP5-based analyses suggest that the existence of an anomalous anticyclone over Northeast China increases the odds of the 2018 summer heat to 6.16 times that without such an anticyclone.

Based on the GPD fits, we found that urbanization over the metropolitan areas might have increased the likelihood of the 2018 summer heat by ~17%. After excluding the urbanization effect, CMIP5-based PR analyses suggest that anthropogenic global warming may have increased the probability of the 2018 summer heat over Northeast China by ~78%. Global warming has strengthened the anticyclonic circulation by ~11%, which may have increased the likelihood (by ~27%) of the 2018 summer heat over Northeast China.

In summary, an anomalous anticyclonic circulation over Northeast China was the main cause of the 2018 summer heat. Global warming and warming-induced circulation intensity change have increased the odds, and urbanization has further exacerbated the 2018 summer heat over Northeast China.

The non-stationarity of the time series would consistently increase the attribution uncertainties for all the factors (Figs. 2d,e), but it does not change our main conclusions.

ACKNOWLEDGMENTS. This study was supported by National Key R&D Program of China (2017YFA0603601), the National Natural Science Foundation of China (41525018), the U.S. National Oceanic and Atmospheric Administration (NA18OAR4310425), and the Swedish VR (2017-03780), STINT (CH2015-6226), and MERGE. A. Dai was also supported by the National Science Foundation (AGS-1353740 and OISE-1743738), the U.S. Department of Energy's Office of Science (DE-SC0012602), and the U.S. National Oceanic and Atmospheric Administration (NA18OAR4310425). We thank Dr. Nikos Christidis, Dr. Stephanie Herring, and Dr. Andrew King for their insightful suggestions.

REFERENCES

Chen, R., and R. Lu, 2015: Comparisons of the circulation anomalies associated with extreme heat in different regions of eastern China. *J. Climate*, **28**, 5830–5844, https://doi.org/10.1175/JCLI-D-14-00818.1.

——, Z. Wen, and R. Lu, 2019: Influences of tropical circulation and sea surface temperature anomalies on extreme heat over Northeast Asia in the midsummer of 2018. *Atmos. Oceanic Sci. Lett.*, **12**, 238–245, https://doi.org/10.1080/16742834.2019.1611170.

Christidis, N., and P. A. Stott, 2015: Extreme rainfall in the United Kingdom during winter 2013/14: The role of atmospheric circulation and climate change [in "Explaining Extreme Events of 2014 from a Climate Perspective"]. *Bull. Amer. Meteor. Soc.*, **96** (12), 46–50, https://doi.org/10.1175/BAMS-D-15-00094.1.

Gelman, A., H. S. Stern, J. B. Carlin, D. B. Dunson, A. Vehtari, and D. B. Rubin, 2013: *Bayesian Data Analysis*. 3rd ed. Chapman and Hall/CRC, 675 pp.

He, Y., K. Wang, C. Zhou, and M. Wild, 2018: A revisit of global dimming and brightening based on sunshine duration. *Geophys. Res. Lett.*, **45**, 4281– 4289, https://doi.org/10.1029/2018GL077424.

Horton, D. E., N. C. Johnson, D. Singh, D. L. Swain, B. Rajaratnam, and N. S. Diffenbaugh, 2015: Contribution of changes in atmospheric circulation patterns to extreme temperature trends. *Nature*, **522**, 465–469, https://doi.org/10.1038/nature14550.

Kalnay, E., and Coauthors, 1996: The NCEP/NCAR 40-Year Reanalysis Project. *Bull. Amer. Meteor. Soc.*, **77**, 437–471, https://doi.org/10.1175/1520-0477(1996)077<0437:TNYRP>2.0.CO;2.

Ren, G., and Coauthors, 2015: An integrated procedure to determine a reference station network for evaluating and adjusting urban bias in surface air temperature data. *J. Appl. Meteor. Climatol.*, **54**, 1248–1266, https://doi.org/10.1175/JAMC-D-14-0295.1.

Schaller, N., and Coauthors, 2016: Human influence on climate in the 2014 southern England winter floods and their impacts. *Nat. Climate Change*, **6**, 627–634, https://doi.org/10.1038/nclimate2927.

Schär, C., P. L. Vidale, D. Lüthi, C. Frei, C. Häberli, M. A. Liniger, and C. Appenzeller, 2004: The role of increasing temperature variability in European summer heatwaves. *Nature*, **427**, 332–336, https://doi.org/10.1038/nature02300.

Sun, Y., X. Zhang, G. Ren, F. W. Zwiers, and T. Hu, 2016: Contribution of urbanization to warming in China. *Nat. Climate Change*, **6**, 706–709, https://doi.org/10.1038/nclimate2956.

Taylor, K. E., R. J. Stouffer, and G. A. Meehl, 2012: An overview of CMIP5 and the experiment design. *Bull. Amer. Meteor. Soc.*, **93**, 485–498, https://doi.org/10.1175/BAMS-D-11-00094.1.

Wu, R., S. Yang, S. Liu, L. Sun, Y. Lian, and Z. Gao, 2011: Northeast China summer temperature and North Atlantic SST. *J. Geophys. Res.*, **116**, D16116, https://doi.org/10.1029/2011JD015779.

Yiou, P., 2017: A statistical framework for conditional extreme event attribution. *Adv. Stat. Climataol. Meteor. Oceanogr.*, **3**, 17–31, https://doi.org/10.5194/ascmo-3-17-2017.

Zhou, C., and K. Wang, 2016: Coldest temperature extreme monotonically increased and hottest extreme oscillated over Northern Hemisphere land during last 114 years. *Sci. Rep.*, **6**, 25721, https://doi.org/10.1038/srep25721.

——, Y. He, and K. Wang, 2018: On the suitability of current atmospheric reanalyses for regional warming studies over China. *Atmos. Chem. Phys.*, **18**, 8113–8136, https://doi.org/10.5194/acp-18-8113-2018.

——, K. Wang, D. Qi, and J. Tan, 2019: Attribution of a record-breaking heatwave event in summer 2017 over Yangtze River Delta [in “Explaining Extreme Events of 2017 from a Climate Perspective”].*Bull. Amer. Meteor. Soc.*, **100** (1), S97–S103, https://doi.org/10.1175/BAMS-D-18-0134.1.

EFFECTS OF ANTHROPOGENIC FORCING AND NATURAL VARIABILITY ON THE 2018 HEATWAVE IN NORTHEAST ASIA

Yitian Qian, Hiroyuki Murakami, Pang-Chi Hsu, and Sarah B. Kapnick

The Northeast Asian 2018 heatwave is an *unlikely* event without anthropogenic forcing; only two have occurred over the last 40 years. By 2050 they will become 1-in-4-yr events.

In the summer (July–August) of 2018 a record-breaking heatwave (HW) spread across Northeast Asia (NEA; 34°–40°N, 120°–143°E; Figs. 1a–c). Maximum 2-m air temperature ($T_{\max}$) anomalies over NEA in that summer were about +1.5°C, more than 1.5 standard deviations above the average using the three reanalysis datasets (Fig. 1d). It was the second highest anomaly since 1980. The subtropical high (Tibetan high) in the middle (upper) troposphere moved northwestward (northeastward) with a positive anomaly over NEA (see Figs. ES1a,b in the online supplemental material). An equivalent barotropic structure (Figs. ES1a,b,f) characterized by large-scale subsidence emerged, providing a favorable condition for extreme hot days in NEA (JMA 2018).

Several processes might have contributed to the 2018 HW (Enomoto 2004; Zhu et al. 2011; Lee and Lee 2016). Anthropogenic warming has contributed to increasing HW frequency and intensity in recent decades (Song et al. 2015; Sippel et al. 2016; Oliver et al. 2018). Natural variability can also contribute to HWs over Asia. Anomalous cyclonic circulation over the Indo-Pacific warm pool region inducing more active convection (Fig. ES1e) and diabatic heating could induce high temperature anomalies near NEA through exciting a Rossby wave train (Chen and Lu 2014; Lee and Lee 2016). This teleconnection may result from tropical sea surface temperature anomalies (SSTAs) associated with El Niño–Southern Oscillation (ENSO). Previous studies (e.g., Zhu et al. 2007; Wu et al. 2010; Lee and Lee 2016) identified a negative relationship between NEA summer temperature and the Niño-3.4 index (area-averaged SSTA over 5°S–5°N, 170°–120°W). The Arctic Oscillation (AO) can also influence circulation anomalies over NEA via a strong circumpolar vortex (Fig. ES1f), shifting the location of the subtropical jet farther north (Fig. ES1c; Lee and Lee 2016). Matsumura and Horinouchi (2016) found that a negative Pacific decadal oscillation (PDO) phase with a warmer surface condition near NEA (Fig. ES1e) could lead to a positive geopotential height anomaly, which could also be related to NEA HWs. In this study, we address the impacts of anthropogenic forcing and natural variability (i.e., ENSO, PDO, and AO) on the occurrence of the 2018 NEA HW and quantify future projections of NEA HWs using a large ensemble of simulations from a global coupled model developed at the Geophysical Fluid Dynamics Laboratory (GFDL).

DATA AND METHODS. Daily $T_{\max}$ is taken from three state-of-the-art reanalysis datasets: ERA-

AFFILIATIONS: Qian—Key Laboratory of Meteorological Disaster of Ministry of Education/Collaborative Innovation Center on Forecast and Evaluation of Meteorological Disasters, Nanjing University of Information Science and Technology, China, and National Oceanic and Atmospheric Administration/Geophysical Fluid Dynamics Laboratory, and Atmospheric and Oceanic Sciences Program, Princeton University, Princeton, New Jersey; Murakami—National Oceanic and Atmospheric Administration/Geophysical Fluid Dynamics Laboratory, Princeton, New Jersey and University Corporation for Atmospheric Research, Boulder, Colorado, and; Hsu—Key Laboratory of Meteorological Disaster of Ministry of Education/Collaborative Innovation Center on Forecast and Evaluation of Meteorological Disasters, Nanjing University of Information Science and Technology, China; Kapnick—National Oceanic and Atmospheric Administration/Geophysical Fluid Dynamics Laboratory, Princeton, New Jersey
CORRESPONDING AUTHOR: Pang-Chi Hsu, pangchi@nuist.edu.cn

DOI:10.1175/BAMS-D-19-0156.1

A supplement to this article is available online (10.1175/BAMS-D-19-0156.2)

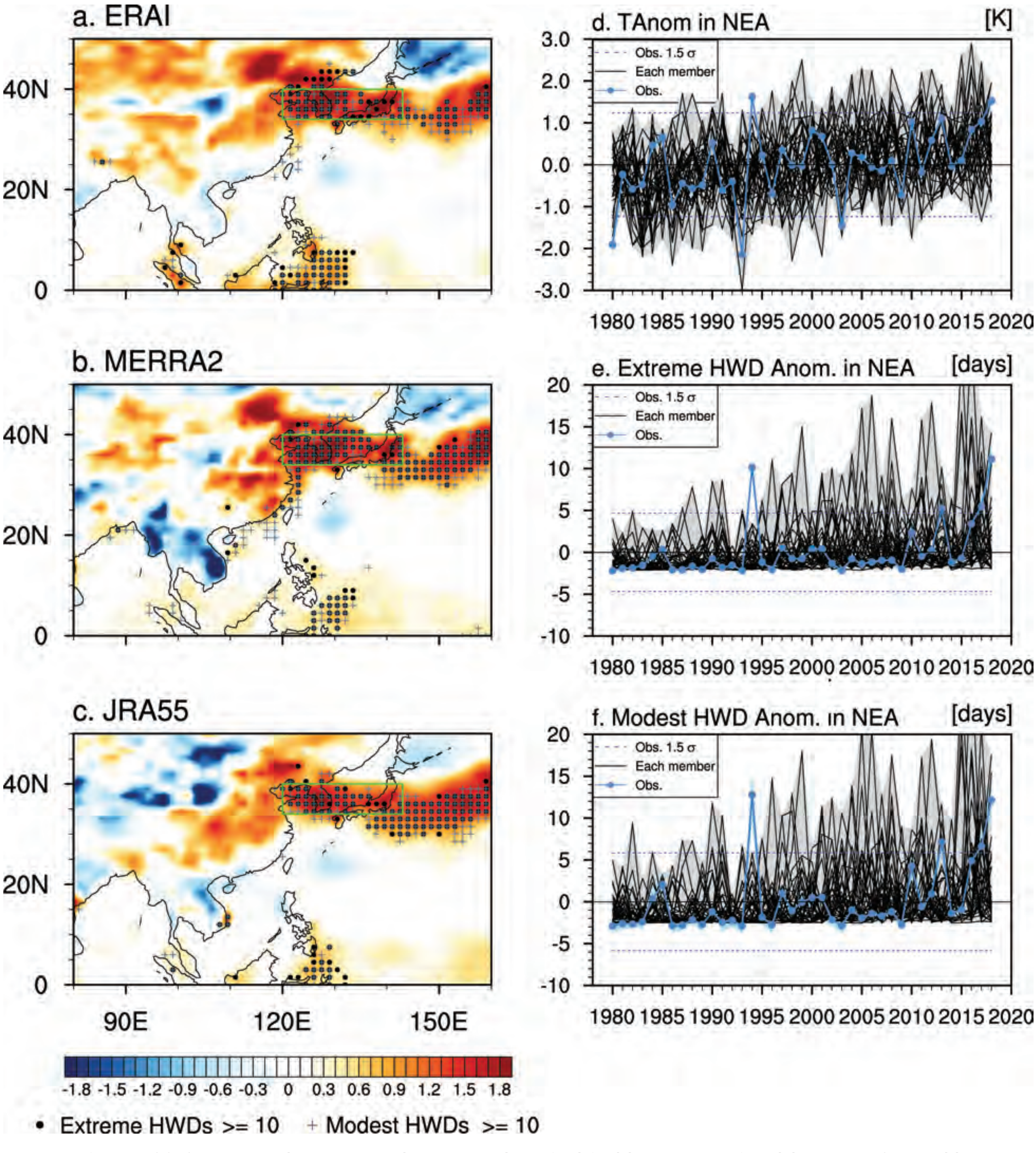

Fig. 1. Daily T_{max} 2018 summer (July–August) anomaly (shading) in (a) ERA-Interim, (b) MERRA2, and (c) JRA55. Black dots (blue pluses) indicate that extreme (modest) HW events occurred for more than 10 days. Interannual variability averaged over NEA (34°–40°N, 120°–143°E; green box in (a)–(c) for (d) daily maximum air temperature anomaly (K), (e) extreme HWD anomaly (days), and (f) modest HWD anomaly (days). Black lines denote individual ensemble members of AllForc (35 total). Blue lines denote the average of three reanalysis datasets (ERA-Interim, MERRA2, and JRA-55). Shadings represent the range from minimum to maximum among the three reanalysis datasets (blue) and 35 ensemble members of AllForc (gray). Blue dashed lines represent ±1.5 standard deviations (σ) of the ensemble mean of the three reanalysis datasets during 1980–2018.

Interim (Dee et al. 2011), MERRA2 (Gelaro et al. 2017), and JRA-55 (Kobayashi et al. 2015). Large-scale atmospheric variables are derived from ERA-Interim. Sea surface temperature (SST) is obtained from HadISST1 (Rayner et al. 2003) and precipitation is obtained from the Global Precipitation Climatology Project (Adler et al. 2003). All datasets are regridded to 1.5° × 1.5°. Observed natural indices (Niño-3.4, PDO, and AO) were downloaded from their official websites (NOAA/ESRL 2019; NOAA 2019; NOAA/CPC 2019). All natural indices are averaged in summer (July–August) and normalized to 1980–2018.

We conduct a suite of simulations using the 50-km-mesh GFDL Forecast-oriented Low Ocean Resolution model (FLOR; Vecchi et al. 2014). We examine two types of multidecadal simulations. One of them is a 35-member multidecadal simulation experiments (AllForc), in which the CMIP5 (phase 5 of the Coupled Model Intercomparison Project) historical natural, anthropogenic, and aerosol forcings up to 2005 are prescribed; future projected levels are based on the CMIP5 RCP4.5 scenario for 2006–50. AllForc is compared with a 30-member 1941 forcing experiments (1941Forc), in which anthropogenic radiative forcing is fixed at the year 1941 value for years 1941–2050; natural forcing varies from year to year in this experiment (Murakami et al. 2015, 2017; Zhang et al. 2017).

We define three HW-related variables in this study. First, we define the $T_{\max}$ anomaly (TAnom). Observed and simulated TAnom is defined as the $T_{\max}$ anomaly relative to the summer climatology over 1980–2018. Next we define two different heat wave day (HWD) events: modest and extreme. For modest HWD events, the 75th percentile of daily $T_{\max}$ for each calendar day during 1 July–31 August with a 15-day window (e.g., 23 June–7 July on 1 July) over 1980–2018 is selected. Thus, 585 samples (15 days × 39 years) for observations and 20,475 samples (15 days × 39 years × 35 members) for AllForc were used. We define a modest HWD event when a daily $T_{\max}$ exceeds the 75th percentile for at least seven consecutive days. An extreme HWD event is calculated in the same way, but when $T_{\max}$ exceeds the 90th percentile for at least three consecutive days. HWDs are the total number of days that meet each HW criteria in a summer. Note that the simulated $T_{\max}$ is calibrated by an inflation method to reduce model bias before computing HW-related variables (Johnson and Bowler 2009; see the supplemental information).

Most of the grids over the NEA region experienced both modest (blue pluses) and extreme (black dots) HWDs for more than 10 days in summer 2018 (Figs. 1a–c). To obtain NEA area-averaged results, the three HW-related variables were first computed on individual grids, and then the area average was taken over the NEA domain. The anomalies of area-averaged extreme and modest HWDs in 2018 were 11.1 and 12.2, respectively; this is comparable to the year with the most HWDs since 1980: 10.2 and 12.7 days in 1994 (Figs. 1e,f).

To assess the simulation ability of FLOR, the three HW-related variables in AllForc are compared with observations. AllForc can capture the amplitude of observed variability of the three HW-related variables well (Figs. 1d–f). Note that the observations are within the range of the ensemble spreads for all but for a few years, justifying our use of the FLOR model for our analysis.

To evaluate the fraction of attributable HW risk to anthropogenic forcing ($\mathrm{FAR}_{\mathrm{AllForc}}$; Jaeger et al. 2008), $\mathrm{FAR}_{\mathrm{AllForc}}$ is defined as $\mathrm{FAR}_{\mathrm{AllForc}} = 1 - (P_{\mathrm{1941Forc}}/P_{\mathrm{AllForc}})$, where P_{AllForc} (P_{1941Forc}) is the occurrence probability of extreme HW years in AllForc (1941Forc). The occurrence probability of an extreme HW year like 2018 [$P(x)$] in AllForc (P_{AllForc}) and 1941Forc (P_{1941Forc}) is

$$P(x) = \frac{\text{Numbers of year with VAR} \geq x}{\text{Total numbers of years}},$$

where VAR is a HW-related variable, and $P(x)$ represents the probability of a year with VAR value being no less than x. Because the observed 2018 HW falls into a 95th percentile or higher extreme year during 1980–2018, we choose x at the 95th percentile of all the VAR values from AllForc ensemble during 1980–2018 [i.e., from 1,365 (35 members × 39 years) sampling years]. The same x value is applied to the AllForc and 1941Forc ensembles to compute P_{AllForc} and P_{1941Forc} over each time period: 1941–79, 1980–2018, and 2019–50. A $\mathrm{FAR}_{\mathrm{AllForc}}$ value close to 1 (ranging from $-\infty$ to 1) implies that the extreme HW year is virtually impossible without an increase in anthropogenic forcing.

RESULTS. The probability density functions for HW-related variables in AllForc have similar distributions with those of the observations, indicating reasonable simulations of the HW-related variables by FLOR (Figs. 2a–c). The three $\mathrm{FAR}_{\mathrm{AllForc}}$ values are in the range of 0.75–0.82, indicating that the potential risk of extreme HW years increases with enhanced anthropogenic forcing.

Figures 2d–f compare P_{AllForc} (light gray bars) with P_{1941Forc} (dark gray bars) for each of the present decades (1980–2018), past decades (1941–79), and

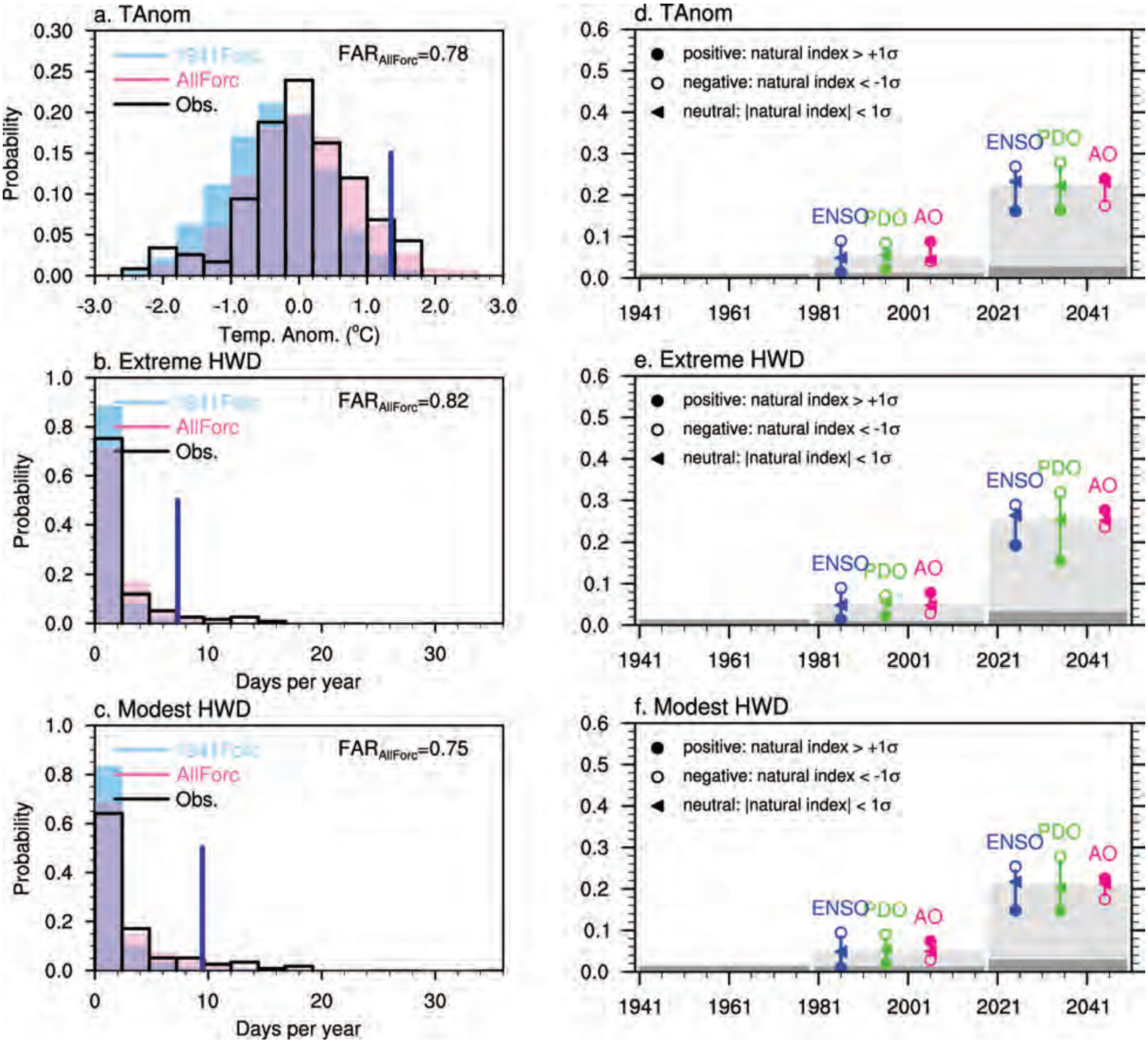

Fig. 2. Probability distribution frequencies of (a) TAnom, (b) extreme HWDs, and (c) modest HWDs based on the three reanalysis datasets (black lines), 1941Forc (sky blue bars), and AllForc (pink bars) during 1980–2018. The thick dark blue lines represent the 95th percentile values in AllForc. FAR$_{AllForc}$ values are shown. Also shown are $P_{AllForc}$ (light gray bars) and $P_{1941Forc}$ (dark gray bars) for (d) TAnom, (e) extreme HWDs, and (f) modest HWDs during the past decades (1941–79), present decades (1980–2018), and future decades (2019–50). The solid (hollow) circles and triangles represent conditional probability of $P_{AllForc}$ during positive (negative) and neutral phases of the ENSO (blue markers), PDO (green markers), and AO (deep pink markers) of present and future decades.

future decades (2019–50). Compared with the rare occurrence of 0.05 (1.5 times per 30 years) of $P_{AllForc}$ during the present decades, $P_{1941Forc}$ is nearly zero, suggesting significant increase of probability due to anthropogenic forcing. Moreover, $P_{AllForc}$ in future decades is projected to increase substantially: up to 0.24–0.28 (7–8 times per 30 years). This implies that an extreme NEA HW year like 2018 would occur about once every four years in the next three decades.

Potential influences of natural variability (e.g., ENSO, PDO, and AO) are also detected by comparing conditional $P_{AllForc}$ for which $P_{AllForc}$ is separately computed during different phases of natural variability [colored markers in Figs. 2d–f; detailed methods are given in Murakami et al. (2015)]. The potential effects of natural variability on $P_{AllForc}$ are measured by the lengths of the colored lines. The increased conditional $P_{AllForc}$ during both the positive phase of the AO and the negative phases of the ENSO and PDO over the present decades indicates that the positive AO (+2σ) and negative PDO (−0.4σ) increase the probability of a HW event. However, the modest El Niño condition (+0.2σ) (Fig. ES2) reduces the likelihood of a HW event. Overall, the effect of natural variability on the occurrence of 2018 HW is not negligible, but appears smaller than that of anthropogenic forcing. However, it is uncertain if FLOR perfectly reproduces the observed relationship between natural variability and HW. This uncertainty reduces our confidence in making clear statements of changes in the influence of natural variability on regional HWs without further research.

CONCLUSIONS. A suite of large ensemble simulations using FLOR allows us to explore the probability of NEA HW events over the period of 1941–2050. We find that anthropogenic climate change increases the probability of the NEA 2018 HW event. Natural variability conditions (negative PDO and positive AO) may have also made the event more likely. Anthropogenic forcing will make extreme HWs (like that in 2018) 5 times more likely in future decades.

ACKNOWLEDGMENTS. The authors thank Dr. Nat Johnson, Dr. Liwei Jia, Dr. Gan Zhang, Dr. Salvatore Pascale, and three anonymous reviewers for their suggestions and comments. This work was partly supported by the National Key R&D Program of China (2018YFC1505804) and the China Scholarship Council (File 201808320271).

REFERENCES

Adler, R. F., and Coauthors, 2003: The version 2 Global Precipitation Climatology Project (GPCP) Monthly Precipitation Analysis (1979–present). *J. Hydrometeor.*, **4**, 1147–1167, https://doi.org/10.1175/1525-7541(2003)004<1147:TVGPCP>2.0.CO;2.

Chen, W., and R. Y. Lu, 2014: The interannual variation in monthly temperature over Northeast China during summer. *Adv. Atmos. Sci.*, **31**, 515–524, https://doi.org/10.1007/s00376-013-3102-3.

Dee, D. P., and Coauthors, 2011: The ERA-Interim reanalysis: Configuration and performance of the data assimilation system. *Quart. J. Roy. Meteor. Soc.*, **137**, 553–597, https://doi.org/10.1002/qj.828.

Enomoto, T., 2004: Interannual variability of the Bonin high associated with the propagation of Rossby waves along the Asian jet. *J. Meteor. Soc. Japan*, **82**, 1019–1034, https://doi.org/10.2151/jmsj.2004.1019.

Gelaro, R., and Coauthors, 2017: The Modern-Era Retrospective Analysis for Research and Applications, version 2 (MERRA-2). *J. Climate*, **30**, 5419–5454, https://doi.org/10.1175/JCLI-D-16-0758.1.

Jaeger, C. C., J. Krause, A. Haas, R. Klein, and K. Hasselmann, 2008: A method for computing the fraction of attributable risk related to climate damages. *Risk Anal.*, **28**, 815–823, https://doi.org/10.1111/j.1539-6924.2008.01070.x.

JMA, 2018: Characteristics and physical mechanisms on the record-breaking heavy rain and heatwave in 2018 July. Japan Meteorological Agency, 21 pp., https://www.jma.go.jp/jma/press/1808/10c/h30goukouon20180810.pdf.

Johnson, C., and N. Bowler, 2009: On the reliability and calibration of ensemble forecasts. *Mon. Wea. Rev.*, **137**, 1717–1720, https://doi.org/10.1175/2009MWR2715.1.

Kobayashi, S. Y., and Coauthors, 2015: The JRA-55 reanalysis: General specifications and basic characteristics. *J. Meteor. Soc. Japan*, **93**, 5–48, https://doi.org/10.2151/jmsj.2015-001.

Lee, W.-S., and M. I. Lee, 2016: Interannual variability of heat waves in South Korea and their connection with large-scale atmospheric circulation patterns. *Int. J. Climatol.*, **36**, 4815–4830, https://doi.org/10.1002/joc.4671.

Matsumura, S., and T. Horinouchi, 2016: Pacific Ocean decadal forcing of long-term changes in the western Pacific subtropical high. *Sci. Rep.*, **6**, 37765, https://doi.org/10.1038/srep37765.

Murakami, H., G. A. Vecchi, T. L. Delworth, K. Paffendorf, L. Jia, R. Gudgel, and F. Zeng, 2015: Investigating the influence of anthropogenic forcing and natural variability on the 2014 Hawaiian hurricane season [in “Explaining Extreme Events of 2014 from a Climate Perspective”]. *Bull. Amer. Meteor. Soc.*, **96** (12), S115–S119, https://doi.org/10.1175/BAMS-D-15-00119.1.

Murakami, H., and Coauthors, 2017: Dominant role of subtropical Pacific warming in extreme eastern Pacific hurricane seasons: 2015 and the future. *J. Climate*, **30**, 243–264, https://doi.org/10.1175/JCLI-D-16-0424.1.

NOAA, 2019: PDO index, accessed April 2019, https://www.ncdc.noaa.gov/teleconnections/pdo/data.csv.

NOAA/CPC, 2019: AO Index, accessed April 2019, https://www.cpc.ncep.noaa.gov/products/precip/CWlink/daily_ao_index/monthly.ao.index.b50.current.ascii.

NOAA/ESRL, 2019: Niño-3.4 index, accessed April 2019, https://www.esrl.noaa.gov/psd/gcos_wgsp/Timeseries/Data/nino34.long.anom.data, https://www.esrl.noaa.gov/psd/gcos_wgsp/Timeseries/Nino34/.

Oliver, E. C. J., S. E. Perkins-Kirkpatric, N. J. Holbrook, and N. L. Bindoff, 2018: Anthropogenic and natural influences on record 2016 marine heat waves [in "Explaining Extreme Events of 2016 from a Climate Perspective"]. *Bull. Amer. Meteor. Soc.*, **99** (1), S44–S48, https://doi.org/10.1175/BAMS-D-17-0093.1.

Rayner, N. A., D. E. Parker, E. B. Horton, C. K. Folland, L. V. Alexander, D. P. Rowell, E. C. Kent, and A. Kaplan, 2003: Global analyses of sea surface temperature, sea ice, and night marine air temperature since the late nineteenth century. *J. Geophys. Res.*, **108**, 4407, https://doi.org/10.1029/2002JD002670.

Sippel, S., F. E. L. Otto, M. Flach, and G. J. van Oldenborgh, 2016: The role of anthropogenic warming in 2015 central European heat waves [in "Explaining Extreme Events of 2015 from a Climate Perspective"]. *Amer. Meteor. Soc.*, **97** (12), S51–S56, https://doi.org/10.1175/BAMS-D-16-0150.1.

Song, L., S. Dong, Y. Sun, G. Ren, B. Zhou, and P. A. Stott, 2015: Role of anthropogenic forcing in 2014 hot spring in northern China [in "Explaining Extreme Events of 2014 from a Climate Perspective"]. *Amer. Meteor. Soc.*, **96** (12), S111–S114, https://doi.org/10.1175/BAMS-D-15-00111.1.

Vecchi, G. A., and Coauthors, 2014: On the seasonal forecasting of regional tropical cyclone activity. *J. Climate*, **27**, 7994–8016, https://doi.org/10.1175/JCLI-D-14-00158.1.

Wu, R., S. Yang, S. Liu, L. Sun, Y. Lian, and Z. Gao, 2010: Changes in the relationship between Northeast China summer temperature and ENSO. *J. Geophys. Res.*, **115**, D21007, https://doi.org/10.1029/2010JD014422.

Zhang, W., and Coauthors, 2017: Influences of natural variability and anthropogenic forcing on the extreme 2015 accumulated cyclone energy in the western North Pacific [in "Explaining Extreme Events of 2015 from a Climate Perspective"]. *Bull. Amer. Meteor. Soc.*, **96**, S131–S143, https://doi.org/10.1175/BAMS-D-16-0146.1.

Zhu, Y., X. Yang, X. Chen, S. Zhao, and X. Sun, 2007: Interdecadal variation of the relationship between ENSO and summer interannual climate variability in China. *J. Trop. Meteor.*, **13**, 132–136.

Zhu, Y., H. Wang, W. Zhou, and J. Ma, 2011: Recent changes in the summer precipitation pattern in East China and the background circulation. *Climate Dyn.*, **36**, 1463–1473, https://doi.org/10.1007/s00382-010-0852-9.

ANTHROPOGENIC INFLUENCES ON THE PERSISTENT NIGHT-TIME HEAT WAVE IN SUMMER 2018 OVER NORTHEAST CHINA

Liwen Ren, Dongqian Wang, Ning An, Shuoyi Ding, Kai Yang, Rong Yu,
Nicolas Freychet, Simon F. B. Tett, Buwen Dong, and Fraser C. Lott

Persistent night-time heat waves like the event of summer 2018 in Northeast China are extremely rare (about a one-in-a-500-year event) in the natural world, but now have become about a one-in-60-year event with anthropogenic warming.

In the summer of 2018, Northeast China was affected by an unprecedentedly long and intense heat wave. The China Meteorological Administration issued 33 days of consecutive "high temperature-alert" warnings from 14 July to 15 August in 2018. Record-breaking hot minimum temperatures were observed in a large area of Northeast China (34°–55°N, 105°–135°E) with a stable spatial pattern on time scales of 20–40 days (Fig. 1a; see also Fig. ES1 in the online supplemental material). Further, minimum temperatures were more extreme, with a much larger record-breaking area than maximum temperatures (Fig. ES1). On 30 July, the number of heat-related hospitalization admissions broke the historical record in Shenyang, a large city in Northeast China (http://news.lnd.com.cn/system/2018/08/01/000008645.shtml). The aquaculture industry in Liaoning Province suffered from economic loss of 6.87 billion renminbi (RMB) (www.zhonghongwang.com/show-256-103674-1.html). Thus, this unprecedented persistent and extreme heat wave event led to severe impacts, including increased human morbidity and mortality, reduced agriculture productivity, and increased strain on power systems and water supplies.

Anthropogenic warming has been shown to drive recent record-breaking heat and summer extremes in different regions of the world (Hansen et al. 2012; Lewis and Karoly 2013). Previous heat event attribution studies in China usually considered seasonal mean and maximum temperature covering a fixed period (e.g., Sun et al. 2016a; Ma et al. 2017), with few studies focusing on consecutive minimum temperatures when there is the strongest signal in summer. Daily minimum temperature allows people and ecosystems to recover from thermal stresses experienced during the previous day (Schwartz 2005) and is a strong predictor for human morbidity and mortality (Laaidi et al. 2012; Madrigano et al. 2015; Murage et al. 2017). Previous studies show that anthropo-

AFFILIATIONS: Ren—State Key Laboratory of Numerical Modeling for Atmospheric Sciences and Geophysical Fluid Dynamics, Institute of Atmospheric Physics, Chinese Academy of Sciences, and University of Chinese Academy of Sciences, Beijing, China; Wang—National Climate Center, China Meteorological Administration, Beijing, China; An and Yu—State Key Laboratory of Severe Weather, Chinese Academy of Meteorological Sciences, Beijing, China; Ding—Department of Atmospheric and Oceanic Sciences, Institute of Atmospheric Sciences, Fudan University, Shanghai, China; Yang—State Key Laboratory of Numerical Modeling for Atmospheric Sciences and Geophysical Fluid Dynamics, Institute of Atmospheric Physics, Chinese Academy of Sciences, Beijing, and Key Laboratory of Meteorological Disaster (KLME), Ministry of Education and Collaborative Innovation Center on Forecast and Evaluation of Meteorological Disasters (CIC-FEMD), Nanjing University of Information Science and Technology, Nanjing, China; Freychet and Tett—School of Geosciences, University of Edinburgh, Edinburgh, United Kingdom; Dong—National Centre for Atmospheric Science, Department of Meteorology, University of Reading, Reading, United Kingdom; Lott—Met Office Hadley Centre, Exeter, United Kingdom

CORRESPONDING AUTHOR: Dr. Dongqian Wang, wangdq@cma.gov.cn

DOI:10.1175/BAMS-D-19-0152.1

A supplement to this article is available online (10.1175/BAMS-D-19-0152.2)

genic influences, including anthropogenic emission of greenhouse gases and urbanization leading to the expansion of urban heat islands, has contributed to higher summer minimum temperatures in Eastern China (Sun et al. 2016b; Wang et al. 2017). Hence, this study aims to investigate whether anthropogenic influences have increased the frequency of the monthly time scale heat waves like the summer 2018 event over Northeast China.

DATA AND METHODS. *Observations.* We used observed daily minimum temperatures at about 2,400 meteorological stations over China for the period 1961–2018. These were quality-controlled and homogenized by National Meteorological Information Center of China (Ren et al. 2012). We also used daily atmospheric circulation field data from ERA-Interim (Dee et al. 2011), including geopotential height, horizontal wind, and specific humidity.

Model. Simulations from the atmosphere model HadGEM3-A-N216 at a horizontal resolution of 0.56° × 0.83° were used in this study (Christidis et al. 2013; Ciavarella et al. 2018). Three ensembles were used:

- An 15-member ensemble of simulations for period 1960–2013, in which the model is forced by observed sea surface temperatures (SST) and sea ice concentrations (SIC) from HadISST (Rayner et al. 2003), and a comprehensive package of historical anthropogenic atmospheric forcing (Historical).
- A 525-member ensemble of simulations for 2018 only (counterfactual world), driven with preindustrial atmospheric forcing and the anthropogenic contribution removed from SST and SIC (HistoricalNatExt; see the online line supplemental information for details).
- A second 525-member ensemble of simulations (factual world), driven as for "Historical" but for 2018 only (HistoricalExt).

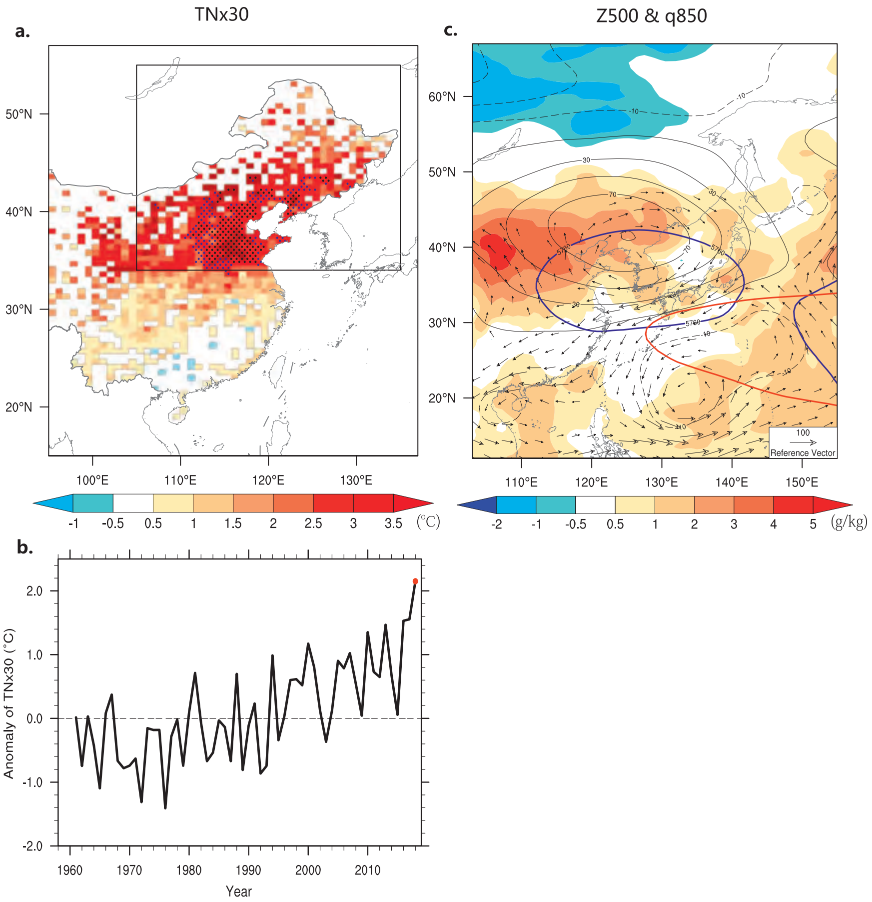

FIG. 1. Observed characteristics of the heat wave in Northeast China during 12 Jul–10 Aug 2018, with maximum consecutive 30-day Tmin anomalies in summer 2018 (TNx30). (a) Spatial pattern of TNx30 (shading; unit: °C) relative to 1961–2013. Locations with record-breaking and second highest values since 1961 are shown with black and blue dots, respectively. (b) Time series of TNx30 anomalies over Northeast China (black rectangle shown in Fig. 1a) from 1961 to 2018. (c) Circulation field from ERA-Interim with specific humidity anomalies (shading; unit: g kg^{-1}) and 850-hPa moisture flux anomalies (vectors). The light black contours denote the 500-hPa geopotential height anomalies. The 12 Jul–10 Aug 2018 mean geopotential height (blue lines) and climatology (red lines) are also shown.

Event definition. An index of 30-day moving average of daily minimum temperature anomalies (TNx30) over the study area was defined. First, to remove the seasonal cycle at each station, daily minimum temperature (T_{min}) anomalies relative to the daily 1961–2013 climatology were computed in each calendar day. We then gridded these anomalies to the 0.56° × 0.83° model resolution by averaging all station anomalies in each grid box. The gridded T_{min} anomalies were then area averaged over Northeast China (34°–55°N, 105°–135°E), and finally used to calculate the hottest 30-day running mean $T_{\min}$ in summer (June–August) for each year. For model datasets, the same process was followed except rather than gridding the simulations, grid points were used only if they were land and there were observations in the grid box. The anomaly of the index TNx30 in summer was used in this study and the value of 2018 event (2.15°C) was chosen as the threshold.

To estimate probabilities, generalized extreme value (GEV) distributions were fitted to both simulated and observed data. A two-sided Kolmogorov–Smirnoff (K-S) test was then applied to test if the distributions of the observations and historical simulations from 1961 to 2013 are from the same population. To estimate the anthropogenic contribution to the heat wave event like 2018 summer in Northeast China, the risk ratio (National Academies of Sciences, Engineering, and Medicine 2016) defined as P(HistoricalExt)/P(HistoricalNatExt) was calculated, where P(HistoricalExt) and P(HistoricalNatExt) are the probability of the event in factual and counterfactual world, respectively. We bootstrapped with replacement 1,000 times to generate PDFs, and then computed 1,000 risk ratios and then used that to compute uncertainties in risk ratios.

RESULTS. *Observed events and model performance.* In summer 2018, the regional average of TNx30 over Northeast China was 3 standard deviations of interannual variability above the 1961–2013 climatology and the highest on record since at least 1961 (Fig. 1b). This heat wave was accompanied by positive geopotential height anomalies over Northeast Asia, induced by the unprecedented northward shift of the western Pacific subtropical high (Fig. 1c; Liu et al. 2019). At low levels (850 hPa), anomalous northwestward moisture transportation from the warm Bohai Sea resulted in increased specific humidity (Fig. 1c) and consequently contributed to significant nighttime warming.

Model performance was evaluated using the ensemble mean of the historical ensemble, which reasonably reproduced the time series of TNx30 anomalies, with a correlation coefficient of 0.70 (Fig. 2a). This means that forcing, SST, and SIC variations explain about half of the observed variance in TNx30. The distributions of observed and simulated TNx30 for summers during 1961–2013 are also statistically indistinguishable based on the K-S test ($p = 0.80$; Fig. 2b). Such good performance of the HadGEM3-A-N216 simulations provides the basis for further attribution analysis.

Anthropogenic impact on the risk of heat waves. There is a shift of the PDF to warm anomalies from HistoricalNatExt to HistoricalExt (Fig. 2c), indicating that anthropogenic influences have increased the probability of heat wave events. Since the magnitude of this event lies at the far warm-end tail of PDF, events like 2018 are very rare in the counterfactual world. Only one member in 525-member HistoricalNatExt ensemble exceeds the 2018 threshold. By contrast, the estimated probability is 0.02 in factual world. These indicate that the 2018-like night-time heat event is extremely rare without anthropogenic warming. The estimated return period of heat wave events hotter than 2018 is about one-in-60-years with anthropogenic warming, with 5th–95th percentile uncertainty ranges of 43–116 years (Fig. 2d). A second threshold was also selected, defined as the second-most extreme year (2017, with an anomaly of 1.55°C). For this threshold, the heatwave is 57 times more frequent in the factual world (P(HistoricalExt) = 0.17) than the counterfactual world [P(HistoricalNatExt) = 0.003], which confirms the role of anthropogenic warming in these heat events. In terms of return period, for a one-in-10-year event, the magnitude of TNx30 in 2018 is estimated to be 1.7°C (1.7°–1.8°; 5th–95th) in the factual world, and 0.8°C (0.8°–0.9°; 5th–95th) in the counterfactual world (Fig. 2d). For a one-in-50-year event, the estimated magnitude of a heat event is 2.1° (2.0°–2.2°) and 1.2°C (1.1°–1.3°) in the counterfactual and factual worlds (Fig. 2d). The change in return level (0.9°C) between counterfactual and factual simulations is generally consistent with mean warming, as the shift in mean state between with (0.95°C) and without (–0.04°C) anthropogenic influence was 0.99°C (Fig. 2c). Besides, the uncertainty range of return periods increases with the rarity of events. We repeat our analyses by using different durations of either a 20-day or 40-day moving average and find similar risk ratio, suggesting the robustness of the results.

CONCLUSIONS AND DISCUSSION. Northeast China experienced a record-breaking nighttime heat wave in 2018 summer. This kind of 30-day nighttime heatwave was a one-in-500-year (or less) event in the counterfactual world. Forced by anthropogenic forcing and the observed 2018 SSTs, it became a one-in-60-year event.

This unprecedentedly long-lasting nighttime heat wave was also related to the northwestward shift of west Pacific subtropical high and the anomalous moisture transportation from the warm ocean. Additionally, the configuration of anomalous anticyclone

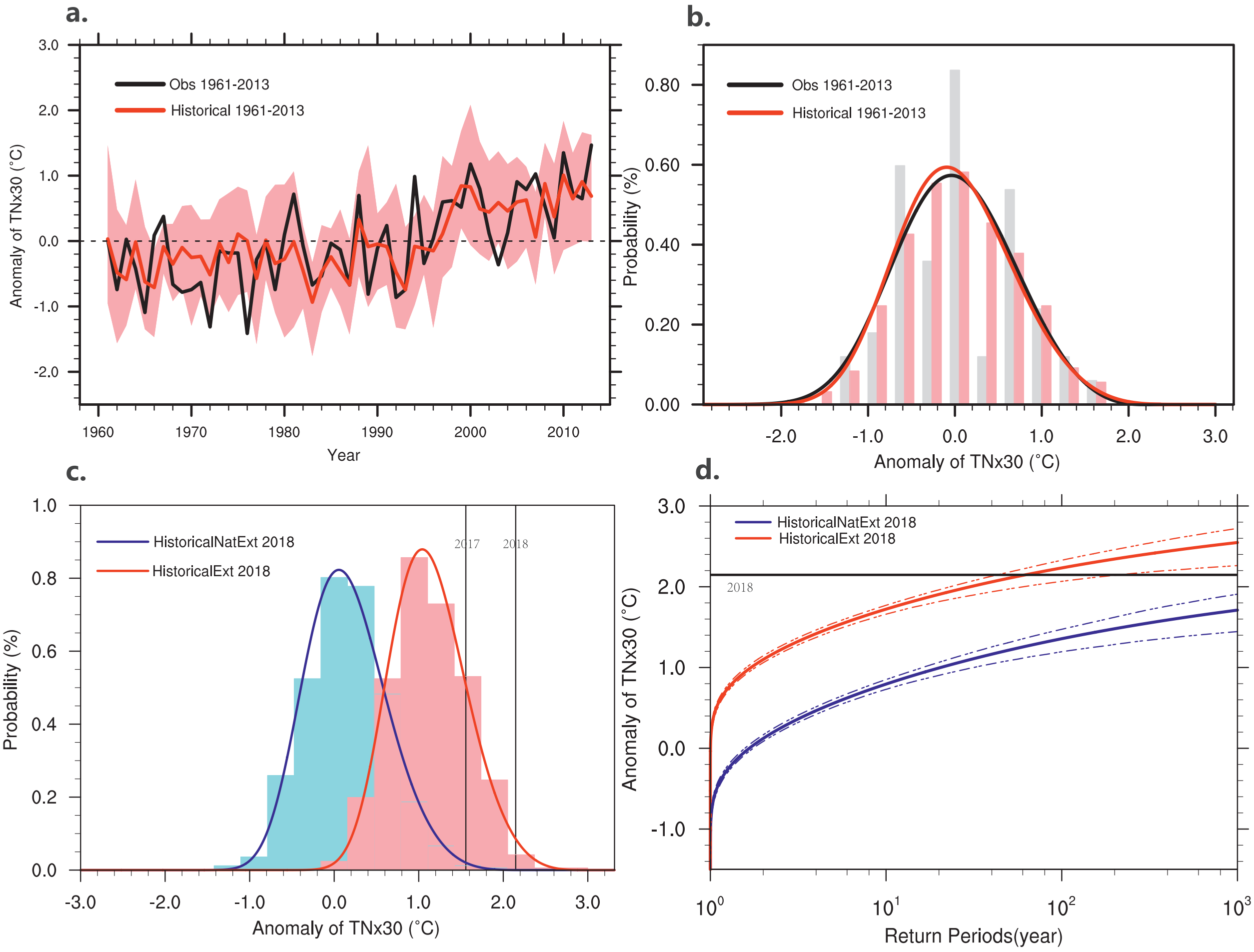

Fig. 2. (a) Time series of observed (black) and simulated ensemble mean (red) of TNx30 anomalies, with 15-member spread shown as light pink shading. (b) Histograms and GEV-fit probability density function of TNx30 anomalies in observations (black line and gray bars) and historical simulations (red line and light pink bars) from 1961 to 2013. (c) Histograms and GEV-fit probability density function (PDF) of TNx30 anomalies in 2018 summer with 525-member HistoricalExt (red) and HistoricalNatExt (blue) simulations. The black lines indicate the TNx30 thresholds of 2018 and 2017. (d) As in (c), but for return periods. Dash-dotted lines indicate the 5th–95th uncertainty range based on 1,000 bootstrap resamples for all-forcing (red) and natural-forcing (blue).

at 500 hPa over Northeast Asia during this heat event was reproduced with the six hottest simulations in study region (Fig. ES2), confirming the role of abnormal high pressure system in this heat wave event. As increased occurrence of anticyclonic circulations in the midlatitudes has made a substantial contribution (one-third to one-half) to the increased summertime temperature extremes over portions of Eurasia since 1979 (Horton et al. 2015), which leaves further questions as to whether anthropogenic warming has contributed to the heat waves like that in summer 2018 through affecting the background circulation. This study used an atmospheric model conditioned on the observed SSTs. Results are inevitably affected by uncertainty in the representation on the SSTs in the counterfactual world, especially for severe events with return periods greater than 50 years (e.g., Sparrow et al. 2018), and more work is necessary to better understand this uncertainty.

ACKNOWLEDGMENTS. This study was largely carried out during a workshop on Operational Attribution at the National Climate Centre sponsored by the U.K.–China Research and Innovation Partnership Fund through the Met Office Climate Science for Service Partnership (CSSP) China as part of the Newton Fund and the National Key Research and Development Program (2018YFC1507702). LR, NA, SD, and KY were supported by the National Key Research and Development Program (2018YFC1507701), the National Natural Science Foundation of China (41822503, 41730959, 41790472), National Key Basic Research Project of China (2015CB453200), and Open Research Fund

Program of Key Laboratory of Meteorological Disaster of Ministry of Education (Nanjing University of Information Science and Technology) Grant KLME201806. NF, SFBT, BD (through the RICHES project), and FCL were supported by the U.K.–China Research and Innovation Partnership Fund through the Met Office Climate Science for Service Partnership (CSSP) China as part of the Newton Fund.

REFERENCES

Christidis, N., P. A. Stott, A. A. Scaife, A. Arribas, G. S. Jones, D. Copsey, J. R. Knight, and W. J. Tennant, 2013: A new HadGEM3-A-based system for attribution of weather- and climate-related extreme events. *J. Climate*, **26**, 2756–2783, https://doi.org/10.1175/JCLI-D-12-00169.1.

Ciavarella, A., and Coauthors, 2018: Upgrade of the HadGEM3-A based attribution system to high resolution and a new validation framework for probabilistic event attribution. *Wea. Climate Extremes*, **20**, 9–32, https://doi.org/10.1016/J.WACE.2018.03.003.

Dee, D. P., and Coauthors, 2011: The ERA-Interim reanalysis: Configuration and performance of the data assimilation system. *Quart. J. Roy.Meteor. Soc.*, **137**, 553–597, https://doi.org/10.1002/qj.828.

Hansen, J., M. Sato, and R. Ruedy, 2012: Perception of climate change. *Proc. Natl. Acad. Sci. USA*, **109**, E2415–E2423, https://doi.org/10.1073/PNAS.1205276109.

Horton, D. E., N. C. Johnson, D. Singh, D. L. Swain, B. Rajaratnam, and N. S. Diffenbaugh, 2015: Contribution of changes in atmospheric circulation patterns to extreme temperature trends. *Nature*, **522**, 465–469, https://doi.org/10.1038/nature14550.

Laaidi, K., A. Zeghnoun, B. Dousset, P. Bretin, S. Vandentorren, E. Giraudet, and P. Beaudeau, 2012: The impact of heat islands on mortality in Paris during the August 2003 heat wave. *Environ. Health Perspect.*, **120**, 254–259, https://doi.org/10.1289/ehp.1103532.

Lewis, S. C., and D. J. Karoly, 2013: Anthropogenic contributions to Australia's record summer temperatures of 2013. *Geophys. Res. Lett.*, **40**, 3705–3709, https://doi.org/10.1002/grl.50673.

Liu, B., C. Zhu, J. Su, S. Ma, and K. Xu, 2019: Record-breaking northward shift of the western North Pacific subtropical high in July 2018. *J. Meteor. Soc. Japan*, **97**, 913–925, https://doi.org/10.2151/JMSJ.2019-047.

Ma, S., T. Zhou, D. A. Stone, O. Angelil, and H. Shiogama, 2017: Attribution of the July–August 2013 heat event in Central and Eastern China to anthropogenic greenhouse gas emissions. *Environ. Res. Lett.*, **12**, 054020, https://doi.org/10.1088/1748-9326/aa69d2.

Madrigano, J., Ito, K., Johnson, S., Kinney, P. L., Matte, T., 2015: A case-only study of vulnerability to heat wave–related mortality in New York City (2000–2011). *Environ. Health Perspect.*, **123**, 672–678, https://doi.org/10.1289/EHP.1408178.

Murage, P., S. Hajat, and R. S. Kovats, 2017: Effect of night-time temperatures on cause and age-specific mortality in London. *Environ. Epidemiol.*, **1**, e005, https://doi.org/10.1097/EE9.0000000000000005.

National Academies of Sciences, Engineering, and Medicine, 2016: Attribution of Extreme Weather Events in the Context of Climate Change. National Academies Press, 186 pp., https://doi.org/10.17226/21852.

Rayner, N. A., D. E. Parker, E. B. Horton, C. K. Folland, L. V. Alexander, D. P. Rowell, E. C. Kent, and A. Kaplan, 2003: Global analyses of sea surface temperature, sea ice, and night marine air temperature since the late nineteenth century. *J. Geophys. Res.*, **108**, 4407, https://doi.org/10.1029/2002JD002670.

Ren, Z., Y. Yu, F. Zou, and Y. Xu, 2012: Quality detection of surface historical basic meteorological data (in Chinese). *J. Appl. Meteor. Sci.*, **23**, 739–747.

Schwartz, J., 2005: Who is sensitive to extremes of temperature? A case-only analysis. *Epidemiology*, **16**, 67–72, https://doi.org/10.1097/01.ede.0000147114.25957.71.

Sparrow, S., and Coauthors, 2018: Attributing human influence on the July 2017 Chinese heatwave: the influence of sea-surface temperatures. *Environ. Res. Lett.*, **13**, 114004, https://doi.org/10.1088/1748-9326/aae356.

Sun, Y., L. Song, H. Yin, B. Zhou, T. Hu, X. Zhang, and P. A. Stott, 2016a: Human influence on the 2015 extreme high temperature events in western China [in "Explaining Extreme Events of 2015 from a Climate Perspective"]. *Bull. Amer. Meteor. Soc.*, **97** (12), S102–S106, https://doi.org/10.1175/BAMS-D-16-0158.1.

Sun, Y., X. Zhang, G. Ren, F. W. Zwiers, and T. Hu, 2016b: Contribution of urbanization to warming in China. *Nat. Climate Change*, **6**, 706–709, https://doi.org/10.1038/nclimate2956.

Wang, J., Z. Yan, X. W. Quan, and J. Feng, 2017: Urban warming in the 2013 summer heat wave in eastern China. *Climate Dyn.*, **48**, 3015–3033, https://doi.org/10.1007/s00382-016-3248-7.

chapter 16

ANTHROPOGENIC CONTRIBUTIONS TO THE 2018 EXTREME FLOODING OVER THE UPPER YELLOW RIVER BASIN IN CHINA

Peng Ji, Xing Yuan, Yang Jiao, Chunqing Wang, Shuai Han, and Chunxiang Shi

Anthropogenic climate change, reservoir operation, and land cover change have decreased the risk of 2018 extreme summer flooding by 34%, 45%, and 11% respectively.

The Upper Yellow River basin (UYRB), located over northwestern China and featuring a semiarid climate, experienced extreme flooding during the summer and autumn of 2018, with June–September rainfall ranked the highest since 1961 (CMA 2019). The extreme flooding affected about 1.4 million people and led to 30 deaths and disappearances. Many reservoirs exceeded their historical water levels to mitigate the floods, but the monthly mean streamflow during rainy season (June–September) over the UYRB still exceeded its historical value since 1987 when a large reservoir started to operate.

In the Anthropocene, water resources management such as reservoir operation changes streamflow characteristics significantly (Yuan et al. 2017). For instance, Yuan et al. (2018a) found that water resources management contributes up to 27% of the long-term changes in streamflow and its extremes over the middle reaches of the Yellow River. However, contributions from different anthropogenic factors (e.g., anthropogenic climate change, local human interventions) to the occurrence of a single extreme hydrological event (e.g., 2018 extreme flooding) remain unclear, especially for regions where both land and water are managed intensively (e.g., the UYRB).

Here we investigate the anthropogenic contributions to the 2018 extreme summer flooding over the UYRB in the context of anthropogenic climate change, regional water resources management, and land cover change, by using observed and naturalized streamflow data together with a high-resolution land surface model driven by different climate forcings.

AFFILIATIONS: Ji—Key Laboratory of Regional Climate-Environment for Temperate East Asia, Institute of Atmospheric Physics, Chinese Academy of Sciences, and College of Earth and Planetary Sciences, University of Chinese Academy of Sciences, Beijing, China; Yuan—Key Laboratory of Regional Climate-Environment for Temperate East Asia, Institute of Atmospheric Physics, Chinese Academy of Sciences, Beijing, and School of Hydrology and Water Resources, Nanjing University of Information Science and Technology, Nanjing, China; Jiao—School of Hydrology and Water Resources, Nanjing University of Information Science and Technology, Nanjing, China; Wang—Hydrology Bureau of Yellow River Conservancy Commission, Zhengzhou, China; Han and Shi—National Meteorological Information Center, China Meteorological Administration, Beijing, China
CORRESPONDING AUTHOR: Xing Yuan, xyuan@nuist.edu.cn

DOI:10.1175/BAMS-D-19-0105.1

A supplement to this article is available online (10.1175/BAMS-D-19-0105.2)

DATA AND METHODS. *Streamflow data.* Daily streamflow observation during 1987–2018 at Lanzhou station, a large hydrological station over the UYRB (orange pentagram in Fig. 1a), was provided by the Yellow River Conservancy Commission (YRCC) to analyze the extreme flooding. Monthly naturalized streamflow during 1987–2010 was also provided by YRCC, which was estimated by adding human consumed water (including agricultural, industrial, and civil uses) back to the observation (Fu et al. 2004; Yuan et al. 2017). The naturalized streamflow was used to evaluate performance of the land surface model.

Meteorological observation data. Monthly geopotential height and vertical integrated water vapor flux during 1979–2018 from the ERA-Interim reanalysis (Dee et al. 2011) were used to show circulation anomalies during the flooding seasons. The meteorological forcings for high-resolution land surface

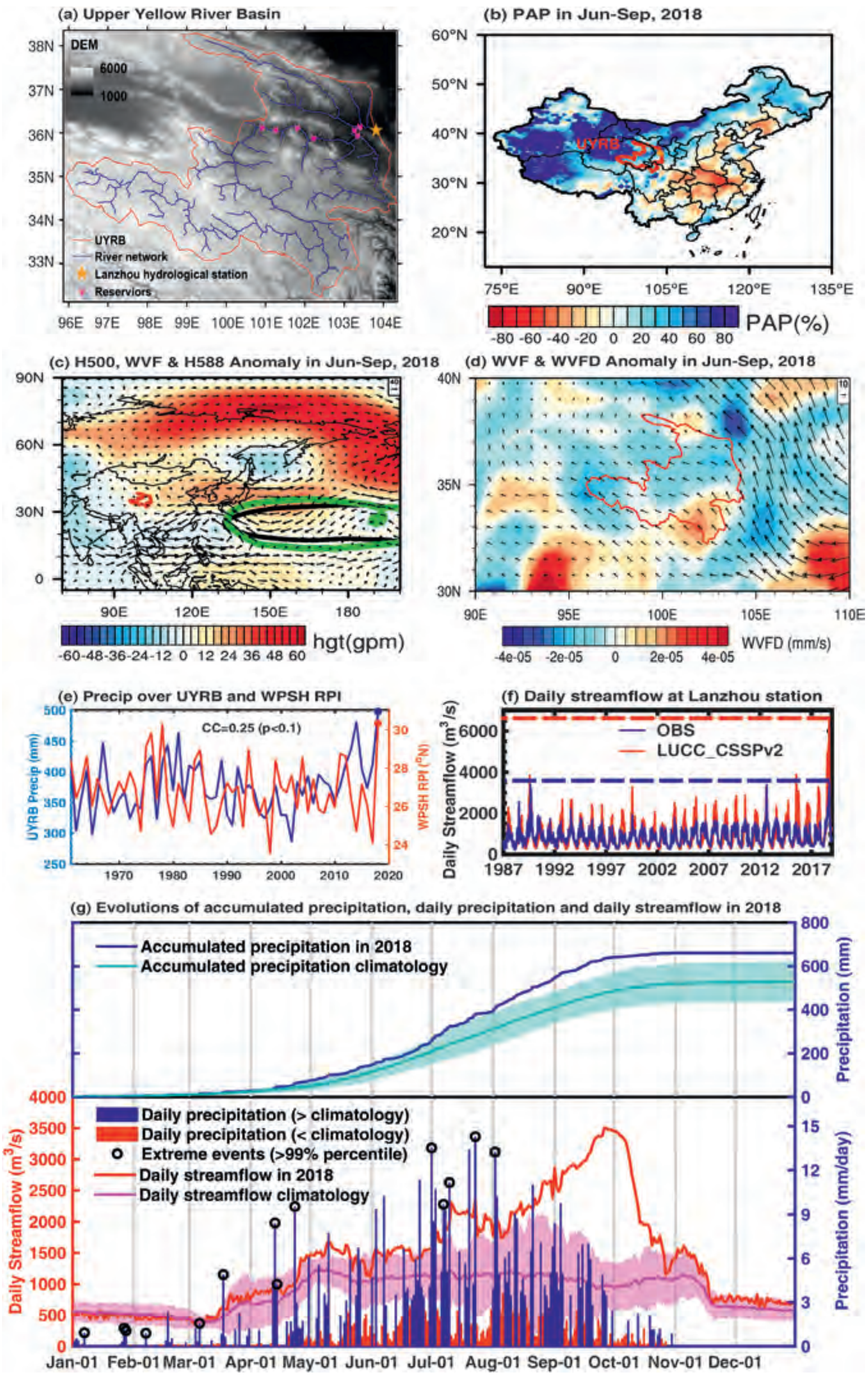

Fig. 1. (a) The Upper Yellow River basin (UYRB). (b) Percentage anomaly of precipitation (PAP) during June–September of 2018 compared with the 1961–2018 climatology. (c) June–September mean geopotential height anomaly at 500 hPa (shading), and integrated water vapor flux (WVF) anomaly (vectors) in 2018. Green and black lines show the 5,880-gpm contours for 2018 and 1979–2018 climatology, respectively. (d) Divergence of WVF over UYRB. (e) Time series of June–September mean precipitation averaged over the UYRB, and western Pacific subtropical high ridge position index. (f) Observed and LUCC_CSSPv2-simulated daily streamflow. (g) Observed 2018 daily precipitation and streamflow as compared with their climatology. Shaded areas are 95% confidence intervals. Red and blue bars represent daily precipitation cases that are smaller and larger than its climatology respectively.

modeling were generated as follows: 1) the 0.5° × 0.5° CRUNCEP dataset (Viovy 2011) during 1951–2016 was first regridded to 10-km resolution; 2) daily precipitation and temperature data were replaced by gridded observational dataset during 1951–2018, which was interpolated from more than 2,470 China Meteorological Administration (CMA) stations in China (Wang et al. 2016; Wu et al. 2017); 3) other forcings including daily specific humidity, surface shortwave radiation, wind speed, and surface pressure were extended to 2018 by using the 0.0625° × 0.0625° CMA Land Data Assimilation System dataset (CLDAS; Meng et al. 2017), where the CLDAS dataset was adjusted to CRUNCEP climatology during the overlap period of 2008–16 through quantile-mapping; and 4) the 0.1° China Meteorological Forcing Dataset during 1979–2014, which performs well in shortwave radiation (He and Yang 2011), was used to correct the systematic bias of CRUNCEP radiation at monthly time scale.

CMIP5 model data. Daily precipitation and temperature from 13 models from phase 5 of the Coupled Model Intercomparison Project (CMIP5) (see Table ES1 in the online supplemental material for the model list) during 1951–2005 under both historical (ALL) and natural (NAT) scenarios were also interpolated to 10-km resolution. The 10-km resolution is chosen to reasonably represent land surface information such as topography and soil texture, which are important for streamflow modeling. All models well capture the temperature and precipitation distribution, with spatial correlation coefficients during rainy season ranging from 0.56 to 0.93. However, the spatial mean biases of annual temperature and precipitation range from −0.7° to −3.7°C and 114 to 720 mm respectively (Figs. ES1a,b), which may cause large biases in streamflow simulations. Thus we reduced the biases by applying a cumulative distribution function (CDF) matching method (Wood et al. 2002) at monthly time scale (see the supplemental material for detailed information).

Experimental design. The land surface model, Conjunctive Surface-Subsurface Process model version 2 (CSSPv2; Yuan et al. 2018b), which well captures hydrological variations over the UYRB (Yuan et al. 2018b), was used for streamflow simulation in this study. Monthly Leaf Area Index (LAI) values during 1982–2018 estimated from the Global Inventory Modeling and Mapping Studies (GIMMS) and MODIS Normalized Difference Vegetation Index (NDVI; Yuan et al. 2018b) were used to represent land cover change.

Differences between observed and naturalized streamflow are attributed to human water intervention (mainly from reservoir operation over the UYRB). Due to the lack of data, the CSSPv2 model was first driven by modified CRUNCEP data with interannual LAI variations (LUCC_CSSPv2) to provide daily naturalized streamflow. Evaluation results (see the online supplement for detailed information) show that LUCC_CSSPv2 well simulates naturalized streamflow with high Nash–Sutcliffe efficiency (up to 0.87) and low relative bias (−3% to −2%). Second, CSSPv2 was driven by the modified CRUNCEP dataset with LAI fixed in 1982 (FIXED_CSSPv2). The difference between LUCC_CSSPv2 and FIXED_CSSPv2 is the impact of land cover change. Third, the CSSPv2 model was forced by bias-corrected CMIP5 model outputs under ALL (ALL/FIXED_CSSPv2) and NAT (NAT/FIXED_CSSPv2) scenarios without land cover change, to distinguish the anthropogenic climate change impacts. Although ALL simulations implicitly include land use/cover change (LUCC) information to some extent, most of them cannot capture the interannual variations of land cover at regional scale due to the deficiencies in the vegetation dynamics models (Bao et al. 2014). Therefore, here we ignore the LUCC effect in these CMIP-driven experiments.

Definition of extreme streamflow and attribution methods. In this study, the annual maximum daily streamflow is defined as high flow, whose distribution was estimated by the generalized extreme value (GEV) distribution. The probability of high flow exceeding a value of 3,500 $m^3\ s^{-1}$ is defined as the probability of extreme flooding like that of 2018. The risk ratio (Fischer and Knutti 2015) is then calculated as $RR_i = P_i/P_{\mathrm{NAT}}$, where i represents different scenarios and P_{NAT} is the probability of extreme flooding without any anthropogenic effects. Due to the errors in CMIP5 simulations, the distribution of ALL/FIXED_CSSPv2 is not necessarily identical to FIXED_CSSPv2. Thus P_{NAT} is not equal to $P_{\mathrm{NAT/FIXED\_CSSPv2}}$. However, assuming that the ALL/FIXED_CSSPv2 and NAT/FIXED_CSSPv2 can provide a reliable estimation of anthropogenic climate change effect through their intercomparison, P_{NAT} can be estimated through the assumption of

$$\frac{P_{\mathrm{ALL/FIXED\_CSSPv2}}}{P_{\mathrm{NAT/FIXED\_CSSPv2}}} = \frac{P_{\mathrm{FIXED\_CSSPv2}}}{P_{\mathrm{NAT}}}.$$

How much impact an anthropogenic factor would have on the likelihood of extreme flooding event can be directly calculated by comparing risk ratios in different experiments (see the supplemental material for detailed information). We repeated the above calculation of risk ratio and return period by doing bootstrapping 10,000 times. During each bootstrap, high flow data under different scenarios were resampled with replacement to get a set of new data with the same length as the original (Paciorek et al. 2018). Median value was used as mean value to avoid outliers (e.g., infinite), while 2.5% and 97.5% percentiles were used to estimate uncertainties at 95% confidence level.

RESULTS. Large positive anomalies of June–September precipitation over northwestern China in 2018 (Fig. 1b) are related to the anomalous position of the western Pacific subtropical high (WPSH). Represented by geopotential height contour at 5,880 gpm, the WPSH in 2018 (green line in Fig. 1c) shifts to the north compared with its climatology position during 1979–2018 (black line in Fig. 1c). The northernmost WPSH, revealed by WPSH Ridge Position Index (RPI) (Fig. 1e), correlates well with UYRB rainfall because the northward WPSH brings sufficient water vapor from northwestern Pacific and South China Sea to the northwestern China through the southeastern wind anomaly, causing a convergence of water vapor in UYRB (Fig. 1d) and thus providing favorable conditions for precipitation. Under this background, precipitation is larger than its climatology for most days during June–September in 2018, with five days showing extreme rainfall events (>99% percentile) (Fig. 1g). Land surface becomes saturated due to this seasonal-scale positive precipitation anomaly, which then reduces infiltration capacity and increases both surface and subsurface runoff. As a result, daily streamflow starts to increase in June, significantly exceeds its climatology during July–September, and reaches its maximum when the accumulated precipitation reaches its maximum in late September. Naturalized streamflow (LUCC_CSSPv2) shows that the high flow could be 6,622 $m^3\ s^{-1}$, with a return period of 242 yr (95% CI: >82 yr) (Fig. 1f). However, due to reservoir operation over the UYRB, the observed value is only 3,500 $m^3\ s^{-1}$, with a return period of 50 yr (95% CI: 27–130 yr).

Figures 2a and 2b show probability distribution functions (PDFs) of high flow with or without LUCC or reservoir operation effects, together with their 95% confidence intervals. The significant leftward shifting of the PDFs suggests that both land cover change and reservoir regulation decrease extreme high flow occurrence. As compared with natural climate change conditions, anthropogenic climate change also decreases probability of extreme high flow (Fig. 2c).

Table 1 shows return period and risk ratio of the 2018 extreme flooding under different scenarios. Without any anthropogenic influence (NAT scenario), this extreme event occurs frequently with a 5-yr (95% CI: 3–10 yr) return period. When anthropogenic climate change, land cover change, and reservoir operation are gradually considered, the risk ratio decreases to 0.66 (95% CI: 0.56–0.82), 0.55 (95% CI: 0.44–0.68), and 0.1 (95% CI: 0.04–0.17) respectively. The risk ratio decreases significantly by 0.34 (95% CI: 0.18–0.44) from NAT to FIXED_CSSPv2, by 0.11 (95% CI: 0.08–0.21) from FIXED_CSSPv2 to LUCC_CSSPv2, and by 0.45 (95% CI: 0.34–0.57) from LUCC_CSSPv2 to YRCC observed streamflow scenarios.

Different from reservoir operation, which reduces the probability of flooding by controlling the surface runoff, increased vegetation cover ($p < 0.01$) over the UYRB (Fig. ES2a) caused by conservation programs (Cuo et al. 2013) increases evapotranspiration during June–September (Fig. ES2b) and reduces soil moisture and thus subsurface runoff (Fig. ES2c). Anthropogenic climate change reduces surface runoff (Fig. ES2e) by significantly reducing the seasonal precipitation (Fig. 2d) instead of the extreme precipitation (Fig. 2e). The negative effect of anthropogenic climate change on seasonal precipitation occurs because the descending branch of Hadley circulation over the edges (~30° to ~40°N) enhances in a warming climate (Su et al. 2014), which inhibits precipitation generation. Moreover, anthropogenic climate change increases evapotranspiration (Fig. ES2d), thus reducing soil moisture

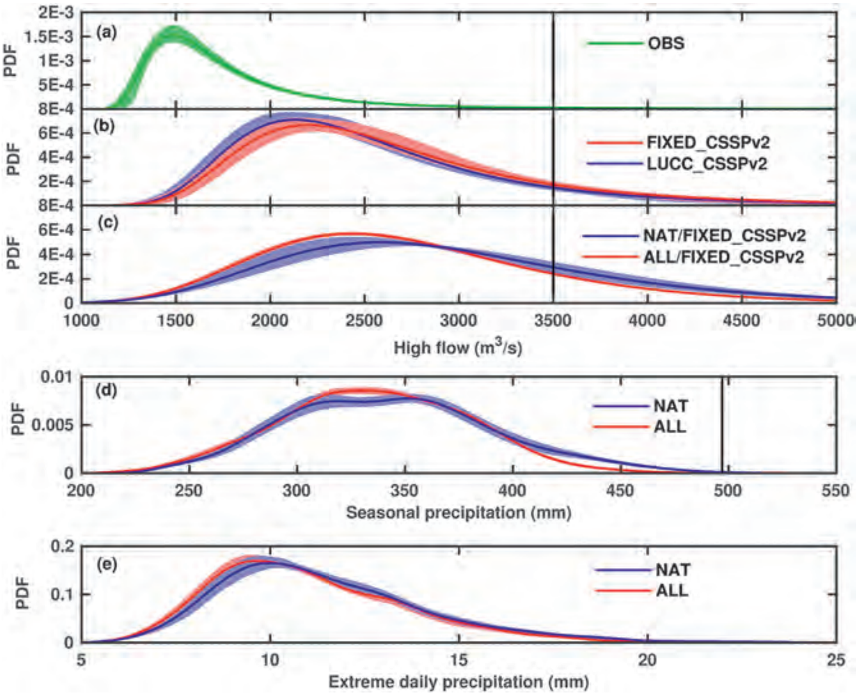

Fig. 2. (a) Probability distribution functions (PDFs) of observed high flow (green). (b) PDFs of CSSPv2-simulated high flows with (LUCC_CSSPv2) or without (FIXED_CSSPv2) land cover changes. (c) PDFs of simulated high flow forced by CMIP5 ALL (ALL/FIXED_CSSPv2) and NAT (NAT/FIXED_CSSPv2) climate output (see Methods section for details). Black lines in (a)–(c) represent the high flow threshold value of 2018. (d) PDFs of June–September mean precipitation under ALL and NAT scenarios, with the black line showing extreme rainfall in 2018. (e) PDFs of extreme daily precipitation (>99% percentile) under ALL and NAT scenarios. All the shading areas represent 95% confidence intervals.

as well as subsurface runoff (Fig. ES2e).

CONCLUSIONS AND DISCUSSION.

Anthropogenic contributions to the 2018 extreme flooding event were analyzed by considering large-scale anthropogenic climate change and local human interventions. The probability for the occurrence of the event decreases by 90% due to those anthropogenic factors, with anthropogenic climate change, land cover change, and reservoir regulation contributing by 34%, 11%, and 45% respectively.

As risk ratios are all relative to the NAT condition in this study, this makes it easy to compare different risk ratio under different scenarios. For example, by comparing the risk ratio of YRCC observed streamflow and LUCC_CSSPv2, reservoir operation decreases the risk of extreme flooding in the LUCC_CSSPv2 scenario by 82%. However, as the probability of extreme flooding in LUCC_CSSPv2 is only 55% of that in NAT scenario, the value will be 45% (0.82 × 0.55) again when we use the extreme flooding probability in NAT scenario as a reference.

The attribution results proposed in this study have uncertainties. For example, the land cover change cannot be interpreted solely as local human intervention as other factors including climate change and CO_2 fertilization also have contributions. However, as climate models have large uncertainty in simulating vegetation dynamics (Bao et al. 2014), it is still a great challenge to attribute land cover changes under different scenarios. Biases in land surface model may cause uncertainties in human water intervention attributions. However, considering the low bias of CSSPv2 in reproducing natural conditions (–3% to –2%), the model uncertainty should be limited and it does not influence the results significantly.

Our results highlight the importance of local-scale human influences in hydrological attributions, as anthropogenic contributions may be underestimated by 60% (56% relative to 90%) without considering them. More efforts should be made to incorporate local-scale human activities in current global climate models (GCMs), as most GCMs do not have representation of water management or vegetation dynamics due to coarse resolution, imperfect parameterizations, etc. (Fisher et al. 2018; Trenberth and Asrar 2014).

Table 1. Summary of return period of the 2018 extreme flooding under different scenarios together with the risk ratio (RR). The 95% confidence intervals are shown in parentheses.

Different scenarios	Return period (95% CI)	RR (95% CI)
NAT	5 yr (3–10 yr)	1
FIXED_CSSPv2	7 yr (5–14 yr)	0.66 (0.56–0.82)
LUCC_CSSPv2	9 yr (7–19 yr)	0.55 (0.44–0.67)
YRCC observed streamflow	50 yr (27–130 yr)	0.1 (0.04–0.17)

ACKNOWLEDGMENTS. We acknowledge the World Climate Research Programme's Working Group on Coupled Modeling, which is responsible for CMIP. This work was supported by National Key R&D Program of China (2018YFA0606002) and National Natural Science Foundation of China (41875105, 91437220).

REFERENCES

Bao, Y., and Coauthors, 2014: Evaluation of CMIP5 Earth system models in reproducing leaf area index and vegetation cover over the Tibetan Plateau. *J. Meteor. Res.*, **28**, 1041–1060, https://doi.org/10.1007/s13351-014-4023-5.

CMA, 2019: China Climate Bulletin 2018. China Meteorological Administration, 56 pp., http://www.cma.gov.cn/root7/auto13139/201903/t20190319_517664.html.

Cuo, L., Y. Zhang, Y. Gao, Z. Hao, and L. Cairang, 2013: The impacts of climate change and land cover/use transition on the hydrology in the upper Yellow River basin, China. *J. Hydrol.*, **502**, 37–52, https://doi.org/10.1016/j.jhydrol.2013.08.003.

Dee, D. P., and Coauthors, 2011: The ERA-Interim reanalysis: Configuration and performance of the data assimilation system. *Quart. J. Roy. Meteor. Soc.*, **137**, 553–597, https://doi.org/10.1002/qj.828.

Fischer, E. M., and R. Knutti, 2015: Anthropogenic contribution to global occurrence of heavy-precipitation and high-temperature extremes. *Nat. Climate Change*, **5**, 560–564, https://doi.org/10.1038/nclimate2617.

Fisher, R. A., and Coauthors, 2018: Vegetation demographics in Earth system models: A review of progress and priorities. *Global Change Biol.*, **24**, 35–54, https://doi.org/10.1111/gcb.13910.

Fu, G., S. Chen, C. Liu, and D. Shepard, 2004: Hydroclimatic trends of the Yellow River Basin for the last 50 years. *Climatic Change*, **65**, 149–178, https://doi.org/10.1023/B:CLIM.0000037491.95395.bb.

He, J., and K. Yang, 2011: China meteorological forcing dataset. Cold and Arid Regions Science Data

Center, accessed March 2019, Lanzhou. https://doi.org/10.3972/westdc.002.2014.db.

Meng, X., H. Wang, Y. Wu, A. Long, J. Wang, C. Shi, and X. Ji, 2017: Investigating spatiotemporal changes of the land-surface processes in Xinjiang using high-resolution CLM3.5 and CLDAS: Soil temperature. *Sci. Rep.*, **7**, 13286, https://doi.org/10.1038/s41598-017-10665-8.

Paciorek, C. J., D. A. Stone, and M. F. Wehner, 2018: Quantifying statistical uncertainty in the attribution of human influence on severe weather. *Wea. Climate Extremes*, **20**, 69–80, https://doi.org/10.1016/j.wace.2018.01.002.

Pall, P., T. Ainu, D. A. Stone, P. A. Stott, T. Nozawa, A. G. J. Hilberts, D. Lohmann, and M. R. Allen, 2011: Anthropogenic greenhouse gas contribution to flood risk in England and Wales in autumn 2000. *Nature*, **470**, 382–385, https://doi.org/10.1038/nature09762.

Su, H., J. H. Jiang, C. X. Zhai, T. J. Shen, J. D. Neelin, G. L. Stephens, and Y. L. Yung, 2014: Weakening and strengthening structures in the Hadley circulation change under global warming and implications for cloud response and climate sensitivity. *J. Geophys. Res. Atmos.*, **119**, 5787–5805, https://doi.org/10.1002/2014JD021642.

Trenberth, K. E., and G. R. Asrar, 2014: Challenges and opportunities in water cycle research: WCRP contributions. *Surv. Geophys.*, **35**, 515–532, https://doi.org/10.1007/s10712-012-9214-y.

Viovy, N. 2011: CRUNCEP dataset [CRUNCEP is for Climatic Research Unit and National Centers for Environmental Prediction]. Accessed March 2019; description available at http://dods.extra.cea.fr/data/p529viov/cruncep/readme.htm; data available at http://dods.extra.cea.fr/store/p529viov/cruncep/V4_1901_2011/.

Wang, L., X. Yuan, Z. Xie, P. Wu, and Y. Li, 2016: Increasing flash droughts over China during the recent global warming hiatus. *Sci. Rep.*, **6**, 30571, https://doi.org/10.1038/srep30571.

Wood, A. W., E. P. Maurer, A. Kumar, and D. P. Lettenmaier, 2002: Long-range experimental hydrologic forecasting for the eastern United States. *J. Geophys. Res.*, **107**, 4429, https://doi.org/10.1029/2001JD000659.

Wu, J., X. Gao, F. Giorgi, and D. Chen, 2017: Changes of effective temperature and cold/hot days in late decades over China based on a high resolution gridded observation dataset. *Int. J. Climatol.*, **37**, 788–800, https://doi.org/10.1002/joc.5038.

Yuan, X., M. Zhang, L. Wang, and T. Zhou, 2017: Understanding and seasonal forecasting of hydrological drought in the Anthropocene. *Hydrol. Earth Syst. Sci.*, **21**, 5477–5492, https://doi.org/10.5194/hess-21-5477-2017.

——, Y. Jiao, D. Yang, and H. Lei, 2018a: Reconciling the attribution of changes in streamflow extremes from a hydroclimate perspective. *Water Resour. Res.*, **54**, 3886–3895, https://doi.org/10.1029/2018WR022714.

——, P. Ji, L. Wang, X. Z. Liang, K. Yang, A. Ye, Z. B. Su, and J. Wen, 2018b: High-resolution land surface modeling of hydrological changes over the Sanjiangyuan region in the eastern Tibetan Plateau: 1. Model development and evaluation. *J. Adv. Model. Earth Syst.*, **10**, 2806–2828, https://doi.org/10.1029/2018MS001412.

chapter 17

ATTRIBUTION OF THE RECORD-BREAKING CONSECUTIVE DRY DAYS IN WINTER 2017/18 IN BEIJING

Jizeng Du, Kaicun Wang, Baoshan Cui, Shaojing Jiang, and Guocan Wu

The record long dry period over Beijing during winter 2017/18 was made more likely by a combination of La Niña, a weak Arctic polar vortex, and long-term anthropogenic warming.

During the winter of 2017/18, Beijing endured the longest consecutive dry day spell (CDD) (145 days; 23 October 2017–16 March 2018) since recordings began in 1951 (see Fig. 1b). There was no effective precipitation during this period, and there was no snow in the winter (November–February) for Beijing for the first time. As a result, the total precipitation was 86.3% below the observed average over North China Plain during 1960–2017 (see Fig. 1a), causing a severe drought and increasing the risk of wildfires.

Starting in November 2017, El Niño–Southern Oscillation (ENSO) entered the La Niña phase and lasted until late April 2018. Coupled with a negative Arctic Oscillation (AO), the Siberian high pressure area and the East Asian trough were both intensified and propagated cold surges toward North China. The stronger cold surges, associated with a subtropical high pressure system in the western Pacific, hindered the wet and warm air from the low-latitude sea moving northward to meet the cold air from Siberia. Such atmospheric circulation conditions cause less precipitation in the Beijing area, which is consistent with existing studies demonstrating the effects of ENSO and AO on the winter climate over East Asia (Chen et al. 2013; Gong et al. 2001; Wang et al. 2000; Yuan et al. 2014).

However, few studies have focused on the impact of ENSO and AO on winter precipitation in Beijing or the North China plain, likely due to the large observational uncertainty in precipitation totals. Here, we select CDD as our target to reduce the impact of observation errors in the amount of precipitation. Furthermore, this study identifies that the likelihood changes of such an extreme CDD event can be attributed to natural variability (ENSO and AO) and anthropogenic forcings (global warming) in different model simulation experiments.

AFFILIATIONS: Du and Cui—School of Environment, Beijing Normal University, State Key Joint Laboratory of Environmental Simulation and Pollution Control, Beijing China; Wang, Jiang, and Wu—College of Global Change and Earth System Science, Beijing Normal University, Beijing, 100875, China
CORRESPONDING AUTHOR: Kaicun Wang, kcwang@bnu.edu.cn

DOI:10.1175/BAMS-D-19-0139.1

A supplement to this article is available online (10.1175/BAMS-D-19-0084.2)

DATASET AND METHOD. We used the latest observation of daily precipitation data for the period of 1960–2018, which were collected from more than 2400 meteorological stations over China, and 19 stations were located in Beijing (see Fig. ES1a in the online supplemental material). The reanalysis dataset from JRA-55 was used to examine large-scale atmospheric circulation and water vapor fluxes to better capture the variability of precipitation in East Asia (Chen et al. 2014). We set 1 mm day^{-1} as the minimum threshold for effective precipitation to calculate the CDD (Jiang et al. 2015).

The HadGEM3-A-based attribution system (hereafter simply called HadGEM3A) is often used for the probabilistic attribution of extreme climate events (Lott et al. 2013; Qian et al. 2018; Zhou et al. 2018). Compared to CMIP5 models, HadGEM3A is an atmosphere-only model with the observed sea surface temperature and sea ice data as model input and provides more realistic boundary conditions for model simulation (Ciavarella et al. 2018). This attribution system has a higher horizontal resolution (~60-km midlatitudes) and adopts a nonhydrostatic dynamical core, which may offer an advantage relative to CMIP5 models at the regional scale (Christidis et al.

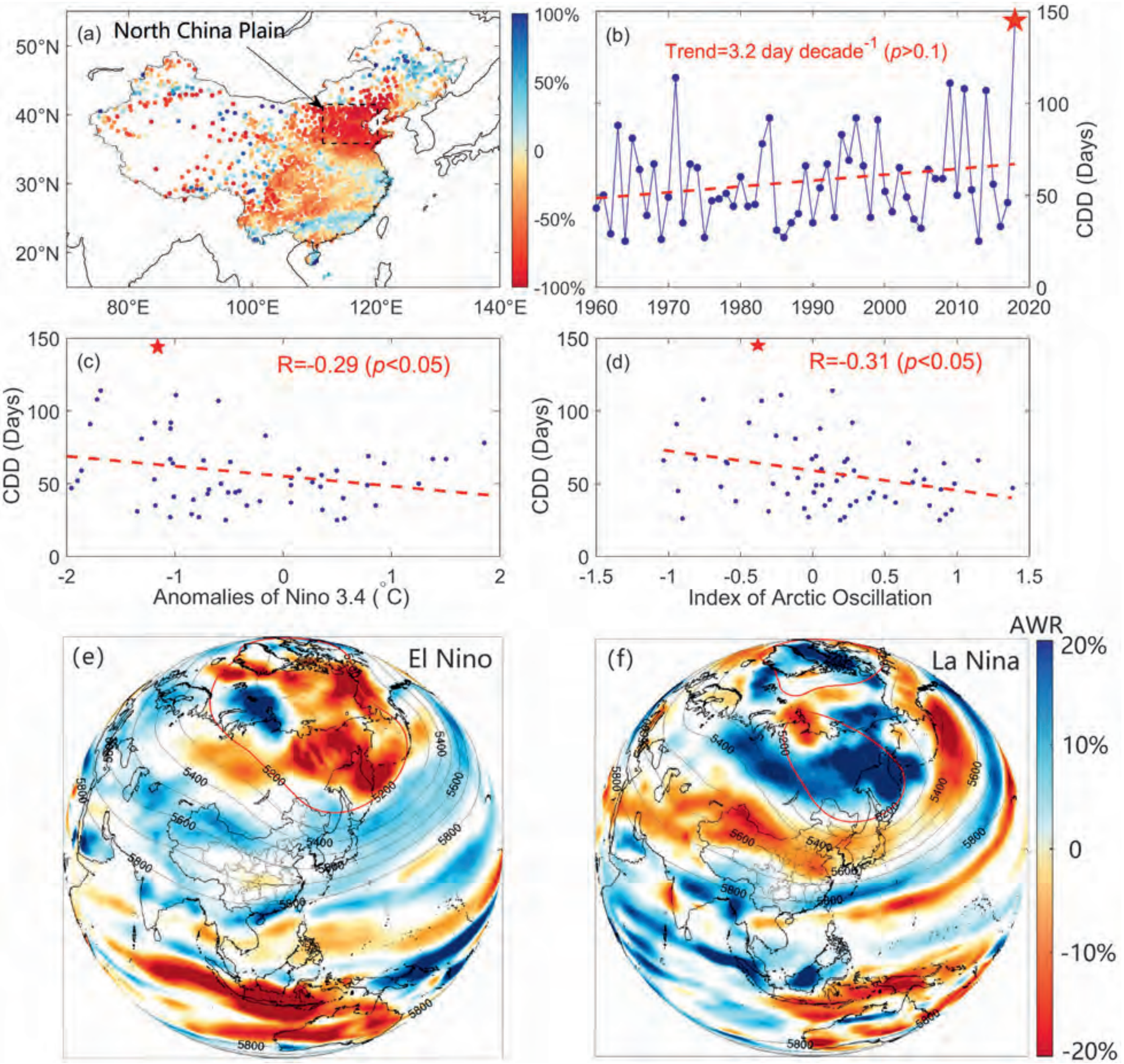

Fig. 1. (a) The anomalies of total precipitation $\left[\mathrm{ATP}=(P_i-\bar{P})/\bar{P}\right]$ are calculated by the total precipitation (P_i) during November 2017–February 2018 (NDJF; defined as winter) and multiyear mean total precipitation $(\bar{P})$ in winters during 1960–2017 over China. (b) The annual variability curve of the CDD of Beijing based on station observations shown in Fig. ES1a. (c) The Niña-3.4 index during and the annual longest CDD in Beijing was significantly correlated at the 95% confidence level (R = −0.29). (d) The AO index and the annual longest CDD in Beijing were significantly correlated at the 95% confidence level (R = −0.31). (e) The anomalies of total water vapor fluxes $\left[\mathrm{AWR}=(W_i-\bar{W})/\bar{W}\right]$ calculated by the total water vapor fluxes (W_i) in winters during four strongest El Niño years and multiyear mean total water vapor fluxes $(\bar{W})$ in winters during 1960–2017 over China. (f) As in (e), but W_i denotes the total water vapor fluxes during four strongest La Niña years. The contour lines in (e) and (f) are the average geopotential height for 500 hPa in the winters during 1979–2016 and in the winter of 2017/18, respectively. The red pentagrams represent the corresponding point of 2018 and red lines represent the contour of 5,200-m geopotential height for 500 hPa, which indicates the shape of the polar vortex.

2013). Two sets of 15 stochastic physics experiments spanned from 1960 to 2013 with the all-forcings (ALL) and natural-forcings only (NAT) conditions in HadGEM3A (Hewitt et al. 2011), and all simulations under ALL conditions have a similar distribution as that observed for CDD (see Fig. ES1d).

In addition, there are 11 CMIP5 models providing 39 simulations for daily precipitation under the ALL and NAT conditions (Taylor et al. 2012). According to their performance in replicating the variability of CDD, 19 simulations from 9 models were selected to determine the effects of anthropogenic climate change and atmospheric circulation anomalies on the CDD in Beijing (see Fig. ES1c). All simulation outputs from the models were interpolated onto a 1° × 1° grid by bilinear interpolation. Jiang et al. (2015) found that the simulated precipitation in most CMIP5 models significantly underestimated the CDD over China due to increased drizzle but decreased heavy rain. Therefore, we used a quantile-matching algorithm to adjust the daily precipitation series in CMIP5 models before the attribution process. The detailed description of the adjusting procedure was given by Wang et al. (2010).

The Niño-3.4 index, an indicator of the ENSO, uses a 5-month running mean of the average equatorial sea surface temperature (SST) anomaly across the Pacific (5°N–5°S, 170°–120°W), and El Niño (La Niña) events are defined when the Niño-3.4 index exceeds 0.4°C (below −0.4°C) for a period of 6 months or more. The AO index is calculated by projecting the AO loading pattern to the daily anomaly 850-hPa geopotential height field over 20°–90°N. The observed SST and geopotential height field are provided by the ERSSTv5 and JRA-55 reanalysis datasets, respectively. Both the SST and geopotential height for the models are obtained from simulations except for the SST for HadGEM3A, which is given by the HadISST1 dataset (Rayner et al. 2003).

In this study, the main statistical techniques used to assess the likelihood and attribution of the extreme CDD in Beijing are as follows:

1) We used the Kolmogorov–Smirnov test to select the model simulations whose distribution of CDD is consistent with the observed distribution (King et al. 2015). Then, a generalized extreme value (GEV) distribution was used to fit the distribution of the CCD in observation and the selected simulations (Coles et al. 2001). The return periods for the record-breaking CDD were calculated as follows:

$$\mathrm{RP} = \frac{1}{1 - f(x)}\ , \tag{1}$$

where RP denotes the return period when CDD equals x and $f(x)$ is the cumulative probability density function of the GEV distribution.

2) Based on the Niño-3.4 index and the AO index, the simulated time series of CDD are divided into years characterized by El Niño, La Niña, positive AO, and negative AO. Through GEV fitting, we can calculate the return periods and occurrence probability of the extreme CDD in 2017/18 with different scenarios.
3) To quantify the anthropogenic influence on the risk of extreme CDD events, the fraction of attributable risk (FAR) and the corresponding probability ratios (PR) were used to estimate the effect of anthropogenic influence and ENSO and AO (Allen 2003; Fischer and Knutti 2015):

$$\mathrm{FAR} = 1 - P_0/P_1 \text{ and } \mathrm{PR} = P_1/P_0. \tag{2}$$

To quantify the anthropogenic influence on the odds of extreme CDD events, P_0 denotes the probability of exceeding the 2018 CDD in the natural-forcing scenarios and P_1 denotes the equivalent for the all-forcings scenarios. To estimate the contribution of ENSO (AO) anomalies on the extreme CDD events, we calculated the FAR and PR with P_1 from the La Niña/El Niño (positive/negative AO) all-forcings simulations and P_0 from the ENSO-neutral (multiyear mean) all-forcings simulations. A Monte Carlo bootstrap procedure was performed 1,000 times to estimate the uncertainty of FAR and PR by resampling (Johnson 2001).

RESULTS. The CDD in 2017/18 (145 days) was the longest since records began in 1951 and was 31 days longer than the previous record (114 days in 1971) and 2.6 times longer than the average (55.7 days) during 1971–2000 (Fig. 1b). The return period of CDD in 2017/18 was approximately 60 years (see Fig. ES1b). In the long term, the CDD of Beijing had a slight increasing trend by 3.2 days decade^{-1} during 1960–2018 but was not significant ($p > 0.1$). In addition, four of the five years during which the CDD was longer than 100 days occurred in the past 10 years (see Fig. 1b). Existing studies have also observed more dry days in the winter over the North China Plain with global warming (Liu et al. 2005; Sun and Ao 2013; Zhou and Wang 2017).

As shown in Fig. 1c, the ENSO index in winter has a significant negative correlation (−0.29, $p < 0.05$) with the CDD in Beijing (see Fig. 1c). Therefore, the La Niña event, which began in August 2017 and lasted until April 2018, may play an important role in the occurrence of the extreme CDD in 2017/18. In the winter, the water fluxes in La Niña years are remarkably low over the North China Plain (see Figs. 1e,f). La Niña events often have a significant effect on East Asia as the western Pacific subtropical high acts to prevent moisture transport to North China resulting in dry conditions in winter over Beijing (Wang et al. 2000; Wang and Chen 2010).

In winter 2017/18, the AO was in an extremely negative phase and had a negative relationship with the CDD of Beijing ($R = -0.31$, $p < 0.05$). As shown in Fig. 1f, the polar vortex broke into two vortices in winter 2017/18 and is not shown as a single vortex as usual (see Fig. 1e). A negative AO is often concurrent with a weak Arctic polar vortex and a strong Siberian high and East Asian trough, which brings anomalously northerly winds and more cold and dry air from the polar regions to China (Gong et al. 2001; Thompson and Wallace 1998).

We compared the likelihood of occurrence of the record-breaking CDD in 2017/18 in HadGEM3A attribution system. Comparing the risk of CDD between the all-forcings and natural-forcings only simulations, we found that anthropogenic influences increased the likelihood by 1.29 times and explained 22.3% ± 10.8% (±95% confidence interval) attributable risk for the record-breaking CDD events like those experienced during winter 2017/18 in Beijing (see Figs. 2a,d). Comparing the all-forcings simulations in La Niña years with ENSO-neutral years, for this record-breaking CDD, the influence of La Niña increased the likelihood by 1.43 times and explained 30.0% ± 61.4% attributable risk (see Figs. 2b,d). The extreme CDD values, such as those experienced during winter 2017/18 in Beijing, negative AO increased the likelihood by 2.51 times and explained 60.1% ± 11.3% attributable risk (see Figs. 2c,d).

According to the different CMIP5 experiments, anthropogenic influences increased the likelihood

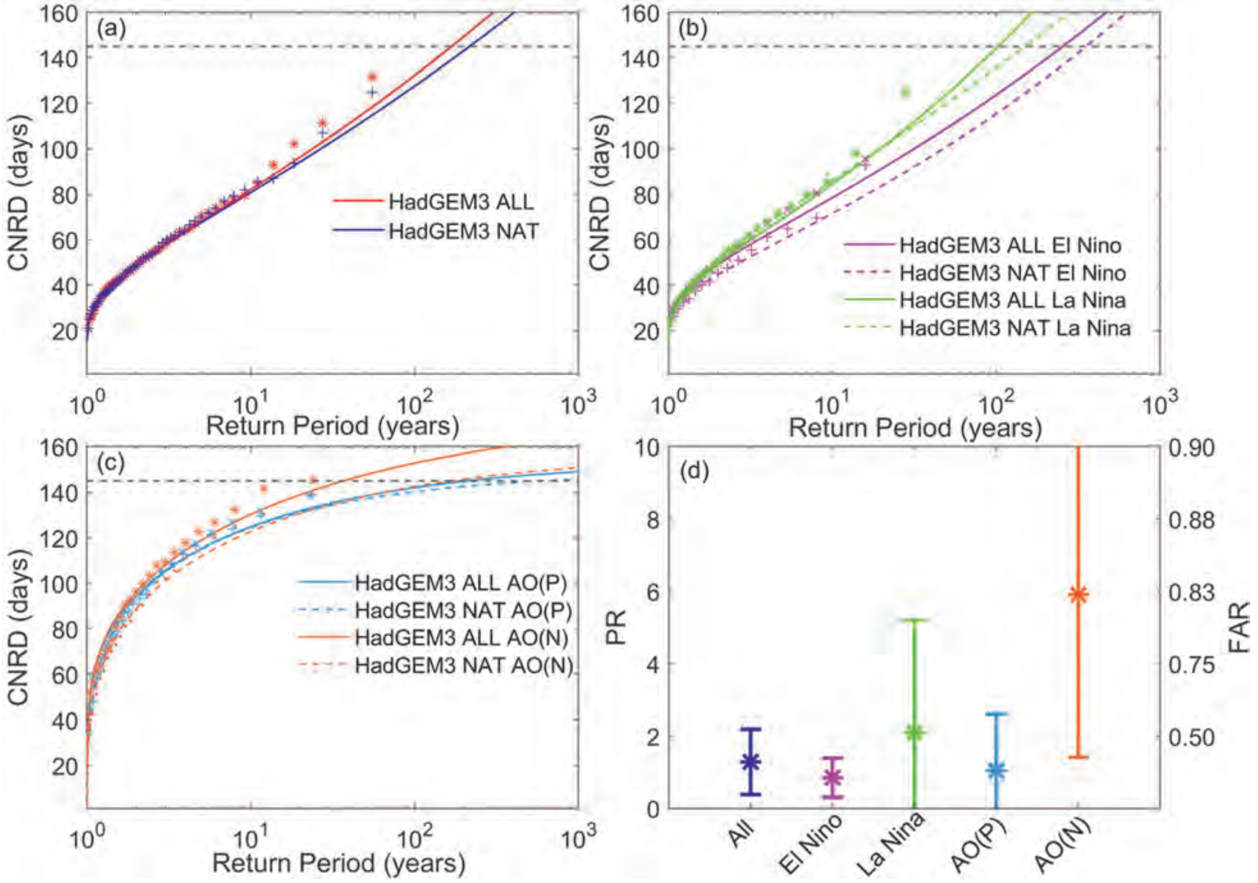

Fig. 2. (a) Return periods for the annual longest CDD during 1950–2005 from HadGEM3A simulations under ALL and NAT forcings, and the black dashed line denotes the observed CDD in 2017/18. (b) As in (a), but during El Niño or La Niña years (see text for definitions). (c) As in (b), but during the AO positive phase (P) or negative phase (N). (d) The fraction of attributable risk (FAR) and corresponding probability ratios (PR) calculated using different scenario combinations for P_0 and P_1 as shown in Eq. (2). The estimation of probability ratios was calculated using a bootstrapping approach (resampling the distributions 1,000 times with replacement); the bars show the interquartile range (5th–95th percentiles); the asterisks indicate the best estimates for the fraction of attribution risk.

Table 1. Statistics (mean and standard deviation) of CDD in Beijing in the winter from 1960 to 2018, which are classified by different phases of ENSO and AO. Each winter is one sample, and the sample number (SN) for each type is also listed. The global mean temperatures (UTC) and Beijing mean temperature (BMT) in the winter in this table refer to anomalies relative to the periods of 1961–90.

ENSO	AO	CDD (days)	UTC (°C)	BMT (°C)	SN
El Niño	Positive	51.5 ± 12.9	0.39 ± 0.20	-0.13 ± 1.15	12
	Negative	55.6 ± 14.6	0.24 ± 0.45	-0.71 ± 0.96	5
La Niña	Positive	65.1 ± 24.8	0.16 ± 0.31	-0.09 ± 0.79	11
	Negative	94.1 ± 34.7	0.26 ± 0.33	-0.92 ± 1.03	7
Neutral	Positive	37.0 ± 11.8	0.11 ± 0.26	-0.01 ± 0.98	13
	Negative	54.3 ± 22.0	0.15 ± 0.25	-0.15 ± 0.97	11

by 2.09 times for the record-breaking CDD in Beijing, explaining approximately 52.1% ± 43.7% of the attributable risk (see Figs. ES2a,d). La Niña and negative AO increased the likelihood of extreme CDD by 4.59 and 6.45 times and explained 78.2% ± 95.1% and 84.5% ± 14.1% attributable risk, respectively (see Figs. ES2b–d). Therefore, based on both HadGEM3-A and CMIP5 models, atmosphere circulation anomalies played a more important role in occurrence of this extreme CDD event in winter 2017/18 in Beijing, while the impact of anthropogenic effects was relatively small.

In addition, the combined effects of ENSO and AO on the winter climate in East Asia exhibited nonlinear characteristics. As shown in Table 1, the mean CDD when La Niña and negative AO are combined is much larger than that in other cases, which agrees well with the finding that La Niña coupled with negative AO is more favorable than other combinations for a weak Arctic polar vortex and an intensified cold surge over East Asia (Chen et al. 2013). However, identifying the combined effects among different factors on CDD in Beijing is difficult due to the limited model sample size.

CONCLUSIONS. Both the observation and the results of attribution analyses indicated that a specific atmospheric circulation pattern (La Niña event coupled with negative AO) led to the extreme CDD during the winter of 2017/18 in Beijing, and anthropogenic influences significantly increased the likelihood of such an event. The simulation experiments in HadGEM3A (CMIP5) showed anthropogenic effects increased the likelihood for this extreme CDD by 1.29 (2.09) times and explained 22.3% (52.1%) attributable risk; the La Niña event and negative AO increased the likelihood of this extreme CDD by 1.43 (4.59) times and 2.51 (6.45) times and explained 30.0% (78.2%) and 60.1% (84.5%) attributable risk, respectively, based on the simulations of HadGEM3A (CMIP5).

With more realistic boundary conditions (using observed SST and sea ice), HadGEM3A has a similar probability distribution to the observations while CMIP5 exhibits a stronger attribution result. But this is not enough to support the attribution result from HadGEM3A being more credible than that from CMIP5 (Fischer et al. 2018). However, both attribution results from HadGEM3A and CMIP5 indicate that the contribution of atmospheric circulation anomalies to the extreme drought event in Beijing was higher than anthropogenic influences, which is consistent with the observation (see Table 1). Additionally, there are also contributions from local climate factors, such as the urban dry island effect in Beijing (Wang and Gong 2010), which need to be further analyzed based on mesoscale weather/climate models and high-resolution observation data.

ACKNOWLEDGMENTS. This study was funded by the National Basic Research Program of China (2017YFA0603601 and 2018YFC1507701), China Postdoctoral Science Foundation (2018M641248), and Postdoctoral Innovation Talent Program (212643). The latest observational data were obtained from the CMA (http://www.cma.gov.cn). Considerable gratitude is owed to several working teams, including the Met Office for the HadGEM3-A-based operational event attribution system (http://catalogue.ceda.ac.uk/), the World Climate Research Programmer's Working Group on Coupled Modelling (http://cmip-pcmdi.llnl.gov/cmip5/) for the CMIP5 model simulations, and the Japan Meteorological Agency (JMA) for the JRA-55 reanalysis dataset (https://jra.kishou.go.jp/JRA-55/).

REFERENCES

Allen, M., 2003: Liability for climate change. *Nature*, **421**, 891–892, https://doi.org/10.1038/421891a.

Chen, G., T. Iwasaki, H. Qin, and W. Sha, 2014: Evaluation of the warm-season diurnal variability over East Asia in recent reanalyses JRA-55, ERA-Interim, NCEP CFSR, and NASA MERRA. *J. Climate*, **27**, 5517–5537, https://doi.org/10.1175/JCLI-D-14-00005.1.

Chen, W., X. Lan, L. Wang, and Y. Ma, 2013: The combined effects of the ENSO and the Arctic Oscillation on the winter climate anomalies in East Asia. *Chin. Sci. Bull.*, **58**, 1355–1362, https://doi.org/10.1007/s11434-012-5654-5.

Christidis, N., P. A. Stott, A. A. Scaife, A. Arribas, G. S. Jones, D. Copsey, J. R. Knight, and W. J. Tennant, 2013: A new HadGEM3-A-based system for attribution of weather- and climate-related extreme events. *J. Climate*, **26**, 2756–2783, https://doi.org/10.1175/JCLI-D-12-00169.1.

Ciavarella, A., and Coauthors, 2018: Upgrade of the HadGEM3-A based attribution system to high resolution and a new validation framework for probabilistic event attribution. *Wea. Climate Extremes*, **20**, 9–32, https://doi.org/10.1016/j.wace.2018.03.003.

Coles, S., J. Bawa, L. Trenner, and P. Dorazio, 2001: *An Introduction to Statistical Modeling of Extreme Values*. Springer, 208 pp.Fischer, E. M., and R. Knutti, 2015: Anthropogenic contribution to global occurrence of heavy-precipitation and high-temperature extremes. *Nat. Climate Change*, **5**, 560, https://doi.org/10.1038/nclimate2617.

Fischer, E. M., U. Beyerle, C. Schleussner, A. King, and R. Knutti, 2018: Biased estimates of changes in climate extremes from prescribed SST simulations. *Geophys. Res. Lett.*, **45**, 8500–8509, https://doi.org/10.1029/2018GL079176.

Gong, D. Y., S. W. Wang, and J. H. Zhu, 2001: East Asian winter monsoon and Arctic oscillation. *Geophys. Res. Lett.*, **28**, 2073–2076, https://doi.org/10.1029/2000GL012311.

Hewitt, H., and Coauthors, 2011: Design and implementation of the infrastructure of HadGEM3: The next-generation Met Office climate modelling system. *Geosci. Model Dev.*, **4**, 223–253, https://doi.org/10.5194/gmd-4-223-2011.

Jiang, Z., W. Li, J. Xu, and L. Li, 2015: Extreme precipitation indices over China in CMIP5 models. Part I: Model evaluation. *J. Climate*, **28**, 8603–8619, https://doi.org/10.1175/JCLI-D-15-0099.1.

Johnson, R. W., 2001: An introduction to the bootstrap. *Teach. Stat.*, **23**, 49–54, https://doi.org/10.1111/1467-9639.00050.

King, A. D., G. J. van Oldenborgh, D. J. Karoly, S. C. Lewis, and H. Cullen, 2015: Attribution of the record high Central England temperature of 2014 to anthropogenic influences. *Environ. Res. Lett.*, **10**, 054002, https://doi.org/10.1088/1748-9326/10/5/054002.

Liu, B., M. Xu, M. Henderson, and Y. Qi, 2005: Observed trends of precipitation amount, frequency, and intensity in China, 1960–2000. *J. Geophys. Res.*, **110**, D08103, https://doi.org/10.1029/2004JD004864.

Lott, F. C., N. Christidis, and P. A. Stott, 2013: Can the 2011 East African drought be attributed to human-induced climate change? *Geophys. Res. Lett.*, **40**, 1177–1181, https://doi.org/10.1002/grl.50235.

Qian, C., and Coauthors, 2018: Human influence on the record-breaking cold event in January of 2016 in eastern China [in "Explaining Extreme Events of 2016 from a Climate Perspective"]. *Bull. Amer. Meteor. Soc.*, **99** (1), S118–S122, https://doi.org/10.1175/BAMS-D-17-0095.1.

Rayner, N., and Coauthors, 2003: Global analyses of sea surface temperature, sea ice, and night marine air temperature since the late nineteenth century. *J. Geophys. Res.*, **108**, 4407, https://doi.org/10.1029/2002JD002670.

Sun, J., and J. Ao, 2013: Changes in precipitation and extreme precipitation in a warming environment in China. *Chin. Sci. Bull.*, **58**, 1395–1401, https://doi.org/10.1007/s11434-012-5542-z.

Taylor, K. E., R. J. Stouffer, and G. A. Meehl, 2012: An overview of CMIP5 and the experiment design. *Bull. Amer. Meteor. Soc.*, **93**, 485–498, https://doi.org/10.1175/BAMS-D-11-00094.1.

Thompson, D. W., and J. M. Wallace, 1998: The Arctic Oscillation signature in the wintertime geopotential height and temperature fields. *Geophys. Res. Lett.*, **25**, 1297–1300, https://doi.org/10.1029/98GL00950.

Wang, B., R. Wu, and X. Fu, 2000: Pacific–East Asian teleconnection: How does ENSO affect East Asian climate? *J. Climate*, **13**, 1517–1536, https://doi.org/10.1175/1520-0442(2000)013<1517:PEATHD>2.0.CO;2.

Wang, L., and W. Chen, 2010: How well do existing indices measure the strength of the East Asian winter monsoon? *Adv. Atmos. Sci.*, **27**, 855–870, https://doi.org/10.1007/s00376-009-9094-3.

Wang, X. Q., and Y. Gong, 2010: The impact of an urban dry island on the summer heat wave and sultry weather in Beijing City. *Chin. Sci. Bull.*, **55**, 1657–1661, https://doi.org/10.1007/s11434-010-3088-5.

Wang, X. L., H. Chen, Y. Wu, Y. Feng, and Q. Pu, 2010: New techniques for the detection and adjustment of shifts in daily precipitation data series. *J. Appl. Meteor. Climatol.*, **49**, 2416–2436, https://doi.org/10.1175/2010JAMC2376.1.

Yuan, Y., C. Li, and S. Yang, 2014: Decadal anomalies of winter precipitation over southern China in association with El Niño and La Niña. *J. Meteor. Res.*, **28**, 91–110, https://doi.org/10.1007/S13351-014-0106-6.

Zhou, C., and K. Wang, 2017: Quantifying the sensitivity of precipitation to the long-term warming trend and interannual–decadal variation of surface air temperature over China. *J. Climate*, **30**, 3687–3703, https://doi.org/10.1175/JCLI-D-16-0515.1.

Zhou, C., K. Wang, and D. Qi, 2018: Attribution of the July 2016 extreme precipitation event over China's Wuhang [in "Explaining Extreme Events of 2016 from a Climate Perspective"]. *Bull. Amer. Meteor. Soc.*, **99** (1), S107–S112, https://doi.org/10.1175/BAMS-D-17-0090.1.

chapter 18

QUANTIFYING HUMAN IMPACT ON THE 2018 SUMMER LONGEST HEAT WAVE IN SOUTH KOREA

Seung-Ki Min, Yeon-Hee Kim, Sang-Min Lee, Sarah Sparrow,
Sihan Li, Fraser C. Lott, and Peter A. Stott

High-resolution large-ensemble simulations indicate that human activities have at least quadrupled the probability of occurrence of the extremely long-lasting heat waves over South Korea as observed in 2018 summer.

During summer 2018, South Korea experienced the strongest and longest heat wave since 1973 (the beginning of the observations from 45 stations). The July–August (JA) mean daily maximum temperature ($T_{\max}$) was on average 2.6°C warmer than 1987–2010 climatology over South Korea, setting its second highest record after 1994 (Figs. 1a,c). A simple analysis based on a long-term CRU TS data suggests that the return time of 2018 $T_{\max}$ is about 26 years, much shorter than about 386 years in 1912 (Fig. ES1), although a large uncertainty related to data homogeneity and urbanization effect should be noted (Park et al. 2017). Unusually hot weather led to record-breaking temperatures over many stations with temperature > 40°C at some stations for the first time. More importantly, the 2018 heat wave had the longest duration on record with 31.5 hot days (total number of days with daily maximum temperature > 33°C) surpassing the previous record of 29.7 days in 1994, and exerted considerable impacts on society and the economy (reported in the *Korea Herald*[1,2]), including 48 heat-related deaths (KCDC 2018). The heat wave also induced crop destruction in North Korea.[3] When using a heat wave duration index (HWDx) defined as maximum consecutive hot days during summer, the 2018 record is extremely high at 18.1 days (Figs. 1b,d). There is a strong correlation between JA mean $T_{\max}$ and HWDx ($r = 0.74$; Figs. 1c,d), indicating a close relation between mean warming and heat wave duration. This long-lasting heat wave is characterized by a persistent anomalous high pressure system in the upper troposphere over Korea (Fig. 1f), which seems to be partly induced by the strong tropical convection over northwestern India and the South China Sea (Fig. 1e), through the well-known teleconnection mechanism (Fig. 1g; Lee and Lee 2016; Kim et al. 2019; Yeo et al. 2019).

This study aims at quantifying human contribution to the 2018 summer longest duration of heat wave in South Korea. The long duration of heat wave is known to be critically important for health (e.g., Anderson and Bell 2011; D'Ippoliti et al. 2010). To address this question for small spatial scale, we utilize high-resolution large-ensemble regional climate model (RCM) (weather@home East Asia; 50 km) and global climate model (GCM) (HadGEM3-A-N216; 60 km at midlatitudes) simulations, each performed with and without anthropogenic forcings (Table ES1). Comparing two models will help assess the confidence of the resulting attribution statement even though both models are from the Hadley model fam-

AFFILIATIONS: Min, Kim, and Lee—Division of Environmental Science and Engineering, Pohang University of Science and Technology, Pohang, Gyeongbuk, South Korea; Sparrow and Li—Oxford e-Research Centre, Department of Engineering, University of Oxford, Oxford, United Kingdom; Lott and Stott—Met Office, Exeter, United Kingdom

CORRESPONDING AUTHOR: Seung-Ki Min, skmin@postech.ac.kr

DOI:10.1175/BAMS-D-19-0151.1

A supplement to this article is available online (10.1175/BAMS-D-19-0151.2)

---

[1] http://www.koreaherald.com/view.php?ud=20180808000476&ACE_SEARCH=1

[2] http://www.koreaherald.com/view.php?ud=20180821000128&ACE_SEARCH=1

[3] https://www.theguardian.com/world/2018/aug/09/south-korean-heatwave-causes-record-deaths

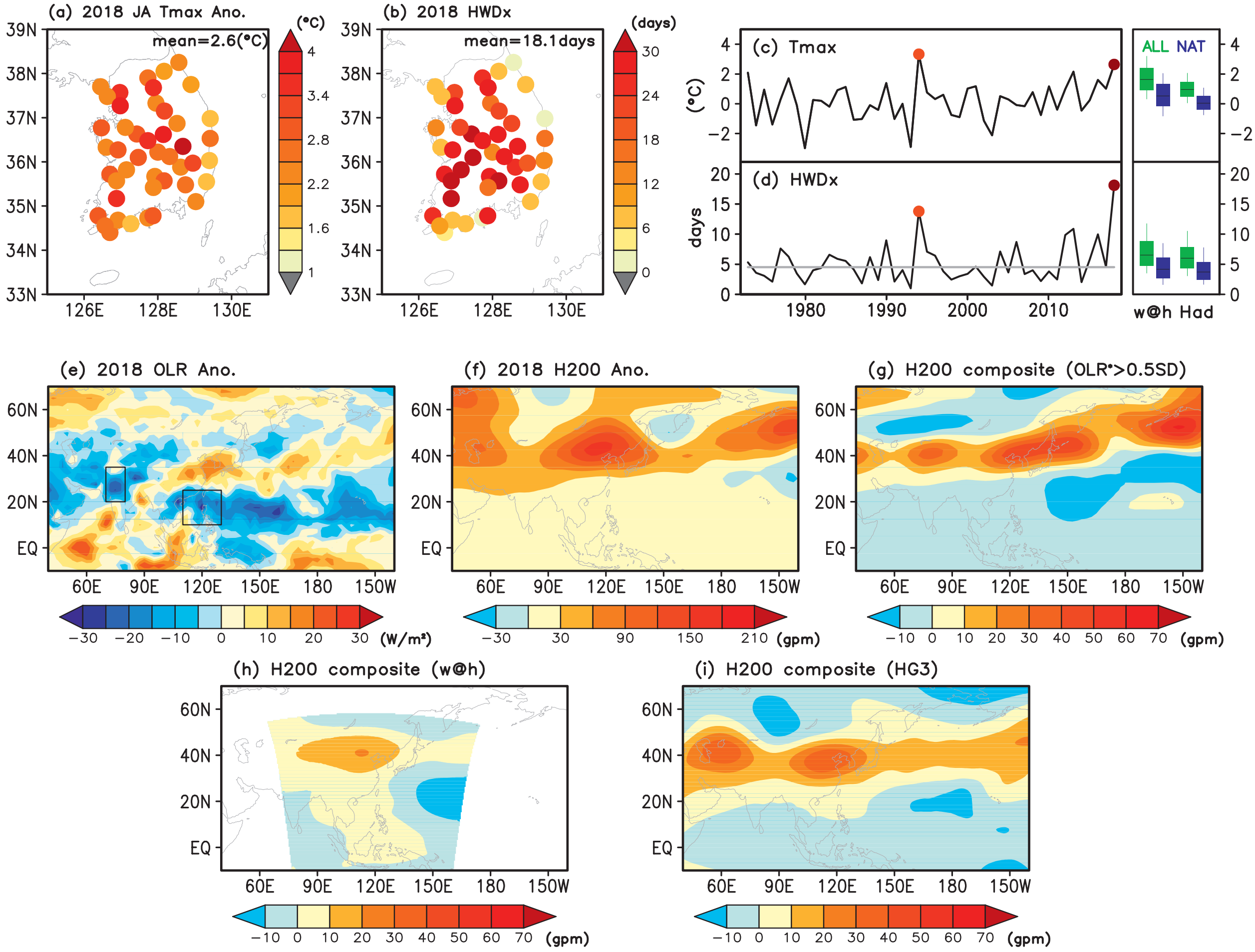

Fig. 1. Distribution of (a) 2018 JA mean daily maximum temperature (T_{max}) anomalies and (b) 2018 JA maximum heat wave duration (HWDx), defined as the maximum consecutive hot days ($T_{max} \geq 33°C$) over South Korea. Also shown are observed time series of South Korean mean (c) T_{max} anomalies and (d) HWDx over 1973–2018, and simulated ranges of 2018 T_{max} anomalies and HWDx from w@h and HadGEM3-A-N216 experiments (box-and-whisker plots); and anomaly distribution of (e) 2018 JA mean OLR (NOAA interpolated data) and (f) 200-hPa geopotential height (NCEP1 reanalysis). Two boxes in (e) indicate the two convection zones of the northwestern India (70°–80°E, 20°–35°N) and South China Sea (110°–130°E, 10°–25°N), selected based on previous studies (Kim et al. 2019; Lee and Lee 2016). Finally, anomaly composites are shown of 200-hPa geopotential height for strong convection years during 1987–2010 (OLR stronger than 0.5 standard deviation) over both convection zones from (g) observations (NCEP1 reanalysis), (h) w@h, and (i) HadGEM3-A-N216 simulations. All anomalies are with respect to 1987–2010 mean.

ily. Using the risk ratio, we compare the probabilities of occurrence of the extremely long duration of heat wave between the real and counterfactual (without human influences) worlds. Further, the influences of tropical convections on the longer-lasting heat wave is examined. In this regard, RCM and GCM are found to reasonably capture the observed teleconnection pattern (cf. Figs. 1h and 1i with Fig. 1g, pattern correlation > 0.6).

DATA AND METHODS. Daily maximum temperatures (T_{max}) from 45 South Korean weather stations are used as observations for 1973–2018. To match the spatial scale between point observations and gridded model outputs, we interpolate daily station observations onto the HadGEM3-A-N216 grid boxes of 0.86° (longitude) × 0.56° (latitude) by taking simple averages of station values within each grid box, assuming a high spatial correlation in daily temperature extremes (Donat et al. 2013). The observed HWDx is calculated using the gridded T_{max} data to obtain South Korean area averaged HWDx. To consider model biases in climatology and variability in T_{max}, we apply a different T_{max} threshold for each model (33.21°C for weather@home and 30.51°C for HadGEM3-A-N216), which corresponds to the same quantile as in the observed threshold (33°C). Using this method, models are found to have similar HWDx means as the observed around 4 days. The analysis domain for South Korea is 34°–38°N and 125°–130°E (land only).

Large-ensemble RCM data from weather@home (abbreviated herein as w@h) East Asia are used in which the HadRM3P RCM is simulated at a 50-km resolution over the East Asia region (domain extent shown in Fig. 1h) driven by the HadAM3P atmospheric GCM (Massey et al. 2015; Guillod et al. 2017). The real world simulations (ALL; 2,300 members) for 2018 were carried out by prescribing the observed sea surface temperature (SST) and sea ice coverage and also by implementing the observed greenhouse gas and aerosol forcings. The counterfactual world simulations (NAT; 3,700 members) for 2018 were performed by using adjusted observed SST and sea ice conditions with anthropogenic changes removed and setting other external forcings as preindustrial levels (see Table ES1 in the online supplemental material; Schaller et al. 2016). HadGEM3-A provides large-ensemble (525 members for ALL and NAT each) GCM data, which have a high resolution of 0.83° × 0.56° (referred to as HadGEM3-A-N216; Ciavarella et al. 2018). The boundary conditions and external forcings for ALL and NAT simulations are very similar to the w@h experiment (Table ES1). One difference is that HadGEM3-A-N216 uses single estimate of the anthropogenic SST changes (delta-SST) while w@h uses 13 different estimates (Table ES2), and its influence on the attribution results is examined. We also use baseline simulations from RCM and GCM for 1987–2010 (data period of w@h runs), which provides a reference climatology for both ALL and NAT runs (Sparrow et al. 2018). Observed anomalies are also based on the 1987–2010 means. When evaluating models using the baseline runs, RCM can capture the observed interannual variabilities for both $T_{\max}$ and HWDx but GCM tends to underestimate the $T_{\max}$ variability. The latter seems to be associated with the lower probability of occurrence of heat waves in the GCM, and consequently our results should be interpreted with caution (see below).

The risk ratio (RR) is analyzed between ALL and NAT simulations to assess the human impact on the probability of occurrence of extreme events, which is calculated as the ratio of the probability of exceeding observed events in ALL (P_{ALL}) and NAT simulations (P_{NAT}), i.e., RR = $P_{\text{ALL}}/P_{\text{NAT}}$ (e.g., Easterling et al. 2016). RR is also calculated using 1994 observations to assess robustness. We use the "likelihood ratio method" (Paciorek et al. 2018) to estimate the 5%–95% confidence intervals of RR, which can provide a confidence interval (at least a lower bound) even when the estimate of the RR is infinity.

RESULTS. Figure 2 shows the return period distributions of the JA mean $T_{\max}$ anomalies and HWDx for ALL and NAT simulations from w@h and HadGEM3-A-N216. Return periods are significantly shortened for $T_{\max}$ anomalies with human influences for both models (Figs. 2a,b). The probability of $T_{\max}$ anomalies higher than the observed 2018 value is 19.8% in ALL (P_{ALL}) and it is reduced to 4.2% in NAT simulations (P_{NAT}) for w@h (Fig. ES2a). This makes RR as large as 4.7 (5%–95% range of 4.1–5.5), indicating that anthropogenic influences increase the risk of extremely warm summer by 4 to 5 times, well consistent with previous studies based on different models (Min et al. 2014; Kim et al. 2018). The large P_{ALL} indicates a possible influence of the observed 2018 SST condition in w@h model, which may occur in this type of single-year atmosphere-only experiment (Risser et al. 2017). A simple comparison with the 2017 experiment results suggests that the observed 2018 SST condition may contribute to a larger warming over northern East Asia including the Korea peninsula through intensified tropical convections (Fig. ES3). However, RR is unlikely to be affected much [RR = 5.15 (3.9–6.9) based on 2017 runs] because of similar SST impact on NAT results (Fig. ES3). HadGEM3-A-N216 has longer return periods due to lower values of P_{ALL} and P_{NAT} for $T_{\max}$ as 3.6% and 0.19%, respectively (Fig. ES2b). This gives a larger RR of 19.0 (4.9–184), which might be in part due to the smaller sample size (cf. Sparrow et al. 2018). When using a stronger threshold (1994 $T_{\max}$ anomalies), results remain similar with RR = 6.5 (5.1–8.4) for w@h and P_{NAT} = 0% for HadGEM3-A-N216 (Table ES1).

HWDx results display shortened return periods of the long-lasting heat waves under anthropogenic influences (Figs. 2c,d). The return periods are generally longer than $T_{\max}$ for both models. P_{ALL} and P_{NAT} are very low as 1.0% and 0.11% from w@h, respectively (Fig. ES2c). The corresponding RR is 9.7 (4.3–26.1), indicating that the risk of 2018-like extremely long-lasting heat wave has increased by about 10 times due to human impacts. In HadGEM3-A-N216, extreme heat wave events longer than the observed 2018 values are extremely rare even with human-induced warming (P_{ALL} = 0.76%) and no events are present without human influences (P_{NAT} = 0%; Fig. ES2d). Although the probability might be this low due to

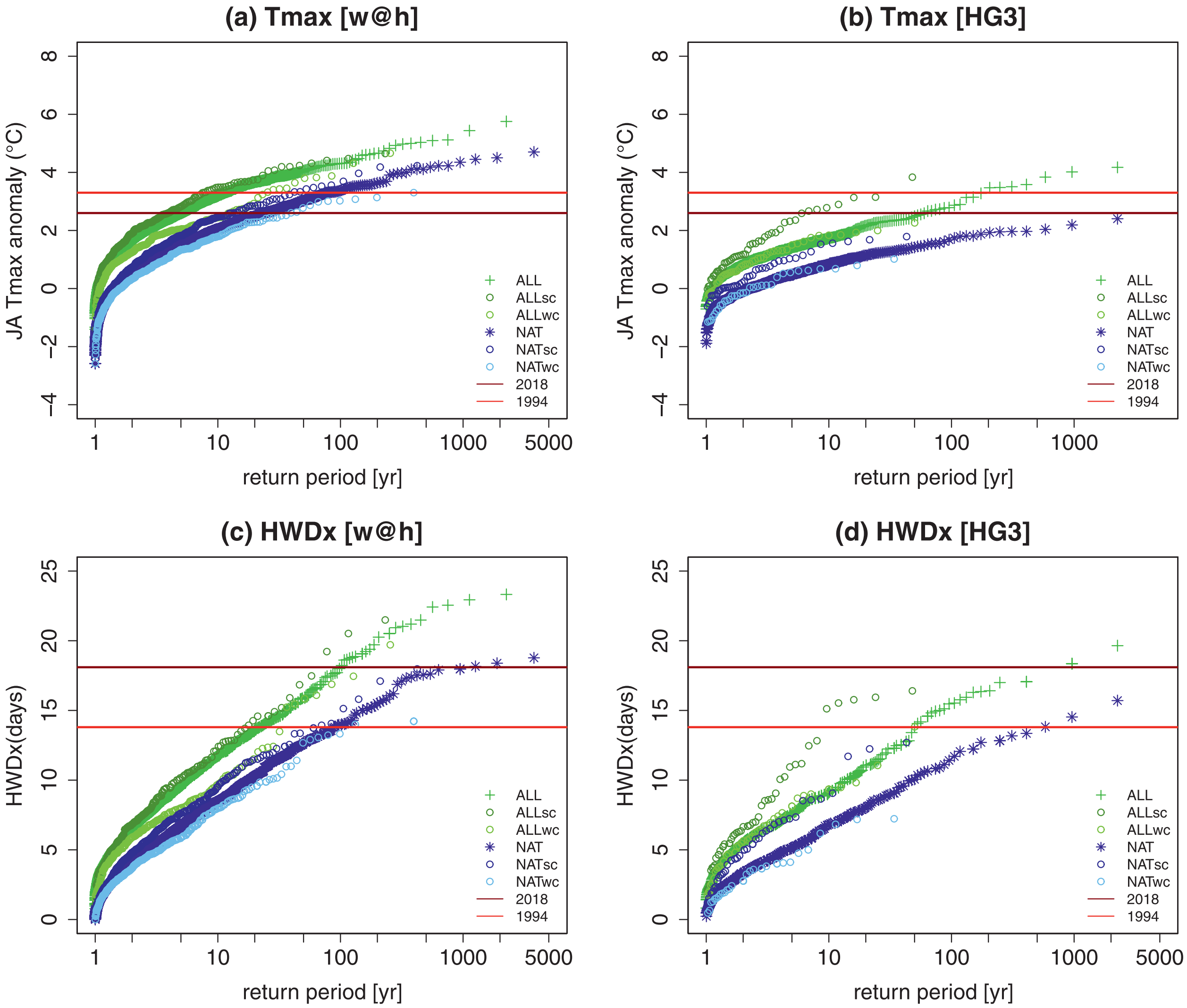

Fig. 2. Return periods of (a),(b) the JA mean T_{max} anomalies and (c),(d) HWDx for ALL (green) and NAT (blue) simulations from w@h and HadGEM3-A-N216 (HG3). Kernel density distributions in Fig. ES2 are used to estimate return periods. The purple and red horizontal lines indicate the observed 2018 and 1994 values, respectively. Minor ticks on the *x* axis indicate 2, 5, 20, 50, 200, 500, etc. Results from subsampled ensemble members are displayed with stronger (OLR below the 30th percentile; ALLsc and NATsc) and weaker convection (OLR above the 70th percentile; ALLwc and NATwc) over two convection zones (see Fig. 1e). For HadGEM3-A-N216, precipitation is used instead of OLR. Refer to Table ES1 for corresponding RR values.

the small sample size and the smaller variability of HadGEM3-A-N216 as mentioned above, the consistent shift of the probability distribution indicates the increased risk of extreme events due to anthropogenic warming. When using the 1994 observed value (13.8 days, second highest record) as another observed threshold, results support this conclusion, providing a large RR of 5.8 (2.6–15.6) with P_{ALL} = 4.4% and P_{NAT} = 0.8% (Table ES1). For w@h, the RR remains large as 4.1 (3.9–5.5).

To examine the influence of boundary SST conditions estimated for NAT (see above), we have divided the w@h ensembles into 13 groups based on the delta-SSTs provided by GCMs (see Table ES2) and repeated our RR analysis. Results show a large spread in RRs across the delta-SST estimates (Fig. ES4), which is found to be significantly related to the different aerosol sensitivity of GCMs that provide the delta-SSTs, reaffirming previous studies (Kim et al. 2018; Min et al. 2019). In spite of the large spread, RRs remain larger than unity in all cases, which supports that the probability of occurrence of 2018-like summer heat wave intensity and maximum duration has increased due to the human activities.

To explore the extent to which the stronger tropical convection has contributed to the 2018 extreme heat wave, we have compared the T_{max} and HWDx distributions constructed from samples with stronger tropical convection with those with weaker tropical convection. The samples with stronger (weaker) convection were selected when OLR anomalies over two convection zones (black boxes in Fig. 1e) are below the 30th percentile (above the 70th percentile). For HadGEM3-A-N216, precipitation was used to construct the distributions because OLR data are not available. Results show that when the tropical convection is stronger, the return times of extreme events decrease for both T_{max} and HWDx, and vice versa (Fig. 2). Accordingly, P_{ALL} increases from 19.8% to 25.9% and P_{NAT} increases from 4.2% to 7.8% for T_{max} from w@h. For HWDx, P_{ALL} increases from 1.0% to 1.7% from w@h and 0.76% to 2.1% from HadGEM3-A-N216 (Fig. ES2). However, the resulting RRs remain overall similar, larger than 3 (Table ES1), indicating consistent human influences on the increased intensity and the extended duration of heat wave, irrespective of the influence of tropical convection. Nevertheless, disproportionate responses in RRs to convection strengths between ALL and NAT imply that the SST warming pattern prescribed can be important (Risser et al. 2017).

CONCLUDING REMARKS. High-resolution large-ensemble simulations from an atmospheric RCM (w@h) and an atmospheric GCM (HadGEM3-A-N216) consistently show increases in the likelihood of a 2018-like extreme heat wave intensity and maximum duration by at least 4 times, when including anthropogenic forcing (mainly due to greenhouse gas increases). Further, comparisons of sub-sampled model simulations suggest that strong tropical convection activity over two regions (northwestern India and South China Sea) seems to have contributed to the increased probability of the heat wave intensity and duration by up to a factor of 2. However, human influences on heat waves, as quantified by RR values, remain overall unaffected by the strength of tropical convection, suggesting that the local thermodynamic factor would be more important than the non-local factors including large-scale teleconnection changes.

ACKNOWLEDGMENTS. This work was supported by the Korea Meteorological Administration Research and Development Program under Grants KMI2018-01214 and 1365003000 and by a National Research Foundation of Korea (NRF) grant funded by the South Korean government (MSIT) (NRF-2018R1A5A1024958). We thank the Met Office Hadley Centre PRECIS team for their technical and scientific support for the development and application of weather@home. We also thank all of the volunteers who have donated their computing time to climateprediction.net and weather@home. Fraser C. Lott and Peter A. Stott were supported by the U.K.–China Research and Innovation Partnership Fund through the Met Office Climate Science for Service Partnership (CSSP) China as part of the Newton Fund.

REFERENCES

Anderson, G. B., and M. L. Bell, 2011: Heat waves in the United States: Mortality risk during heat waves and effect modification by heat wave characteristics in 43 U.S. communities. *Environ. Health Perspect.*, **119**, 210–218, https://doi.org/10.1289/ehp.1002313.

Ciavarella, A., and Coauthors, 2018: Upgrade of the HadGEM3-A based attribution system to high resolution and a new validation framework for probabilistic event attribution. *Wea. Climate Extremes*, **20**, 9–32, https://doi.org/10.1016/j.wace.2018.03.003.

D'Ippoliti, D., and Coauthors, 2010: The impact of heat waves on mortality in 9 European cities: results from the EuroHEAT project. *Environ. Health*, **9**, 37, https://doi.org/10.1186/1476-069X-9-37.

Donat, M. G., and Coauthors, 2013: Updated analyses of temperature and precipitation extreme indices since the beginning of the twentieth century: The HadEX2 dataset. *J. Geophys. Res.*, **118**, 2098–2118, https://doi.org/10.1002/JGRD.50150.

Easterling, D. R., K. E. Kunkel, M. F. Wehner, and L. Sun, 2016: Detection and attribution of climate extremes in the observed record. *Wea. Climate Extremes*, **11**, 17–27, https://doi.org/10.1016/j.wace.2016.01.001.

Guillod, B. P., and Coauthors, 2017: weather@home2: Validation of an improved global-regional climate modeling system. *Geosci. Model Dev.*, **10**, 1849–1872, https://doi.org/10.5194/gmd-10-1849-2017.

KCDC, 2018: Annual report on the notified patients with heat-related illness in Korea (in Korean). Korea Centers for Disease Control and Prevention, 56 pp.

Kim, M.-K., J.-S. Oh, C.-K. Park, S.-K. Min, K.-O. Boo, and J.-H. Kim, 2019: Possible impact of the diabatic heating over the Indian subcontinent on heat waves in South Korea. *Int. J. Climatol.*, **39**, 1166–1180, https://doi.org/10.1002/joc.5869.

Kim, Y.-H., S.-K. Min, D. A. Stone, H. Shiogama, and P. Wolski, 2018: Multi-model event attribution of the summer 2013 heat wave in Korea. *Wea. Climate Extremes*, **20**, 33–44, https://doi.org/10.1016/j.wace.2018.03.004.

Lee, W.-S., and M.-I. Lee, 2016: Interannual variability of heat waves in South Korea and their connection with large-scale atmospheric circulation patterns. *Int. J. Climatol.*, **36**, 4815–4830, https://doi.org/10.1002/joc.4671.

Massey, N., and Coauthors, 2015: weather@home—Development and validation of a very large ensemble modelling system for probabilistic event attribution. *Quart. J. Roy. Meteor. Soc.*, **141**, 1528–1545, https://doi.org/10.1002/qj.2455.

Min, S.-K., Y.-H. Kim, M.-K. Kim, and C. Park, 2014: Assessing human contribution to the summer 2013 Korean heat wave [In "Explaining Extreme Events of 2013 from a Climate Perspective"]. *Bull. Amer. Meteor. Soc.*, **95**, S48–S51, https://journals.ametsoc.org/doi/pdf/10.1175/1520-0477-95.9.S1.1.

——, ——, I.-H. Park, D. Lee, S. Sparrow, D. Wallom, and D. Stone, 2019: Anthropogenic contribution to the 2017 earliest summer onset in South Korea. *Bull. Amer. Meteor. Soc.*, **100** (1), S73–S77, https://doi.org/10.1175/BAMS-D-18-0096.1.

Paciorek, C. J., D. A. Stone, and M. F. Wehner, 2018: Quantifying statistical uncertainty in the attribution of human influence on severe weather. *Wea. Climate Extremes*, **20**, 69–80, https://doi.org/10.1016/j.wace.2018.01.002.

Park, B.-J., Y.-H. Kim, S.-K. Min, M.-K. Kim, Y. Choi, K.-O. Boo, and S. Shim, 2017: Long-term warming trends in Korea and contribution of urbanization: An updated assessment. *J. Geophys. Res.*, **122**, 10 637–10 654, https://doi.org/10.1002/2017JD027167.

Risser, M. D., D. A. Stone, C. J. Paciorek, M. F. Wehner, and O. Angélil, 2017: Quantifying the effect of interannual ocean variability on the attribution of extreme climate events to human influence. *Climate Dyn.*, **49**, 3051–3073, https://doi.org/10.1007/s00382-016-3492-x.

Schaller, N., and Coauthors, 2016: Human influence on climate in the 2014 southern England winter floods and their impacts. *Nat. Climate Change*, **6**, 627–634, https://doi.org/10.1038/nclimate2927.

Sparrow, S., and Coauthors, 2018: Attributing human influence on the July 2017 Chinese heatwave: The influence of sea-surface temperatures. *Environ. Res. Lett.*, **13**, 114004, https://doi.org/10.1088/1748-9326/aae356.

Yeo, S.-R., S.-W. Yeh, and W.-S. Lee, 2019: Two types of heat wave in Korea associated with atmospheric circulation pattern. *J. Geophys. Res.*, **124**, 7498–7511, https://doi.org/10.1029/2018JD030170.

chapter 19

THE HEAVY RAIN EVENT OF JULY 2018 IN JAPAN ENHANCED BY HISTORICAL WARMING

Hiroaki Kawase, Yukiko Imada, Hiroshige Tsuguti, Toshiyuki Nakaegawa,
Naoko Seino, Akihiko Murata, and Izuru Takayabu

The unprecedented precipitation total in Japan during the heavy rain event of July 2018 was increased by approximately 7% due to recent rapid warming around Japan.

Extremely heavy precipitation occurred from central to western Japan in July 2018, which was named the "heavy rain event of July 2018" by the Japan Meteorological Agency (JMA). The JMA has approximately 1,300 in situ stations. The 48- and 72-h total precipitation records were broken at 125 and 123 in situ stations, respectively, from 28 June to 8 July (the dates are different in the individual in situ stations). The 10-day total precipitation accumulated at all Japanese in situ stations was the highest for any 10-day periods starting on the 1st, 11th, and 21st of the month since 1982 (Fig. 1a) (Shimpo et al. 2019; TCC JMA 2018). During the heavy rainfall event, there were 221 fatalities, and more than 6,000 buildings were destroyed by floods and landslides (Cabinet Office, Government of Japan 2018). The continuous lower-level moisture transport maintained the active stationary weather front for a couple of days and the passage of the upper-level trough enhanced the heavy precipitation at the end of this heavy rainfall event (Shimpo et al. 2019; TCC JMA 2018). Mesoscale line-shaped precipitation systems appeared locally and strengthened the heavy precipitation in some areas of western Japan (Tsuguti et al. 2019).

AFFILIATIONS: Kawase, Imada, Nakaegawa, Seino, Murata, and Takayabu—Meteorological Research Institute, Japan Meteorological Agency, Ibaraki, Japan; Tsuguti—Japan Meteorological Agency, Tokyo, Japan
CORRESPONDING AUTHOR: Hiroaki Kawase, hkawase@mri-jma.go.jp

DOI:10.1175/BAMS-D-19-0173.1

A supplement to this article is available online (10.1175/BAMS-D-19-0173.2)

In recent years, the surface air temperature during the summer has been increasing rapidly in Japan. The moisture that the atmosphere may hold has increased by approximately 7% K^{-1} as dictated by the Clausius–Clapeyron relationship. The observed specific humidity at 850 hPa in July shows a rapid increase around Japan from 1981 to 2018 (Shimpo et al. 2019; TCC JMA 2018). It is possible that recent warming and moistening due to global warming contributed to the heavy rain event of July 2018.

Event attribution (EA) is useful for the attribution of specific extreme events, such as heat waves and drought, to global warming due to anthropogenic forcing (e.g., Stott et al. 2004; Shiogama et al. 2013, 2014; Imada et al. 2014). EA uses large ensemble historical and non-warming simulations performed by general circulation models (GCMs) and probabilistically attributed the extreme event to global warming. For the latest extreme event in Japan, Imada et al. (2019) revealed that the July 2018 heat wave event in Japan would have been virtually impossible without anthropogenic global warming. Kim et al. (2019, personal communication) revealed that the combination of extreme events in Japan, such as the serious flood and heatwave events that occurred in 2018, could be heavily influenced by global warming, even though the intermodel variability is large. However, it is difficult to adapt the EA to heavy precipitation events. Imada et al. (2013) attributed the heavy precipitation event occurring in southwestern Japan in 2012 to global warming using the atmospheric GCM (AGCM) with approximately 150-km horizontal resolution, while they could not simulate the local-scale heavy precipitation. Higher-resolution simulations, such as 5-km grid spacings, are needed to directly reproduce such heavy precipitation influenced by the complex orography in Japan.

The storyline approach (Shepherd et al. 2018) is the other approach to evaluating the impact of

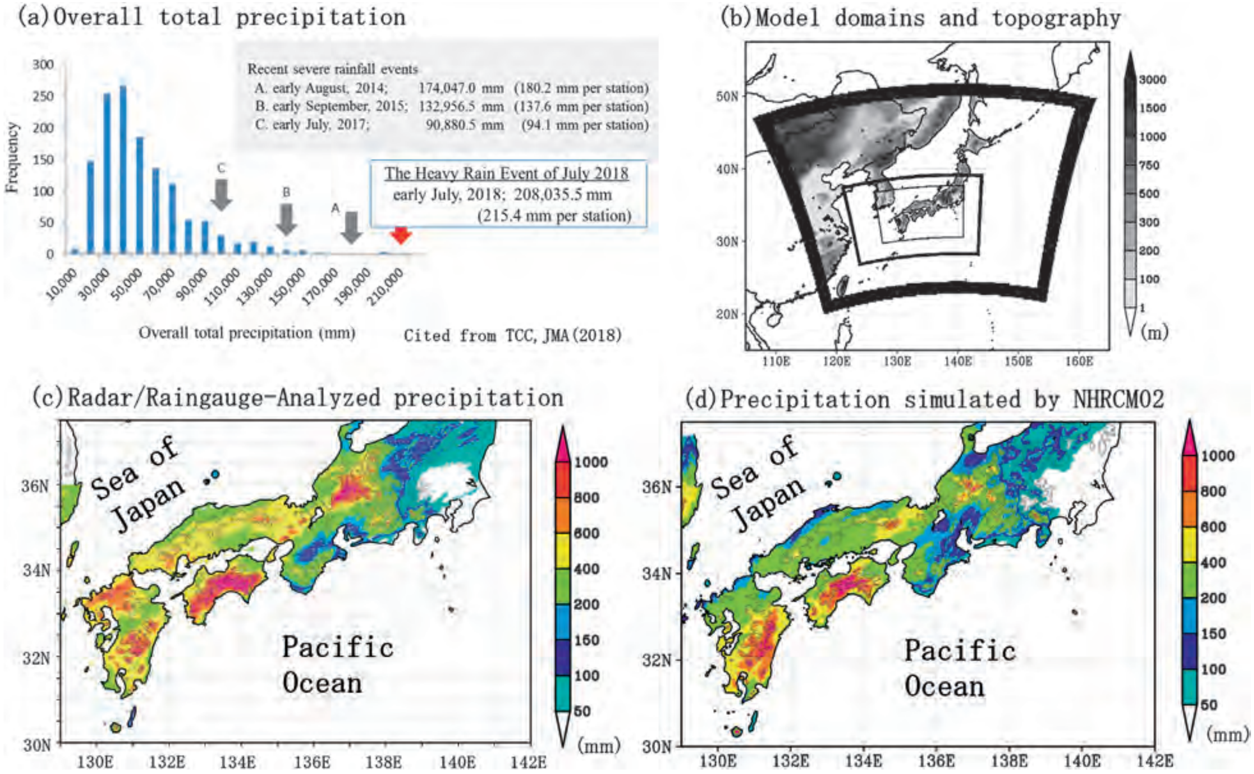

Fig. 1. (a) Frequency distribution of overall total precipitation at 966 selected in situ stations throughout Japan for 10-day periods (TCC JMA 2018). (b) Model domains and topography. Outer, middle, and inner areas represent domains of NHRCM20, NHRCM05, and NHRCM02, respectively. (c) Radar/rain gauge-analyzed precipitation from 0000 JST 28 Jul to 2300 JST 8 Aug 2019. (d) As in (c), but showing total precipitation simulated by NHRCM02.

global warming on extreme events. In the storyline approach, specific extreme events are simulated by the high-resolution regional climate model with realistic boundary conditions based on the reanalysis data. Then, the impact of global warming is quantitatively evaluated by the counterfactual simulations without the historical warming component estimated by the reanalysis data or global climate simulations. The storyline approach is useful for extreme events caused by mesoscale systems such as stationary weather fronts and tropical cyclones (e.g., Takayabu et al. 2015). For the heavy rain event of July 2018 in Japan, we applied the storyline approach using a regional climate model and evaluated the impact of recent warming and moistening on precipitation amounts.

METHODS. We reproduced the heavy rain event of July 2018 using the Non-Hydrostatic Regional Climate Model (NHRCM) (Sasaki et al. 2008). The boundary conditions were obtained from the Japanese 55-Year Reanalysis (JRA-55) (Kobayashi et al. 2015) whose horizontal resolution is 1.25°. The horizontal grid spacings of NHRCM were 20, 5, and 2 km in the outer, middle, and inner domains (hereafter referred to as NHRCM20, NHRCM05, and NHRCM02), respectively (Fig. 1b). Both the cumulus convective parameterization scheme (Kain and Fritsch 1993) and a cloud microphysics scheme (Ikawa et al. 1991) were used in NHRCM20 and NHRCM05. Only the cloud microphysics scheme was used in NHRCM02, which is a so-called convection-permitting model. The convection-permitting model can simulate local-scale heavy precipitation influenced by the complex orography and mesoscale convective systems (Prein et al. 2015). The initial date of NHRCM20 was 20 June 2019. NHRCM05 runs started on five different initial dates, from 22 to 26 June, for conducting simplified ensemble experiments. The initial date of NHRCM02 was 27 June in all ensemble experiments. These hindcast experiments are hereafter called CTL2018 runs. The radar/rain gauge-analyzed precipitation amount produced by JMA was used to validate the precipitation simulated by NHRCM02.

We calculated four kinds of linear trends of regional-mean air temperature at each pressure level and sea surface temperature (SST) during the summer [an average of June–August (JJA)] and each month (June, July, and August separately) from 1980 to 2018, when the temperature rise was accelerated around Japan. The regional-mean JJA temperature at 1,000 hPa showed a rapid increase with a large interannual variability (Fig. 2a). The warming trend was largest in July (1.11 K per 39 years at 1,000 hPa) and smallest in June (0.75 K), whereas the trend in August (1.04 K) was similar to that in JJA (0.96 K). Note that the temperature trend in reanalysis data includes a natural decadal variability in addition to human-induced global warming. We performed a similar hindcast simulation using the JRA-55 without these four recent warming trends, which are hereafter called the DeTRND2018_JJA, DeTRND2018_JUN, DeTRND2018_JUL, and DeTRND2018_AUG runs, respectively. Each experiment had five ensemble runs using the different initial dates of NHRCM05.

RESULTS. The ensemble mean of five CTL2018 runs well reproduces the horizontal distribution of total precipitation during the heavy rain event of July 2018 (Figs. 1c,d). Time sequences of regional mean precipitation show that NHRCM02 simulates the timing of heavy precipitation periods on 29–30 June, 3–4 July, and 5–7 July (Fig. 2c). The total precipitation amount is, however, underestimated over land. The observed and simulated regional mean total precipitation over land are 357.0 and 269.2 mm, respectively, in 129°–142°E and 30°–37.5°N. The underestimation of precipitation over the coastal areas along the Sea of Japan corresponds to the bias in the location of the stationary weather front simulated by NHRCM02.

Figure 2b shows the difference in the total precipitation over land between the ensemble mean of the CTL2018 runs and the ensemble mean of the DeTRND2018 runs. The majority of areas show that the precipitation amount is larger in CTL2018 than that in DeTRND2018, suggesting that the recent warming might strengthen the heavy precipitation. We compared the time sequences of the accumulated precipitation amounts between CTL2018 and DeTRND2018 during the heavy precipitation period (Fig. 2c). The difference in the ensemble mean precipitation amounts became larger after 5 July. At the end of the heavy precipitation event, the difference in accumulated precipitation between CTL2018 and ensemble-mean DeTRND2018 runs was 17.0 mm, which is equivalent to 6.7% relative to DeTRND2018. To consider the uncertainty in the detrending method, the discrepancies among the DeTRND2018 ensemble runs (thin blue lines), which result from the four temperature trends eliminated from JRA-55, are also estimated. The percentages of differences in precipitation amounts are +7.4%, +6.5%, +2.7%, and +10.7% relative to DeTRND2018_JJA, DeTRND2018_JUN, DeTRND2018_JUL, and DeTRND2018_AUG, respectively. The variation using five different initial dates is much smaller than that using four different temperature trends (Fig. 2d). The difference of precipitation in DeTRND2018_JUL is smallest among four experiments, while the difference of air temperature at 1,000 hPa is the largest among them. These results indicate that the changes in precipitation due to warming do not necessarily correspond to the low-level temperature changes.

Changes in SST influence the low-level moisture because most water vapor is derived from the ocean around Japan. In addition, the atmospheric moist stability is modulated by changes in the vertical profiles of equivalent potential temperatures and saturated equivalent potential temperatures. Our experiments indicate that changes in the moist stability (i.e., $\theta_e 1000 - \theta_e^* 600$ in the table in Fig. 2) contribute to changes in precipitation amounts. DeTRND2018_AUG (DeTRND2018_JUN) shows the largest (smallest) changes in stability and results in the largest (smallest) increase in precipitation. Hibino et al. (2018) pointed out that, in the future climate, the effect of moistening due to global warming on extreme precipitation in Japan could be cancelled out by the suppression of convection due to the enhancement of thermal stability.

According to the JRA-55 reanalysis data, the increases in air temperature at 1,000 hPa are 0.96, 0.75, 1.11, and 1.04 K in JJA, June, July, and August, respectively. If we assume 7% increase for every degree according to the Clausius–Clapeyron relation, the percentages are 6.7%, 5.3%, 7.8%, and 7.3%, respectively. Approximately 6.7% increase in precipitation is in the expected range. However, our results indicated that the changes in heavy precipitation are also influenced by the changes in atmospheric moist stability, which can be additional uncertainty sources in changes in heavy precipitation due to global warming. Therefore, evaluations of not only atmospheric warming but also changes in atmospheric moist stability due to global warming are necessary to quantitatively assess the impact of global warming on long-lasting heavy precipitation events, such as the heavy rain event of July 2018.

Additional experiments are conducted assuming a warmer climate than the current climate and using five initial dates. Here, the JJA temperature trends are extrapolated by the past temperature trend for same term (39 yr) and added into 2018. Mean total precipitation increases by 6.1% relative to CTL2018 in the warmer condition (see Fig. ES1 in the online supplemental material).

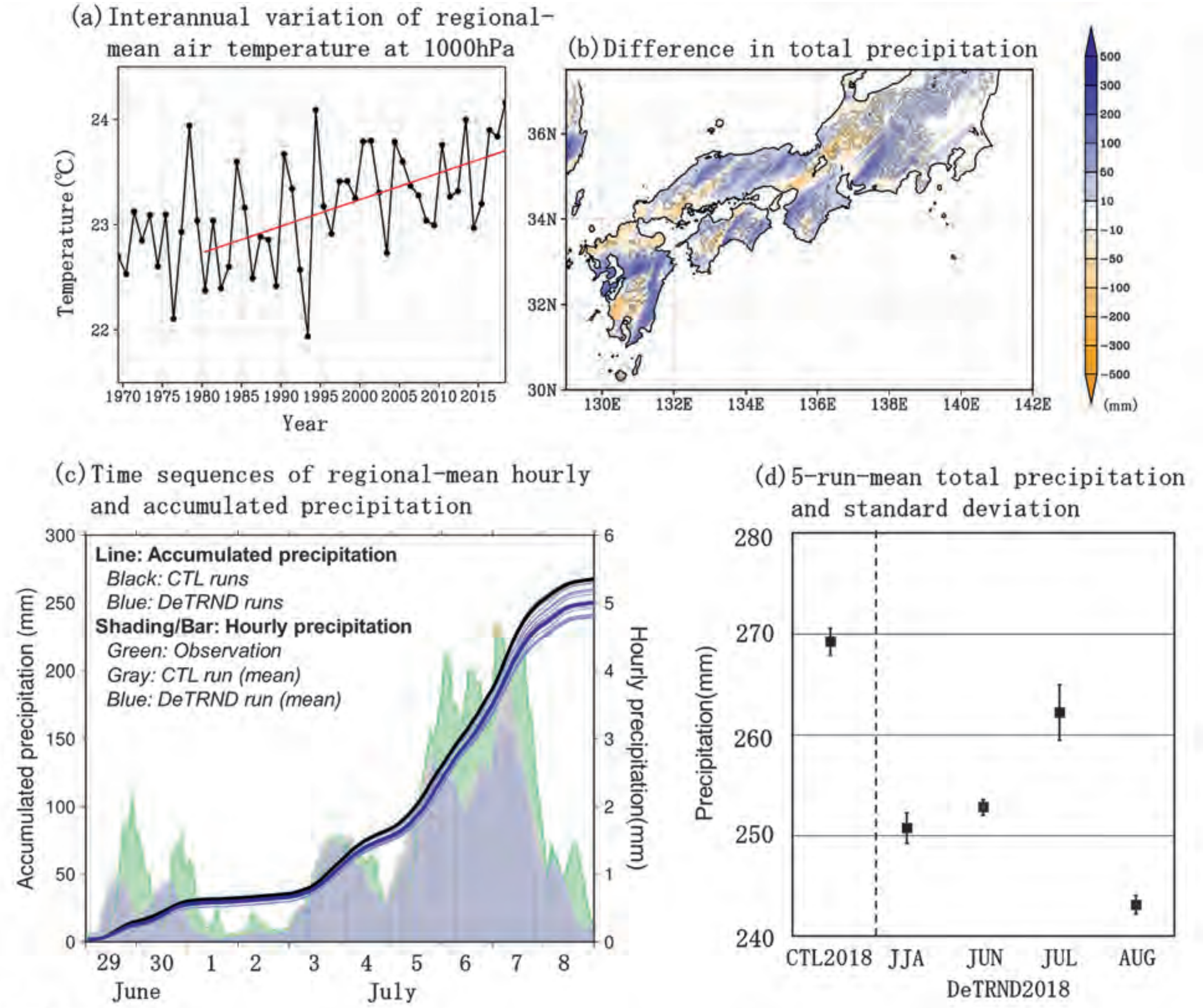

Table

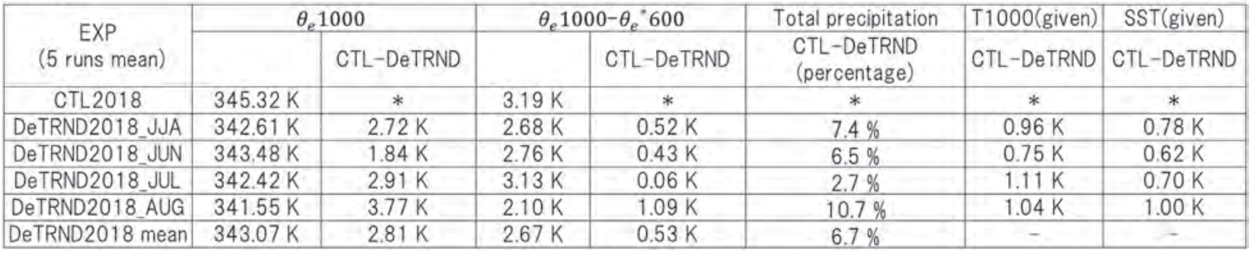

EXP (5 runs mean)	θ_e1000		θ_e1000−θ_e^*600		Total precipitation	T1000(given)	SST(given)
		CTL−DeTRND		CTL−DeTRND	CTL−DeTRND (percentage)	CTL−DeTRND	CTL−DeTRND
CTL2018	345.32 K	*	3.19 K	*	*	*	*
DeTRND2018_JJA	342.61 K	2.72 K	2.68 K	0.52 K	7.4 %	0.96 K	0.78 K
DeTRND2018_JUN	343.48 K	1.84 K	2.76 K	0.43 K	6.5 %	0.75 K	0.62 K
DeTRND2018_JUL	342.42 K	2.91 K	3.13 K	0.06 K	2.7 %	1.11 K	0.70 K
DeTRND2018_AUG	341.55 K	3.77 K	2.10 K	1.09 K	10.7 %	1.04 K	1.00 K
DeTRND2018 mean	343.07 K	2.81 K	2.67 K	0.53 K	6.7 %	–	–

Fig. 2. (a) Interannual variation of regional-mean air temperature at 1,000 hPa at 120°–145°E, 30°–40°N in JJA. A red line represents a linear trend from 1980 to 2018. (b) Difference of total precipitation between the ensemble means of CTL2018 and DeTRND2018. Blue (orange) colors indicate that the precipitation amount in CTL2018 is larger (smaller) than that in DeTRDN2018. (c) Time sequence of regional-mean overland precipitation in central and western Japan. Black and blue lines represent regional-mean accumulated precipitation simulated by the CTL2018 and DeTRND2018 runs, respectively. Bold lines represent the corresponding ensemble means. Shadings and bars show the regional-mean hourly precipitation: the observation (green), CTL2018 (gray), and DeTRND2018 (blue). (d) Mean total precipitation and standard deviations simulated by each experiment. (table) Differences of several indices between CTL2018 and DeTRND2018. T1000, θ_e1000 and θ_e^*600 represent temperature at 1,000 hPa, equivalent potential temperature at 1,000 hPa, and saturated equivalent potential temperature at 600 hPa, respectively.

CONCLUSIONS. The contribution of historical global warming on the heavy rain event of July 2018 in Japan was quantitatively evaluated by using NHRCM02 forced by the JRA-55 reanalysis data. The NHRCM02 well simulated the horizontal distribution and timing of heavy rainfall over western and eastern Japan. Sensitivity experiments, in which linear trends of summer-mean and each monthly-mean temperature from 1980 to 2018 are eliminated from the boundary conditions, showed the increases in total precipitation due to recent warming. Total precipitation in the CTL2018 runs is approximately 6.7% (+2.7% to +10.7%) larger than that in the ensemble-mean DeTRND2018 runs. These changes in precipitation are induced by not only changes in atmospheric temperature, which relates to Clausius–Clapeyron relationship, but also changes in the SST and atmospheric moist stability. Either way, our results indicate that historical warming definitely contributed to the increase in total precipitation of the heavy rain event of July 2018 in Japan. This study employs a storyline approach to control for the specific weather phenomena associated with this extreme event. Future work is required to assess the change in frequency of background synoptic conditions causing the heavy rain event of July 2018 in Japan.

ACKNOWLEDGMENTS. This work was supported by the TOUGOU program of the Japanese Ministry of Education, Culture, Sports, Science and Technology (MEXT) and also supported by Japan Science and Technology Agency (JST) and Japan Society for the Promotion of Science (JSPS) Grants-in-Aid for Scientific Research (KAKENHI) Grants 16H01844 and 18K19951.

REFERENCES

Cabinet Office, Government of Japan, 2018: Summary: The damage situations caused by the heavy rain in July 2018 (in Japanese). 204 pp., http://www.bousai.go.jp/updates/h30typhoon7/pdf/300905_1700_h30typhoon7.pdf.

Hibino, K., I. Takayabu, Y. Wakazuki, and T. Ogata, 2018: Physical responses of convective heavy rainfall to future warming condition: Case study of the Hiroshima event. *Front. Earth Sci.*, **6**, 35, https://doi.org/10.3389/feart.2018.00035.

Ikawa, M., H. Mizuno, T. Matsuo, M. Murakami, Y. Yamada, and K. Saito, 1991: Numerical modeling of the convective snow cloud over the Sea of Japan—Precipitation mechanism and sensitivity to ice crystal nucleation rates. *J. Meteor. Soc. Japan*, **69**, 641–667, https://doi.org/10.2151/jmsj1965.69.6_641.

Imada, Y., M. Watanabe, M. Mori, M. Kimoto, H. Shiogama, and M. Ishii, 2013: Contribution of atmospheric circulation change to the 2012 heavy rainfall in southwestern Japan [in "Explaining Extreme Events of 2012 from a Climate Perspective"]. *Bull. Amer. Meteor. Soc.*, **94** (9), S52–S54, https://doi.org/10.1175/BAMS-D-13-00085.1.

——, H. Shiogama, M. Watanabe, M. Mori, M. Ishii, and M. Kimoto, 2014: The contribution of anthropogenic forcing to the Japanese heat waves of 2013 [in "Explaining Extreme Events of 2013 from a Climate Perspective"]. *Bull. Amer. Meteor. Soc.*, **95** (9), S52–S54.

——, M. Watanabe, H. Kawase, H. Shiogama, and M. Arai, 2019: The July 2018 high temperature event in Japan could not have happened without human-induced global warming. *SOLA*, **15**, 8–12, https://doi.org/10.2151/SOLA.15A-002.

Kain, J. S., and J. M. Fritsch, 1993: Convective parameterization for mesoscale models: The Kain–Fritsch scheme. The Representation of Cumulus Convection in Numerical Models, Meteor. Monogr., No. 46, er165–170.

Kobayashi, S., and Coauthors, 2015: The JRA-55 Reanalysis: General specifications and basic characteristics. *J. Meteor. Soc. Japan*, **93**, 5–48, https://doi.org/10.2151/jmsj.2015-001.

Prein, A. F., and Coauthors, 2015: A review on regional convection-permitting climate modeling: Demonstrations, prospects, and challenges. *Rev. Geophys.*, **53**, 323–361, https://doi.org/10.1002/2014RG000475.

Sasaki, H., K. Kurihara, I. Takayabu, and T. Uchiyama, 2008: Preliminary experiments of reproducing the present climate using the non-hydrostatic regional climate model. *SOLA*, **4**, 25–28, https://doi.org/10.2151/SOLA.2008-007.

Shepherd, T. G., and Coauthors, 2018: Storylines: An alternative approach to representing uncertainty in physical aspects of climate change. *Climatic Change*, **151**, 555–571, https://doi.org/10.1007/s10584-018-2317-9.

Shimpo, A., and Coauthors, 2019: Primary factors behind the Heavy Rain Event of July 2018 and the subsequent heat wave in Japan. *SOLA*, **15A**, 13–18, https://doi.org/10.2151/sola.15A-003.

Shiogama, H., M. Watanabe, Y. Imada, M. Mori, M. Ishii, and M. Kimoto, 2013: An event attribution of the 2010 drought in the South Amazon region using the MIROC5 model. *Atmos. Sci. Lett.*, **14**, 170–175, https://doi.org/10.1002/asl2.435.

——, M. Watanabe, Y. Imada, M. Mori, Y. Kamae, M. Ishii, and M. Kimoto, 2014: Attribution of the June–July 2013 heat wave in the southwestern United States. *SOLA*, **10**, 122–126, https://doi.org/10.2151/SOLA.2014-025.

Stott, P. A., D. A. Stone, and M. R. Allen, 2004: Human contribution to the European heatwave of 2003. *Nature*, **432**, 610–614, https://doi.org/10.1038/nature03089.

Takayabu, I., K. Hibino, H. Sasaki, H. Shiogama, N. Mori, Y. Shibuya, and T. Takemi, 2015: Climate change effects on the worst-case storm surge: A case study of Typhoon Haiyan. *Environ. Res. Lett.*, **10**, 064011, https://doi.org/10.1088/1748-9326/10/6/064011.

TCC JMA, Japan Meteorological Agency, 2018: Primary factors behind the Heavy Rain Event of July 2018 and the subsequent heatwave in Japan from mid-July onward. Tokyo Climate Center, Japan Meteorological Agency, 24 pp., https://ds.data.jma.go.jp/tcc/tcc/news/press_20180822.pdf.

Tsuguti, H., N. Seino, H. Kawase, Y. Imada, T. Nakaegawa, and I. Takayabu, 2019: Meteorological overview and mesoscale characteristics of the Heavy Rain Event of July 2018 in Japan. *Landslides*, **16**, 363–371, https://doi.org/10.1007/s10346-018-1098-6.

DECONSTRUCTING FACTORS CONTRIBUTING TO THE 2018 FIRE WEATHER IN QUEENSLAND, AUSTRALIA

Sophie C. Lewis, Stephanie A. P. Blake, Blair Trewin, Mitchell T. Black,
Andrew J. Dowdy, Sarah E. Perkins-Kirkpatrick, Andrew D. King, and Jason J. Sharples

Factors including the circulation pattern and antecedent conditions contributed to 2018 northeast Australian fires. High background temperatures also played a role for which model evidence suggests an anthropogenic influence.

EVENT DESCRIPTION AND STUDY APPROACH. Significant wildfires occurred across various regions in 2018. The 2018 bushfire season was declared early in many Australian jurisdictions. By 30 November 2018, 130 bushfires in Queensland, northern Australia, had caused significant damage and burned nearly 3/4 million hectares (see Australian Bureau of Meteorology 2018). Bushfires on the scale of the 24 to 29 November event (hereafter simply called "the fires") occurring in this coastal Queensland location (see Fig. 1) were unprecedented.

The McArthur Forest Fire Danger Index (FFDI) is used to assess dangerous bushfire weather conditions in Australia (Noble et al. 1980). The FFDI increased considerably in the last week of November and was the highest on record (from 1950) in some areas. During 24–29 November, daily FFDI values were "extreme" (FFDI ≥ 75) for large parts of Queensland and "catastrophic" (FFDI ≥ 100) in some locations. The FFDI includes a measure of fuel moisture content calculated from antecedent rainfall and temperature, daily temperature, relative humidity (RH), and wind speed (V). The 99th percentile FFDI (number of days > 99th percentile) is discussed here as indicative of the extreme end of the fire risk spectrum based on these weather conditions.

The 2018 fire occurred during a period of synoptic- and large-scale extremes. This is typical of a compound extreme event (Zscheischler et al. 2018) and makes definition and analysis of the event as a single variable limited. Prior research cautions that direct attribution of the FFDI to specific forcings (e.g., anthropogenic greenhouse gases) is complicated by the index's integration of multiple dependent variables (Black 2017). Model bias correction of one variable (e.g., temperature) requires its relationship with others (e.g., humidity) to be preserved. While explicit examination of the FFDI may be possible with multivariate bias correction (e.g., Cannon 2018), we adopt an alternative approach and instead examine FFDI components separately. As individual variables have different weightings in the FFDI calculation and are affected by climate change differently (Black 2017), it is valuable to examine each separately in order to determine the factors contributing to the extreme fire and heatwave period. We deconstruct the observed key synoptic features during November and the conditioning heatwave event (defined as 24 to 29 November 2018, hereafter "the event") and large-scale 2018 conditions [antecedent conditions in spring (September–November) and in November only, and large-scale modes of variability). Using two climate model attribution [CMIP5 (Taylor et al. 2012) and weather@home (Black et al. 2016)] frameworks, we examine whether aspects of these observed

AFFILIATIONS: Lewis and Blake—School of Science, University of New South Wales, Canberra, Australian Capital Territory, Australia; Trewin, Black, and Dowdy—Bureau of Meteorology, Melbourne, Victoria, Australia; Perkins-Kirkpatrick—Climate Change Research Centre, University of New South Wales, Sydney, New South Wales, Australia; King—School of Earth Sciences, The University of Melbourne, Parkville, Victoria, Australia; Sharples–School of Science, University of New South Wales, Canberra, Australian Capital Territory, and Bushfire and Natural Hazards Cooperative Research Centre, Level 1, East Melbourne, Victoria, Australia.
CORRESPONDING AUTHOR: Sophie C. Lewis, s.lewis@adfa.edu.au

DOI:10.1175/BAMS-D-19-0144.1

A supplement to this article is available online (10.1175/BAMS-D-19-0144.2)

conditions were made more likely due to anthropogenic forcings.

OBSERVED LARGE-SCALE FACTORS.

We focus on the state of Queensland and the region of highest observed fire danger (hereafter "fire region"), which encompasses the major areas burnt.

Temperature. Observed daily maximum temperatures (T_{max}) were anomalously high during November (Fig. 1b). High Tmax and daily minimum temperature (T_{min}) were persistent throughout the event particularly for T_{min} (see Fig. ES1 in the online supplement). Over this period, Queensland area-averaged minimum temperatures are above the observed 95th percentile, and records were broken in many locations (Australian Bureau Of Meteorology 2018). Above-average temperatures also occurred in both regions over spring and November.

Precipitation. Seasonal rainfall was below average over the antecedent spring period (Fig. 1c), which likely favored drier soil moisture conditions and increased Tmax values (Kirono et al. 2017). While rainfall occurred across the state in the days prior to the event (Fig. ES1c), the heatwave event itself lacked significant rainfall. In the major fire-affected regions, August to October is the driest period of the year, and November marks the transition between the dry and wet seasons; for example, Mackay (northern

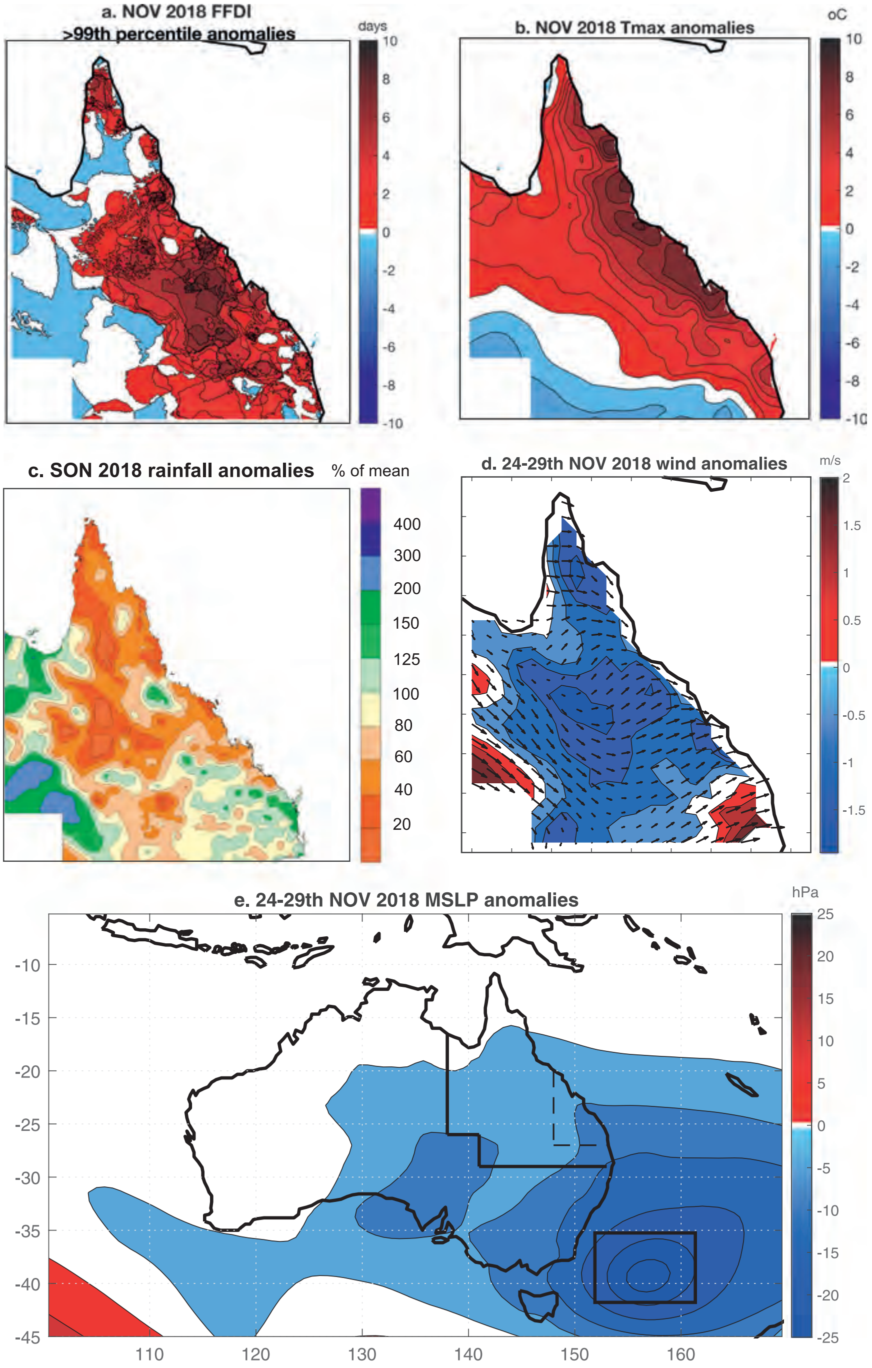

Fig. 1. Summary of key observed meteorological and climatological conditions in Queensland state, northeastern Australia, during the November 2018 fire event. (a) FFDI anomaly (number of days for November 2018 > 99th percentile from 1950–2017 compared to long-term November average from 1950). (b) November 2018 average of daily Tmax anomalies (°C) (relative to long-term average from 1911). (c) Precipitation anomalies for SON (%) relative to mean). (d) Wind speed (m s-1) and (e) direction, and (f) MSLP anomalies (hPa) for the event (24–29 Nov, relative to long-term November mean from 1979). Queensland state is shown, with area of interest for fire shown by dashed box, and the area of anomalously low MSLP in the Tasman Sea.

Table 1. Summary of observed 2018 meteorological and climatological conditions for Queensland and large-scale indices. For the FFDI, the count of FFDI days above the 99th percentile is given for the fire region for November, as are temperature and precipitation values for the fire region for 5-day periods and the annual average large-scale index values. Maximum (or minimum) observed anomalies and ranking of 2018 anomalies (relative to 1961–90) are indicated.

Variable (QLD)	2018 anomaly	Maximum/minimum anomaly	Ranking
FFDI days > 99th percentile (NOV)	4	4 (2018)	1st since 1950
Temperature (EVENT)	3.9°C	3.9°C (2018)	1st since 1950
Temperature (NOV)	1.65°C	2.8°C (2014)	4th since 1950
Precipitation (EVENT)	-1.9 mm day^{-1}	-2.1 mm day^{-1} (2006)	7th since 1950
Precipitation (SON)	-0.2 mm day^{-1}	-0.7 mm day^{-1} (2002)	31st since 1950
Index	2018	Maximum Anomaly	Ranking
ENSO (ANN)	0.66	2.3 (2015)	13th since 1950
SAM (ANN)	2.4	2.4 (2018)	1st since 1950
IOD (ANN)	0.9	1.3 (1997)	2nd since 1950

point of fire region) averages 83 mm for the August–October period and 88 mm for November.

Large-scale context. The state of large-scale ocean–atmosphere modes of variability during 2018 are summarized in Table 1. Most notably, strong positive southern annular mode (SAM) and Indian Ocean dipole (IOD) conditions were observed; however, both these modes are typically associated with rainfall variations over southern Australia, with minimal impact in the north (Risbey et al. 2009; Ummenhofer et al. 2009; Hendon et al. 2016). El Niño–Southern Oscillation (ENSO) conditions were largely neutral. We note that subseasonal drivers, particularly the Madden–Julian Oscillation (MJO), were also influential during the fire event, with MJO-associated tropical cloud and rainfall bands likely contributing to the observed anomalous westward wind flow (Australian Bureau of Meteorology 2018).

OBSERVED SYNOPTIC-SCALE FACTORS.

Wind speed and direction. During the event, anomalous westerly winds (at 10 m) were observed (Fig. 1d). While wind speed was below the long-term November average for most of Queensland (except in coastal southern Queensland), the westerly direction was anomalous for this time of year, which usually experiences landward flow, with westerly winds reported at some tropical coastal sites where they are historically extremely rare in November (Australian Bureau of Meteorology 2018). Anomalous wind features are hence both a risk factor and a key driver of temperature and humidity extremes.

MSLP. Composited daily mean sea level pressure (MSLP) during the 5-day event shows a key low pressure system over southeastern Australia and the Tasman Sea (Fig. 1e), which was noted as a driver of the anomalous southwest to westerly wind flow over Queensland (Australian Bureau Of Meteorology 2018). We use the region of observed anomalously low MSLP in the Tasman Sea (36°–42°S, 152°–162°E) to examine synoptic factors in model simulations.

Humidity. Relative humidity (at 2 m) observed during the event was significantly below average, particularly for the coastal regions of Queensland (not shown).

MODELED LARGE-SCALE CONTRIBUTING FACTORS.

Background climatic conditions observed in 2018 are first examined using CMIP5 monthly and seasonal model data, with risk ratios (RRs) associated with anthropogenic forcings calculated for exceeding 2018 observed anomalies for each variable (see section 2 in the online supplemental material). RRs are a quantification of the change in the probability of an extreme that can be attributed to anthropogenic forcings (e.g., an RR value of 2 indicates a doubling of attributable risk).

Temperature. Notable differences in the distribution of temperatures in the fire region occur in CMIP5 experiments with different forcings (Fig. 2a), with a substantial warm shift in temperatures in RCP8.5 simulations compared to historicalNat scenarios. The shift in probabilities is particularly the case for warm tail temperatures anomalies, consistent with previous studies quantitatively attributing observed Australian temperature extremes to anthropogenic forcings (e.g., Black et al. 2015; Lewis and Karoly 2013; Perkins and Gibson 2015). The RR for exceeding observed 2018 November temperature anomalies is 4.5.

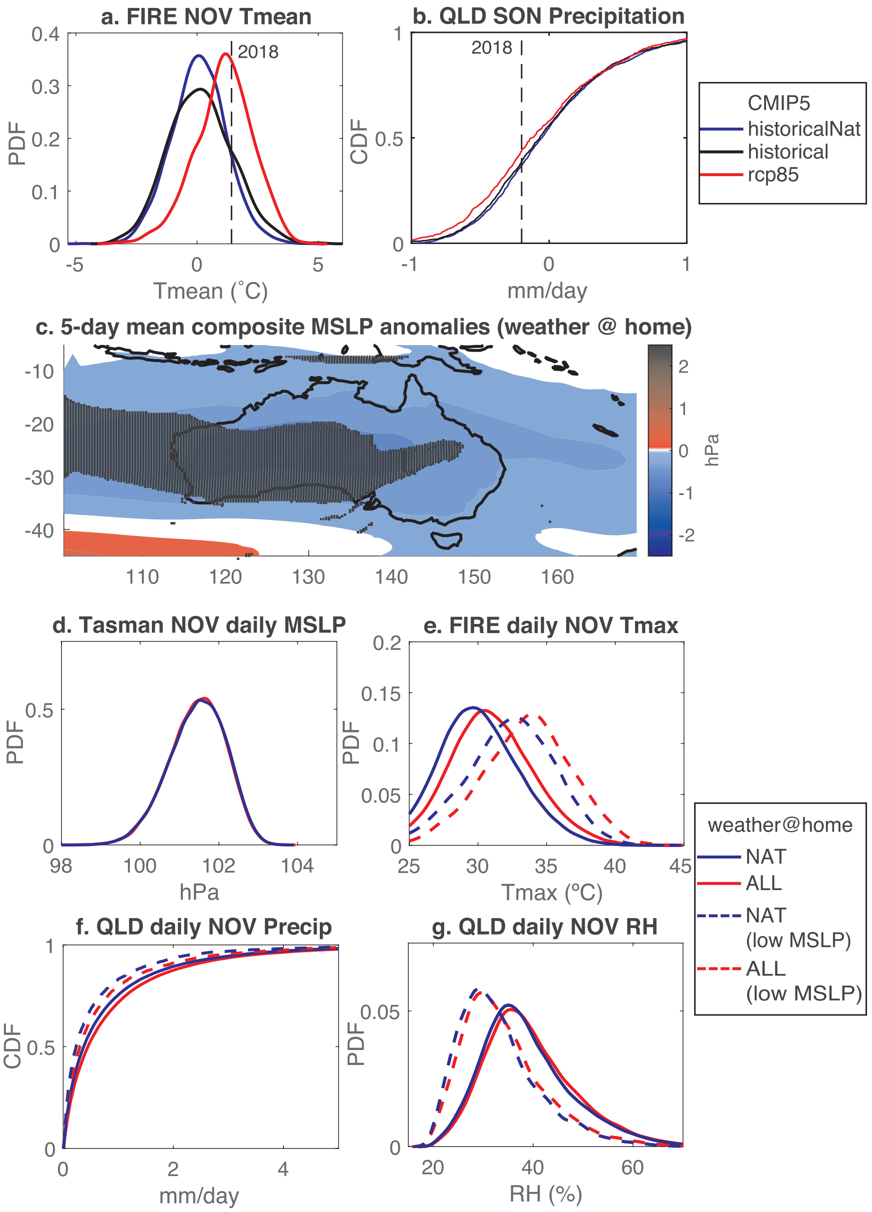

FIG. 2. Summary of modeled conditions in Queensland. Plot shows comparison of CMIP5 historicalNat (blue), historical (black), and RCP8.5 (red) experiments for (a) daily fire region area-averaged November temperature (°C) probability distributions and (b) Queensland (QLD) area-average SON precipitation (mm day−1) cumulative distributions for anomalies relative to each model's 1961–90 climatology, with 2018 observed anomalies noted by a vertical dashed line. For the weather@home ensemble, plots shows (c) anomalies (ALL − NAT) of 5-day running mean MSLP(hPa) with stipples showing anomalies larger than the standard deviation of daily November values. PDFs are given for weather@home (d) daily November MSLP conditions in Tasman region for ALL (red) and NAT (blue), (e) daily fire region area-averaged November temperature (°C), and QLD area-average (f) precipitation (mm day−1) and (g) relative humidity (%). For weather@home plots, dashed lines show distributions of variables during times only when 5-day running mean MSLP in the Tasman Sea box is below the 10th percentile of all days.

Precipitation. The distributions of area-average Queensland September–November (SON) rainfall differ between the CMIP5 historicalNat and RCP8.5 simulations at the dry end of the distribution (Fig. 2b; see also Fig. ES2b). This indicates that conditions drier than average are simulated to occur somewhat less often under anthropogenically forced runs (years 2005–36) compared to natural runs. The RR for rainfall deficits lower than observed conditions in spring 2018 is 1.5. We note that observed regional rainfall trends are weak and rainfall projections are model dependent (Kirtman et al. 2013), and attribution of events may be spatiotemporal scale or definition dependent (Angélil et al. 2017).

MODELED SYNOPTIC-SCALE CONTRIBUTING FACTORS. We next explore synoptic-scale factors in a large single-model ensemble of atmosphere-only simulations [weather@home; see Black et al. (2016) and section 3 of our online supplemental material]. The fires were characterized by a distinct synoptic evolution over the 5-day period beginning 24 November and notably low MSLP in the Tasman Sea.

MSLP. We compare the occurrence of low area-average MSLP anomalies in the Tasman region (Fig. 1e) between the experiments conducted with present-day atmospheric composition (ALL) and preindustrial atmospheric composition and composite surface field modified by removing different anthropogenic response pattern estimates (NAT). There are no significant changes in 5-day mean November daily MSLP patterns in these scenarios (Fig. 2c) and the daily area-average Tasman Sea MSLP distributions are indistinguishable between experiments (Fig. 2d).

Temperature. There is a clear warm shift in November daily temperatures in both the fire region (Fig. 2e) and QLD (Fig. ES2a) in the ALL forcing simulations. There is an additional contribution to warm simulated temperatures from prevailing low MSLP patterns. When daily temperature anomalies in the fire region are compared for all simulated with those where area-average Tasman region MSLP anomalies are below the 10th percentile value of all values (MSLPLOW), a further warm shift in temperatures occurs.

Precipitation. For daily area-average Queensland, low precipitation values in November are most likely in the NAT simulations and particularly days sorted by MSLPLOW. While CMIP5 analysis indicated antecedent rainfall deficits were more likely under greenhouse gas forcings, low daily rainfall in Queensland does not have a discernible anthropogenic influence (Fig. 2f), although we note that persistent low daily rainfall or consecutive dry day indices were not examined.

Humidity. There was little notable difference simulated between daily November conditions in the ALL and NAT scenarios for humidity (Fig. 2g), although low daily humidity values in Queensland are more likely for MSLPLOW.

SUMMARY. We have provided a qualitative examination of the extreme fire and heatwave event of November 2018 in Queensland by deconstructing various contributing factors. As the FFDI measure combines multiple, interdependent variables, we explored components separately in observations and climate models (summarized in Table 2). The fires (and conditioning heatwave) were a complex compound extreme event with multiple contributing factors occurring on a range of spatiotemporal scales. The high 2018 November temperatures and low antecedent spring rainfall in Queensland were

Table 2. Summary of (i) observed 2018 meteorological and climatological conditions, (ii) assessment of their influence (higher/lower) on the extreme observed FFDI during November and the event, (iii) assessment of whether these were conditions were lower, higher, or the same in weather@home simulations during low Tasman Sea MSLP occurrences, and (iv) assessment of whether observed conditions are altered by simulated anthropogenic forcings influences (higher/lower or same probability with and without anthropogenic forcings, or N/A for not assessed) in CMIP5 [where the risk ratio (RR) is provided] and weather@home (where qualitative assessment is made).

Variable	(i) 2018 anomaly (relative to climatology)	(ii) Contribution to FFDI (lower or higher FFDI)	(iii) Lower/higher/ same with low Tasman MSLP	(iv) Lower/ higher/same with anthropogenic GHG
FIRE temperature (NOV)	H	H	H	H (RR = 4.5)
FIRE temperature (EVENT)	H	H	H	H
QLD precipitation (SON)	L	H	N/A	L (RR = 1.5)
QLD precipitation (NOV)	L	H	L	L
QLD humidity (EVENT)	L	H	L	S
Tasman MSLP (EVENT)	L	H		S
QLD/FIRE WINDS (EVENT)	L (and westerly direction)	H	N/A	N/A

key contributors to the elevated fire risk, in addition to the evolution of synoptic conditions that resulted in low humidity and anomalous westerly winds.

Sustained low rainfall and extreme high temperatures were notable antecedent conditions prior to the event, and these large-scale factors, in particular, are thought to result in increased availability of larger fuel elements, which can lead to increases in fire intensity and energy release from a fire (Sharples et al. 2016). Both CMIP5 and weather@home model datasets indicate that anthropogenic forcings in model simulations increase the likelihood of higher Queensland and fire region temperatures. CMIP5 models also provide some evidence of increased likelihood of dry spring conditions with enhanced anthropogenic greenhouse gases. The large-scale ocean–atmosphere modes of climate variability that were anomalously positive in 2018 (IOD and SAM) do not typically influence northern Australian climates, although negative SAM is strongly correlated with high FFDI in southern Australia.

As with all short-duration extremes, the evolution of synoptic conditions was critical to the fire event. These conditions included a significantly late start to the wet season, a sustained low pressure system to the south of the state, and unusual westerly wind flow. These conditions occurred in conjunction with a severe and persistent heatwave (high minimum and maximum temperatures) and very low humidity, leading to FFDI measures of "extreme" or "catastrophic" over much of Queensland. This synoptic pattern was not shown to be more likely in ALL forcings simulations of weather@home as diagnosed by low MSLP conditions in the Tasman Sea. MSLPLOW days in weather@home were associated with warmer temperatures and low humidity in Queensland.

FUTURE CLIMATE RISKS. Although complex events are challenging to understand, attempts to evaluate possible changes in future fire danger in eastern Australia are critical for adaption. While we have not provided a quantitative extreme event attribution assessment of this event, ours is one of many results that points to increasing fire danger risks in eastern Australia. In Australia, an overall increase in the FFDI has been observed in many regions, particularly for southern and eastern Australia in recent decades (Dowdy 2018), with future projections clearly showing an increase in the FFDI throughout Australia based on a comprehensive set of modeling approaches (Dowdy et al. 2019).

Previous notable heatwave events in the region in 1995, 1994, and 1969 were also associated with strong low pressure systems to the south and westerly wind flow, but were not accompanied by compound bushfires in northern or central Queensland (Australian Bureau of Meteorology 2018). The 2018 conditioning heatwave event was more severe and persistent than previous analogs, with no event of this scale previously occurring at such northerly coastal locations. Events that are unprecedented in a given region, such as the 2018 event, reveal that firefighting preparation and training cannot rely on previous events as guidance for the most dangerous conditions they can expect in the current and future climate in which large-scale fires occur more regularly. This demonstrates that providing information to regions with developing future risk of extreme or catastrophic FFDI measures, or with enhanced risk outside the historical fire season, is of critical importance.

Future exhaustive examinations of fire events should additionally consider the evolution of synoptic conditions during the event, the accumulated antecedent rainfall and soil moisture deficits, the weighting of these variables in indices such as the FFDI, and the ability of models to simulate each variable for the region and season in question. Under this comprehensive framework, quantitative attribution statements may provide insight.

ACKNOWLEDGMENTS. S.C.L (DE160100092), S.E.P.-K. (FT170100106), A.D.K (DE180100638), and J.J.S. (IN140100011, IN160100029) are funded through the Australian Research Council. A.J.D. is funded through the Australian Government's National Environmental Science Program.

REFERENCES

Angélil, O., D. Stone, M. Wehner, C. J. Paciorek, H. Krishnan, and W. Collins, 2017: An independent assessment of anthropogenic attribution statements for recent extreme temperature and rainfall events. *J. Climate*, **30**, 5–16, https://doi.org/10.1175/JCLI-D-16-0077.1.

Australian Bureau of Meteorology, 2018: Special Climate Statement 67—An extreme heatwave on the tropical Queensland coast. Bureau of Meteorology, 30 pp., http://www.bom.gov.au/climate/current/statements/scs67.pdf.

Black, M. T., 2017: An attribution study of southeast Australian wildfire risk. Ph.D. thesis, University of Melbourne, 179 pp., http://hdl.handle.net/11343/123669.

——, D. J. Karoly, and A. D. King, 2015: The contribution of anthropogenic forcing to the Adelaide and

Melbourne, Australia, heat waves of January 2014 [in "Explaining Extreme Events of 2014 from a Climate Perspective"]. *Bull. Amer. Meteor. Soc.*, 96 (12), S145–S148 , https://doi.org/10.1175/BAMS-D-15-00097.1.

——, and Coauthors, 2016: The weather@home regional climate modelling project for Australia and New Zealand. *Geosci. Model Dev.*, **9**, 3161–3176, https://doi.org/10.5194/gmd-9-3161-2016.

Cannon, A. J., 2018: Multivariate quantile mapping bias correction: An N-dimensional probability density function transform for climate model simulations of multiple variables. *Climate Dyn.*, 50, 31–49, https://doi.org/10.1007/S00382-017-3580-6.

Dowdy, A. J., 2018: Climatological variability of fire weather in Australia. *J. Appl. Meteor. Climatol.*, **57**, 221–234, https://doi.org/10.1175/JAMC-D-17-0167.1.

——, H. Ye, A. Pepler, M. Thatcher, S. L. Osbrough, J. P. Evans, G. Di Virgilio, and N. McCarthy, 2019: Future changes in extreme weather and pyroconvection risk factors for Australian wildfires. *Sci. Rep.*, **9**, 10073, https://doi.org/10.1038/s41598-019-46362-x.

Hendon, H. H., D. W. J. Thompson, and M. C. Wheeler, 2016: Australian rainfall and surface temperature variations associated with the Southern Hemisphere annular mode. *J. Climate*, 20, 2452–2467, https://doi.org/10.1175/JCLI4134.1.

Kirono, D. G. C., K. J. Hennessy, and M. R. Grose, 2017: Increasing risk of months with low rainfall and high temperature in southeast Australia for the past 150 years. *Climate Risk Manage.*, **16**, 10–21, https://doi.org/10.1016/j.crm.2017.04.001.

Kirtman, B., and Coauthors, 2013: Near-term climate change: Projections and predictability. Climate Change 2013: The Physical Science Basis. T. F. Stocker et al., Eds., Cambridge University Press, 953–1028.

Lewis, S. C., and D. J. Karoly, 2013: Anthropogenic contributions to Australia's record summer temperatures of 2013. *Geophys. Res. Lett.*, **40**, 3705–3709, https://doi.org/10.1002/grl.50673.

Noble, I. R., A. M. Gill, and G. A. V. Barry, 1980: McArthur's fire-danger meters expressed as equations. *Aust. J. Ecol.*, **5**, 201–203, https://doi.org/10.1111/j.1442-9993.1980.tb01243.x.

Perkins, S. E., and P. B. Gibson, 2015: Increased risk of the 2014 Australian May heatwave due to anthropogenic activity [in "Explaining Extreme Events of 2014 from a Climate Perspective"]. *Bull. Amer. Meteor. Soc.*, **96** (12), S154–S157, https://doi.org/10.1175/BAMS-D-15-00074.1.

Risbey, J. S., M. J. Pook, P. C. McIntosh, M. C. Wheeler, and H. H. Hendon, 2009: On the remote drivers of rainfall variability in Australia. *Mon. Wea. Rev.*, **137**, 3233–3253, https://doi.org/10.1175/2009MWR2861.1.

Sharples, J. J., and Coauthors, 2016: Natural hazards in Australia: Extreme bushfire. *Climatic Change*, **139**, 85–99, https://doi.org/10.1007/s10584-016-1811-1.

Taylor, K. E., R. J. Stouffer, and G. A. Meehl, 2012: An overview of CMIP5 and the experiment design. *Bull. Amer. Meteor. Soc.*, **93**, 485–498, https://doi.org/10.1175/BAMS-D-11-00094.1.

Ummenhofer, C. C., M. H. England, P. C. Mclntosh, G. A. Meyers, M. J. Pook, J. S. Risbey, A. Sen Gupta, and A. S. Taschetto, 2009: What causes southeast Australia's worst droughts? *Geophys. Res. Lett.*, **36**, L04706, https://doi.org/10.1029/2008GL036801.

Zscheischler, J., and Coauthors, 2018: Future climate risk from compound events. *Nat. Climate Change*, **8**, 469–477, https://doi.org/10.1038/s41558-018-0156-3.

A 1-DAY EXTREME RAINFALL EVENT IN TASMANIA: PROCESS EVALUATION AND LONG TAIL ATTRIBUTION

Carly R. Tozer, James S. Risbey, Michael R. Grose, Didier P. Monselesan, Dougal T. Squire, Amanda S. Black, Doug Richardson, Sarah N. Sparrow, Sihan Li, and David Wallom

Attribution of an extreme magnitude 1-day rainfall event in Hobart is inhibited by small sample size. For moderate magnitude Hobart daily rainfall extremes, models suggest that the associated extratropical lows will deliver more rainfall with weaker pressure anomalies in a warmer world.

On 10 May 2018, Hobart, Tasmania, experienced an extreme rainfall event, which caused flash flooding, infrastructure damage, and major disruption across the capital city, leading to $100 million in insurance claims (Cooper 2019). Gauged records indicate that 130 mm of rain fell during the event, which ranks as the second highest autumn rainfall day over the ~120-yr record, with the largest occurring in 1960. The frequency and magnitude of daily autumn wet extremes show interannual to multidecadal variability over the gauged record and no clear linear trend (Fig. 1a). Future projections, however, indicate that in a warmer world these types of events are likely to increase in both frequency and magnitude across Tasmania (White et al. 2013). Given its extreme magnitude, we thus ask whether an anthropogenic contribution is already apparent in the autumn 2018 event.

Anthropogenic attribution assessments typically rely on general circulation models (GCMs) to characterize the expected signal. Daily rainfall extremes present a novel challenge for event attribution in GCMs because the rainfall process is at least partly parameterized. To have confidence in the use of GCMs for attribution studies, it is important to assess not only their ability to simulate the statistics of extreme events (e.g., magnitude and frequency) but also the associated atmospheric circulation (Grose et al. 2012; Otto 2016; Sillmann et al. 2017; Tozer et al. 2020). This provides confidence that a model is producing rainfall extremes for the right reasons (Eyring et al. 2019).

In our approach to this event attribution study we include an evaluation of our selected model's ability to simulate 1-day wet extremes in Hobart and their associated synoptic- and large-scale circulation. We utilize the atmosphere-only HadAM3P model from the weather@home project (Massey et al. 2015; Guillod et al. 2017). Weather@home provides simulations of both an "actual" and "natural" world (effectively, with and without anthropogenic climate change), which allows us to estimate changes in climate extremes in the current climate relative to a climate unaltered by anthropogenic influence (Massey et al. 2015; Schaller et al. 2016; Black et al. 2016).

AFFILIATIONS: Tozer, Risbey, Grose, Monselesan, Squire, Black, and Richardson—CSIRO Oceans and Atmosphere, Hobart, Tasmania, Australia; Sparrow, Li, and Wallom—Oxford e-Research Centre, Department of Engineering, University of Oxford, Oxford, United Kingdom.
CORRESPONDING AUTHOR: Carly Tozer, carly.tozer@csiro.au

DOI:10.1175/BAMS-D-19-0219.1

DATA AND METHODS. We use 450 simulations of autumn 2018 from the actual (ACT) and natural (NAT) weather@home experiments (equivalent to 40,500 days each). The ACT simulations are produced under 2018 sea surface temperatures (SSTs), sea ice concentrations, and atmospheric forcings. NAT uses preindustrial forcings and an SST field that has the estimated anthropogenic SST change pattern removed. This change pattern is derived from estimates from multiple GCMs contributing to CMIP5 (Schaller et al. 2016). We extract rainfall for the model grid box encompassing Hobart. Geopotential height anomalies at

500 hPa (z500), calculated relative to the mean of all NAT or ACT autumn 2018 simulations, respectively, are used to represent the atmospheric circulation.

For observed rainfall we use a gridded rainfall product from the Australian Water Availability Project (AWAP). AWAP provides interpolated gauged data at a grid resolution of 0.05° longitude × 0.05° latitude (Raupach et al. 2006; Jones et al. 2009) from 1900 to present. To allow a fair comparison with the lower-resolution model, we spatially averaged all AWAP grid boxes within the relevant HadAM3P grid box (1.875° longitude × 1.25° latitude, inset Fig. 1b). We also refer to point data recorded in Hobart (Australian Bureau of Meteorology gauge 094029). The Japanese 55-Year Reanalysis (JRA: Kobayashi et al. 2015) is used as our observed reference for atmospheric circulation and is available from 1958 to the present.

Figure 1a presents the highest daily rainfall recorded in each autumn across the 1900–2018 period. The magnitudes of the highest autumn rainfall days in 1909, 1960, and 2018 far exceed those in other years. There is clearly a small sample of these "extreme" extremes, which makes attribution challenging. For the purposes of analysis we include "extreme" extremes (including the autumn 2018 event) as part of a broader range of 1-day extreme wet events (National Academies of Sciences, Engineering, and Medicine 2016; Bellprat et al. 2019). We identify 1-day extreme wet events in Hobart (in the AWAP, gauge, and model datasets) as any day greater than the 99th percentile daily rainfall, where the 99th percentile value is calculated per calendar day, to account for the seasonal cycle. Daily rainfall series are noisy, so to provide a reasonable sample size from which to calculate the 99th percentile values, we use a moving 15-day window centered on the day in question (Perkins and Alexander 2013). For example, for calendar day 8 May, we include days from 1 May to 15 May across the 1900–2018 period in the analysis pool (i.e. close to 2,000 days). For the gauged record the threshold percentile values range from ~18–27 mm across autumn days. For the AWAP extreme events the threshold values range from ~16–31 mm and for modeled extremes this range is ~10–22 mm.

To evaluate the model simulations we compare the distributions of wet events identified in the model (ACT) with the AWAP and gauged data distributions (Fig. 1b). We then average the z500 anomalies associated with each wet event to form a composite of the circulation associated with wet events in Hobart in both the observations (in this case AWAP and JRA) and model (ACT) simulations. This approach is based on the methodology presented in Tozer et al. (2020).

For the event attribution component we assess both the rainfall and circulation associated with wet extremes in the ACT and NAT simulations. Specifically,

1) We identify 1-day wet events in NAT and ACT, with both cases referenced to the NAT percentile values. The NAT thresholds provide a baseline to determine any changes in the extreme rainfall distribution from the "natural" to the "actual" world.
2) We extract z500 anomalies for the model grid box approximately encompassing the highest negative z500 anomaly associated with wet events (as identified in the composite analysis). We assess the z500 anomaly distribution for NAT and ACT wet events to determine if there are changes in the intensity of z500 associated with wet events in a warming world.

RESULTS AND DISCUSSION.

Model evaluation. We compare the magnitude of autumn 1-day wet events in the gauged, AWAP and model (ACT) data in Fig. 1b. For the gauged data, it is clear that (a) there is a large range of magnitudes that exceed the 99th percentile threshold; and (b) the extreme event distribution has a long tail (i.e., few high-magnitude extremes). Most events range between 20 and 50 mm (median of 29 mm) and occur at a frequency of almost one event per year. The autumn 2018 event sits far in the tail of the distribution. The AWAP wet events have a slightly higher median of 31 mm but have reduced extreme magnitudes relative to the gauged data (e.g., the autumn 2018 event sits in the 70–80-mm range), a result of the spatial averaging (discussed above), and because it is a gridded product (Tozer et al. 2012; King et al. 2013). The modeled wet events have further reduced magnitude with a median value of 21 mm.

Both AWAP and the model have a slightly lower frequency of wet events relative to gauged. Common across all datasets is the long tail of the wet event magnitude distribution, highlighting that there are very few "extreme" extremes in both observations and large model simulations.

As seen in Fig. 1c, Hobart 1-day wet events are typically associated with an intense low pressure system (Fox-Hughes and White 2015), which is cut off from the westerly flow by a blocking high in the Tasman Sea (Pook et al. 2010). These synoptic structures are associated with a large-scale wave train in the polar jet (Tozer et al. 2018). Figure 1d indicates that the model successfully captures these synoptic and large-scale processes, which builds confidence in

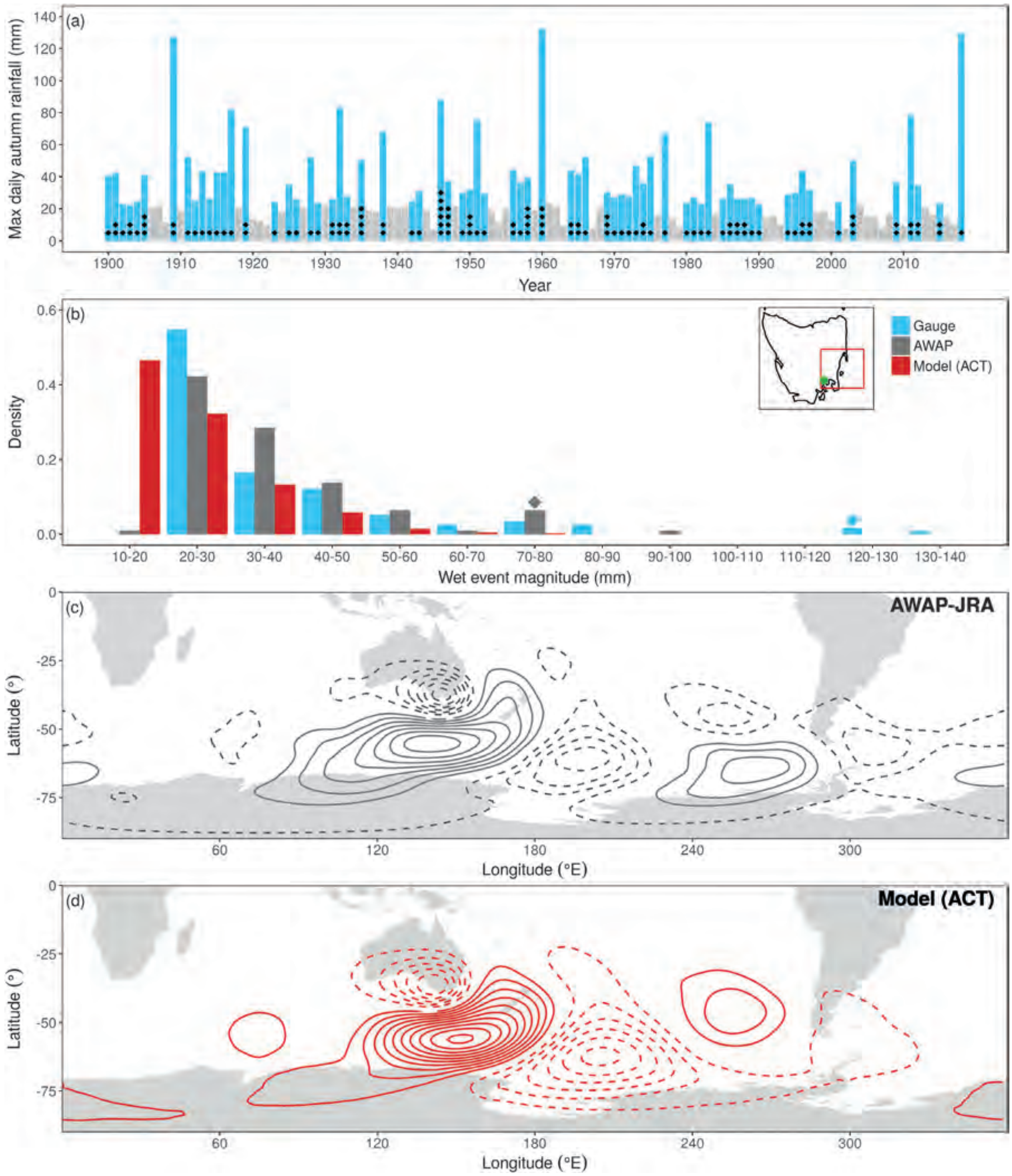

Fig. 1. Model evaluation. (a) Maximum daily rainfall in each autumn in Hobart (Ellerslie Rd., gauge no. 094029). Blue bars indicate that the rainfall event is classed as a wet event as per the shifting window method described in section 2. Years without any daily wet extreme events are indicated in gray. The number of wet events occurring in each year is shown with black dots (e.g., 3 dots means 3 wet events occurred that year). Linear trend analysis found no significant trend in the magnitude of the maximum daily autumn rainfall (*p* value = 0.25) or the number of extreme daily wet events (*p* value = 0.41) over the gauged record. (b) Histogram of gauged (blue bars), AWAP (gray bars) and modeled (ACT; red bars) wet events. Diamonds indicate where the autumn 2018 event sits in the gauged and AWAP distributions. Gauged and AWAP analyses performed over the 1900–2018 period. 450 autumn 2018 ACT simulations were used for the model analysis, with ACT wet events identified relative to ACT percentiles. Inset shows the location of Hobart (green dot) and relevant model grid box (red square). (c) Composite of JRA z500 anomalies for AWAP derived wet events in Hobart region. Solid (dashed) contours indicate positive (negative) geopotential height anomalies with contours every 15 m. (d) As in (c), but using modeled ACT (red contours).

its representation of real-world wet extremes for the following attribution assessment.

Event attribution. The NAT and ACT wet event magnitude histograms have similar shapes (Fig. 2a), with a Kolmogorov–Smirnoff (KS) test suggesting that there is no significant difference between the histograms at the 5% level (*p* value of 0.18). As in the observations, the NAT and ACT extreme event distributions have a long tail. Also of interest is that while the overall number of wet extremes in NAT and ACT are similar, there is a higher number of events in the 30–50-mm range in ACT. Figure 2c presents the return period of daily rainfall in NAT and ACT. Again it is clear that there are very few days with rainfall >50 mm in both simulations. The confidence intervals for NAT and ACT for these high-magnitude rainfall days are both large and overlapping. These results show that even in a large number of model simulations, these "extreme" extremes are very rare in Hobart. We cannot draw statistically robust conclusions about the anthropogenic influence on the autumn 2018 event from only a handful of events of that size. Some comment may be made about events in the 30–50-mm range ("mid-range" extremes) given their larger sample size. Figure 2c clearly shows that return periods for rain days in this range are lower in ACT relative to NAT (i.e., rain days of this magnitude are more frequent in ACT). For example, a 35-mm rainfall day in ACT has a return period of ~8.5 yr relative to ~13 yr in NAT (Fig. 2c inset).

We now assess variability in the intensity of the low pressure systems associated with Hobart wet events (Fig. 2d). There is a clear displacement of probability mass toward lower magnitude (i.e., less negative) z500 anomalies for ACT events in Fig. 2c relative to NAT. This suggests that wet events in ACT can occur in association with a weaker cutoff low intensity, which is also evident in the composite ACT and NAT circulations (Fig. 2b). A KS test indicates that the shift in the distributions is significant at the 5% level (*p* value of 0.02).

We further explore this observation in Fig. 2e. Here we focus on the z500 anomaly range in which the majority of the wet extremes occur (i.e., 0 to –200 m; Fig. 2d) and plot the distribution of wet extreme magnitude for z500 anomalies in bins spanning 10 m each. Figure 2e reveals a tendency for wet extreme magnitudes in ACT to be greater than NAT for the same z500 anomaly, particularly in the –160- to –90-m z500 anomaly range. These results thus indicate that wet extremes in ACT occur in association with reduced (i.e., less negative) pressure anomalies relative to NAT or, alternately, for the same size pressure anomaly there is a tendency for higher magnitude wet events in ACT relative to NAT. These results lend support to the idea that extratropical baroclinic eddies (e.g., cutoff lows) may be weaker in a warmer climate (e.g., as represented here by the ACT world), but more efficient in that the increased moisture in the atmosphere makes for more intense rainfall extremes (Held 1993; Schneider et al. 2010).

CONCLUSIONS. We have examined whether the autumn 2018 extreme 1-day rainfall event in Hobart had an apparent anthropogenic contribution. We first undertook a process evaluation of the HadAM3P model and found that although modeled wet events tend to have lower magnitudes compared to observed, the associated atmospheric circulation is well captured in the model, which gives confidence in its use in this attribution study.

Based on the assessment of ACT and NAT simulations from the weather@home project, we draw no clear conclusions (either way) about the anthropogenic influence on very extreme rainfall days (like the autumn 2018 event), given the very small sample size of events of this magnitude. There are, however, indications in the model simulations that moderate magnitude 1-day wet extremes in Hobart in a warmer world (represented here by the ACT simulations) are associated with higher rainfall magnitudes for the same or weaker (i.e., less negative) circulation anomalies. To provide further confidence that extratropical lows are becoming more efficient in delivering extreme rainfall events both in Hobart and more generally, additional models, seasons and study regions should be tested.

ACKNOWLEDGMENTS. Thank you to Paola Petrelli (University of Tasmania) for providing access to the weather@home dataset. This work was supported by the Decadal Climate Forecast Project, DIGISCAPE Future Science Platform at CSIRO, Hydro Tasmania and the National Environmental Science Program's Earth Systems and Climate Change Hub.

REFERENCES

Bellprat, O., V. Guemas, F. Doblas-Reyes, and M. G. Donat, 2019: Towards reliable extreme weather and climate event attribution. *Nat. Commun.*, **10**, 1732, https://doi.org/10.1038/s41467-019-09729-2.

Black, M. T., and Coauthors, 2016: The weather@home regional climate modelling project for Australia and New Zealand. *Geosci. Model Dev.*, **9**, 3161–3176, https://doi.org/10.5194/gmd-9-3161-2016.

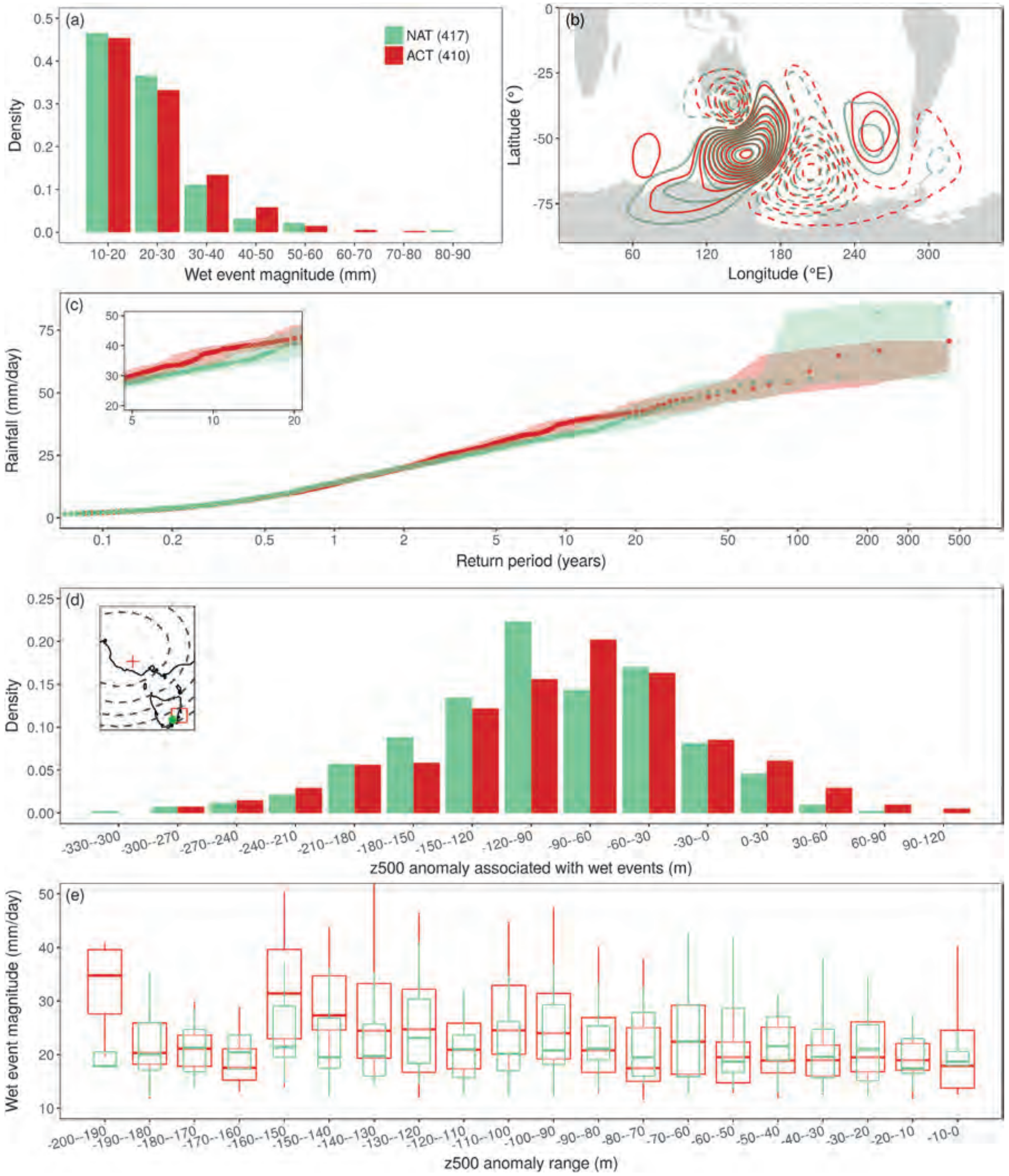

Fig. 2. Event attribution. (a) Histogram of NAT (green) and ACT (red) wet event magnitude. Wet events in NAT and ACT identified relative to the NAT percentiles. Bracketed numbers show number of wet events identified for each dataset. NAT wet event thresholds ranged from 9.5–21.5 mm and for ACT 9.6–21.9 mm. (b) NAT (green contours) and ACT (red contours) wet extreme composite z500 patterns. The mean z500 anomaly for the selected model grid point locating the cutoff low [red cross in inset in (d)] in ACT is −85.6 m compared with −96.6 for NAT. (c) Return period (autumns) for NAT and ACT daily rainfall. Shaded areas indicate the 95% confidence interval using bootstrap resampling. Inset zooms in on selected rainfall and return period range. (d) NAT and ACT z500 anomalies associated with wet events for selected model grid point (red cross in inset). (e) Boxplots of NAT and ACT wet event magnitude for different negative z500 anomaly ranges. The boxes indicate the 25th and 75th percentile range. The solid bars across the boxes indicate the median. Whiskers indicate the 5th and 95th percentile. Note that for all figures NAT is represented by the color green and ACT by the color red.

Cooper, E., 2019: Tasmania's $100m floods still affecting homes and businesses one year on. Australian Broadcasting Corporation, 9 May 2019, https://www.abc.net.au/news/2019-05-09/tas-hobart-floods-one-year-on/11091120.

Eyring, V., and Coauthors, 2019: Taking climate model evaluation to the next level. *Nat. Climate Change*, **9**, 102–110, https://doi.org/10.1038/s41558-018-0355-y.

Fox-Hughes, P., and C. J. White, 2015: A synoptic climatology of heavy rainfall in Hobart. *36th Hydrology and Water Resources Symposium: The Art and Science of Water*, Hobart, Tasmania, Engineers Australia, 1010.

Grose, M. R., M. J. Pook, P. C. McIntosh, J. S. Risbey, and N. L. Bindoff, 2012: The simulation of cutoff lows in a regional climate model: Reliability and future trends. *Climate Dyn.*, **39**, 445–459, https://doi.org/10.1007/S00382-012-1368-2.

Guillod, B. P., and Coauthors, 2017: weather@home 2: Validation of an improved global–regional climate modelling system. *Geosci. Model Dev.*, **10**, 1849–1872, https://doi.org/10.5194/gmd-10-1849-2017.

Held, I. M., 1993: Large-scale dynamics and global warming. *Bull. Amer. Meteor. Soc.*, **74**, 228–242, https://doi.org/10.1175/1520-0477(1993)074<0228:LSDAGW>2.0.CO;2.

Jones, D. A., W. Wang, and R. Fawcett, 2009: High-quality spatial climate data-sets for Australia. *Aust. Meteor. Oceanogr. J.*, **58**, 233–248, https://doi.org/10.22499/2.5804.003.

King, A. D., L. V. Alexander, and M. G. Donat, 2013: The efficacy of using gridded data to examine extreme rainfall characteristics: A case study for Australia. *Int. J. Climatol.*, **33**, 2376–2387, https://doi.org/10.1002/joc.3588.

Kobayashi, S., and Coauthors, 2015: The JRA-55 reanalysis: General specifications and basic characteristics. *J. Meteor. Soc. Japan*, **93**, 5–48, https://doi.org/10.2151/JMSJ.2015-001.

Massey, N., and Coauthors, 2015: weather@home—Development and validation of a very large ensemble modelling system for probabilistic event attribution. *Quart. J. Roy. Meteor. Soc.*, **141**, 1528–1545, https://doi.org/10.1002/qj.2455.

National Academies of Sciences, Engineering, and Medicine, 2016: *Attribution of Extreme Weather Events in the Context of Climate Change*. The National Academies Press, 186 pp.

Otto, F., 2016: The art of attribution. *Nat. Climate Change*, **6**, 342–343, https://doi.org/10.1038/nclimate2971.

Perkins, S. E., and L. V. Alexander, 2013: On the measurement of heat waves. *J. Climate*, **26**, 4500–4517, https://doi.org/10.1175/JCLI-D-12-00383.1.

Pook, M., J. Risbey, and P. McIntosh, 2010: East coast lows, atmospheric blocking and rainfall: A Tasmanian perspective. *IOP Conf. Ser.: Earth Environ. Sci.*, **11**, 012011, https://doi.org/10.1088/1755-1315/11/1/012011.

Raupach, M. R., C. M. Trudinger, P. R. Briggs, and E. A. King, 2006: Australian water availability project. Tech. Rep., Commonwealth Scientific and Industrial Research Organisation, 56 pp, http://www.cmar.csiro.au/e-print/open/raupachmr_2006d.pdf.

Schaller, N., and Coauthors, 2016: Human influence on climate in the 2014 southern England winter floods and their impacts. *Nat. Climate Change*, **6**, 627–634, https://doi.org/10.1038/nclimate2927.

Schneider, T., P. A. O'Gorman, and X. J. Levine, 2010: Water vapor and the dynamics of climate changes. *Rev. Geophys.*, **48**, RG3001, https://doi.org/10.1029/2009RG000302.

Sillmann, J., and Coauthors, 2017: Understanding, modeling and predicting weather and climate extremes: Challenges and opportunities. *Wea. Climate Extremes*, **18**, 65–74, https://doi.org/10.1016/j.wace.2017.10.003.

Tozer, C. R., A. S. Kiem, and D. C. Verdon-Kidd, 2012: On the uncertainties associated with using gridded rainfall data as a proxy for observed. *Hydrol. Earth Syst. Sci.*, **16**, 1481–1499, https://doi.org/10.5194/hess-16-1481-2012.

——, J. S. Risbey, T. J. O. Kane, D. P. Monselesan, and M. J. Pook, 2018: The relationship between wave trains in the Southern Hemisphere storm track and rainfall extremes over Tasmania. *Mon. Wea. Rev.*, **146**, 4201–4230, https://doi.org/10.1175/MWR-D-18-0135.1.

——, ——, D. P. Monselesan, D. T. Squire, M. A. Chamberlain, R. J. Matear, and T. Ziehn, 2020: Assessing the representation of Australian regional climate extremes and their associated atmospheric circulation in climate models. *J. Climate*, **33,** 1227–1245, https://doi.org/10.1175/JCLI-D-19-0287.1.

White, C. J., K. L. McInnes, R. P. Cechet, S. P. Corney, M. R. Grose, G. K. Holz, J. J. Katzfey, and N. L. Bindoff, 2013: On regional dynamical downscaling for the assessment and projection of temperature and precipitation extremes across Tasmania, Australia. *Climate Dyn.*, **41**, 3145–3165, https://doi.org/10.1007/S00382-013-1718-8.

ATTRIBUTION OF THE WARMEST SPRING OF 2018 IN NORTHEASTERN ASIA USING SIMULATIONS OF A COUPLED AND AN ATMOSPHERIC MODEL

Ying Sun, Siyan Dong, Ting Hu, Xuebin Zhang, Peter Stott

Anthropogenic forcing has increased the occurrence probability of the warmest spring in northeastern Asia. Similar increases in probability are obtained from two different model setups.

In the spring of 2018, anomalously high temperatures were observed in northeastern Asia (including Northern China, Mongolia, and southern Russia; the box bounded by 90°–120°E, 35°–55°N in Fig. 1). The mean, maximum, and minimum temperatures were the highest on record since 1961 when China started to have reliable observations. Accompanied by these high temperatures were precipitation deficits, resulting in severe drought in the northern and northeastern parts of China. Some crops, such as corn, could not be sown as scheduled. More than 50 million hectares of crops were affected (CMA 2019; NCC 2019). This high temperature event also influenced surrounding regions including Mongolia and southern Russia. For example, spring temperature in Mongolia was the highest on record (NOAA NCEI 2019).

Previous studies have investigated human influence on high summer and spring temperature events in Asia and some parts of China (Takahashi et al. 2016; Min et al. 2015; Sun et al. 2014, 2016; Song et al. 2015). They consistently show that anthropogenic forcing has increased the occurrence probability of these events. Some studies (e.g., Min et al. 2015; Sun et al. 2014) examine changes in event probability conditional on the observed external forcing using coupled model (CMIP-type) simulations. Other studies (e.g., Takahashi et al. 2016) analyze changes in event probability conditional on both the observed external forcing as well as state of atmospheric–oceanic circulation based on simulations of atmospheric models (AMIP-type). Here, we examine event probabilities based on both types of conditioning, involving simulations by a coupled model and an atmospheric model.

DATA AND METHODS. The observational data used in this study are monthly mean temperature anomalies of HadCRUT4, which is a gridded data product with resolution of 5° × 5° (available at https://www.metoffice.gov.uk/hadobs/hadcrut4/). The temperature anomalies (relative to 1961–90 average) for the grid boxes within the northeastern Asia during spring [March–May (MAM)] are averaged to obtain the regional mean temperature anomalies.

We use ensemble simulations from a coupled model and an atmospheric model. The coupled model is the Canadian Earth System Model version 2 (CanESM2; Arora et al. 2011). The CanESM2 simulations are 50-member ensemble runs on a T63 triangular truncation (about 2.81° resolution), driven by combined historical anthropogenic and natural forcings (ALL) and by historical natural forcing (NAT) for the period 1950–2004. From 2005 until 2020, the ALL simulations are forced with the RCP8.5 while the NAT simulations are forced with natural forcing by repeating the solar forcing during the last period cycle alone, without any volcano eruptions (Fyfe et al. 2017). The atmospheric model is HadGEM3-A-N216

AFFILIATIONS: Sun—National Climate Center, China Meteorological Asminstration, Beijing, China, and Collaborative Innovation Center on Forecast and Evaluation of Meteorological Disasters, Nanjing University of Information Science & Technology, Nanjing, China; Dong and Hu—National Climate Center, China Meteorological Administration, Beijing, China; Zhang—Climate Research Division, Environment and Climate Change Canada, Toronto, Canada; Stott—Met Office Hadley Centre, Exeter, United Kingdom

CORRESPONDING AUTHOR: Ying Sun, sunying@cma.gov.cn

DOI:10.1175/BAMS-D-19-0264.1

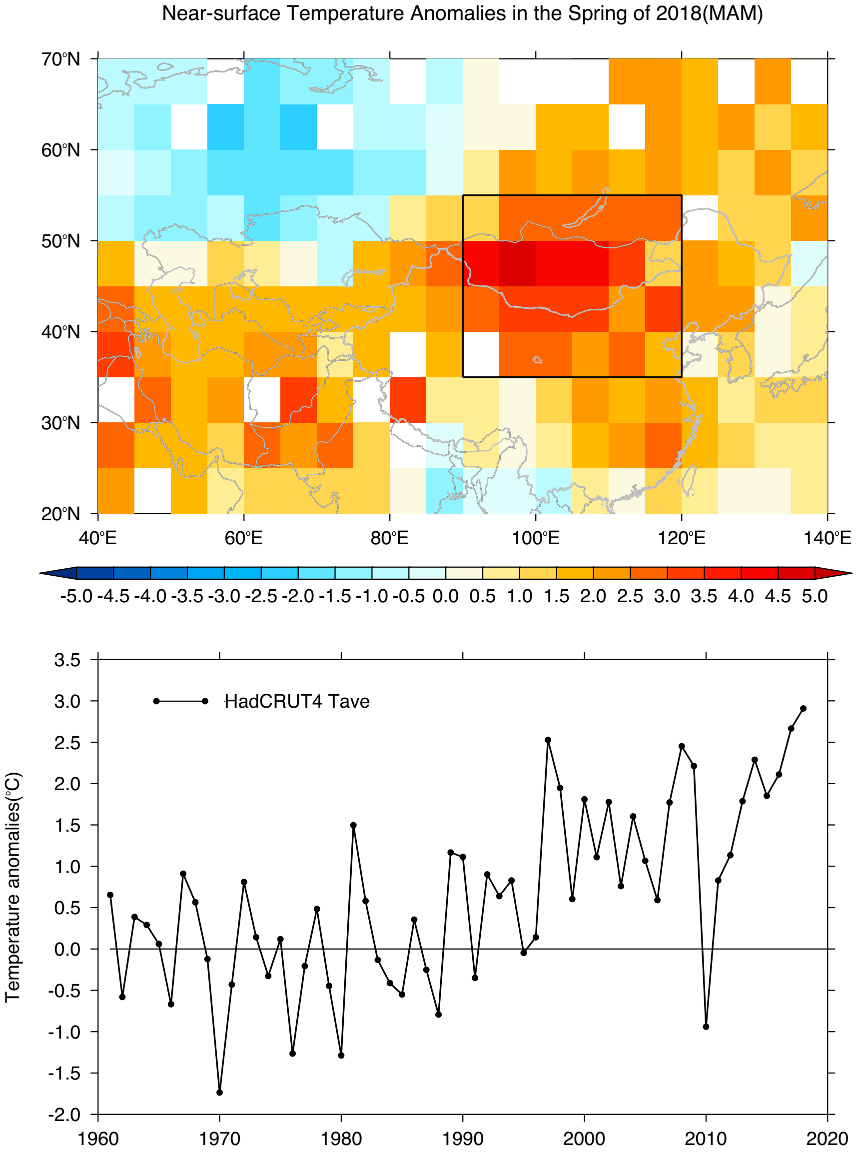

Fig. 1. Top panel: A map of spring mean temperature anomalies in 2018 (relative to 1961–90 average) based on HadCRUT4 data. The box shows the area under investigation for observation, CanESM2 and HadGEM3. Lower panel: Time series of spring temperature anomalies (relative to 1961–90 average) based on HadCRUT4.

with a horizontal resolution of 0.56° × 0.83° (Christidis et al. 2013; Ciavarella et al. 2018). The simulations conducted with this model consist of two sets of experiments: 1) The historical simulation is forced with ALL and the observed sea surface temperatures (SST) and sea ice concentrations (SIC) from HadISST (Rayner et al. 2003). 2) Historical NAT simulations forced by preindustrial forcing and the observed SST and SIC with anthropogenic contribution removed (Christidis et al. 2013). For the period of 1961–2013, there are 15 simulations for ALL and NAT experiments. While for 2018, a 525-member ensemble for ALL and NAT experiments is used to investigate anthropogenic influence as simulated by HadGEM3.

The analyses include the following steps: 1) For observations and model simulations, all the regional mean temperatures are calculated as anomalies relative to the 1961–90 average in northeastern Asia. We compare the observed spring mean temperature anomaly in 2018 (denoted as TA_{OBS}) with model simulations. 2) CanESM2 has a high climate sensitivity (with a transient climate response 3°C; IPCC 2013) and its simulated global mean near-surface temperature (GMST) warms rapidly since mid-twentieth century. The CanESM2 simulated GMST for 2007–16 has increased by 1.45°C above preindustrial level, which is much warmer than the observed ~1°C increase of GMST in the climate of 2018. This too rapid increase in GMST could affect the attribution results and needs to be adjusted. As global temperature response scale well with external forcing and as regional temperature increase also scales well with the global value, we consider a 10-year period (1995–2004) in model simulations whose multi-run ensemble mean temperature is about 1°C warmer than the preindustrial level, which is consistent with the human-induced warming in the climate around 2018 (Allen et al. 2018). This GMST-based adjustment is reasonable but there is also a caveat that the aerosols effects in different period could be different. The occurrence probability of the 2018-like temperature simulated by CanESM2 $P_{ALL\text{-}CanESM}$ is determined by computing the probability for temperature anomalies above TA_{OBS} during 1995–2004. The occurrence probabiliity in the natural world ($P_{NAT\text{-}CanESM}$) is determined similarly based on the NAT 50-run simulations. 3) For

HadGEM3 simulations, we used the 525 runs for the year 2018 under the world with or without human influence. This is because the transient simulation has only 15 runs. The occurrence probabilities, denoted as $P_{\text{ALL-HadGEM}}$ and $P_{\text{NAT-HadGEM}}$ for 2018-like spring, are estimated by computing the probability for temperature anomalies above TA_{OBS} in the ALL and NAT simulations, respectively. 4) In all cases, the normal distribution is used when estimating the probability because regional mean temperature should follow a normal distribution according to the central limit theorem, although the histogram does show some degree of skewness (Fig. 2e). The risk ratio RR for the event probability in ALL and NAT worlds is calculated by $P_{\text{ALL}}/P_{\text{NAT}}$. The confidence interval in the risk ratio is estimated using 1000 bootstrap samples with replacement. For example, when estimating the confidence interval for the case of CanESM2 simulation, we draw 50 samples of 10-yr data from 50 ALL runs and 50 NAT runs, separately, with replacement. We then estimate P_{ALL} and P_{NAT} and compute an RR based on these samples. This procedure is repeated for 1,000 times. The 5th and the 95th percentiles are used to represent the 90% confidence interval.

RESULTS. Figure 1 shows spring temperature anomalies in 2018 in Asia and time series for 1961–2018 in the studied region. There were positive temperature anomalies centered in northern China and Mongolia, with the largest anomaly value around 4.8°C. The regional mean temperature anomaly in 2018 is the highest on record at 2.9°C above the 1961–90 average and exceeds 2.7 times the observed standard deviation computed from 1961–2017. The 500-hPa geopotential height (not shown) illustrate that an anomalous high pressure ridge was controlling northeastern Asia during the spring. The subsidence airflow related to this sets important circulation background for the high temperature event.

It is difficult to evaluate the fitness of climate model simulations for the purpose of this study because of the relatively small scale at which it is difficult to quantify natural variability and climate response from the observations. The limited availability of observational data adds more complexity to this problem. Nevertheless, we compared some statistics in the observations and simulations to provide some sense about model's performance. Figure 2 shows observed and simulated time series along with their histograms. In general, both models broadly reproduce the observed changes and the model spreads also cover the range of the observations (Figs. 2a,b). Over 1961–2013, the observed spring mean temperature has increased by 0.034°C yr^{-1} (90% confidence interval: 0.020 to 0.049). The median trend of the CanESM2 simulation is 0.031°C yr^{-1} (model spread: 0.018 to 0.044; Fig. 2a). The corresponding values of the HadGEM3 simulations are 0.017°C yr^{-1} (model spread 0.002 to 0.026; Fig. 2b). The HadGEM3 ensemble shows less warming than the observations. It warms less than that simulated by CanESM2 as expected, since CanESM2 has high climate sensitivity. The standard deviations for observation and simulations are also roughly comparable though variability in HadGEM3 simulation seems to be high (Figs. 2c,d). When a linear trend is not removed from the series, the standard deviation in the observation is 0.98°C, and the median value of standard deviation is 1.11°C (spread: 0.93 to 1.25) in CanESM2 simulation and 1.23°C (spread: 1.04 to 1.37) in the HadGEM3 simulations, respectively. It seems that variability in HadGEM3 simulation is larger than that in the observation, which can result in larger risk ratio estimate for the same amount of warming. When the trend is removed from the series, the above values become 0.83°C for observations, 0.98°C (spread: 0.79 to 1.17) for the CanESM2 simulation and 1.18°C (spread: 1.03 to 1.34) for the HadGEM3 simulation. Overall, the model simulations may not be perfect but should be reliable enough for the purpose of this study.

The histograms of the model simulations under ALL forcing clearly shift to warmer temperatures when compared with that under NAT forcing, suggesting an increase of probability of extreme high temperatures due to human influence (Figs. 2e,f). In CanESM2 simulations, the probability of 2018-like temperature is 2.02% (90% CI: 1.44% to 2.65%) under ALL forcing and it is 0.11% (90% CI: 0.09% to 0.14%) under NAT forcing. This gives a risk ratio of 18.4 (90% CI: 11.9 to 25.7). In the HadGEM3 simulations for 2018, the probability of 2018-like temperature is 6.67% (90% CI: 5.55% to 8.12%) under ALL forcing and it is 0.38% (90% CI: 0.25% to 0.58%) under NAT forcing, resulting in a risk ratio of 17.5 (90% CI: 11.2 to 28.5).

CONCLUSIONS AND DISCUSSION. We have examined human influence on the probability of occurrence of 2018-like spring temperature in northeastern Asia. We used simulations from a coupled model and an atmospheric model. Taking into account caveats in the observations and simulations, including problems in observational data and differences in model simulated trends and variability when compared with those in the observations, the balance of evidence clearly indicates that human influence has increased the probability of temperature

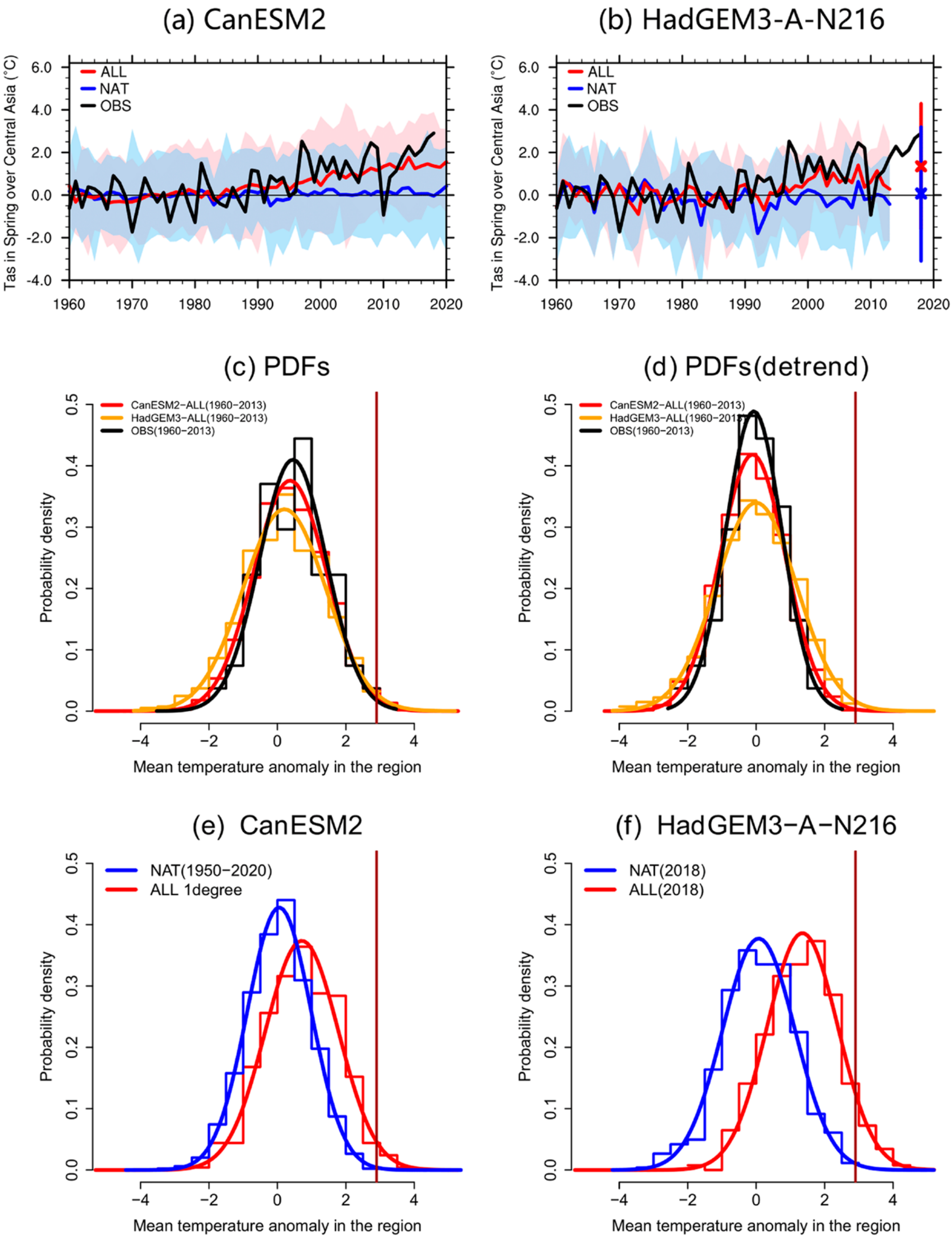

extremes substantially, with the probability of 2018-like extreme temperatures increasing by as much as 18 times.

The risk ratio that is conditional on the historical forcing as simulated by CanESM2 is of similar magnitude to that conditional on the anthropogenic

Fig. 2. (a) Observed (black) and CanESM2 simulated spring mean temperature anomalies (relative to 1961–90 average) in the region during 1960–2020. The multi-run averages under ALL and NAT forcing are illustrated by red and blue lines and the model spread is represented by red and blue shadings, respectively. (b) As in (a), but for HadGEM3-A-N216. The mean and spread of 2018 temperature anomalies (relative to 1961–90 average) under ALL (red) and NAT (blue) forcing are marked by cross and vertical bars, respectively. (c) Probability density functions (PDFs) of spring temperature anomalies during 1961–2013 for observation (black) and model simulations under ALL forcing based on CanESM2 (red) and HadGEM3-A-N216 (orange). (d) As in (c), but for the results with linear trends in 1961–2013 removed. (e) PDFs of spring mean temperature anomalies under 1°C warming period (red) and NAT (blue) forcing for CanESM2. (f) PDFs of spring temperature anomalies in 2018 under ALL (red) and NAT (blue) forcing for HadGEM3-A-N216.

forcing and the historical SST pattern as simulated by HadGEM3-A; this similarity is not necessarily a proof that the two are the same in the real world because there are uncertainties from multiple sources. We note that the CanESM2 has a high climate sensitivity but the effect on the estimation of risk ratio has already been accounted for. HadGEM3-A has a smaller long-term trend than the observations but this is not necessarily an indication of underestimation by the model. The external forcing and natural variability may have both contributed to the trend since the observed trend is more comparable to simulations by a high sensitivity model. More careful analyses are required to better quantify the role of human influence and natural variability in the occurrence of event like 2018 spring temperature anomalies. Nevertheless, to first-order approximation, human influence has clearly increased the occurrence probability by 10–30 times of temperature extremes such as the 2018 event.

ACKNOWLEDGMENTS. We thank three anonymous reviewers for their helpful suggestions. Y. S., S. D., and T. H. are supported by China funding agencies through multiple grants: China 2018YFC1507702, NSFC 41675074, 2018YFA0605604, CCSF 201805 and CCSF201906. PAS was supported by the U.K.-China Research and Innovation Partnership Fund through the Met Office Climate Science for Service Partnership (CSSP) China as part of the Newton Fund, the EUCLEIA project funded by the European Union's Seventh Framework Programme [FP7/2007–13] under Grant Agreement 607085 and by the Joint U.K. DECCBEIS/Defra Met Office Hadley Centre Climate Programme (GA01101).

REFERENCES

Allen, M. R., and Coauthors, 2018: Framing and context. Global Warming of 1.5°C. An IPCC Special Report on the impacts of global warming of 1.5°C above pre-industrial levels and related global greenhouse gas emission pathways, in the context of strengthening the global response to the threat of climate change, sustainable development, and efforts to eradicate poverty, V. Masson-Delmotte et al., Eds., https://www.ipcc.ch/site/assets/uploads/sites/2/2019/05/SR15_Chapter1_Low_Res.pdf.

Arora, V. K., and Coauthors, 2011: Carbon emission limits required to satisfy future representative concentration pathways of greenhouse gases. *Geophys. Res. Lett.*, **38**, L05805, https://doi.org/10.1029/2010GL046270.

Christidis, N., P. A. Stott, A. A. Scaife, A. Arribas, G. S. Jones, D. Copsey, J. R. Knight, and W. J. Tennant, 2013: A new HadGEM3-A-based system for attribution of weather- and climate-related extreme events. *J. Climate*, **26**, 2756–2783, https://doi.org/10.1175/JCLI-D-12-00169.1.

Ciavarella, A., and Coauthors, 2018: Upgrade of the HadGEM3-A based attribution system to high resolution and a new validation framework for probabilistic event attribution. *Wea. Climate Extremes*, **20**, 9–32, https://doi.org/10.1016/j.wace.2018.03.003.

CMA, 2019: China Climate Bulletin 2018 (in Chinese with English abstract). China Meteorological Administration, 50 pp., http://www.cma.gov.cn/root7/auto13139/201903/t20190319_517664.html.

Fyfe, J. C., and Coauthors, 2017: Large near-term projected snowpack loss over the western United States. *Nat. Commun.*, **8**, 14996, https://doi.org/10.1038/ncomms14996.

IPCC, 2013: *Climate Change 2013: The Physical Science Basis.* T. F. Stocker et al., Eds., Cambridge University Press, 1535 pp.

Min, S. K., Y. Kim, S. Paik, M. Kim, and K. Boo, 2015: Anthropogenic influence on the 2014 record-hot spring in Korea [in "Explaining Extreme Events of 2014 from a Climate Perspective"]. *Bull. Amer. Meteor. Soc.*, **96** (12), S95–S99, https://doi.org/10.1175/BAMS-D-15-00079.1.

NCC, 2019: China Monthly Climate Bulletin 2018. National Climate Center of China Meteorological Administration, 10 pp., https://cmdp.ncc-cma.net/influ/moni_china.php.

NOAA National Centers for Environmental Information, 2018: State of the Climate: Global Climate Report for May 2018, accessed 5 April 2019, https://www.ncdc.noaa.gov/sotc/global/201805.

Rayner, N. A., D. E. Parker, E. B. Horton, C. K. Folland, L. V. Alexander, D. P. Rowell, E. C. Kent, and A. Kaplan, 2003: Global analyses of sea surface temperature, sea ice, and night marine air temperature since the late nineteenth century. *J. Geophys. Res.*, **108**, 4407, https://doi.org/10.1029/2002JD002670.

Song, L. C., Y. Sun, S. Y. Dong, B. T. Zhou, P. A. Stott, and G. Y. Ren, 2015: Role of anthropogenic forcing in 2014 hot spring in Northern China [in "Explaining Extreme Events of 2014 from a Climate Perspective"]. *Bull. Amer. Meteor. Soc.*, **96** (12), S111–S115, https://doi.org/10.1175/BAMS-D-15-00111.1.

Sun, Y., X. B. Zhang, F. W. Zwiers, L. C. Song, H. Wan, T. Hu, H. Yin, and G. Y. Ren, 2014: Rapid increase in the risk of extreme summer heat in Eastern China. *Nat. Climate Change*, **4**, 1082–1085, https://doi.org/10.1038/nclimate2410.

——, L. C. Song, H. Yin, X. B. Zhang, P. Stott, B. T. Zhou, and T. Hu, 2016: Human influence on the 2015 extreme high temperature events in Western China [in "Explaining Extreme Events of 2015 from a Climate Perspective"]. *Bull. Amer. Meteor. Soc.*, **97** (12), S102–S106, https://doi.org/10.1175/BAMS-D-16-0158.1.

Takahashi, C., M. Watanabe, H. Shiogama, Y. Imada, and M. Mori, 2016: A persistent Japanese heat wave in early August 2015: Roles of natural variability and human-induced warming [in "Explaining Extreme Events of 2015 from a Climate Perspective"]. *Bull. Amer. Meteor. Soc.*, **97** (12), S107–S112, https://doi.org/10.1175/BAMS-D-16-0157.1.

ATTRIBUTION OF THE 2018 OCTOBER–DECEMBER DROUGHT OVER SOUTH SOUTHERN AFRICA

Shingirai Nangombe, Tianjun Zhou, Lixia Zhang, and Wenxia Zhang

The HadGEM3 (CAM5) model suggests that anthropogenic emissions increased the chances of the October–December 2018 drought over the southernmost area of southern Africa by 1.4 (0.97–1.96) times [4.3 (3.43–5.46) times], with higher influence on reference evapotranspiration than on precipitation.

Across Africa, droughts are a major type of natural disaster and a household insecurity trigger. The south southern Africa region (SSA; encompassed by the 22°–35°S, 18°–32°E rectangle) experienced extremely poor rainfall during the first half [i.e., October–December 2018 (OND)] of the October 2018 to March 2019 rainfall season (Fig. 1a). The OND subseason marks the important first half of southern Africa's rainfall season (Landman and Mason 1999). Late rainfall onset dates normally lead to below normal seasonal rainfall in southern Africa (Dunning et al. 2016). Dry conditions during OND 2018 led to a 2-month delay in sowing in parts of southern Africa (SADC CSC 2018), which translated to reduced regional crop yield, where livelihoods are principally agriculture-based. In South Africa's large cereal-producing provinces, 40%–50% reduced rains delayed plantings and curbed sown areas (FAO 2019; FEWSNET 2019). Late rain onset acted as a disincentive to farmers to take risks of sowing outside of the optimal planting window (FAO 2019). This contributed to Zambia and South Africa (the main regional grain suppliers) recording below-average harvests, thereby reducing exportable surplus from 7.5 to 1.4 million tons (SADC RVAA 2019), hence affecting regional food security.

The poor rains were also accompanied by water loss through above average reference evapotranspiration (Fig. 1b). This exacerbated the drought impact, considering the region's large population. Water loss worsened the water supply situation since dam and river water levels were already low due to the three previous consecutive droughts (Richman and Leslie 2018).

This study investigates how extreme the OND 2018 SSA drought was, and explores the related anthropogenic influences.

DATA AND METHODS. Gridded observational temperature, from the Global Historical Climatology Network Gridded v2 and Climate Anomaly Monitoring System dataset (GHCN-CAMS; Fan and van den Dool 2008) is used here available at 0.5° horizontal grid resolution. A precipitation average of the Global Precipitation Climatology Centre v2018 (GPCC-FD v2018; Schneider et al. 2015) dataset available at 1° horizontal grid resolution and the Climate Research Unit v4.0.3 (CRU-TS 4.03; Harris et al. 2014) dataset available since 1901 at 0.5° horizontal resolution is also utilized.

Two C20C+ Detection and Attribution project (Folland et al. 2014; Stone et al. 2019) global mod-

AFFILIATIONS: Nangombe—LASG, Institute of Atmospheric Physics, Chinese Academy of Sciences, Beijing, China; Meteorological Services Department, Harare, Zimbabwe; University of Chinese Academy of Sciences, Beijing , China; Zhou—LASG, Institute of Atmospheric Physics, Chinese Academy of Sciences, Beijing, China; CAS Centre for Excellence in Tibetan Plateau Earth Sciences, Chinese Academy of Sciences, Beijing, China; University of Chinese Academy of Sciences, Beijing, China; Zhang—LASG, Institute of Atmospheric Physics, and CAS Centre for Excellence in Tibetan Plateau Earth Sciences, Chinese Academy of Sciences, Beijing, China; Zhang—LASG, Institute of Atmospheric Physics, Chinese Academy of Sciences, Beijing, China
CORRESPONDING AUTHOR: Shingirai Nangombe, ssnangombe@lasg.iap.ac.cn

DOI:10.1175/BAMS-D-19-0179.1

A supplement to this article is available online (10.1175/BAMS-D-19-0179.2)

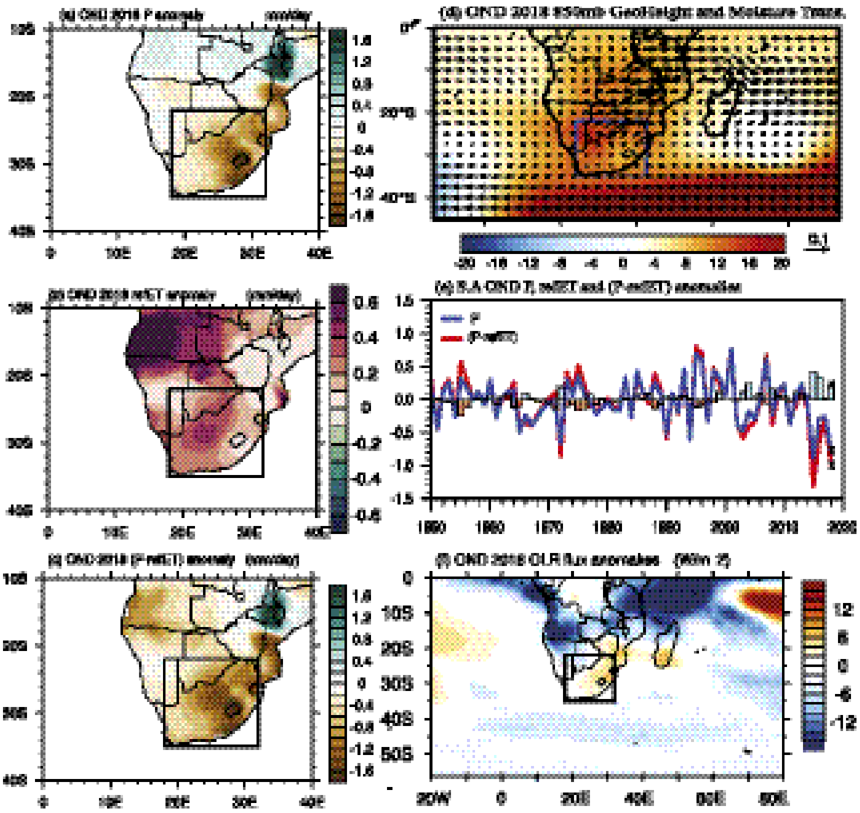

Fig. 1. The OND 2018 anomalies of (a) precipitation derived from the GPCC and CRU averaged datasets, (b) reference evapotranspiration calculated from GHCN-CAMS, and (c) difference between precipitation and reference evapotranspiration (*P*-refET) denoting the drought index. (d) Map of geopotential height (shading; hPa) and moisture transport (vector; kg kg^{-1} m s^{-1}) anomalies at 850 hPa during OND 2018 derived from the JRA-55 reanalysis (Kobayashi et al. 2015). (e) SSA area-averaged OND P (blue) and *P*-refET (red) with overlaid refET (sky-blue and brown bars). (f) Map of OND 2018 outgoing longwave radiation flux anomalies (W m^{-2}). SSA is shown by a black box in (a)–(d) and (f). All the anomalies are calculated from a 1960–2013 climatology. The units are in mm day^{-1} unless stated otherwise.

els are employed here in evaluating anthropogenic influence on this drought occurrence: HadGEM3 (Ciavarella et al. 2018) and CAM5 (Risser et al. 2018). These comprise two suites of simulations representing the actual climate (All-Hist) and a hypothetical natural climate excluding anthropogenic influence (Nat-Hist). In HadGEM3, both All-Hist and Nat-Hist have 15 realizations ranging from 1960 to 2013; in CAM5, there are 50 realizations ranging from 1960 to 2017.

To factor in high temperatures, a drought index that incorporates reference evapotranspiration is used: specifically, OND averaged *P*-refET, where *P* and refET denote precipitation and reference evapotranspiration, respectively. The Hamon method is used to estimate refET (Haith and Shoemaker 1987) from temperature data using the *refevt_hamon* function (Brown et al. 2019). The online supplemental information and Eq. (7) in Haith and Shoemaker (1987) provide details of refET calculation.

The Gaussian distribution (Wellmer 1998) was fitted to the observed OND averaged data, and return period of the 2018 event derived, separately for *P*, refET, and *P*-refET. Using 810 and 2900 model years from HadGEM3 and CAM5 All-Hist simulations respectively, OND averaged *P*, refET, and *P*-refET indices were extracted. Then Gaussian distributions are fitted to the All-Hist-based indices and used to derive the drought events that have similar return periods as the 2018 observed one. Last, as in Stott et al. (2004) and Ma et al. (2017), the probability ratio (PR = P1 / P0) and the fraction of attributable risk (FAR = 1 – P0 / P1) are estimated, where P1 (P0) is the likelihood of an event occurring in the All-Hist (Nat-Hist) simulations. Here, a null hypothesis of existing human influence against an alternative hypothesis of no human influence on the drought occurrence is used. However, in some cases like precipitation where high model uncertainty exists, the null hypothesis may be disproved. A total of 1,000 bootstrapping samples are used to estimate the 5th–95th confidence intervals for PR and FAR.

RESULTS. The observed OND precipitation area-averaged over SSA in 2018 was 0.68 mm day^{-1} (46%) below normal (1960–2013 baseline), while refET was 0.23 mm day^{-1} above normal (Fig. 1e). These precipitation and refET anomalies were ranked as the second lowest and third highest since 1950, respectively. Consequently, *P*-refET was the second record-breaking event with -0.91 mm day^{-1} (–60%) anomaly (Figs. 1c,e) and a 72-yr return period. Precipitation (refET) had a 40-yr (32-yr) return period (not shown).

SSA in OND is normally characterized by northeasterly moisture transport from the tropical Indian Ocean (Fig. S1a), leading to precipitation. However, in 2018, there was weak southerly moisture flux into SSA (Fig. 1d). A cyclonic anomaly in the Indian and Atlantic Oceans dominated the 850-mb moisture flux, hence diverting moisture flow away from SSA (Fig. 1d). Moreover, late 2018 was associated with El Niño conditions (Fig. S1b). Typically, during El Niño in austral summer, southern Africa receives drought (Hoell and Cheng 2018; Manatsa et al. 2017) while temperatures are usually above average (Nangombe et al. 2018). Likewise, Figs. S1c and S1d show a positive (negative) relationship between the OND ENSO index and OND SSA refET (*P*-refET) index.

Meanwhile, using outgoing longwave radiation (OLR) as a proxy for tropical temperate trough (TTT) events, anomalously high OLR over SSA in OND 2018 indicates a decrease in convection linked to TTTs (Fig. 1f). TTTs are the main rainfall bearers to SSA (Cook et al. 2004). Therefore, sea surface temperatures in the Pacific and Indian Oceans accompanied by anomalous low TTTs over SSA contributed to below normal 2018 OND precipitation in SSA.

On evaluating the model performance, correlation coefficients of *P*-refET, *P*, and refET area-averaged over SSA between the HadGEM3 (CAM5) All-Hist ensemble-mean and observation are 0.36, 0.31, and 0.38 (0.34, 0.21, and −0.1), respectively, with about 1 to 2 mm day^{-1} overestimation of the models. All the correlations based on the HadGEM3 (CAM5) model are significant (insignificant) at the 0.05 level. Nonetheless, results from both models under All-Hist and Nat-Hist cover the observed range (Figs. S2a,b). Additionally, there are statistical similarities between the density distributions of the All-Hist simulations and observation/reanalysis (Figs. S2c,d), hence our confidence in using these models.

In exploring the anthropogenic influence, CAM5 depicts a distinct leftward shift of the probability functions of the OND P-refET in All-Hist compared to Nat-Hist, while HadGEM3 suggests a slight shift (Figs. 2a,b). This signifies a likely anthropogenic influence on *P*-refET in the SSA. The shift is even more pronounced for refET, albeit in the rightward direction (Figs. 2e,f). Conversely, for precipitation, there is no obvious shift in All-Hist compared to Nat-Hist simulations of HadGEM3, while CAM5 depicts a moderate shift (Figs. S2e,f). In HadGEM3 (CAM5), −2.02 mm day^{-1} (−1.79 mm day^{-1}) of *P*-refET is selected as the threshold for attribution of SSA drought since it has a return period similar to the observed 2018 *P*-refET. For refET (*P*), the thresholds used are 3.32 (1.33) mm day^{-1} and 3.59 (1.84) mm day^{-1}, respectively. The HadGEM3 (CAM5) model estimates PR and FAR to be 1.36 (0.97–1.96) [4.34 (3.43–5.46)] and 26% (−3% to 49%) [77% (71%–82%)], respectively, for *P*-refET. The attributable influence from anthropogenic forcings is weaker in HadGEM3 than in CAM5, as the lower bound of the confidence interval of PR from HadGEM3 is slightly less than 1. Nonetheless, HadGEM3 simulations suggest PR and FAR values of 157.16 (86.90–310.74) and 99% (99%–100%) for refET while CAM5 suggests 105.75 (77.04–146.45) and 99% (99%–99%), respectively. We note that the PR and FAR estimates calculated from the CAM5 simulations are substantially affected by the nonstationarity of the ALL-Hist simulations (in terms of greenhouse gas concentrations) compared to estimates from the HadGEM3 simulations (not shown).

Furthermore, using simulations from composite El Niño years in estimating P-refET, HadGEM3 and CAM5 estimate PR values of 0.75 (0.24–2.77) and 2.19 (0.68–8.03) respectively. Thus, comparing with the other PR values, this portrays a reduction in the anthropogenic influence on drought of similar magnitude to that of OND 2018 in SSA during El Niño years.

Examining precipitation associated with the 2018 drought, CAM5 estimates the related PR (FAR) to be 1.95 (1.63–2.33) [49% (39%–57%)], whereas HadGEM3 suggests 0.76 (0.59–0.98) and −32% (−2% to −69%) PR (FAR) values, respectively, hence implying a reduced probability of occurrence due to anthropogenic forcing. Thus, comparing the two models, the anthropogenic forcing impact on precipitation-based drought in SSA is uncertain. Also, Yuan et al. (2018) highlighted that the major sources of uncertainty in detecting/attributing flash droughts over southern Africa are soil moisture and precipitation variation. Plus, the interannual variability of precipitation is much higher in African regions, hence making it difficult to distinguish anthropogenic signal from noise (Otto et al. 2013). Nonetheless, although low precipitation seasons such as OND 2018 are not necessarily more likely due to anthropogenic emissions, they may have severe impacts in an anthropogenically warmed world due to increased temperatures and hence increased refET.

CONCLUDING REMARKS. SSA experienced an extreme drought event in OND 2018 accompanied by extremely low rainfall and high reference evapotranspiration. This translated to substantial delay in the planting season hence affected the regional 2018/19 crop yield where livelihoods are largely agriculture-based.

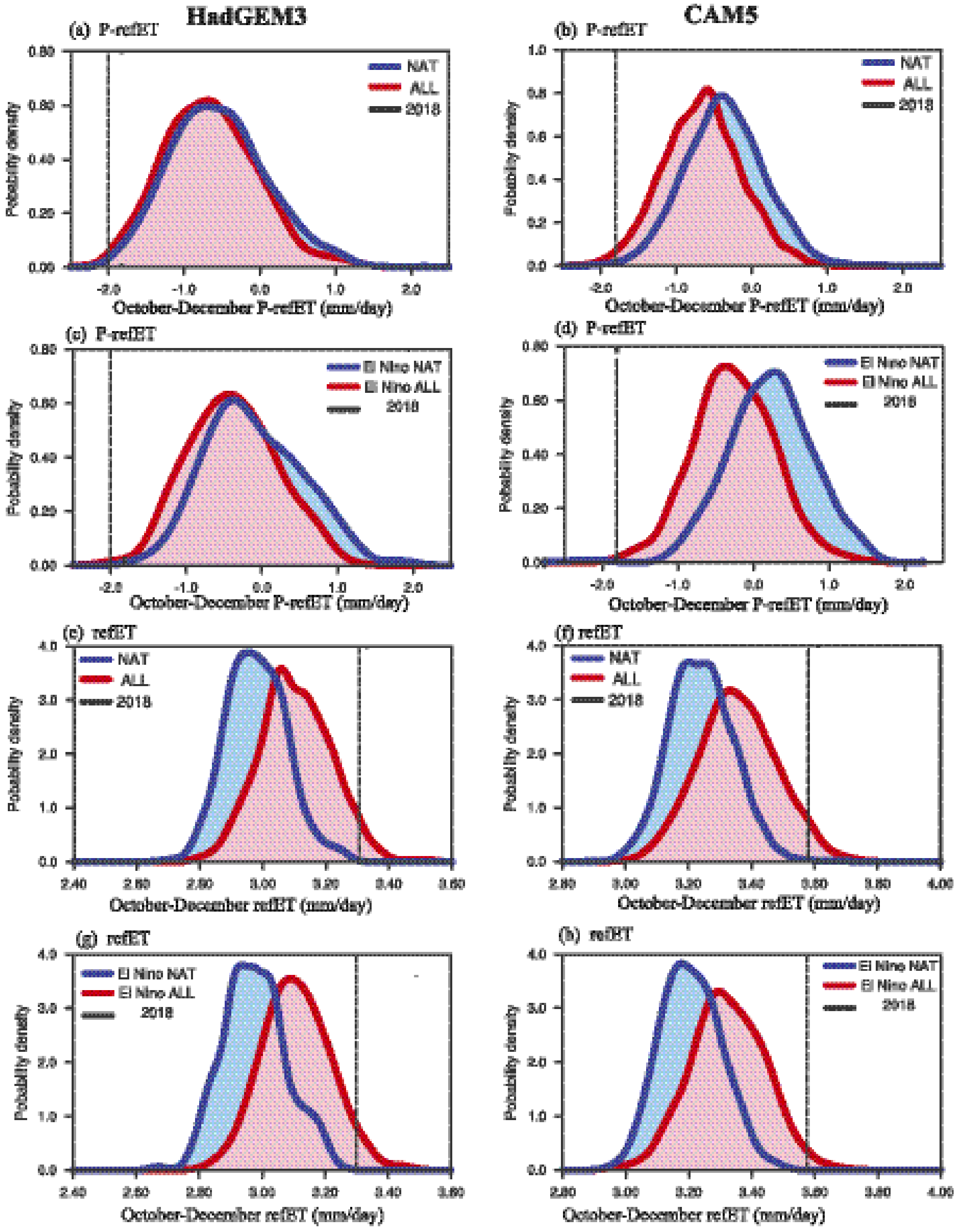

Fig. 2. HadGEM3's probability density functions (PDFs) of October–December (a) *P*-refET from all years, (c) *P*-refET El Niño years, (e) refET all years, and (g) refET El Niño years, area-averaged over the SSA region. (b),(d),(f),(h) As in (a),(c),(e),(g), but for the CAM5 model. All-Hist simulations and Nat-Hist simulations are represented by red and blue PDFs, respectively. The PDFs of HadGEM3 are based on 15-member realizations of both All-Hist and Nat-Hist ranging from 1960 to 2013 while CAM5 PDFs are based on 50-member realizations of both All-Hist and Nat-Hist ranging from 1959 to 2016. The dashed lines are the thresholds similar to the observed 2018 values. PDFs are calculated by the Gaussian kernel density estimator.

Here, the HadGEM3 model suggests that anthropogenic influence may have increased the probability of SSA droughts, such as the OND 2018 drought (*P*-refET), by 1.4 times [0.97, 1.96], and the CAM5 model indicates 4.3 times [3.43, 5.46]. The high anthropogenic influence on refET mostly contributed to this drought occurrence. El Niño conditions may also have had an influence. Therefore, the increase in temperature accompanied by rainfall decrease projected over southern Africa might result in increase in drought occurrence of at least OND 2018 magnitudes in the future (Kusangaya et al. 2014; Niang et al. 2014; Maúre et al. 2018; Nikulin et al. 2018; Nangombe et al. 2018).

ACKNOWLEDGMENTS. This research was supported by the National Natural Science Foundation of China Grants 41661144009 and 41675076. The first author is a recipient of a research studentship provided by the CAS-TWAS President fellowship. Special thanks go to the C20C+ Detection and Attribution project for providing global models we used.

REFERENCES

Allen, R. G., L. S. Pereira, D. Raes, and M. Smith, 1998: Crop evapotranspiration—Guidelines for computing crop water requirements. FAO Irrigation and Drainage Paper 56, 300 pp., www.fao.org/docrep/X0490E/X0490E00.htm.

Brown, D., R. Brownrigg, M. Haley, and W. Huang, 2019: The NCAR NCAR Command Language (NCL) (version 6.6.2). UCAR/NCAR Computational and Information Systems Laboratory.Command Language. https://doi.org/10.5065/D6WD3XH

Ciavarella, A., and Coauthors, 2018: Upgrade of the HadGEM3-A based attribution system to high resolution and a new validation framework for probabilistic event attribution. *Wea. Climate Extremes*, **20**, 9–32, https://doi.org/10.1016/j.wace.2018.03.003.

Compo, G. P., and Coauthors, 2011: The Twentieth Century Reanalysis Project. *Quart. J. Roy. Meteor. Soc.*, **137**, 1–28, https://doi.org/10.1002/qj.776.

Cook, C., C. J. C. Reason, and B. C. Hewitson, 2004: Wet and dry spells within particularly wet and dry summers in the South African summer rainfall region. *Climate Res.*, **26**, 17–31, https://doi.org/10.3354/cr026017.

Fan, Y., and H. van den Dool, 2008: A global monthly land surface air temperature analysis for 1948–present. *J. Geophys. Res.*, **113**, D01103, https://doi.org/10.1029/2007JD008470.

Dunning, C. M., E. C. L. Black, and R. P. Allan, 2016: The onset and cessation of seasonal rainfall over Africa. *J. Geophys. Res.,* **121,** 11 405–11 424, https://doi.org/10.1002/2016JD025428

FAO, 2019: Southern Africa: Dry weather conditions reduce agricultural production prospects in 2019, Food and Agriculture Organization of the United Nations, 4 pp., https://reliefweb.int/sites/reliefweb.int/files/resources/ca3071en_0.pdf.

FEWSNET, 2019: Delayed start of season and significant rainfall deficits negatively impacting cropping conditions. Famine Early Warning System Network, 2 pp., https://fews.net/southern-africa/alert/february-1-2019.

Folland, C., D. Stone, C. Frederiksen, D. Karoly, and J. Kinter, 2014: The International CLIVAR Climate of the 20th Century Plus (C20C+) Project: Report of the Sixth Workshop. *CLIVAR Exchanges*, CLIVAR, Southampton, United Kingdom, 57–59, https://crd.lbl.gov/assets/pubs_presos/FollandCStoneDetalii2014.pdf.

Haith, D. A., and L. L. Shoemaker, 1987: Generalized watershed loading functions for stream flow nutrients. *J. Amer. Water Resour. Assoc.*, **23**, 471–478, https://doi.org/10.1111/j.1752-1688.1987.tb00825.x.

Harris, I., P. D. Jones, T. J. Osborn, and D. H. Lister, 2014: Updated high-resolution grids of monthly climatic observations—The CRU TS3.10 dataset. *Int. J. Climatol.*, **34**, 623–642, https://doi.org/10.1002/joc.3711.

Hoell, A., and L. Cheng, 2018: Austral summer southern Africa precipitation extremes forced by the El Niño–Southern Oscillation and the subtropical Indian Ocean dipole. *Climate Dyn,* **50**, 3219–3236, https://doi.org/10.1007/s00382-017-3801-z.

Kalnay, E., and Coauthors, 1996: The NCEP/NCAR 40-Year Reanalysis Project. *Bull. Amer. Meteor. Soc.*, **77**, 437–471, https://doi.org/10.1175/1520-0477(1996)077<0437:TNYRP>2.0.CO;2.

Kobayashi, S., and Coauthors, 2015: The JRA-55 reanalysis: General specifications and basic characteristics. *J. Meteor. Soc. Japan*, **93**, 5–48, https://doi.org/10.2151/jmsj.2015-001.

Kusangaya, S., M. L. Warburton, E. A. van Garderen, and G. P. Jewitt, 2014: Impacts of climate change on water resources in southern Africa: A review. *Phys. Chem. Earth*, **67–69**, 47–54, https://doi.org/10.1016/j.pce.2013.09.014.

Landman, W. A., and S. J. Mason, 1999: Operational long-lead prediction of South African rainfall using canonical correlation analysis. *Int. J. Climatol.* **19**, 1073–1090, https://doi.org/10.1002/(SICI)1097-0088(199908)19:10<1073::AID-JOC415>3.0.CO;2-J

Ma, S., T. Zhou, O. Angélil, and H. Shiogama, 2017: Increased chances of drought in southeastern periphery of the Tibetan Plateau induced by anthropogenic warming. *J. Climate*, **30**, 6543–6560, https://doi.org/10.1175/JCLI-D-16-0636.1.

Manatsa, D., T. Mushore, and A. Lenouo, 2017: Improved predictability of droughts over southern Africa using the standardized precipitation evapotranspiration index and ENSO. *Theor. Appl. Climatol.*, **127**, 259–274, https://doi.org/10.1007/s00704-015-1632-6.

Maúre, G., and Coauthors, 2018: The southern African climate under 1.5°C and 2°C of global warming as simulated by CORDEX regional climate models. *Environ. Res. Lett.*, **13**, 065002, https://doi.org/10.1088/1748-9326/aab190.

Nangombe, S., T. Zhou, W. Zhang, B. Wu, S. Hu, L. Zou, and D. Li, 2018: Record-breaking climate extremes in Africa under stabilized 1.5°C and 2°C global warming scenarios. *Nat. Climate Change*, **8**, 375–380, https://doi.org/10.1038/s41558-018-0145-6.

Niang, I., O. C., Ruppel, M. A., Abdrabo, C. Essel, J. Padgham, P. Urquhart, K. K. E. Abdrabo, 2014: Africa. *Climate Change 2014: Impacts, Adaptation and Vulnerability*, Cambridge University Press, 1199–1265, https://doi.org/10.1017/CBO9781107415386.002.

Nikulin, G., and Coauthors, 2018: The effects of 1.5 and 2 degrees of global warming on Africa in the CORDEX ensemble. *Environ. Res. Lett.* **13**, 065003, https://doi.org/10.1088/1748-9326/aab1b1.

Otto, F. E. L., R. G. Jones, K. Halladay, and M. R. Allen, 2013: Attribution of changes in precipitation patterns in African rainforests. *Philos. Trans. Roy. Soc. London*, **B368**, 20120299 https://doi.org/10.1098/rstb.2012.0299.

Poli, P., and Coauthors, 2016: ERA-20C: An atmospheric reanalysis of the twentieth century. *J. Climate*, **29**, 4083–4097, https://doi.org/10.1175/JCLI-D-15-0556.1.

Richman, M. B., and L. M. Leslie, 2018: The 2015–2017 Cape Town drought: Attribution and prediction using machine learning. *Procedia Comput. Sci.*, **140**, 248–257, https://doi.org/10.1016/j.procs.2018.10.323.

Risser, M. D., and Coauthors, 2018: A basis set for exploration of sensitivity to prescribed ocean conditions for estimating human contributions to extreme weather in CAM5.1-1degree. *Wea. Climate Extremes*, **19**, 10–19, https://doi.org/10.1016/j.wace.2017.12.003.

SADC CSC, 2018: Early warning bulletin update of the 2018-19 southern Africa regional rainfall season. Southern African Development Community Climate Services Centre, 14 pp., https://www.sadc.int/files/8715/4764/2883/SADC_CSC_Regional_Early_Warning_Bulletin_Update_for_2018-19_Rainfall_Season.pdf.

SADC RVAA, 2019: Synthesis report on the state of food and nutrition security and vulnerability in southern Africa 2019. Southern African Development Community Regional Vulnerability Assessment and Analysis Programme, 21 pp., https://reliefweb.int/sites/reliefweb.int/files/resources/SADC_2019_Synthesis_Report_on_the_State_of_Food_and_Nutrition_Security_and_Vulnerability_in_Southern_Africa.pdf.

Schneider, U., and Coauthors, 2015: GPCC full data reanalysis version 7.0 at 0.5°: Monthly land-surface precipitation from rain-gauges built on GTS-based and historic data. Global Precipitation Climatology Centre, accessed 14 April 2019, https://doi.org/10.5676/DWD_GPCC/FD_M_V6_050.

Stone, D. A., and Coauthors, 2019: Experiment design of the international CLIVAR C20C+ detection and attribution project. *Wea. Climate Extremes*, **24**, 100206 https://doi.org/10.1016/j.wace.2019.100206.

Stott, P. A., D. A. Stone, and M. R. Allen, 2004: Human contribution to the European heatwave of 2003. *Nature*, **432**, 610–614, https://doi.org/10.1038/nature03089.

Wellmer, F. W., 1998: The normal distribution. *Statistical Evaluations in Exploration for Mineral Deposits*, Springer, 27–30, https://doi.org/10.1007/978-3-642-60262-7_4.

Yuan, X., L. Wang, and E. F. Wood, 2018: Anthropogenic intensification of southern African flash droughts as exemplified by the 2015/16 season. *Bull. Amer. Meteor. Soc.*, **99**, S86–S90, https://doi.org/10.1175/BAMS-D-17-0077.1.